UNIVERSITY OF SOUTHAMPTON

FACULTY OF ENGINEERING AND ENVIRONMENT

Fluid Structure Interactions Group

Application of 3-D CFD modelling for dynamic behaviour of Ship in waves

by

Lakshmynarayanana. P. Arun

Thesis for the degree of Doctor of Philosophy

April 2017

UNIVERSITY OF SOUTHAMPTON

ABSTRACT

Modern seakeeping computations are carried out using a variety of techniques ranging from two-dimensional (2-D) strip theory employing potential flow to three-dimensional (3-D) computations using fully nonlinear unsteady RANS (Reynolds-averaged Navier-Stokes equations) codes. The ever increasing size of ships and off-shore platforms has resulted in 'softer' hull which require hydroelastic effects to be taken into account when predicting fluid-structure interactions. Majority of such investigations are carried out numerically using potential flow solvers. Although nonlinear potential flow methods are also used, RANS/CFD can fully take into account the nonlinearities and viscous effects. It is important, therefore, to verify and validate the predictions from such numerical predictions.

This thesis aims to investigate the symmetric motions and responses of flexible floating bodies by coupling RANS/CFD and Finite Element software. The two-way interaction between a fluid solver, Star-CCM+, and a structural solver, Abaqus, is applied by exchanging pressures and nodal displacements more than once every time step, namely implicit scheme. A combination of overset and mesh morphing approaches and finite volume solution to allow for the motions of a body at the free surface is used. The air-water interface is captured using a VOF method and improved using HRIC scheme.

The proposed method is applied for a validation case for a flexible barge and a containership in regular head waves for a range of wave frequencies and wave heights. The computational results are compared with experimental measurements and 2-D linear hydroelastic predictions. It is shown that the numerical predictions of flexible bodies can be carried out using the present two-way coupling method. The nonlinearities in wave loads arising from severe flare impact and green water (containership) are well predicted, which also provides some initial insights into the nature of 2-node flexible component.

Table of Contents

List of Tables vii

List of Figures ix

DECLARATION OF AUTHORSHIP xv

Acknowledgements xvii

Nomenclature xix

Chapter 1: 1

Introduction 1

1.1 Motivation 1

1.2 Aims and Objectives 2

1.3 Thesis Structure 3

Chapter 2: 5

Literature Review 5

2.1 Historical Background 5

2.2 Strip Theory and 2-D methods 6

2.3 Influence of 3-D Geometry and Forward Speed 8

2.4 Nonlinear Rigid Ship Responses 10

2.5 Dynamics of Flexible Ship Structures 14

2.6 Nonlinear Hydroelasticity 16

2.7 Experimental Hydroelasticity 20

2.8 Fluid-Structure Interaction Methods and Instabilities 21

2.9 CFD/RANS Approach 24

2.10 Conclusions from Literature Review 30

Chapter 3: 33

Numerical Methods 33

3.1 Computational Methods for fluid flows 33

3.2 Selection of CFD software 34

3.3 Finite Volume Method 35

3.4 Equation Constraints and Solution 38

3.4.1 Numerical Boundary Constraints 38

3.4.2 SIMPLE Algorithm 38

3.4.3 Under Relaxation Factor 39

3.4.4 Temporal discretisation 39

3.4.5 Overset Mesh for motion 40

3.5 Finite Element method 40

3.5.1 Numerical method and solution to equations 40

3.5.2 Element formulation 42

3.6 Coupling of CFD and FEM 44

3.7 Co-Simulation between Star-CCM+ and Abaqus 45

3.7.1 Coupling schemes 45

3.7.2 Field exchange 46

3.7.3 Grid Adaptation 47

3.7.4 Data mappers 48

3.7.5 Time and Motion in coupling 48

3.8 2-D Linear Hydroelasticity 49

3.9 Verification and Validation 49

3.10 Chapter Summary 50

Chapter 4: **51**

Numerical Wave Tank **51**

4.1 Wave simulations **51**

4.1.1 Simulation Details 51

4.1.2 Results and Discussion 54

4.1.2.1 Results for 350m wave 54

4.1.2.2 Results for 700m wave 61

4.1.2.3 Results for 70m wave 62

4.1.2.4 3-D numerical wave tank 64

4.2 Chapter Summary **66**

Chapter 5: **67**

Response of Barge in waves **67**

5.1 Barge Characteristics **67**

5.2 Test Cases **69**

5.3 Computational Domain **70**

5.4 Meshing Strategy & Boundary Conditions **71**

5.5 Rigid body Simulations **74**

5.5.1 Boundary Conditions, Motion & Solver settings 74

5.6 Co-Simulation of the barge **76**

5.6.1 Time discretisation of Flexible barge simulations 77

5.6.2 Boundary Conditions, Motion and Solver Settings 79

5.6.3 FE Model 81

5.7 Results and Discussion **83**

5.7.1 Modal Analysis 83

5.7.2 Vertical Displacement in waves 84

5.7.3 Vertical bending moments and shear forces in waves 90

5.7.4 Influence of nonlinearities 95

5.7.5 Verification assessment 97

5.8 Conclusions **100**

Chapter 6: **103**

Wave loads on a flexible containership **103**

6.1 Review of Experiments **103**

6.2 Experimental Measurements **105**

6.2.1 Model Particulars 105

6.2.2 Test Matrix and Measurements 106

6.2.3 Computational Domain and Grid Design 109

6.2.4 F E model of S-175 114

6.2.5 Boundary Conditions and Solver Settings 118

6.3 Results and Discussion **120**

6.3.1 Modal Analysis 120

6.3.2 Regular wave measurements 121

6.3.3 Heave, Pitch and Vertical Acceleration in waves 123

6.3.4 Vertical Bending Moments in waves 129

6.3.5 Nonlinear effects in wave load of S-175 in head waves 140

6.3.6 Effect of structural damping on the wave loads 156

6.3.7 Asymmetry in Hogging and Sagging wave loads 162

6.4 Conclusions **163**

Chapter 7: **165**

Conclusions and Recommendations **165**

7.1 Motion and responses of S-175 containership **1685**

7.2 Numerical wave simulations **168**

7.3 Fluid and structural meshing strategy **168**

7.4 FSI coupling settings **170**

7.5 Wave Loads **171**

7.6 Future work 172

References 174

Appendix A 185

Appendix B 194

Appendix C 204

List of Tables

Table 1 : Different Levels of nonlinearity 11
Table 2: Comparisons between State-of-Art CFD methods 25
Table 3: Morpher Boundary Condition 49
Table 4 : Summary of wavelengths investigated and their respective domain sizes 52
Table 5: Mesh configuration for various refinement 53
Table 6: Wave Test cases 53
Table 7: Absolute Maximum difference for cell refinements in x direction 55
Table 8: Absolute maximum difference for cell refinement in y direction 58
Table 9: Barge characteristics 68
Table 10: Measuring points from aft of barge 69
Table 11: Test Conditions 70
Table 12: Domain sizes for regular wave periods and lengths (*port side only) 71
Table 13: Boundary condition for rigid body case 74
Table 14: Solver settings for rigid body case 76
Table 15: Relationship between the beam cross-section and critical time step 79
Table 16: Solver settings for co-simulation 81
Table 17: Material and Geometric data of FE model 81
Table 18: Symmetric Dry Hull natural frequencies (rad/s) 83
Table 19: Relative percentage error of vertical displacements between experiments and coupled simulations 87
Table 20: Relative percentage error of VBM amidships between 2-D and coupled simulations 93
Table 21: Relative percentage error in VBM between 2-D and coupled simulations for smaller wave 96
Table 22: Three different grid levels used for verification studies and 99
Table 23: Grid Convergence verifications parameters for three variables namely the vertical displacements amidships, vertical force and the vertical bending moment amidships 100
Table 24: Principal particulars of S-175 containership (Wu et al. 2003) in full scale and model scale. * denotes the values calculated as per the law of similitude. 106

Table 25: Summary of certain key model and boundary conditions from the experiments 107
Table 26: S-175 test cases simulated using the coupling technique. 107
Table 27: Model locations where the motions and responses are calculated 107
Table 28: Distances in meters and with respect to the length between perpendiculars ($L_{pp)}$ of various boundaries in the CFD model from the ship. 111
Table 29: Total cell count of the fluid grid showing the distribution in the boundary and overset regions. 113
Table 30: S-175 F E model sectional properties 116
Table 31: The boundary conditions used in the CFD model 118
Table 32: The solver settings and parameters in the CFD model 119
Table 33: Dry natural symmetric frequencies (Hz/rad/s) of the S-175 FE model 120
Table 34: Average wave heights from the simulations for 10 wave periods 122
Table 35: Heave calculated for two wave frequencies with and without viscosity compared with experimental measurements and 2-D linear 126
Table 36: VBM amidships for two wave conditions (H/L=1/50) in zero speed condition. 130
Table 37: Comparison between various grid configurations used to estimate the responses for λ/L=2.0 131
Table 38: Non-linear strip theory methods (ISSC. 2000) used for comparison with the coupled analysis 134
Table 39: Relative percentage difference of VBM amidships between the experiments and present predictions at all locations and wave frequencies investigated for H=L/50. The values in brackets are for H=L/30. 136
Table 40: Relationship between the wave encounter frequency and the 2-node component calculated in the VBM amidships using FFT and their respective higher-order. 154
Table 41: Ratio of sagging/hogging for different wave frequencies. * corresponds to H/L=1/30 163

List of Figures

Figure 1: Mesh refinement on free surface 52
Figure 2: Time history of wave elevation for 350m wave for refinement in x direction 57
Figure 3: y (a) and x (b) orbital velocities for 350 m wave under wave crest (left) and trough (right) across depth for refinement in x direction 57
Figure 4: Pressure variation across depth for 350 m wave under wave crest (left) and trough (right) for refinement in x direction 58
Figure 5: Time history of wave elevation for 350m wave for refinement in y direction 59
Figure 6 : y (a), x (b) orbital velocities and pressure variation (c) across depth for 350m wave under crest (left) and trough (right) for refinement in y direction 60
Figure 7 : Time history of wave elevation for 1st order and 2nd order time discretisation 60
Figure 8 : Time history of wave elevation for 700m wave 61
Figure 9: y (a), x (b) orbital velocities and pressure variation (c) across depth for 700 m wave under crest (left) and trough (right) 62
Figure 10: Time history of wave elevation for 70 m wave compared with theoretical wave elevation for 2 different time steps 63
Figure 11: y (a), x (b) orbital velocities across depth for 70 m wave under crest (left) and trough (right) 64
Figure 12: Time history of wave elevation for 700m wave for 3-D domain 65
Figure 13: Time history of wave elevation for 350m wave for 3-D domain 65
Figure 14: Time history of wave elevation for 70m wave for 3-D domain 66
Figure 15: Hydroelastic model of the flexible barge used in the experiments 68
Figure 16: Mesh distribution and refinement on the free surface and body for wave period of 1.8 sec. 73
Figure 17: Mesh configurations for flexible barge for a wave frequency of 1.2 s 80
Figure 18: Finite Element mesh with beam and dummy surface linked using kinematic coupling 83
Figure 19: Plot of mode shape obtained from MARS and Abaqus 84
Figure 20: Contour plots of mode shapes obtained from Abaqus 84

Figure 21: Wave elevation at L_{pp} in front of the barge for 1.6 secs wave. 85
Figure 22: Heave, Pitch RAOs and principal coordinates of the barge 88
Figure 23: RAOs of vertical displacements along the barge, point 12 near the stern and point 1 near the bow, for both rigid and flexible body analyses 89
Figure 24: Instantaneous wave contour around the rigid body (a) and flexible (b) at 11.5s wave frequency of 3.926 rad/s 90
Figure 25: Instantaneous wave contour around the rigid body (a) and flexible (b) at 9. 5s wave frequency of 6.28 rad/s 90
Figure 26: RAOs of VBM and vertical displacement along the barge at x/L=0.33, 0.5, 0.66, and 0.83 92
Figure 27: RAOs of VSF along the barge at x/L=0.33, 0.5, 0.66, and 0.83 94
Figure 28: Instantaneous wave contour around the flexible body for wave height (a) 0.1m and (b) 0.02m at 15s wave frequency of 3.926 rad/s 95
Figure 29: Instantaneous wave contour around the flexible body for wave height (a) 0.1m and (b) 0.02m at 15s wave frequency of 5.235 rad/s 96
Figure 30: RAOs of VBM for two wave heights (0.1 m & 0.02 m) compared with 2-D linear. 97
Figure 31: Convergence of pressure on the barge for twelve arbitrary time steps in the coupled simulation for wave frequency of 5.235 rad/s 98
Figure 32: Pictorial representation depicting the side and top view of the point probes placed on the model to calculate responses (Chen et al. 2001). 108
Figure 33: Overview of the computational domain and the distances towards the boundaries from the body. The extent of the overset boundaries in the three-dimensions is also shown. 110
Figure 34: Three-dimensional representation of the fluid domain used for S-175 computations. The boundary on the far right corresponds to the inlet boundary 110
Figure 35: Grid refinement provided in the bow and wake region to capture the violent deck flows and the diffracted and radiated waves. 113
Figure 36: Contour plots of the CFD simulations for λ/L=1.3 showing significant amount of water on deck. 114
Figure 37: Perspective of S-175 FE model. The red coloured line is the beam model whose inputs are specified as per Table 29. 117

Figure 38: The time history of VBM amidships with and without the boundary condition to restrict the unphysical drift in longitudinal axis. H=L/50 and λ/L= 1.0. 118
Figure 39: The first four symmetric modes shapes of the FE model. 121
Figure 40: Non-dimensional amplitudes of second and third harmonics of the tested regular waves (H=L/50) 123
Figure 41: Non-dimensional heave amplitudes predicted from coupled simulations with other numerical and experimental measurements. 124
Figure 42: Comparison between the green water and flare impacts from the two wave heights investigated for λ/L=1.3. Contour plots a & c are for H/L=1/50 and b & d are for H/L=1/30. 127
Figure 43: Non-dimensional pitch amplitudes predicted from coupled simulations with other numerical and experimental measurements. 128
Figure 44: Non-dimensional vertical acceleration predicted from coupled simulations with other numerical and experimental measurements. 129
Figure 45: Non-dimensional second and third harmonics of vertical accelerations for the two wave heights investigated. 129
Figure 46: Non-dimensional amplitude of first harmonic VBM amidships calculated using coupling method and numerical and experimental measurements for two wave heights. 132
Figure 47: FFT signal for two wave frequencies (H/L=1/50). The non-dimensional first harmonic VBM amplitudes are plotted against the encounter frequency. The first peak is the wave frequency and subsequent ones are the higher harmonics 133
Figure 48: Non-dimensional amplitudes of first harmonic VBM amidships calculated by the coupled method and the weakly nonlinear methods by ISSC (2000). Measurements from Chen (2001) also shown. 135
. Figure 49: Non-dimensional amplitude of first harmonic VBM at Pt.1 (0.95 m from aft Lpp) calculated using coupling method and numerical and experimental measurements. 137
Figure 50: Non-dimensional amplitude of first harmonic VBM at Pt.2 (1.35.m from aft Lpp) calculated using coupling method and numerical and experimental measurements. 137

Figure 51: Non-dimensional amplitude of first harmonic VBM at Pt.4 (2.25 m from aft Lpp) calculated using coupling method and numerical and experimental measurements. 138
Figure 52: Non-dimensional amplitude of first harmonic VBM at Pt.5 (2.65 m from aft Lpp) calculated using coupling method and numerical and experimental measurements. 138
Figure 53: Non-dimensional amplitude of first harmonic VBM at Pt.1 (0.95 m from aft Lpp) calculated using coupling method and Wu & Hermunstad (2002). Experimental measurements of Chen (2001) & Watanabe (1989) also plotted for comparison 139
Figure 54: Non-dimensional amplitude of first harmonic VBM at Pt.5 (2.65 m from aft Lpp) calculated using coupling method and Wu & Hermunstad (2002). Experimental measurements of Chen (2001) & Watanabe (1989) also plotted for comparison. 140
Figure 55: Non-dimensional amplitudes of second harmonic component of VBM amidships. 141
Figure 56: Non-dimensional amplitudes of second harmonic component at Pt.5 (2.65 m from aft Lpp). 142
Figure 57: Non-dimensional amplitudes of second harmonic component at Pt.1 (0.95 m from aft Lpp). 143
Figure 58: Deck impact pressure at forward perpendicular for H/L=1/50 143
Figure 59: Deck impact pressure at forward perpendicular for H/L=1/30 144
Figure 60: Time instances of the coupled CFD simulations showing the bow emerging in and out of water surface. The left- side is for H/L=1/50 and right-side for H/L=1/30 145
Figure 61: Non-dimensional amplitudes of the third harmonics in VBM amidships. 147
Figure 62: Non-dimensional amplitudes of the third harmonics in VBM at Pt.5 (2.65 m from the aft perpendicular) 147
Figure 63: Non-dimensional amplitudes of the 2-node in VBM amidships 148
Figure 64: Percentage contribution of 2-node to total vertical bending moment in experiments (Chen et al. 2001) 149
Figure 65: Time histories of total VBM amidships from coupled simulations for four wave frequencies (H/L=1/50) (a) λ/L=1.0 (b) λ/L=1.1 (c) λ/L=1.2 (d) λ/L=1.3 149

Figure 66: Time history of total VBM from coupled simulation for λ/L=1.3 with no forward velocity.....150
Figure 67: FFT of the VBM amidships for λ/L=1.3 with no forward velocity.....151
Figure 68: FFT signals of the VBM amidships at certain frequencies emphasizing on the 2-node high frequency component.....155
Figure 69: FFT signals of the VBM amidships at wave frequencies exhibiting nonlinear higher order. 155
Figure 70: Non-dimensional amplitudes of first harmonic of VBM amidships compared with and without Rayleigh's structural damping in the FE model of S-175. 157
Figure 71: Non-dimensional amplitudes of second harmonic of VBM amidships compared with and without Rayleigh's structural damping in the FE model of S-175. 157
Figure 72: Non-dimensional amplitudes of third harmonic of VBM amidships compared with and without Rayleigh's structural damping in the FE model of S-175. 158
Figure 73: Non-dimensional amplitudes of 2-node flexible component of VBM amidships comparison with and without Rayleigh's structural damping in the FE model of S-175. 158
Figure 74: Time history of VBM amidships with and without damping in the FE model of S-175 159
Figure 75: Non-dimensional amplitude of 2-node flexible component of VBM at Pt.1 (0.95 m from aft Lpp) with and without Rayleigh's structural damping in the FE model of S-175. 160
Figure 76: Non-dimensional amplitude of 2-node flexible component of VBM at Pt.2 (1.35 m from aft Lpp) with and without Rayleigh's structural damping in the FE model of S-175. 160
Figure 77: Non-dimensional amplitude of 2-node flexible component of VBM at Pt.4 (2.25 m from aft Lpp) with and without Rayleigh's structural damping in the FE model of S-175. 161
Figure 78: Non-dimensional amplitude of 2-node flexible component of VBM at Pt.5 (2.65 m from aft Lpp) with and without Rayleigh's structural damping in the FE model of S-175. 161

Figure 79: Non-dimensional amplitudes of hogging and sagging VBM amidships with and without Rayleigh's structural damping is vs measurements from Chen (2001) 162

DECLARATION OF AUTHORSHIP

I, Puramharikrishnan Arun Lakshmynarayanana declare that this thesis entitled 'Application of 3-D CFD modelling for dynamic behaviour of a ship in waves' and the work presented in it are my own and has been generated by me as the result of my own original research.

I confirm that:

1. This work was done wholly or mainly while in candidature for a research degree at this University;
2. Where any part of this thesis has previously been submitted for a degree or any other qualification at this University or any other institution, this has been clearly stated;
3. Where I have consulted the published work of others, this is always clearly attributed;
4. Where I have quoted from the work of others, the source is always given. With the exception of such quotations, this thesis is entirely my own work;
5. I have acknowledged all main sources of help;
6. Where the thesis is based on work done by myself jointly with others, I have made clear exactly what was done by others and what I have contributed myself;
7. Either none of this work has been published before submission, [or] Parts of this work have been published as:

Signed:.....

Date: .....

Acknowledgements

I would like to express my gratitude to the University of Southampton who provided me this wonderful opportunity to pursue my PhD in this great country. I would like to render a special thanks my supervisors Professor Pandeli Temarel and Dr Zhimin Chen who have supported me and guided me every time, when I was in doubt. Their valuable ideas have helped me in the carrying out of the present work. I thank my internal examiner Professor Stephen Turnock for his valuable suggestions.

I thank the Star-CCM+ staff for their services and support. I would like to gratefully acknowledge my sponsors Lloyd's Register and Lloyd's Register Foundation through its University Technology Centre.

I would also like to thank all my family and friends, my brother and sister whose moral support has been invaluable.

I express my deep gratitude to my mother and wife whose patience and support have made all this possible. I dedicate this thesis to my one year old son Vyom and my late father.

Nomenclature

Symbols defined in the text are summarised in this section. All symbols used more than once are included in nomenclature. Where the same symbol has dual meanings, it is explicitly stated in the text. The co-ordinate system is Cartesian unless otherwise stated, i.e. (*x, y, z*) coordinates are used.

Latin Symbols

Symbol	Description	SI Units
A	area	$[m^2]$
a_f	face area	$[m^2]$
a_w	wave amplitude	$[m]$
B	breadth	$[m]$
b	body forces/ unit mass	$[Nkg^{-1}]$
b_φ	scalar sink	
C	damping	$[kgm^{-1}s^{-2}]$
C_A	non-dimensional acceleration	
C_M	non-dimensional bending moment	
C_Z	non-dimensional bending heave	
c	volume fraction	
f	natural frequency	$[Hz]$
G	shear modulus	$[kgm^{-1}s^{-1}]$
G_f	grid flux intensity	$[ms^{-1}]$
g	Acceleration due to gravity	$[ms^{-2}]$
H, H_w	Wave height	$[m]$
I	unit tensor	
I_{y0}	moment of inertia along y axis at the centroid	$[kgm^{-2}]$
I_{yy}	moment of inertia along y axis	$[kgm^{-2}]$
I_{yy}	moment of inertia along y axis	$[kgm^{-2}]$
K	stiffness	$[kgm^{-1}s^{-2}]$
K_a	shear stiffness	$[kgm^{-1}s^{-2}]$
k	wave number	$[m^{-1}s^{-1}]$
L	length	$[m]$
L_{pp}	length between perpendiculars	$[m]$
M	mass	$[kg]$
n	unit normal vector to surface	
S	surface	
T	stress tensor, time	$[kgm^{-1}s^{-2}]$,$[s]$

t	time	*[s]*
U	fluid velocity	*[ms^{-1}]*
u	displacement	*[m]*
$\dot{u}$	velocity	*[ms^{-1}]*
$\ddot{u}$	acceleration	*[ms^{-2}]*
$\bar{u}$	virtual displacement	*[m]*
V	volume	*[m^{3}]*
v	fluid velocity vector	*[ms^{-1}]*
v_b	velocity vector of control volume	*[ms^{-1}]*
v_g	grid velocity	*[ms^{-1}]*
Z	heave amplitude	*[m]*
$\ddot{Z}$	vertical acceleration	*[ms^{-2}]*

Greek symbols

Γ	diffusivity coefficient	*[m^{2}s^{-1}]*
Δ	infinitesimal change	
$\bar{\varepsilon}$	virtual strain	
ζ_a	surface wave amplitude	*[m]*
η	wave elevation	*[m]*
λ	wave length	*[m]*
ρ	fluid density	*[kgm^{-3}]*
σ	stress	*[kgm^{-1}s^{-2}]*
φ	transport variable (scalar)	
ω	wave frequency	*[rads^{-1}]*

Mathematical operators

∇	divergence
d/dt	time derivative

Abbreviations and acronyms

ALE	Arbitrary lagrangian-eulerian
BEM	Boundary element method
CAD	Computer aided-modelling
CG	Centre of gravity
CIP	Constrained Interpolation Profile

CFD	Computational fluid dynamics
CFL	Courant number
CV	Control volume
DES	Detached eddy simulation
DNS	Direct numerical simulation
FEA	Finite element analysis
FEM	Finite element method
FLNG	Floating liquefied natural gas
FPSO	Floating production storage and of-floading
FSI	Fluid structure interaction
FV	Finite volume
GCI	Grid convergence index
HRIC	High-resolution interface capturing
JIP	Joint industrial project
LES	Large eddy simulation
LNG	Liquefied natural gas
MEL	Mixed-eulerian lagrangian
MOL	Mitsui O. S. K. Lines
MPI	Moving-particle semi-implicit
MSC	Mediterranean Shipping Company
PDE	Partial differential equations
RANS	Reynolds-averaged Navier-Stokes
RAO	Response amplitude operator
SCF	Slenderness compensation factor
SPH	Smooth particle hydrodynamics
TEU	Twenty- foot equivalent unit
URANS	Unsteady Reynolds-averaged Navier-Stokes
URF	Under relaxation factor
VBM	Vertical bending moment
VOF	Volume of fraction
VSF	Vertical shear force
V&V	Verification and Validation

Chapter 1:

Introduction

1.1 Motivation

An accurate prediction of global wave-induced motions and loads is crucial in the design of ships and offshore platforms. In traditional seakeeping analysis, the structural responses of these structures are calculated considering them as rigid bodies. Increase in the size of ships and offshore platforms have resulted in flexible structures which require the dynamics of the structure to be taken into account when calculating motions and responses. In such cases, the response of the structure could significantly affect the flow field and the fluid loading, resulting in a fully coupled system. The study of this fully coupled fluid-structure interaction is termed as hydroelasticity. Hydroelastic effects can have an important influence on the global loads and bending moments of a realistic ship. The increased size of ships, particularly in length, has resulted in a lowering of the 2-node natural frequency of vibration of the hull (Hirdaris & Temarel 2009). Consequently, resonance can occur when the encountered frequency of the wave is close to the 2-node natural frequency, resulting in a phenomenon known as springing.

Springing is a wave-excited steady state global hydroelastic hull girder vibration which has a significant effect in the fatigue strength of ships (Bishop & Price 1979). Hydroelastic effects on ship structures can also be seen as a local phenomenon. Local bow and stern slamming in extreme sea condition can introduce ringing vibrations in a hull, known as whipping. The concept design of an 8100 TEU modern containership shows the hogging wave bending moments may increase by about 11% when whipping/springing are included in the computations. It increases to 42% in sagging wave bending moments (Hirdaris et al. 2010). Hence, the influence of hydroelastic responses is overwhelming and needs to be accurately evaluated.

The rule based approach adopted by Classification Societies for the design and calculation of the strength of ship structures is based on empirical formule derived from theory and experience. Hydroelastic effects are only considered as a small part of class rules structural design, while they can have a significant influence on

failure. The calculated design bending moments neglecting such effects for a large containership can be low compared to the required design values. The structural failures of ships such as MSC Napoli, MSC Carla, MOL Comfort etc. highlight the importance of hydroelaticity on structural design. Hence, it is important to improve the present design methods and carry out hydroelastic predictions early in the design stage of a vessel or offshore units like FPSO, FLNG etc.

Hydroelastic investigations are predominantly experimental, using flexible backbone models, or numerical ranging from linear to partially nonlinear potential flow solvers. The conventional linear hydroelasticity analyses, using 2D or 3D potential flow within a modal analysis framework and a beam or 3D finite element (FE) structural representation, are unable to capture violent free surface flows as a consequence of the assumptions involved. Incorporation of some nonlinear effects in the aforementioned analyses lead to some improvement in predictions depending, for example, on wave steepness (see chapter 2). Nevertheless, the improvements attained are constrained by environmental conditions and, naturally, do not allow for viscous effects which are quite important, for example, where roll motion is concerned.

The increase in computational power has made it possible to solve RANS equations computationally and apply them to predict performance of ships. RANS solvers can fully take into account the nonlinearities associated with free surface flows and also the viscous effects of the fluid. Investigations using RANS solvers to calculate wave-induced loads are predominantly using a one-way coupling, where the ship is considered rigid in the fluid solver and an added mass is included in the structural response calculations using finite element analysis (FEA). In a one-way coupling, the structural distortions do not have an effect on the fluid loading, thus omitting important fluid-structure interactions. A strong or two-way coupling between RANS/CFD and FEA codes have to be established to accurately model the hydroelastic behaviour of body floating/travelling in a seaway.

1.2 Aims and Objectives

This work is aimed at applying a coupling of CFD and FEA codes to model the 3-D dynamic behaviour of floating structures in waves, treated as flexible bodies. The fluid solver used for the applying the coupling is Star-CCM+ (version 8.04) and the

FEA code is Abaqus (version 6.13-1). The focus is on investigating the symmetric responses (vertical bending) of ships in regular waves in order to provide a unified method for predicting wave-induced loads and motions. The coupling technique will be first investigated and validated for a case of a flexible barge, due to the geometric simplicity and no forward speed. Motions and responses of the barge will be predicted using the coupling method and compared with experimental measurements and other available hydroelastic predictions. Subsequently, the coupling technique will be extended to a realistic ship, such as a large flexible containership, to calculate the wave-induced loads in regular waves. Special focus will be given to springing and influence of higher order wave harmonics. To help achieve this, the following objectives have been outlined, to:

- assess the suitability of Star-CCM+ to model a numerical wave tank using first and second order wave formulation, for different wave lengths.
- establish a clear understanding on the mesh density required in the wave propagation and wave height direction and their effect on the accuracy of the wave simulations.
- carry out spatial and temporal discretisation study on the numerical wave tank simulations.
- calculate the rigid body motions of a barge in regular head waves, for a range of wave frequencies.
- implement the coupling method, treating the barge as flexible, to calculate vertical displacements at a number of locations in regular head waves, for the same wave frequencies as above.
- calculate the wave-induced loads for the flexible barge in regular head wave and the occurrence of 2-node resonance and its influence on the wave-induced bending moment.
- investigate hydroelastic behaviour of a containership in regular head waves using the present coupling method to model global motions and responses.
- predict the 2-node resonance and higher order harmonic component of the wave loads of the containership .
- compare numerical predictions with various experimental measurements and identify areas of discrepancy.
- identify possible reasons and suggest methods to improve the accuracy of predictions.

1.3 Thesis Structure

Having given the motivation for the present research and the aims and objectives in this Chapter, Chapter 2 presents a review of the work carried out by various researchers to tackle ship-wave interaction problem. An insight into some historical

as well as landmark techniques are outlined before discussing in detail the existing computational work on hydroelasticity. Chapter 3 gives a summary of the numerical method implemented and the coupling technique used. The work carried out to achieve the research problem is divided into three chapters. Chapter 4 presents results to ascertain the suitability of Star-CCM+ to model a numerical wave tank, whilst Chapter 5 presents the results of motion response of a rigid and flexible barge in waves. Chapter 6 deals with the motions and wave load predictions of a containership model in regular head waves. The conclusions and future work plan is outlined in Chapter 7.

Chapter 2:

Literature Review

2.1 Historical Background

An in-depth understanding of the wave forces and moments acting on floating bodies is prudent in accurately predicting the responses, and further the design and strength of the structures. The pioneering work in examining the motion responses of ships in waves was carried out experimentally by Froude (1861) and Kriloff (1898). The studies presented by these 2 researchers laid down the classical definition of the "Froude-Kriloff" hypothesis, which quantifies the hydrodynamic pressure acting on the hull due to the incident wave.

The solution to the classical problem of the motion of water surface consisting of a travelling wave system due to local disturbances was given by Havelock (1929). These mathematical formulations using potential theory can be applied to the case of waves generated by small amplitude oscillations of a body. Around the same time Lewis (1929) carried out an evaluation of the 2-D boundary value problem of a vibrating ship by purely mathematical methods. His effort was to compute the added mass or 'water inertia effect', as referred in his paper, by using conformal mapping technique, which approximates the ship sections by what is popularly known as Lewis sections. Ursell (1949) investigated the added inertia of an infinitely long 2-D cylinder assumed to lie on a free surface, heaving with small amplitude about a mean position. He used an infinite series of multipoles to represent the divergent wave train and satisfy the frequency dependent free surface condition. The frequency dependent added mass coefficients were successfully obtained using this method and provided a rough estimate of the hydrodynamic coefficients for a ship at zero forward speed in regular waves.

Havelock (1945) made one of the first attempts to calculate the fluid damping force experienced by a vessel with zero forward velocity heaving and pitching in regular wave train. He later extended this work to investigate the damping coefficient for the simple case of a long narrow plank translating and pulsating in a fluid (Havelock 1958).

In reality, ocean waves are irregular and formulating all ship motion analysis using regular wave system was an obvious approximation made by the researchers. The application of spectral analysis by St.Denis & Pierson (1953) opened doors for the investigation of ship motions in irregular waves. Ship responses in irregular wave train can be considered as the sum of responses to regular waves whose amplitude is determined from a spectrum. Ship motions using linear theory could now be defined by a new quantity known as the Response Amplitude Operator, i.e. response to regular wave of unit amplitude. Wehausen & Laitone (1960) described a source distribution technique of a pulsating source for calculating the velocity potential Φ. These two theories put together started to be widely applied in formulating ship seakeeping problems numerically and for experimental setups.

2.2 Strip Theory and 2-D methods

The advent of strip theory in the 50's brought about the first motion theory suitable for numerical investigation of hydrodynamic problems of floating bodies. Korvin-Kroukovsky (1955) investigated a potential solution for the hydrodynamic coefficients of a ship heaving and pitching in regular waves using "strip method". In his theory the three dimensional ship was divided into a finite number of sections and each section was treated hydrodynamically as a section of an infinitely long cylinder. The resulting boundary value problem is simplified to a forced oscillation of cylinder and solved using potential theory. A sequel to this method was later published by Korvin-Kroukovsky & Jacobs (1957) and the 'ordinary strip method' predictions for two vessels were compared to experimental estimations. The wave exciting force is calculated using the "Froude-Kriloff" hypothesis and integrated on the mean wetted area of the hull.

Strip theory are based on a few assumptions which simplify the complex three dimensional boundary value problem into a two dimensional problem. All the waves that are produced by the ship are assumed to travel in the transverse direction only. The minimum L/B ratio of 3 justifies this assumption as the fluid velocities in the longitudinal direction would be much less than the transverse velocities. With small amplitude of motion and velocities and high frequency of oscillation, the free surface can be replaced by a zero speed condition and the kinematic boundary condition neglected.

A variant of the above theory presented by Ogilvie & Tuck (1969) considered the exact 3-D boundary value problem and then methodically simplified it to more or less the strip method, which they termed as the "rational" strip theory. Unfortunately the formulations presented were complex and some integrals were impossible to evaluate. Also the validity of predictions at lower frequencies and emergence of forward-speed only as higher order effects makes in unsatisfactory it a rational viewpoint. Salvesen et al. (1970) however, retained the forward-speed terms and presented a new strip theory for predicting heave, pitch, sway, roll and yaw motions of ships advancing at a constant forward velocity in oblique regular waves. This method was less complex than the "rational" strip theory and improved prediction in low frequency region.

Strip theories are known to give reasonable results in predicting motion for ships travelling at relatively low speed in waves of moderate amplitude. They are successfully applied to investigate vertical motions and loads but exhibit discrepancies for horizontal motions due to their inherent nonlinearity (ISSC 2012).

One of the drawbacks of the strip theory is that it is invalid at low encounter frequencies and does not provide a good insight into the forward speed effects or interference in the longitudinal direction. Slender body theory is another 2-D low-frequency method which assumes the wavelength to be large when compared to the beam and draft of the ship (Newman 1964). Newman (1977) established a good agreement at low forward speeds but it was not applicable to ships with higher forward speeds. Newman (1980) later provided a "unified" theory by amalgamating the high-frequency strip theory and the low-frequency slender body theory and this approach offers improvement in predictions over the other strip theories.

An entirely different method using boundary-integral equations for solving the 2-D boundary value problem was proposed by Frank (1967). He divided the body into a finite number of segments, N, a technique motivated by the strip method. At the centre of each segment a singularity, namely a source, a dipole or both are placed that has a known normal velocity for the motion of the cylinder. The singularities satisfied zero speed linearised free surface condition, Laplace equation and an appropriate condition at infinity. Velocity potential was expressed using Green's second identity. One of the shortcomings of this method is the presence of irregular frequencies where the integral equation employing Green's function fails to give a finite solution. The irregular frequencies have no physical significance. The multi

parameter conformal mapping provides improvement to Lewis form to describe hull forms more accurately and is computationally less expensive (Tasai 1960).

2.3 Influence of 3-D Geometry and Forward Speed

2-D Strip theory is less successful when applied to ships with forward speed due to the inherent assumptions. The boom in offshore industry required response prediction of non-slender floating structures, and strip theories are not valid for such cases. New methods which include 3-D and forward speed effects were sought. The majority of methods that emerged, which included 3-D and forward speed effects, were based on a singularity distribution.

Inglis & Price (1980) used strip theory formulations of Salvesen et al. (1970) to include forward speed effects into 3-D singularity distribution technique using a pulsating source. The singularities were based on the mean wetted surface. One major drawback of this method was that, unless the frequency of oscillation is high and speed is low, the velocity potential of the pulsating source failed to satisfy the speed dependent free surface condition. A more efficient method was developed and could be easily incorporated for ship response calculation (Inglis & Price 1981a). They calculated the velocity potential of a translating and pulsating unit source satisfying the exact speed and frequency dependent linearised free surface condition. The speed dependent term is retained in the linearised free surface condition. It was noted that the behaviour of the potential is more sensitive and influenced by forward speed effect than by frequency.

For forward speed condition, the total velocity potential can be separated into two parts: 1. Time independent steady component due to forward motion 2. Time dependent component associated with the incident wave and unsteady motions, which constituted of the incident, diffracted and radiation potentials (Salvesen et al. 1970). The steady flow problem is nonlinear and must be simplified before determining the unsteady velocity potential. This is carried out in two ways (Inglis & Price 1981b):

- The steady flow problem is solved and used to formulate the boundary conditions of the unsteady flow problem.
- The unsteady flow problem is directly solved neglecting the perturbations in steady flow.

The first method is rather difficult to apply as the steady flow problem is solved first by retaining the pulsating, translating source in body boundary condition. Inglis & Price (1981c) illustrated this method by using a combination of translating and pulsating source distribution technique and a three dimensional panel method to predict the heave, pitch, yaw and sway hydrodynamic coefficients for an ellipsoid moving forward and oscillating. It was noted that including the steady flow contribution in body boundary condition may cause significant changes in the hydrodynamic coefficients. The inclusion of interaction effect causes an increase in added mass/inertia coefficients in all modes of motion but this effect is small at higher frequencies. The assumption in second method implies that the ship is considered thin. Neglecting the perturbation in the steady flow and subsequently calculating the hydrodynamic coefficients have also shown good agreement with the zero speed case (Chang 1977). He compared two models (one which included speed modifications to free surface and another without it) with experiments. This method was validated for the zero speed case, but for the forward speed case computations without speed modifications in free-surface condition showed poor results.

Following this, Inglis & Price (1981a,b) provided an exhaustive review of three dimensional source distribution methods using different boundary conditions for forward speed case. The methods were validated for Series-60 model and hydrodynamic coefficients were obtained for head, bow and beam seas. It was noted that strip theories fails to take into account the wave scattering from ships and hence underestimates diffraction effects. Three dimensional methods were found to agree well with experiments, for zero-speed case. In forward speed, the predictions improved when the perturbations of steady flow are included in the boundary condition, but at the cost of high computational effort.

In the singularity distribution method or boundary integral method, the source strengths are derived by integral equation or Green's function and they satisfy the body boundary condition. It is a well-known fact that these integral equations do not produce finite solution at certain frequencies, which is termed as irregular frequencies. Their occurrences have been more evident after the introduction of computers to solve numerical problems. The positions of occurrence based on length, beam and draught of a floating body was provided by (Inglis & Price 1981b). In the case of a ship, they were observed at higher frequencies and their exact position could be estimated. If the ship is considered as flexible, these irregularities could

become a serious hurdle in predicting the responses since they occur at frequencies of resonance of ships (Inglis & Price 1982). Du et al. (2011) proved that the irregular frequency exists only for the zero speed case and not when forward speed is considered.

The 3-D potential flow problem is also solved using Boundary element method (BEM), commonly using the Rankine source method. The wetted surface of the hull and the free surface are discretised using panels. The panels must be refined enough to be able to capture the diffraction and radiated waves to sufficient accuracy. Rankine sources of known strengths are based on the body and free surface. In theory, the method is applicable to both linear and nonlinear free-surface condition and uses a simple Green function. Nakos & Sclavonous (1990) developed the program SWAN-1 in the frequency domain which was based on this method. The time domain variants were later developed by Nakos et al. (1993) and Huang & Sclavonous (1998) which were named as SWAN-2. The two programs were integrated into one system SWAN (Sclavonous et al. 1997). One of the draw back of the Rankine source method is the reflection of waves at the fluid domain boundaries. Numerical damping is required for this formulation at the far field to absorb outgoing waves and the damping has to be carefully designed for a wide range of frequencies. Apart from numerical damping at the outer edge, they also require a larger domain size to prevent these reflections. As an alternative formulation, the mixed-source formulation requires a matching surface; an outer surface surrounding the hull and free surface. The Rankine-source formulation is used in the inner fluid domain inside the matching surface and the outer fluid domain is formulated by transient Greens function. In terms of computational effort, mixed-source formulations are very time consuming as it requires computations of transient Greens function on the matching surface (Weems et al. 1998, Dai & Wu 2008).

2.4 Nonlinear Rigid Ship Responses

Nonlinearities in ship motions can be classified due to two major factors – free surface condition and body boundary condition. It is still very difficult and computationally expensive to consider the free surface nonlinearities. The second nonlinearity arises from body nonlinearities, i.e. the geometric change of hull shape under the free surface, which is easier to calculate. Commonly, nonlinear geometric cor-

rections to the Froude-Krylov force are incorporated by integrating pressures over the actual wetted surface of the hull. The nonlinearities in hydrodynamic effects are neglected and this is justified by the orders of magnitude of Froude-Krylov force. But for ship motions in steep seas, the nonlinear hydrodynamic effects can attain the same order of magnitude as the nonlinear Froude-Krylov force, hence, cannot be neglected (Huang & Sclavonous 1998).

For the forward speed case, different methods for motions and response prediction are available and can be classified into 6 levels (ISSC. 2009,2012) (see Table 1). The methods given in 2-4 are partially nonlinear:

Table 1 : Different Levels of nonlinearity

Level	Description
1. Linear	-hydrodynamic pressures evaluated on mean free surface -solved in frequency domain -linear strip theory and 3-D singularity techniques
2. Froude-Krylov nonlinear	-hydrostatic/Froude-Krylov force obtained on instantaneous position of hull under incident wave. -both time and frequency domain. -more preferred than Level 3 due to computational time. -LAMP-2
3. Body nonlinear	-disturbance potential obtained on instantaneous position of hull under mean free surface -requires regridding and recalculation at every time step -high computational cost
4. Body exact (weak scatter)	-wetted surface defined by instantaneous position of hull under incident wave -complex for Green's function in time-domain -scattered waves assumed small when compared to incident wave. -SWAN-2, LAMP-4
5. Fully nonlinear (smooth waves)	-scattered waves no longer assumed small and included in boundary value problem -Mixed Eulerian-Lagrangian method
6. Fully nonlinear	-time domain solutions -body and free surface nonlinearity considered -RANS, particle methods etc -viscosity also can be included and hence can deal with wave breaking.

Faltinsen et al. (1991) presented a nonlinear theory (2.5 D) for ships motions for high speed ships. The steady flow problem, which is generally neglected in strip theories, is considered nonlinear and the unsteady flow is based on linear theory. Although predictions were better than strip theory, discrepancies were observed in wave profile, vertical force and added mass distributed in heaving in the bow and stern regions of ship. Strong nonlinearities present in the steady flow have to be modelled for accuracy in predicting the hydrodynamic behaviour in these region (Faltinsen et al. 1991).

Sea keeping problems and ship response evaluation are commonly carried out in frequency domain. They provide faster and accurate solution which can be used in early design stage. To represent weak nonlinearities under the linear hypothesis (small amplitude motions and waves), small perturbations can be applied in frequency domain (Zhao & Faltinsen 1993), but this model is inaccurate when nonlinearities increases due to large amplitude motions. Focus on investigating nonlinearities associated with seakeeping problems has encouraged researchers to use time domain solutions. Time domain methods are hence becoming more popularly applied to ship seakeeping analysis (ITTC. 2011).

A comparison between frequency domain linear and partially nonlinear potential time-domain flow analyses (Bailey et al. 1998) for heave and pitch motions of S175 container ship was studied by Chapchap et al. (2011). In the time domain nonlinear method, the incident wave and restoring forces are calculated on the instantaneous wetted surface of the hull, and radiation and diffraction components on the mean wetted surface using Impulse response function. Based on their study, it was concluded that the partly nonlinear methods offers improvements in predicting heave and pitch responses. However, to concretely establish their range of applicability, more comparisons with experimental measurements are necessary.

A benchmark study by comparing different nonlinear time-domain computer codes for evaluating the vertical wave-induced bending moments was done by Watanabe & Guedes Soares (1999). They compared a list of time domain codes from six different organisations that are based on such weakly nonlinear methods.

The LAMP system is a 3-D time-domain program used specifically to predict nonlinear motions and responses of a ship operating in extreme conditions (Lin et al. 1994),(Lin & Yue 1990). It uses a time stepping approach where the forces and

moments are computed at each time step and the six degree of motion (DOF) is updated in time domain. An initial boundary value problem is solved using a potential flow boundary element method to compute the 3-D perturbation problem. A combined (forward speed+ radiation+ diffraction) body boundary condition is imposed. The various levels of LAMP system is given below

- LAMP-1 (body linear): perturbation potential and hydrostatic/Froude-Krylov forces over the mean wetted hull surface. 3-D linear hydrodynamics
- LAMP-2 (approximate body nonlinear): perturbation solved over mean surface while hydrostatic/Froude-Krylov over instantaneous surface. 3-D linear hydrodynamics
- LAMP_3: same as LAMP-2 in calculation of forces. 3-D Large amplitude motions.
- LAMP-4 (body nonlinear): Perturbation and hydrostatic/Froude-Krylov solved over instantaneous hull. 3-D large amplitude motions.

Shin et al. (1997) applied the LAMP system to study the motion and responses of the S-175 containership. Heave was over predicted by LAMP-2 when compared to LAMP-4, whereas the pitch predictions agreed well. LAMP-4 is more accurate than LAMP-2 but the calculations require 5-10 times more computational time.

Fully nonlinear methods are also gaining popularity even with the presence of difficulties like being computationally intensive and complexities in modelling the fully nonlinear behaviour of a hydrodynamic problem. In fully nonlinear methods, the waves scattered by the body in motion is no longer neglected. Mixed-Eulerian-Lagrangian (MEL) approach, CFD methods employing RANS (Weymouth et al. 2005) or even URANS models (Wilson et al. 1998), and particle methods (Baso et al. 2010),(Gao et al. 2012) are now being widely considered to investigate the nonlinear behaviour associated with symmetric, antisymmetric and extreme responses of large floating structures.

MEL methods approximate the nonlinear boundary value problem by solving a linear problem at each time step. The first step provides a Eulerian solution to the initial linear boundary value problem using the conventional boundary integral method. In the second step a Lagrangian time integration of the nonlinear free surface is carried out by updating the position and velocity potential of the instantaneous free surface. This is done with the help of the velocity potential calculated in the first step. Yan & Liu (2010) presented a highly efficient time-domain MEL method to investigate fully nonlinear 3-D wave interactions problem with or with-

out forward speed. The challenge remains in accurately tracking the wave-body interaction in bow region of ships, especially at forward speeds.

Arbitary Lagrangian-Eulerian (ALE) methods (Hirt et al. 1974) are also now widely used for a time-dependent multidimensional flow problems with large deformations. It can model flow problems which have moving boundaries, multiple boundaries and regions of shearing flow. Hirt et al. (1974) used a finite difference mesh that may be deformed with the fluid (Lagrangian), or held fixed (Eulerian), or may be moved in any prescribed motion. It is now being employed in many CFD codes to solve fluid problems with large mesh motion (STAR-CCM+ 2012) (Seng et al. 2012).

2.5 Dynamics of Flexible Ship Structures

Hydroelastic response of ships is generally classified as- springing and whipping. Bishop & Price (1979) pioneered the research by developing the theory of hydroelasticity of ships which aimed at unifying the linear dynamic analysis of ship response. This theory introduced the concept of generalised modes which accounts for distortional degrees of freedom rather than just predefined rigid body modes. They used a non-uniform Timoshenko beam to represent the structure, and two dimensional (2-D) strip theory to describe the hydrodynamics. The structure is decomposed into mode shapes which include both rigid body and distortional modes, and the solution for a finite number of modal coordinates is obtained. Forward speed is taken into account through encounter frequency. The approach was used to investigate the symmetric responses (vertical bending modes in head or following seas only). It was later extended to antisymmetric (coupled horizontal and torsional modes in oblique/beam seas) (Bishop et al. 1980) and unsymmetric (coupled vertical, horizontal and torsional modes) responses.

Bishop et al. (1986) elucidated the linear 3-D hydroelasticity theory based on frequency domain potential theory where the dynamic behaviour of a three-dimensional structure *in vacuo* is evaluated using a finite element approach. The ship structure is modelled as finite elements and the fluid actions (radiation) are determined using a pulsating source Green's function. The boundary conditions are applied by using the generalised Timman-Newman formulation (Bishop & Price 1979). For simplification, the perturbation of steady velocity potential effects is ig-

nored and the unsteady problem is solved without prior definition of the steady potential.

A great deal of progress has been achieved since then in the development and application of 2-D and 3-D hydroelasticity. This includes methods like frequency-domain linear analysis accounting for forward speed and steady flow contributions, time-domain nonlinear methods, experimental techniques, numerical methods to evaluate motions of vessels in rogue waves.

For example, Du et al. (1998) presented an advanced frequency domain linear 3-D hydroelastic analysis. The forward speed effect is included using a translating, pulsating source Green's function. Comparisons were made for a flexible S-175 container by both considering and neglecting the effect of non-uniform steady flow. It was noted that the non-uniform potential provides significant influence on the hydrodynamic coefficients, motion responses and distortions. A frequency domain 3-D Green's function method coupled with a finite element beam model can be seen in the works of Malencia et al. (2003) and Senjanovic et al. (2009). The beam model is able to capture the horizontal bending-torsion coupling and warping deformation. Validation of the method was done by comparison with model tests conducted on a flexible barge in irregular waves (Senjanovic et al. 2008). They reported good agreement for most of the cases but discrepancies were noted at the areas of response peaks. The reason for the discrepancy was mainly due to high nonlinearity induced due to a strong coupling between rigid and distortional modes.

Wu & Cui (2009) reviewed the developments and achievements of various 3-D hydroelasticity ranging from linear hydroelasticity in frequency domain to nonlinear time domain analysis. One of the conclusions was the possibility of extending linear 3-D hydroelastic analyses based on time domain potential theory to nonlinear time domain analysis for evaluation of pressures at instantaneous position of the hull at each time step.

Kim & Kim (2009) presented a time domain approach which directly couples BEM and FEM to investigate the hydroelasticity of flexible floating structures. They used higher order B-spline Rankine panel method for the fluid solver and a Vlasov beam element to calculate the structural response. The coupling between the two domains was done using the Newton method and the structural distortions was solves using a direct time integration scheme, such as the Newmark-ß second order

implicit scheme. Vertical motions were calculated at various locations along the barge and validated against experimental measurements carried out by Remy et al. (2006). Good agreement was between the predictions and experimental measurements but discrepancies were noted at the stern and bow locations, especially when the wave frequency approaches the 2-node wet frequency. Kim et al. (2013) later applied this method to study the springing phenomena of S-175 containership. The RAOs of vertical, horizontal and torsional bending moment were calculated for both rigid body and flexible body. It was shown that the rigid and flexible body responses of the ship may differ significantly due to the occurrence of flexible body frequencies.

Comparisons between frequency domain and time domain solutions of linear springing problem was done by Kim et al. (2009). The frequency domain solution uses the method developed by Malencia et al. (2003) and (Senjanovic, Tomasevic, et al. 2009) and the time domain solutions were obtained using the coupling method of Kim & Kim (2009). Investigations were performed on a flexible barge and a containership. The results for the flexible barge using the two methods showed good correspondence with each other and the experimental measurements. The symmetric responses showed good correlation but discrepancies were noted in the case of antisymmetric responses, where the time-domain simulations agreed better.

Time-domain simulations using convolution integrals (Wu & Moan 1996) can be computationally very expensive depending on the time step, total simulation time and degrees of freedom. Taghipour et al. (2008) presented a time domain hydroelastic analysis that replaces the convolution integrals by state-space forms and validated it on a flexible barge (Remy et al. 2006). In general the agreement was good, but discrepancies were noted at the bow and stern section close to 2-node wet frequency.

2.6 Nonlinear Hydroelasticity

Since the development of linear hydroelasticity theory, many nonlinear models have also been presented ranging from 2-D to 3-D; the majority of them falling under the former category.

For instance, nonlinear 2-D quadratic strip theories formulated in frequency domain can be used for predicting the wave loads and ship responses in moderate seas (Jensen & Pedersen 1979). The method uses a perturbation analysis where the linear terms are formulated using the classical strip theory model, while the higher order terms arise due to nonlinearities present in exciting waves, flare of the hull and hydrodynamic forces. Jensen & Pedersen (1981) extended this approach to study the nonlinear effects of ship springing adopting a hydroelastic approach.

The committee of ISSC (2000) presented a comparison between predictions using established nonlinear strip theory methods and experimental measurements for wave-induced loads on S-175. Their general conclusion was that although the comparisons between measured and calculated wave bending moments using various nonlinear strip theory methods are able to predict with sufficient engineering accuracy, a large scatter is observed in the higher order harmonics. Even though the prescribed methods provide good computational efficiency, care must be taken when applying such procedures for design calculations of ships with unconventional hull forms.

Chen et al. (2006) presented a review of existing hydroelasticity theories. They had classified the present nonlinear approaches into broadly two categories. In the first approach, the rigid body motion and the structural problem is considered separately. The second one resembles a hydroelasticity analysis where the fluid interactions and structural responses are considered as a coupled problem. The review concluded that development of nonlinear hydroelastic theories in time domain should be the main target.

A nonlinear strip theory in time domain to calculate the vertical wave loads and ship responses was presented by Xia et al. (1998), where the structure was considered as a Timoshenko beam. The hydrodynamic memory effect due to free surface was approximated using quadratic differential equation. An efficient nonlinear hydroelastic method for wave- and slamming-induced vertical motions and structural response of ships was developed. Numerical predictions using this theory was done for S-175 container and compared with the experimental results. Though the method fitted the experimental results better than linear results, it was noted that inclusion of only nonlinearities of slamming and restoring force is not enough to arrive at accurate predictions of vertical motions and ship responses.

A nonlinear time domain formulation to accurately evaluate whipping loads due to slamming was developed and compared well with experimental results for S-175 container by Wu & Hermundstad (2002). The total vertical force was divided into a linear and nonlinear modification. The nonlinear modification composed of the hydrodynamic force caused due to slamming and the non-linear modifications of the Froude-Krylov, hydrostatic restoring, radiation and diffraction forces was obtained by a convolution of the impulse response function and the hydrodynamic forces. Park & Temarel (2007) applied this theory to present 2-D time-domain nonlinear hydroelastic analysis of S-175 for the symmetric motions and distortions, accounting for nonlinearities. In their study two methods were used which comprised the convolution integral and the direct integration method. In the direct method, the hydrostatic and hydrodynamic forces were evaluated on the instantaneous wetted surface. Both methods produced results which were close to each other and confirmed the validity of both methods. It was noted that the influence of bow-flare slamming can have a major influence when carrying out nonlinear modifications, for a range of speeds and wave amplitudes.

Wu et al. (1997) presented a three dimensional nonlinear hydroelasticity theory where the contribution of the first order velocity potential and the second order hydrodynamic force due to variation in instantaneous wetted surface was discussed on a flexible body. The structure was assumed to behave linearly and nonlinear equations of motions were formulated in both frequency- and time-domain. A hybrid time domain nonlinear simulation that introduced the peak over threshold (POT) method as one of the stochastic analysis procedure was presented by Wu & Moan (2006,2007). This method was used to predict the short-term nonlinear wave-induced extreme hydroelastic responses. Two ships, namely a SL-7 class containership and a modern LNG carrier, were chosen to validate the method and investigate the influence of hydroelasticity and structural damping on the short-term prediction of extreme vertical load effects.

Nonlinear springing in regular waves has also been observed in model tests. When the wave encounter frequency is equal to $1/n$ of the 2-node natural frequency, where n is an integer, i.e. we can refer to as second-order, third order and higher order nonlinear springing. Shao & Faltinsen (2012) used a time-domain higher-order boundary element method based on cubic shape function as a numerical tool to study the second-order sum-frequency wave-excitation in regular head waves.

The investigations on a Wigley hull showed that the second-order velocity potential contributes towards the second-order wave excitation of ship springing in the wave frequency region where sum-frequency springing occurs.

Miyake et al. (2010) carried out a comparative verification between experimental and numerical results using time-domain nonlinear strip method (Mikami & Kashiwagi 2008) was presented for a 12,000 TEU containership. The experimental measurements for validation were obtained from Miyake et al. (2009). The numerical prediction presented for the 2nd, 3rd and 4th harmonic showed good agreement with experimental results for the smaller wave amplitude. However, the VBM at amidships for the higher order harmonic frequencies were overestimated for the higher amplitude wave. In the numerical simulations, at short wavelengths, no wave breaking took place in the bow. Consequently this resulted in bow flare slamming and additional whipping loads, which did not occur in the experiments. Song et al. (2010) carried out a validation of the experimental measurements (Hong et al. 2008) using a 3D time-domain seakeeping code WISH, a weakly nonlinear method, based on Rankine panel method. The influence of higher order harmonics, though sufficiently small, was seen in the experimental measurements of VSF (vertical shear force) and VBM (vertical bending moment), and was not captured by the numerical tool. They stated that the higher order contribution is from the hydroelastic behaviour and a numerical method or procedure which can take into account the fluid-structure coupling could possibly predict these high frequency peaks in experiments. Kim & Kim (2014) carried out springing and whipping analysis on a 60m barge, 6500 TEU and 10,000 TEU containership using the BEM/FEM coupling (Kim & Kim 2009). They noted good agreement in linear responses to waves but discrepancies were observed in nonlinear springing and whipping responses.

Kim & Yu (2010) compared model test results of a 6500 TEU and 10,000 TEU containership conducted in two phases of a JIP (Joint Industrial Project). The model test results were compared with nonlinear time-domain seakeeping program, NLOAD3D, and prescriptive rule calculations. NLOAD3D is a 3D time-domain Rankine source panel method based on a weakly-nonlinear scheme. The measured sagging and hogging were higher than the rule values and numerical predictions, due to the presence of high frequency component (transient vibration in slamming), which was not reflected in the other two calculations. It was demonstrated that the results of VBM of the elastic model clearly showed springing component as com-

pared to a rigid body model. For the cases tested it was concluded that the second-order springing can be severe in specific areas and third-order is negligible.

The above investigations are a good indication that the rule based BMs might not be sufficient for the strength assessments of large containerships and direct calculations based on dynamic loads which also consider the nonlinearities involved, is very important.

(Faltinsen 2014a) mentions that although a number of numerical investigations are being carried out to study the influence of higher order harmonics and nonlinear excited springing, it is hard from a numerical point of view to go beyond second-order nonlinear excited springing using a perturbation analysis due to the difficulty in computing the higher order terms in the equation.

2.7 Experimental Hydroelasticity

The majority of hydrodynamic analysis codes are based on potential flow analysis and the same is applied for hydroelastic analysis. Various numerical methods have been developed for carrying out accurate numerical predictions of flexible ships; however, the experimental measurements with flexible models are few. Experimental estimations of S175 container ship using flexible models have been extensively validated for various conditions (Watanabe et al. 1989).

Fonseca & Guedes Soares (2004a, b) reported an exhaustive experimental investigation of nonlinear effects on vertical motions and loads of S-175 in regular and irregular waves. In both cases, strong nonlinearities were detected and the contribution of higher harmonics to the vertical bending moments. The harmonic transfer functions for the second and third harmonic amplitudes for S-175 showed that it reaches maximum for the ratio of wavelength to ship length is about 1.2. The contribution is not significant for the ratio less than 0.8. The amplitudes of second harmonics for the VBM amidships were about 40-60% of the first harmonics and 15% for the third harmonic amplitude.

The influence of higher order harmonics than third, which excited two-node vertical vibration, has also been observed through experimental results for a containership with an overhanging stern and pronounced flare using a flexible model (Drummen et al. 2009). The measurements showed that the magnitude of fourth

and sixth harmonic of VBM amidships had a maximum of between 25% and 50% of the first harmonic.

A model test campaign for a 6500 TEU containership was carried out as a JIP to validate the design wave loads obtained from major classes of wave load analysis programs (Hong et al. 2008). Nonlinearities and speed effects investigated in the model tests were reasonably predicted using the numerical codes adopted by classification societies.

Experimental results presented by (Zhu et al. (2011) of a backbone model of an ultra large container carrier in steep regular waves indicated that the hogging VBM was approximately 30% more than the sagging moment. He indicated that due to the large, flat bottom the change in added mass induced a large suction pressure. The nonlinear pressure under the bow is believed to be the main reason for the unexpected phenomena if larger hogging moments, which is widely reported for ultra large container carriers (Drummen et al. 2009, Andersen & Jensen 2014, Storhaug et al. 2010).

2.8 Fluid-Structure Interaction Methods and Instabilities

For the majority of fluid-structure interaction problems, solutions using analytical methods are near to impossible, and quantitative experimental investigations are limited. It is more feasible to model these complex interactions using numerical methods. A comprehensive review of existing techniques for simulating fluid-structure interaction problems and recent developments in the area is discussed in Hou et al. (2012). Not only do they categorise various numerical methods, but also critically comment on their accuracy, efficiency and challenges faced by the researchers.

Numerical algorithms used to simulate FSI problems can be mainly classified into two categories. Algorithms which treat the governing fluid and structural equations as a unified system of equations, which is then solved concurrently is called as a monolithic scheme. When separate solvers for fluid and structures are employed such that single fields are exchanged at the interface sequentially and solved iteratively, it is termed as partitioned algorithms. An advantage of partitioned algorithms is that the time required in developing new codes is reduced, as

they can be implemented in existing codes (fluid and structural) that have been thoroughly validated for wide range of engineering applications. The coupling presented falls in the second category. Although, the monolithic approach can be more accurate than the partitioned algorithms, the latter are computationally efficient and easier to implement; thus more favoured for FSI problems. The biggest challenge, however, in partitioned methods is to coordinate the FSI interface in the codes, which deforms in time. This requires efficient tracking and conservation of related quantities (mass, momentum, energy) at the interface that can be tedious in some engineering problems leading to instabilities and accuracy issues (Tu et al. 2015) .

The subiteration method is commonly employed in partitioned scheme, i.e., the fluid and structural equations are solved alternatively, subject to complementary partitions of the fluid-structure interface conditions (Brummelen 2009). When the structural deformations and accelerations are small, the numerical solution can be obtained using an explicit or loosely coupled time integration scheme. In an explicit scheme subiterations are performed only once a time step and the interface conditions are updated at the end of each time step, before proceeding to the next. Another alternative is the strongly coupled partitioned method, where in subiterations are repeated within the discretised time steps. A potential drawback of subiterating is that the number of iterations required could easily go up to, say even 40-50 iterations per time step, depending on the application; requiring massive computational effort.

Förster et al. (2007) found that when dealing with transient dynamic problems where the structural velocities and loading changes, the loosely coupled approach exhibit serious convergence issues and instabilities, especially when the flow is considered incompressible. The apparent added mass effect becomes dominant when the ratio of mass densities of the structure and fluid approaches unity, being the main reason for the instabilities (Causin et al. 2005). This effect originates because of the inertia added when a body in motion moves some volume of fluid around it, since the structure and the fluid cannot occupy the same physical space simultaneously. Brummelen (2009) studied the added mass effect in both compressible and incompressible flows on partitioned methods, and found that in compressible flows this quantity is proportional to the time step size, whereas when the flow is incompressible the added mass approaches a constant as time step de-

creases. Additionally, they state that partitioned schemes are stable and convergent for compressible flows for sufficiently small time steps. However, in incompressible flows, they start to become unstable for sufficiently small time steps. In compressible flows the pressure perturbations and the displacements of the interface are only affected in the immediate vicinity of the interface due to the finite sound speed, however, for incompressible flows the pressure perturbations transverse globally in the fluid domain. Förster et al. (2007) also investigated the effect of added mass instabilities and confirmed that restrictions on time steps have to be expected in the loosely coupled problems. Stability of the scheme improves with coarser time steps, albeit the accuracy of solution could be seriously hampered. Often due to the time step restrictions and instability issues it is generally preferred to use strongly coupled schemes over loosely coupled. However, due to added mass effect even a strongly coupled subiteration scheme may exhibit divergence in incompressible flows (Causin et al. 2005) (Idelsohn et al. 2009). Chorin (1967) introduced an artificial compressibility term in the incompressible Navier-Stokes equations with the aim of solving steady state problems. This artificial compressibility term δ was proportional to the inverse of square of the speed of sound. With the introduction of this term the perturbed pressure waves reduces from infinite speed of sound in the incompressible flow equations to a finite speed of sound which is chosen to accelerate convergence and improve stability. The artificial compressibility method was further extended to investigate its applicability to unsteady incompressible Navier-Stokes equations. The unsteady problem in real time is transformed to a pseudo-steady problem using a fictitious time called dual time stepping (Jameson 1991). A comprehensive list of different versions of artificial compressibility is discussed in Madsen & Schäffer (2006). Artificial compressibility source term can also added in the pressure equation to stabilize partitioned schemes that are known to suffer from instabilities otherwise (Degroote et al. 2010)(Riemslagh et al. 2000).

Idelsohn et al. (2009) put forth the evidence that the numerical instabilities that occur due to added-mass effect in incompressible flow are a consequence of the pressure segregation wherein the pressure is separated from the velocity during the solution process. It is possible that the pressure segregation, in both monolithic and partitioned methods (explicit and implicit), will produce pressure divergences or inaccurate solutions. They can be magnified when:

1. The density of fluid and structure is similar
2. The time steps are too small
3. The stiffness of the structure is small.

In the case of fluid flow computations with moving grids an additional conservation equation, namely space/geometric conservation has to be satisfied in addition to the mass, momentum and energy conservation equations (Demirdzic & Peric 1988)(Thomas & Lombard 1979).

2.9 CFD/RANS Approach

Boundary integral methods based on potential theory cannot model viscous effects due to flow separation and eddy generation, breaking of waves or green water effects effectively. Such inaccuracies could lead to underestimation of fluid damping effects. Potential theories are known to underestimate roll damping effects and require solutions to RANS equations as it cannot take into account the dissipation of vortex due to viscosity. (Chen et al. 2001) observed that the measurements of heave, pitch and vertical accelerations of an elastic S-175 model influenced by flare impact and green water effects were underestimated using a 2-D hydroelastic method by about 30%. A similar conclusion was made by (Watanabe et al. 1989) and they concurred it to be emanating due to the omission of viscous effects. Carrica et al. (2006) investigated the forward speed diffraction problem of a model in head waves using an unsteady-RANS (URANS) approach. URANS equations are the usual RANS equations, but with transient (unsteady time dependent) term retained. Medium speed and high speed cases were studied and compared with the experimental data for resistance, heave forces, pitching moments and unsteady free surface elevations. In the high speed case, forces and moments exhibit nonlinear behaviour with a strong second harmonic component. Such complex interactions between boundary layer and incident waves and also the flow patterns in the wake region cannot be predicted using potential flow codes. When dealing with nonlinear springing loads, modelling these complex hydrodynamic interactions could be of great importance to improve the accuracy of numerical predictions (Faltinsen 2014a).

With increasing computational power, fully nonlinear methods can be developed using RANS equations and particle methods, also known as gridless methods, such

as Smoothed Particle methods (SPH), Moving Particle Semi-Implicit (MPS) and Constrained Interpolation Profile (CIP) techniques (ISSC 2012). The State-of-Art CFD methods available are shown in Table 2.

Table 2: Comparisons between State-of-Art CFD methods

Method	Application & Advantages	Disadvantages
RANS	-model impact of turbulence on mean flow -wave breaking and viscous effects -Free surface flows -Ship motions -Resistance & manoeuvring -Slamming	-Significant CPU time -Poor accuracy in memory flow -averages out turbulent fluctuations
URANS	-similar to RANS but with transient term included -time accurate solution -separate time scale of mean motion and turbulent motion	- higher computational requirements than RANS
LES (Large eddy Simulation)	-Applied to high Reynolds number flows -computational cost better than DNS -resolves large structures and model impact of small structures -propeller, air turbine, open flows such as wake of -propeller	-high computational time when compared to RANS -accuracy strongly dependent on grid employed
DES (Detached Eddy Simulation)	-modification of RANS -hybrid between RANS and LES -not commonly used in ship motion and response problems	-excessive damping induced by RANS may affect LES result -grid generation more complicated than RANS
DNS (Direct numerical simulation)	-Full range of turbulence scales can be resolved	-Large number of grid cells required; large computational time -Limited to moderate Reynolds number flows -difficult for flows with complex geometry
SPH & MPI	-Mainly local flows -Limited ship motion problems -Motion responses of damage ships	-Very high computational time -not yet validated enough

Querard et al. (2008) calculated the 2-D hydrodynamic coefficients of a flexible uniform barge using RANS and potential flow, to assess the influence of viscosity on the dynamic response. Symmetric and antisymmetric distortions were considered in the investigation. They reported notable differences between the 2 methods, both in hydrodynamic coefficients and dynamic response, especially in the antisymmetric motions and distortions.

The coupling between fluid and structural solvers to predict fluid-structure interactions can be broadly classified as one-way and two-way coupling. In the one-way

coupling method, only the fluid pressures acting on the structure is transferred to the structural solver. The structural deformations are also fed back into the fluid solver causing mesh deformations in the two-way coupling. The two-way coupling can be further broken down into strong and weak coupling. The exchange of pressure and displacements takes place more than once in a time step for the strong coupling. For the weak two-way simulations the data is exchanged once every time step. When the structure undergoes large deformations the two-way coupling is considered to be more accurate. Energy conservation at the interface is not guaranteed in one-way coupling, but is in two-way. However, the computational time in one-way is nearly three to four times lesser and additionally the deformation of the fluid mesh is not required maintaining a constant quality mesh (Benra et al. 2011). It can circumvent the numerical instabilities surrounding mesh deformation and mass and momentum conservations in the deforming cells close to the interface.

Benra et al. (2011) discusses the differences between the results obtained using the two methods for two simple flexible models. Their general conclusion after carefully looking at various cases was that when dealing with relatively large structural deflections the one-way coupling under predicts the responses by a large amount. The two-way coupling produces results closer to the reality, whereas one-way coupling gives plausible predictions in some cases. Hence, the application of the methods to specific problems must be done with caution.

Paik et al. (2009) presented a coupled fluid-structure interaction method and compared the results of rigid, one-way and two-way coupling of S-175 containership with experiments. CFDShip-IOWA and ABAQUS were coupled for this investigation to study motions and structural loads during slamming event. The predictions were validated against the experimental measurements of Ramos et al. (2000). The ship was allowed to freely heave and pitch so that the influence of springing and whipping on motions and loads could be investigated. They concluded that the one-way coupling approach provided overall a similar quality of solution, i.e. it captured the trends well, to the two-way coupling, a conclusion which requires further validation for various test cases. However, only the two-way coupling captured the effects of structural deformations in the amplitude and phase of VBM and the oscillations in rigid body accelerations.

Comparisons between two numerical methods and experimental measurements to evaluate the hydroelastic response of a 9600-TEU containership sailing in head sea at 15 knots was presented by Seng et al. (2012). The two numerical methods were a non-linear strip theory (weakly nonlinear) code Shipstar and direct calculation of Navier-Stokes equations using OpenFoam (CFD). The predictions made from one-way and two-way CFD coupling matched very well with the experiments. The asymmetry in hogging and sagging was of the same ratio only in the CFD calculations. The peak values of VBM amidships predicted by CFD (two-way) and Shipstar were found to be 35% smaller than the measurements in one of the test cases. With significant vibration occurring in the above case, the one-way coupling could not capture the hydroelastic effect of the hull girder vibration. One-way coupling was also unable to predict the resonance occurring between the 4^{th} harmonic and 2-node vertical mode. El Moctar et al. (2011) performed two-way coupled simulations using finite volume CFD using VOF method and a Timoshenko beam model. The method successfully predicted the VBM amidships in irregular seas. However, they concluded that the computational time required for coupled simulations limits their applicability to realistic ship investigations and apply directly at the initial design stage. Oberhagemann et al. (2012) carried out time-domain simulations using non-linear Navier-Stokes solver COMET and linear structural solver, based on finite element Timoshenko beam approach to study long term extreme value analyses on marine structures. The paper concluded that the discretisation errors are a critical issue and using coarse grids, especially in the case of flexible ships, lead to under-estimated responses. They presented an extrapolation approach combined with coarse grids to improve accuracy in predictions. Torsional and transverse vibration in oblique seas for a 10,000 TEU containership using RANS/FE coupling was later presented by Oberhagemann, Kromer, et al. (2012). This was the first paper that investigated torsional vibration using a CFD based coupled solver.

Coupled fluid structure interactions have also been investigated to study the hydroelastic effects during slamming. Piro & Maki (2013) used a tightly-coupled finite volume CFD with VOF scheme and a modal structure to study the importance of entry and exit on structural response of 2-D elastic wedges. They stated that a hydroelastic factor which commonly used for constant velocity impact to identify cases when the hydroelastic effects are important is difficult to define for entry and exit problems.

In real life scenarios the deformation of the structure can alter the slamming pressures, oftentimes decrease the magnitude when compared to a rigid structure (Bereznistki 2001). Stern slamming of a LNG carrier has been studied using CFD and FEA in a one-way coupling (Kim et al. 2008) (Oberhagemann et al. 2009) (Maki et al. 2010). The slamming loads were predicted using CFD solver with sufficient discretisation and further transferred to an FE mode. Oberhagemann et al. (2009) accounted for the added mass due to the flexibility using hydrodynamic masses from 2-D Lewis sections and distributed it to the appropriate shell nodes. Although this method is better than the rigid body assumption (Kim et al. 2008), it is debatable on how the hydrodynamic masses can accurately account for the added mass due to the flexure modes. Maki et al. (2010) improved this by distributing acoustic elements to account for the added mass due to flexure and also used modal basis to describe the wet structure.

The one-way coupling approach to predict hydroelastic response requires much lesser computational time providing quick and cheaper approach when compared to a two-way coupling. In the on-way approach the ship is considered rigid and the added mass is calculated using an empirical approach to match the 2-node wet frequency Mukhopadhyay (1989). Whipping response of a ship in waves revealed reasonable comparisons, however, the wave responses were higher and the local pressure variation at the bow was not captured (Dhavalikar et al. 2015). The lack of structural deformations not given back to the fluid is causing the differences. The added mass is uniformly applied on the underwater surface and this cannot account for fluid interaction with the flexible deformations in calculating the responses. One-way coupling might be useful at the initial design stage but to get accurate responses for large vessels one would need methods like two-way coupling to capture the complex interactions. Also most of the one-way investigations (Paik et al. 2009, Dhavalikar et al. 2015, Thomas et al. 2003) have investigated only symmetric responses. The prediction in oblique seaways needs attention.

When the local deformations are small, the mesh can be kept rigid and the local deformation can be accounted using a velocity boundary condition (Piro & Maki 2013). This might prove effective for practical applications for small deformations but otherwise can considerably reduce accuracy of the body boundary condition as the mesh is no longer fitted on the FSI interface. Seng et al. (2014), however, en-

sured that the mesh is kept fitted to the flexible body interface and the body boundary condition is satisfied accurately at all times.

Time domain hydroelastic code combining the fluid solver OpenFoam with a structural solver where the elastic deformations are described by a modal superposition of dry mode shapes has shown potential of applying to simulate springing and slamming behaviour of ships moving in waves (Cabos et al. 2011) (Seng et al. 2014). Nevertheless, it requires more systematic validations to be certain that this potential is realised.

Investigations of a constant velocity impact of a flexible panel with water using a strong two-way coupling using CFD/FEA showed that the number of iterations and minimum exchanges per time step are important for convergence and numerical stabilities (Camilleri et al. 2015). The numerical stability further improved by treating the fluid as compressible with a lower speed of sound, without compromising on accuracy.

Kim et al. (2015) analysed the slamming and whipping response of an 18000 TEU containership utilising a 2-D Rankine panel method, 1-D/3-D finite element methods and a 2-D generalised Wagner model coupled strongly in time domain. Generally, vertical bending moment for a range of wave frequencies agreed well with the experiments but showed significant underestimation as the wavelength became shorter. The second harmonic springing component estimated using an 1-D and 3-D beam model showed very similar magnitudes, although were smaller than the measurements.

They also found that the classical approach of decoupling motion and slamming by post process calculation of the whipping response tend to overestimate when compared to model tests. The fully coupled analysis performs better due to interaction of slamming and pitch motion resulting in a mutual suppression; a phenomenon closer to the actual physics.

When considering structural discontinuity, a 1-D beam model exhibits very similar behaviour to a 3-D FE model, even in torsional response (Kim & Kim 2014) (Senjanovic, Malenica, et al. 2009).

2.10 Conclusions from Literature Review

Application of CFD to hydroelastic investigation is limited and hence it is too early to draw any conclusions. Geometric and free surface nonlinearities induced by large amplitude motions, extreme sea conditions and even due to flexibility can be substantial that they cannot be overlooked in scantling calculations. When considering hull flexibility it has been noted in both experimental and full scale measurements that the order of magnitude of these nonlinearities in wave loads could be high. Nonlinear springing on large container ships could have a big influence on the symmetric and antisymmetric response. This phenomenon is not well predicted by weakly nonlinear time-domain techniques, and requires a fully nonlinear coupled method.

A more realistic modelling of the hydroelastic behaviour of ships could be established by a two-way coupling between a CFD and FEM code, so that the data is exchanged at every time step. A few attempts have been carried out to strongly couple the codes mainly to study slamming, whipping and springing. The coupling technique has to be further investigated for symmetric, antisymmetric and asymmetric motions. It was noted that the one-way coupling approach in some aspects provided a similar quality of solution as the two-way coupling, at a much lower cost (Paik et al. 2009), (Seng et al. 2012). But such investigations are limited. Application of two-way coupling is computationally intensive compared to the other methods but could be more realistic and accurate in some cases where nonlinearities are dominant. Large containerships like the ones experimentally investigated by Drummen et al. (2009) or Hong et al.(2008), which induce several nonlinearities could be more appropriate when hydroelastic validations of global responses is carried out using coupling methods.

A thorough Verification and Validation (V&V) needs to be performed before any numerical code can be considered suitable for carrying out accurate predictions. Validation is a process of comparing the numerical results with real world observations like experimental or full scale measurements. Although it is a requisite that we validate our numerical results systematically, it is also crucial to understand what conditions the numerical method performs better and what are its short comings? The reason numerical codes are applied or developed in marine industry is to make predictions within a reasonable amount of time and apply them directly into

the design cycle of a ship. For instance, if the bending moments of a large containership in regular head wave can be accurately calculated by Level 2-4 methods in Table 1 that are computationally less expensive and cheaper than a one-way or two-way CFD coupling, then it is definitely better to apply it to the initial design phase. However, if the influence of nonlinearities is compelling, a more accurate method like two-way coupling should be sought for a more accurate strength analysis of the vessel. Simulation based design can also give us insight into interesting hydrodynamic interactions which can provide understanding of the flow behaviour which when combined with experiments can give us important insights into the fluid-structure interactions. It can help us design our experiments/simulations efficiently and consider which test cases need to be simulated. Essentially, the choice of a method is a decision to be made keeping in mind the accuracy required and their practical applicability.

Where does the two-way coupled analysis fit in design cycle of a vessel? For what conditions does this method need to be considered and where can we get away using simpler techniques? Where are the stumbling blocks in the present method? Apart from validating the numerical method presented, this thesis tries to address these imperative questions. The two-way coupling investigations are limited and this thesis will add to the existing knowledge but also try to realise the practical application of the two-way coupling.

According to Moore's Law, the computer processing power will double every two year, which still holds true after nearly a half century (Sneed 2015). Even if presently the practical application of these high-fidelity methods in early design phase of a vessel looks bleak, in a few years we will have the computational power to run the two-way coupled simulations within a reasonable time, and perhaps to be included in the design of a large containership. Having a good understanding of the method before the technology arrives will be beneficial.

Chapter 3:

Numerical Methods

Key features of the software used in this report to calculate the motion and response of a body at a free surface are outlined. The CFD software used for all computations is Star-CCM+ and Abaqus is used for the FE analysis, both commercially available software. A brief summary of the approaches used to solve the governing equations are highlighted. Furthermore, the numerical method implemented for two-way coupling in the software is discussed in detail.

3.1 Computational Methods for fluid flows

Computational simulation of any fluid flow problem consists of three major steps: 1. problem definition, 2. fluid flow model, 3.computational solution. The first step is to idealise the physical problem of interest considering appropriate fluid flow characteristics, initial states and boundary conditions. Once the physical problem is idealised, it is mathematically represented using general governing (continuity, momentum, energy etc.) equations. In the case of fluid dynamics the Navier-Stokes equations are considered to be an accurate representation. The third and the final step involves solving these complex equations computationally. The numerical solutions to the above partial differential equations (PDEs) can be carried out using finite difference method, finite element method, finite volume method or particle methods.

The finite difference method is one of the oldest methods used to obtain the numerical solutions to the governing PDEs. The fluid domain is divided into a number of grids and at each grid finite difference approximations are obtained to the PDEs using Taylor series, simplifying them to algebraic equations. Although it is simple to apply, it requires a high degree of structured grids. The spacing of the grids also imposes limits on the stretching factor or distortion that is possible. This potential drawback of the method arises due to the grid resolution which makes it difficult when handling complex geometries or moving boundaries in three dimensions (Ozisik 1994).

The finite element method was developed to compute stresses and displacements associated with structural analysis. When applied to fluid dynamics, the fluid domain or continuum is divided into a finite number of elements. Both structured and unstructured grids are possible, and the latter aids the handling complex geometries (Zienkiewicz et al. 2014). The solution is obtained by considering an integral form of the PDEs rather than the PDE itself. Finite Element methods are not extensively used in CFD since it generally requires greater computational resources than Finite Volume method (Noor & Dwoyer 1988).

The finite volume method is the most popular of the three methods used for solving the Navier-Stokes equations. The complete solution domain is divided into control volumes (CVs) where the integral form of conservation equations is discretised. The integral equations are then simplified to algebraic equations and solved iteratively. A finite volume CFD software is used in all the investigations carried out in this thesis.

3.2 Selection of CFD software

There are both commercial and open-source software that can be used to investigate the hydrodynamic problem of floating bodies in a seaway, ANSYS CFX, ANSYS FLUENT, OpenFOAM, Star-CCM+, CFD Ship Iowa to name a popular few. To model hydroelastic response of ships in waves fluid and structural solvers have to be coupled. The coupling can be established using a third party code which promotes the exchange and mapping of related quantities between the solvers (Joppich & Kürschner 2006). Star-CCM+ (fluid solver) and Abaqus (structural solver) have inbuilt co-simulation libraries which facilitate coupling without any third party code. The coupling capability has been implemented in similar studies and has shown encouraging results (Peric 2012, Aagaard 2013, Bloxom 2014). Few coupled investigations have been carried out using OpenFoam. When using OpenFoam and a structural solver the data exchange and mapping has to be entirely established by the user. This is not of interest in this particular study as the main objective is to examine the symmetric behaviour of flexible bodies in comparatively severe head seas for which the preferred choice is to naturally go for an established coupling scheme. It is to be noted that this research work is also not intended for developing a coupling from scratch, since it is already available. The drive behind

the work is to apply this method to predict hydroelastic behaviour focusing mainly on the nonlinearities and investigate the effects of modelling parameters. It is expected that when using commercial software where the user does not have complete control on the source code some numerical issues might arise which might be harder to solve than using codes where the user has complete control. Such numerical issues will be discussed and suggestions to avoid the problems will be highlighted. A few advantages and disadvantages of the CFD software Star-CCM+ are listed below:

Advantages

- The software is widely validated for investigation of floating bodies in wave, both in two-dimensional and three-dimensional domain (Peric et al. 2007,Chen et al. 2014).
- A completely integrated package; inbuilt CAD modelling option, fluid solver, post processing all in one window.
- It can be coupled with Abaqus without any third party code.
- Well-structured manual which gives detailed explanations on the workflow in CFD, solvers and settings.
- Has a real time Graphical user interface which helps the user to monitor the problem as it progresses in time.

Disadvantages

- Restricted license
- High License cost
- Unlike an open source code where the user has full control on solver settings and the code, restricted control is only available in commercial packages. This sometimes makes error detection tedious and occasionally impossible.

3.3 Finite Volume Method

The numerical method used in Star-CCM+ is a finite volume (FV) method in which the flow is assumed to be governed by RANS equations (Ferziger & Peric 2003). The RANS equations reduce to the well-known Euler equations for the case of inviscid flow. First, the spatial fluid domain is discretized into a finite number of control volumes (CVs). The integral form of conservation equations (with the initial and boundary conditions) is then applied to cell centres and simplified into an algebraic system of equations solvable by the computer. The governing equations not

only contain surface and volume integrals but also time and spatial derivatives. Apart from the conservation equations, the general transport equation for scalar quantities ϕ must also be satisfied in the control volume centres. When motion of CVs is employed, an additional space conservation equation must also be satisfied. The space conservation equation ensures that the continuity and momentum equations are satisfied when the control volumes are deforming (Ferziger & Peric 2003). The conservation equations, the general transport equation and the space-conservation equation in the integral form are:

Continuity Equation:

$$\frac{d}{dt}\int_V \rho dV + \int_S \rho(v - v_b)\cdot n dS = 0\,; \tag{3.1}$$

Momentum Equation:

$$\frac{d}{dt}\int_V \rho v dV + \int_S \rho(v - v_b)\cdot n dS = \int_S (T - pI)\cdot n dS + \int_S \rho b dV\,; \tag{3.2}$$

Transport equation for scalar quantities

$$\frac{d}{dt}\int_V \underset{transient\,term}{\rho\phi dV} + \int_S \underbrace{\rho\phi(v - v_b)\cdot n dS}_{convection} = \int_S \underbrace{\Gamma\nabla\phi\cdot n dS}_{diffusive\ flux} + \int_S \underbrace{\rho b_\phi dV}_{source\,term}\,; \tag{3.3}$$

Space-Conservation equation:

$$\frac{d}{dt}\int_V dV - \int_S v_b \cdot n dS = 0\,. \tag{3.4}$$

In these equations v represents the fluid velocity vector; v_b is the velocity of CV surface, n is the unit normal vector to the CV surface whose area and volume is S and V respectively. The fluid stresses are expressed in the form of a tensor T, I is the unit tensor, ϕ is the scalar quantity, Γ is the diffusive coefficient. The vector of body forces/unit mass is represented as b and b_ϕ is the source or sink (vectors) of the scalar quantity.

All integrals are computed using the midpoint rule, implying that the value of the integrand is first evaluated at the centre of the integration domain (face centres for surface integral, CV centres for volume integrals and time level for time integrals)

and then multiplied by the range of integration (face area, volume or time step). In order to compute the diffusive fluxes, gradients are also needed at cell faces. The Hybrid Gauss-Least Square gradient method is used to solve the transport equations.

Free surface flows are implemented using the Volume of Fluid (VOF) tracking method (Hirt & Nichols 1981). In order to account for the position of free surface in multiphase flows and allow for its arbitrary deformation, an additional transport equation is solved for the volume fraction *c*. This volume fraction takes a value between 0 and 1 in the VOF scheme. When *c* is equal to 0 the cell entirely consists of air and when it is equal to 1 it is filled with only water. The air-water interface is represented by a volume fraction of 0.5. A first-order upwind convective scheme to solve the convective transport of the two fluids (air and water) produces high numerical diffusion which can result in smearing and mixing of the fluids. A simple higher order scheme, for example, a central differencing scheme, would produce lesser diffusion, however, would fail to define the interface when there is a large spatial variation of phase volume fractions (STAR-CCM+ 2012). Hence, in order to maintain a sharp interface, the HRIC (High Resolution Interface Capturing) discretization scheme is used for free surface flow along with the VOF tracking in Star-CCM+. HRIC scheme is a carried out by blending of upwind and downwind schemes and further corrected depending on the local Courant number (Muzaferija et al. 1998). Basically there is a lower and higher local Courant number limit for the HRIC scheme which is by default in Star-CCM+ set to 0.5 and 1, respectively. When the local courant number on the air-water interface is less than 0.5 the HRIC scheme is activated. When the Courant number is between 0.5 and 1 a blend of HRIC and first-order upwind scheme is used and for a courant number greater than 1 the first-order scheme is used to define the interface. This default number can be changed to ensure that the HRIC scheme is activated all the time during the simulation to maintain a sharp interface. In the case of all the simulations carried out in Chapter 5 &6 the lower and higher local courant number was changed to 5 and 10, respectively.

3.4 Equation Constraints and Solution

3.4.1 Numerical Boundary Constraints

Prescribed Boundary conditions fall into two categories: Neumann (fixed value) and Dirichlet (fixed gradient). Some common and generic description of boundary conditions used is provided here.

Velocity Inlet: The velocity vector is prescribed when the velocity profile is known at the inlet. The scalar properties of the flow are also defined at the boundaries. This is a Dirichlet boundary condition.

Pressure outlet: This is a Neumann condition where, the pressure at the outlet as static or gauge pressure is prescribed. Usually it is assumed to be constant at this boundary. In the case of wave simulations the hydrostatic pressure of the wave is defined at this boundary condition. This boundary should be placed far enough to ensure that the flow is fully developed so that no fluctuations or reflections occur in the direction of flow.

Wall: In a no-slip wall condition, the normal velocity at the boundary is set to zero and the wall velocity is equal to the tangential velocity.

Symmetry: This condition is used to reduce the computational effort. It is used when the flow field and the geometry is symmetric. The normal velocity and the normal gradients of all variables are zero at the symmetry plane.

3.4.2 SIMPLE Algorithm

The governing equations are solved using a segregated iterative method, SIMPLE (Semi-Implicit Method for Pressure-Linked Equations) algorithm (Patankar & Spalding 1972). At a particular time step, an approximate velocity field is obtained by solving the momentum equations. The gradient of pressure is calculated from the pressure distribution from the previous time step or using an initial estimate. A pressure correction equation is formulated using the uncorrected mass fluxes computed (inner iteration). The pressures and cell velocities are then corrected at each cell to obtain a new pressure distribution. Furthermore, the volume fraction is updated on each CV and this continues (outer iteration) until all the nonlinear and

coupled equations satisfy a given tolerance, (E.g. for maximum number of iterations) before moving to the next time step.

Spatial and temporal discretisation results in coupled nonlinear equations which are solved iteratively. It is difficult to solve these equations as a single system of nonlinear equations, and, hence they are treated in parts. In the first step, each equation is treated having a single unknown and treating the other variables as known (initial guess or from previous time step). These equations are solved iteratively as linear equations. This level corresponds to the inner iterations. Then the coefficient matrices and the source vectors (see page 36) are updated treating the equations in a coupled manner to ensure the solution satisfies all of them. This is the outer iteration level. The process is then repeated.

3.4.3 Under Relaxation Factor

At each outer iteration the value of the new generic variable ϕ^{n+1} is used for the next iteration. In some cases, where the solution changes a lot at every iteration using the iterate ϕ^{n} could cause instability and the solver to diverge. Hence, a fraction of the difference of the new and old iterate ϕ^{n-1} is used to increase stability, namely equation 3.5. This is called the under relaxation factor (URF), ω. Ideally, an under relaxation factor of 1 is preferred. A lower under relaxation factor would slow down the speed of convergence but increases stability and decreases oscillations or fluctuations in transient simulations. Consequently, the maximum number of iterations might have to be increased to ensure convergence.

$$\phi^{n+1} = \omega\phi^{n} + (1-\omega)\phi^{n-1} \qquad (3.5)$$

3.4.4 Temporal discretisation

In Equation 3.3, the first term which is included in transient calculations is time dependent. This term must also be discretised to obtain the value at each time step. The Implicit Unsteady solver in Star-CCM+ offers two temporal discretisation options: first order and second order. The first order discretises the transient term by using the solution at current level and the previous time level. It is also referred to as the Euler Implicit. On the other hand, the second-order uses the solution at the current time level and from two previous time levels.

3.4.5 Overset Mesh for motion

Overset mesh, also called as Chimera or overlapping grids are used to discretise the computation domain and idealise the motion of one or multiple moving bodies in a very effective way. In the overset meshing methodology, two regions, background and overset are created, where the free surface refinement is also extended in the background grid. The overset grids are attached to the floating body and move with it freely depending on the motion response. The background region is fixed in space and the overset mesh can move freely relative to the background region. The governing equations are discretised on the overset mesh boundaries and solved simultaneously for all the cells in the overlapping region, that is, the coupling between the meshes are implicit. The grid position is recalculated at the end of every time step which has to be done for any moving mesh method, so this is not a drawback. Each overset mesh is attached to one frame of reference and requires an interpolation from one reference frame to another (the background region having a different frame of reference) at the overlapping interface. This step is an additional effort in the method (Ferziger & Peric 2003). In the case of rigid body motion simulations presented in this work, an overset mesh is used to idealise the motion of the body. For the coupled simulations a combination of overset and mesh morpher is used which is briefed later in Section 3.7.3.

3.5 Finite Element method

3.5.1 Numerical method and solution to equations

Finite element method is a numerical technique used for obtaining approximate solutions to boundary value problems. In this procedure the domain is discretised into finite elements, and solution to the partial differential equation is obtained by imposing a set of boundary conditions.

There are number of commercially available finite element software; Abaqus being one of them. Abaqus is used to represent and solve the structural part of the floating body. Solutions to displacements, deformations, stresses and forces are calculated for an applied loading. The exact solution requires that both forces and moments are in equilibrium at all times over any arbitrary volume of the body. However, a displacement method is based on approximating this equilibrium by replac-

ing it with a weaker requirement i.e., the equilibrium must be maintained in an average sense over a finite number of divisions of the volume of the body. Abaqus is a displacement-based method where the basis of the finite element solution is the principle of virtual work or virtual displacements (Dassault Systèmes 2013). According to the principle of virtual work, for any infinitesimal displacement applied to the body in its state of equilibrium, the total internal work which represents the stresses and strains is equal to the total external virtual work due to the applied loads (Bathe 2007).

The equation that represents the principle of virtual work is:

$$\underbrace{\int_{\Omega} \delta\bar{\varepsilon}^{T} \sigma d\Omega}_{Internal virtual work} = \underbrace{\int_{\Omega} \delta\bar{u}^{T} b d\Omega}_{External virtual work (body force)} + \underbrace{\int_{\Gamma} \delta\bar{u}^{T} t d\Gamma}_{External virtual work (traction)} \tag{3.6}$$

where $\bar{\varepsilon}$, $\bar{u}$ are virtual strains and virtual displacements; b, t are the external body force and the surface/traction force Ω, Γ represent the volume and surface, respectively.

The stresses are in equilibrium with the external applied load and the virtual strains are corresponding to the virtual displacements (Bathe 2007).

The governing equations for the dynamic response of an elastic body is idealised using finite elements (Clough & Penzien 1993) (Bathe 2007):

$$M\ddot{u} + C\dot{u} + Ku = R \tag{3.7}$$

M, C, K are the mass, damping and stiffness matrices, R is the external load vector applied, $\ddot{u}$, $\dot{u}$, u are the acceleration, velocity and displacement vectors of the finite element nodes. The left hand side of the equation represents the time-dependent inertia, damping and restoring forces (or moments).

The equation is solved primarily using two methods 1. Direct integration 2. Modal superposition. A direct step-by-step integration is adopted in the CFD/FEA coupling used in the dynamic analysis of floating bodies in waves in the present work where the equations are integrated over discretised time steps Δt (Bathe 2007) (Dassault Systèmes 2013). The solution to equations is satisfied at discrete time intervals, instead of any time t, which means that equilibrium is satisfied at discrete points. An approximate solution at discrete intervals is established using an

appropriate integration scheme. The solution to the discretised equation can be obtained using an explicit or implicit integration scheme. In an explicit method the solution for time t+Δt is calculated by considering equilibrium condition at time t, whereas in the case of an implicit method the equilibrium is considered at time t+Δt. The solution time increases with decrease in the time interval Δt, consequently errors in direct integration are mainly due to large time steps. Dynamic-implicit uses the Hilber-Hughes-Taylor implicit operator for time integration. This operator is an extension of the Newmark-β scheme where the numerical damping parameters α and β can be changed depending on the application. In implicit analysis, the integration operator matrix must be inverted and a set of nonlinear equilibrium equations must be solved at each time increment. Oberhagemann et al. (2012), Paik et al. (2009) and Seng et al. (2014) carried out FSI investigations using CFD and FEA solver based on modal decomposition unlike the present study where a direct integration FEA technique is used. In mode superposition the solution is decoupled and the response of the structure is represented by a finite number of modes. The main difference between the two methods is that the solution to direct integration uses all the mode shapes in the calculating the response of the structure. The advantage of mode superposition over direct integration is to exclude trivial high frequency modes in the formulation. This feature enables the use of larger time steps, hence, less computational time. These high frequency modes are not required for global hydroelastic analysis. Nevertheless, Clough & Penzien (1993) state that for the dynamic analysis of structure a direct step-by-step integration procedure is more accurate than modal superposition for highly nonlinear systems. The choice of one over the other is dependent on the numerical effectiveness. Direct integration finite element analysis is selected in the present study even though the interest is predominantly global response of the vessel so that this method can be extended straight away to investigate high frequency oscillations, relating to, for example slamming.

3.5.2 Element formulation

A brief description of the elements used to model the geometric representation and structure properties of the floating structures in this thesis is described. In this present study only vertical responses are of interest, hence, B31 Timoshenko beam elements are used to represent the flexibility of the structures and the hull surface

is modelled using 4-node quadrilateral elements SFM3D4. When considering torsional responses a Timoshenko beam is not applicable and would require a 3-D FE model or use Vlassov beam (Dvorkin et al. 1988).

Timoshenko beam element formulation uses both linear and quadratic formulation, and in addition, allows for shear deformation implying that beam cross-section need not necessarily remain normal to the beam axis. The linear formulation was used in the present work. Unless specified, Abaqus automatically calculates the transverse shear stiffness values required in the formulation of element (Dassault Systèmes 2013). A beam profile can be defined as a regular geometric section such as a box, rectangle, pipe, cylinder etc. or as a 'generalised' beam section. The 'generalised' beam section is defined by specifying the area and moments of inertia along the cross-sectional axes (local axis 1, 2) of the beam.

The beam mass and inertia properties can be formulated using an isotropic formulation or using an exact inertia formulation. Unless specified an exact formulation is chosen. In the exact formulation, the offset between a beam's node and the centre of mass is included in the mass and inertia matrix formulation where as in isotropic approximations any offset is neglected.

The moment of inertia I_{yy} and I_{zz} can be defined as

$$I_{yy} = \int_V \rho_B (y_c)^2 dV$$

$$I_{zz} = \int_V \rho_B (z_c)^2 dV$$

where y, z are measured from the centre of mass of the cross-section.

The moment of inertia with respect to the centroid of the beam which is offset from the centre of mass is given by the vector $\hat{r} = z_c - z_0$

$$I_{y0} = I_{yy} + mr^2 + m\hat{r}^2$$

where the parallel axes theorem is modified by an additional term $m\hat{r}^2$ which incorporates the offset in the exact beam formulation. This additional term will have an effect on the bending moments calculated for a beam section since Abaqus calculates bending moments about the centroid of the beam section.

Membrane elements in Abaqus are surface elements which have no bending or transverse stiffness but may have mass/unit area. These elements can be used to transmit in-plane forces. SFM3D4 4-node quadrilateral membrane elements are used to represent the FSI surface in the two-way coupling applied in the following investigations. In the present method, structures modelled as 3-D beam elements (B31) to represent the flexibility cannot be directly coupled with the fluid model in Star-CCM+ since the CFD model can only be coupled with another 3-D surface representing the wetted surface. Hence, the surface elements are used to represent the wetted surface area of the ship and the beam nodes representing the flexibility are connected to them.

3.6 Coupling of CFD and FEM

In general, the term FSI can be used for rigid body and elastic body interactions with the fluid. In solving FSI problems for flexible bodies, the fluid and structural solvers should run in a coupled manner. The coupling of fluid and structural solver can be broadly classified as:

1. One-way coupling

and

2. Two-way coupling

When the deformations of the structure can be considered to have negligible effect on the fluid loading such that it has little effect on the fluid, a one-way coupling can be applied. In the majority of marine simulations, the structure is assumed rigid as the fluid loading is calculated using CFD. The resulting pressures are then applied as a load history on to the structural model to calculate the responses. Fluid loading is calculated neglecting structural deformations, which may be sufficient in many cases. In FSI problems where the deformations are large and significantly affect the flow field, a two-way coupled method is required. In two-way coupling, the structural deformations are fed back into the fluid solver to redefine the body mesh. The full system of equations for both the fluid and structural used in the present study are approximating the simultaneous solution by feeding back and forth. Hydroelasticity refers to a two-way coupled simulation.

A two-way coupling can be further classified into a 'loose' and 'strong' coupling. For example, let us consider the static deformation of a flexible aerofoil or wing in 'steady-state' airflow. The bending of the structure can have a significant change in the airflow around the structure; nevertheless, the interaction between the fluid and the structure will approach a steady-state solution where the structural velocities will approach very small values or even zero. In this situation the coupling can be considered 'loose' since in steady-state the structure imparts a negligible motion on the fluid. In such cases, a 'loose' coupling would be sufficient to arrive at the end steady-state solution. Loose coupling refers to problems where response times of structure to a perturbation in the fluid or vice-versa is relatively slow (STAR-CCM+ 2012). On the contrary, in the case of a 'strong' coupling, the mutual dependency in time is high, and a small change in one will have an immediate response in other. A 'strong' coupling is often associated with fluid-structure interaction problems where the hydrodynamic loading and structural velocities changes drastically. In such cases, it may be required to exchange information (pressure, velocities, deformations) between the solvers more than once per time step for the simulation to be stable.

3.7 Co-Simulation between Star-CCM+ and Abaqus

Abaqus (version 6.13-1) was chosen as the finite element solver which will be used to carry out co-simulations (coupled) of ship-wave interactions with Star-CCM+ (version 8.04). The simulations are run in Star-CCM+ environment and depending on the coupling algorithm and user defined time intervals, Abaqus solves the structural problem.

3.7.1 Coupling schemes

The coupling schemes control the sequence of data exchanges in the simulations. There are two coupling schemes in Star-CCM+. For a loosely coupled problem an explicit scheme can be chosen. In this scheme the data or field exchange takes places once every time step. The implicit scheme is chosen when a strong coupling is sought where the field exchanges between the software takes place more than once every time step. The number of exchanges per time step is defined by the user so that the calculated co-simulations displacement has converged in a coupling ex-

change. For example if the total number of inner iterations per time step is 20 with 4 exchanges then for every data exchange 5 inner iterations take place. It must be ensured that the co-simulations displacement residual converges before the next exchange take place. In the case where the co-simulation residuals have not converged then the number of iteration and the exchanges need to be increased to arrive at a converged solution before moving to the next time step. This is critical for the stability and accuracy of the coupled simulations. Bloxom (2014) in his study of predicting the forces and displacements of a flexible bow seal used 20 inner iterations with 4 exchanges per time step resulting in 5 inner iterations per time step. Camilleri et al. (2015) also recommend similar coupling parameters for the constant velocity impact of a flexible wedge in water. A total of 15 inner iterations were performed per time step and 3 exchanges were performed with 5 inner iterations per exchange. The co-simulation residuals were checked in all the simulations carried out in the present study and they decreased by 5-7 orders after the chosen total number of iterations and exchanges.

3.7.2 Field exchange

The coupling is done by exchanging pressure and nodal displacements between Star-CCM+ and Abaqus. The geometry of the floating body must have the same dimensions and geometric coordinates in both software; otherwise the co-simulation will fail due to inconsistency in topology.

Grid flux term represents the ratio of volume swept due to the movement of cell faces from one time step to the next time step. The grid flux corresponds to the reponse of the fluid grid to the structural velocities of the deforming body, i.e. the structural velocities are applied via the grid flux term which is the primary coupling variable at the FSI interface.

For a moving reference the grid flux can be written as:

$$G_f = v_g \cdot a_f \tag{3.8}$$

where v_g is the grid normal velocity and a_f is the face area.

For strongly coupled problems, this term cannot be neglected as the change in fluid states and the flow field is important to arrive at the final deformed state. In tran-

sient simulations, the initial conditions are far from realistic, and for the simulation to settle down in the initial phase of simulation it is recommended to relax the grid flux term by lowering the grid flux under relaxation factor (URF). Large fluctuations in pressure at the interface after each time step can be decreased by using a lower value of grid flux URF. However, a value of URF less than 0.5 will lead to an unrealistic, time-inaccurate solution, especially for problems requiring dynamic accuracy (Peric 2012). The vessel experienced no buoyancy and sunk when the grid flux term was set to zero. Under relaxation of grid flux term was applied to provide stability. The URF for grid flux is stated in Chapter 5 & 6.

3.7.3 Grid Adaptation

When the motion of a body at a free surface is also involved, the position of the body is updated at each outer iteration. The equation of motions of the body is solved to obtain the velocities, and subsequently the displacements and rotations are updated. The fluid grid is adjusted at every outer iteration to follow the updated position of the moving body. Grid adaptation to follow the motion of the body is implemented using two different methods, namely morphing/deforming mesh and overset grids.

The deformation of the body is carried out using morphing. The mesh morpher collects a number of control points and their associated displacements to create an interpolation field and redistributes the mesh vertices. The displacement of a control point within a time step is specified using a displacement vector. Control points can be initialised using existing mesh vertices on a boundary or specified by the user in a control point table. In the case of a two-way coupling, the nodal displacements imported from Abaqus redistribute the mesh vertices by generating an interpolation field throughout domain. The deformation of the fluid grid must conform to the body and also maintain a good quality of finite volume grid. The arbitrary motion of the mesh vertices is taken into account when solving the fluid transport equations. Star-CCM+ uses a “space conservation law” to balance the volume of a CV as a function of time and the motion of the surface (Ferziger & Peric 2003).

The finite volume mesh and finite element mesh used in Star-CCM+ and Abaqus is of a different resolution and FSI coupling is possible even when the meshes are not conformal. Star-CCM+ uses the natural shape function of the finite element topolo-

gy to map field data between fluid and structure meshes. The field data is mapped from one solver to other using interpolation techniques which are decided on the basis of whether the source data is face-centric or node-centric. A brief explanation on how the data mapping is done between the software is given in the next section.

3.7.4 Data mappers

Finite volume codes store the scalar quantities at each cell or the face centroid of the mesh. Finite element codes store the solution at the vertices of the mesh. In the present coupling method, face-to face mapping in the coupling uses least square interpolations and node to face uses shape function interpolation. The fluid pressures at the interface is a stored at the face centroid is mapped on the face centres of the SFM3D4 surface elements using least square interpolation. When the nodal displacements are mapped from a finite element mesh to a finite volume mesh a shape function interpolation is used. To define the relationships between fluid cell centres and finite element nodal locations the co-simulation mappers automatically create import and export mapper functions. The CFD and FE mesh need not be conformal for mapping data.

3.7.5 Time and Motion in coupling

1st order temporal discretisation provides stability to the solution due to the dissipation. The disadvantage is that the time accuracy of transient behaviour will be sacrificed. Furthermore, for wave simulations the second-order provides more accurate and stable wave propagations. Hence, all the simulations were run using a 2nd order temporal discretisation. Morphing for a boundary can be specified under the morpher boundary condition node in Star-CCM+ and the options are shown in the Table 3. Morphing could create problems in the case of large body motions and waves. The deformation of the entire grid could result in the free surface to fall outside the refined region of the grid, resulting in high numerical diffusion before the wave reaches the body. Hence, it will require a larger refinement to simulate motion of ship in waves, thus increase the global cell count, requiring more computational power. To avoid this problem, an overset grid can be used. This feature of overset mesh allows a considerable decrease in computational cost, and also allows sufficient grid refinement at the free surface and around the body. The disadvantage of overset grids is that it is difficult to enforce global conservation in main-

ly 3-D problems. For this reason the overset approach should be avoided for flows subjected to large solution gradients or large regions of separated flows (Wang 1995), (Tang et al. 2003). Overset grids are highly efficient in the case of free surface flow, where the body undergoes large motions in waves.

Table 3: Morpher Boundary Condition

Morpher Boundary Condition	**Description**
Fixed	Mesh vertices are taken for calculating interpolation field but displacement associated with the nodes on this surface is zero.
Floating	The mesh vertices on this boundary are not constrained and move in response to the interpolation field created by morpher.
Co-Simulation	This boundary condition is applied when nodal displacements are received from Abaqus involving mechanical coupling. When displacements at each time step are relative to the initial condition, Morph from Zero is selected from the solver.

3.8 2-D Linear Hydroelasticity

The two-dimensional hydroelasticity method by Bishop et al. (1977) is used as a comparator for the applications. 2-D strip theory is used to calculate the hydrodynamic actions on the body. The structure will be represented as a Timoshenko beam. Lewis form conformal transformation is done to represent the shape of the wetted surface using inputs of beam, water plane area and draft of each strip. Added mass and damping coefficients are evaluated using potential flow theory. Modal summation is employed to represent the vertical displacement, bending moment and shear force at a specified location. The resultant unified equations of motion in regular waves provide the requisite principal coordinates for a range of wave frequencies. Rigid body displacements are evaluated by excluding distortions.

3.9 Verification and Validation

Verification is by and large concerned with the mathematical uncertanities in the models through comparison to analytical results. Verification can be divided into 2 aspects (i) Verification of code (ii) Verification of calculation. Verification of calculation involves uncertainty estimation by determining the accuracy of a single solution and quantifying the errors. This is done by performing a grid convergence

analysis and determining the order of convergence, percentage errors and the grid convergence index (Roache 1998). Spatial and temporal convergence is demonstrated in grid convergence studies, which is also commonly termed as a grid refinement study. The process involves refining the grids (grid cells become smaller and the total mesh size in the domain increases) by two or three levels and to check that the solutions are within asymptotic range. Commonly, a grid refinement of $\sqrt{2}$ is employed in CFD grid refinement studies. When the numerical solution is consistent, it will provide a result that approaches the actual solution as the grid resolution approaches zero. In such a case, the discretised equations will approach the solution of the actual equations. It also requires a high amount of computation power to run calculations on highly refined grids. Validation is the process of determining if we are solving the right equations and if the model is an accurate representation of the real world. The most popular approach to validate a CFD code is to compare its results with experimental results. Although, it is considered as an ultimate test of a CFD code, the basis for carrying out such comparisons has been a subject of discussion for long. Merely comparing the results with experiments to ensure that difference is small is not adequate to consider the CFD code to be validated. The question is if we are comparing the CFD predictions with poor-quality measurements having a large uncertainty, can we consider our CFD method to be validated? Thus the barometer for validation is twofold: (i) The difference between the experimental measurements and CFD is small (ii) The experimental uncertainty or scatter is small. On this basis we can consider the numerical method to be validated.

3.10 Chapter Summary

This Chapter discusses and outlines the modelling technique and numerical methods used in this work. Commercial software Star-CCM+ and Abaqus is used in this research. To demonstrate an understanding of the theory and the effect of various parameters pertaining to this research, a brief description of the numerical method is provided.

Chapter 4:

Numerical Wave Tank

The advent of high speed computing has introduced the possibility of analysing complex fluid flows using numerical methods. Application of Computational Fluid dynamics (CFD) in the maritime industry has seen a steady growth and improvement in recent years. CFD has the capacity to offer an invaluable design and analysis tools to naval architects. One such tool that it offers, is the possibility of modelling a numerical wave tank. Physical wave tanks are still used to a large extent, but they have the limitations of size and scale of the testing facility. However, a numerical wave tank can be helpful in studying the scale effects and understand the flow field results better. A number of investigations have been carried out to study wave simulations using numerical methods, especially using CFD codes (Westphalen et al. 2008) (Peric et al. 2007). The accuracy of numerical wave modelling will have a significant effect on the motion and responses of a body floating in waves. Before any confidence can be placed on the accuracy of numerical results from a CFD code, a verification process should be performed to assess the computational implementation and the results should be validated against a physical model or a known analytical solution.

4.1 Wave simulations

4.1.1 Simulation Details

The suitability of using Star-CCM+ to model a numerical wave tank is presented in this section. To save computational resources, the investigations are carried out using a 2-D model (one cell width), with x along the length and y in vertical direction. In this study, we follow a wave tank geometry and setup which can be used to study the seakeeping problem of containership of length L=350m in head waves. Three wavelengths (λ) are selected for this study corresponding to 2L, L and 0.2L, i.e. 700m, 350m and 70m, respectively. The particulars of the numerical tanks are summarised in Table 4. Amplitude of wave is decided so that the ratio H/λ (steepness ratio) is less than 1/50.

Table 4 : Summary of wavelengths investigated and their respective domain sizes

Wave number	Wave period	Wavelength	Amplitude	Length of Domain	Depth of domain from mean water level	Length Break up
W1	21.1 sec	700 m	3.5 m	5250 m	350 m	2λ+L+3λ+2λ
W2	15 sec	350 m	3.5 m	2800 m	350 m	2L+L+3L+2λ
W3	6.7 sec	70 m	0.7 m	2240 m	350 m	2L+L+3L+2λ

Wave elevations, horizontal and vertical velocities and pressure were monitored at a distance of 2L from the inlet. The calculations were carried out using trimmed Cartesian mesh which predominantly consists of hexahedral cells. The interface between air and water is captured using a Volume of fraction method (VOF) and the HRIC scheme mimics the convective transport equations of the immiscible fluids, resulting in a sharp high resolution interface.

For accurate representation of free surface waves, a sufficient resolution of mesh size and time step are required to avoid excessive numerical damping. STAR-CCM+ (2012) recommend a minimum of 80 cells per wavelength and 20 cells per wave height at the free surface region. Volumetric controls are used for locally refining the free surface region. At the outlet a numerical wave damping is given for a length of 2 wave lengths from the outlet region to prevent any wave to reflect back towards the inlet. Calculations using coarser and finer mesh at the free surface were also carried out to study grid dependency. The orbital velocities decrease exponentially with depth; hence, the mesh size along the depth is progressively increased using volumetric controls so that the orbital velocities are computed accurately. Figure 1 shows the mesh generated (xy plane) for a 350 m wave.

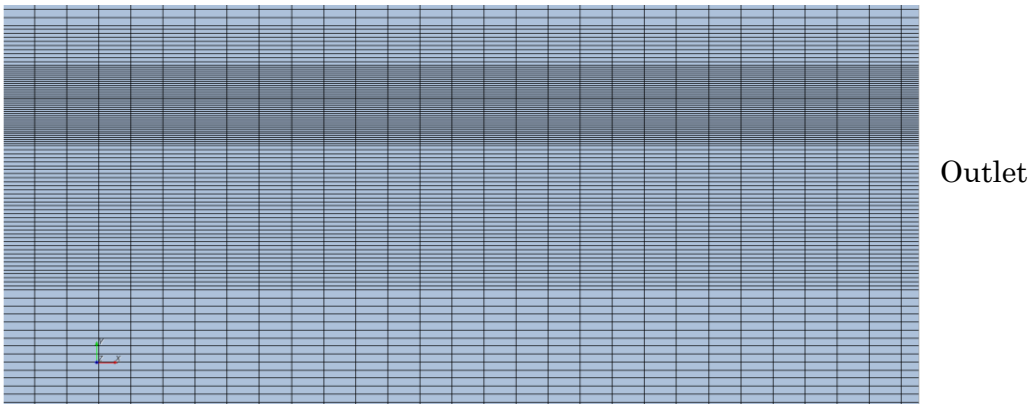

Figure 1: Mesh refinement on free surface

One of the major problems that are commonly encountered in numerical wave tank simulations is that the wave height decreases considerably or there is a significant numerical diffusion after a few wave periods. Hence all the wave simulations were run for a total of 15 wave periods to locate any such discrepancies in numerical predictions. Four different grids are used to compare the effects of refinement and to check convergence. The details of various grid configurations are shown in Table 5. For the vertical (in y direction) refinement, only medium and fine meshes are presented. The medium mesh used is same for both x and y refinements which is referred to as Medium_x (or y). For the sake of simplicity, a refinement ratio (fine mesh size/coarse mesh size) of 2 is used.

Table 5: Mesh configuration for various refinement

Refinement	No. of cells/wavelength	No. of cells/ wave height
Coarse_x	40	20
Medium_x (or y)	80	20
Fine_x	160	20
Fine_y	80	40

For this investigation, total of eight simulations were carried out and the details of the simulations are also shown in Table 6. One case with 1< Courant number <2 was simulated for W3 to discuss the importance of time stepping in numerical wave predictions using Star-CCM+, and is referred to as Case 6 in Table 6. Please note that for the simulations in this Chapter the local and higher courant number limit for HRIC was not altered as mentioned in Section 3.3.

Table 6: Wave Test cases

Cases	Meshes	Wavelength	Time Step	Total mesh count	Temporal Discretization
Case 1	Coarse_x	W2	0.03	Inviscid	2nd order
Case 2	Medium_x (or y)	W2	0.03	Inviscid	2nd order
Case 3	Fine_x	W2	0.01	Inviscid	2nd order
Case 4	Fine_y	W2	0.01	Inviscid	2nd order
Case 5	Medium_x (or y)	W2	0.03	Inviscid	1st order
Case 6	Medium_x (or y)	W3	0.03	Inviscid	2nd order
Case 7	Medium_x (or y)	W3	0.01	Inviscid	2nd order
Case 8	Medium_x (or y)	W1	0.03	Inviscid	2nd order

Although the simulations were run using a 2nd order temporal discretization scheme, the effect of 1st order temporal discretization was also studied for the 350 m wave (W2 and Case 5). The 2nd order scheme is more accurate, but with VOF and HRIC scheme, the local courant number on the free surface interface is important. Hence for all the wave simulations the courant number on the free surface is less than 0.5.

At the velocity inlet, orbital velocities of the wave are prescribed together with the volume fraction of water and air. The hydrostatic pressure of the first order wave is prescribed at the pressure outlet boundary along with the volume fraction of both phases. The remaining boundaries are defined as non-slip wall condition. Simulations of the numerical wave tank were carried out using the inviscid option in Star-CCM+.

The simulations were run in parallel mode with single precision on the University of Southampton high power computing facility Iridis 3. It consists of a total of 11760 cores and each node is made up of 12 cores consisting of 2.4GHz and 2 GB RAM.

4.1.2 Results and Discussion

The numerical wave tank simulation results for the three wavelengths, using a VOF method are presented in this section. Wave elevations (η), horizontal (x) and vertical (y) velocities across depth and pressure variations (static + dynamic) across depth are plotted and compared with the theoretical solution of a first order wave. These physical quantities were monitored using line and point probes at 2L distance from the inlet of the domain, i.e. where the bow of the ship will be located in the next chapters.

4.1.2.1 Results for 350m wave

The wave height used to simulate a wave of length 350 m is 7 m for all cases. Three grid refinements in x direction and two grids in y direction are investigated (see Table 6). When refining the grids in x directions, the cells in y direction is kept constant with 20 cells per wave height, and refined grids in y direction has 80 cells per wavelength.

For calculation purpose the average height of peak-to-trough is considered over ten wave periods. The post-processing is done using a MATLAB code. The time history plot of wave elevation for the coarse, medium and fine grids in x direction, denoted by Coarse_x, Medium_x, Fine_x, is compared with the theoretical calculations denoted by η_theory, in Figure 2. A good agreement is observed between the numerical predictions and theoretical calculation of the wave elevation. The wave is considerably stable in all three grid configurations and there is no phase lag or a large decrease in wave height observed. Table 7 shows the absolute maximum difference of average wave height over ten wave periods in numerical predictions and the theoretical wave height (7m) expressed in percentages. The maximum difference is observed for the coarse mesh which is still less than 10%. The variation from one grid to another is not monotonic and it is not unusual that such variation is observed, especially when unstructured grids are used. The least difference is observed on the medium grid, which is also the recommended grid configuration by Star-CCM+. In the case of fine grids the aspect ratio of the cells at the free surface is around 9, which could be the reason for a slight deterioration in the result.

Table 7: Absolute Maximum difference for cell refinements in x direction

Mesh Type	Total number of cells	Average wave height	Absolute maximum difference
Coarse_x	52160	6.65053	4.99 %
Medium_x (or y)	94080	6.974445	0.365 %
Fine_x	173440	6.9265	1.05 %

Figure 3 shows the plots of vertical (y) and horizontal (x) velocities under a wave crest and trough after 10 wave periods. Very good agreement is seen in the case of horizontal velocities. However, slight scatter is seen very close to the free surface region and this is more pronounced in the case of vertical velocities. The trends of vertical velocity predictions in coarse and medium mesh is better and the scatter is highest in the fine mesh. There is bound to be such scatter in the free surface region, and it is due to the inherent nature of the computational method. Orbital velocities are characteristics of the water particles and trying to predict them accurately on the free surface region using a control volume method is difficult. In the control volume method the equations are discretised at the cell centroids and

the value of the derivatives are calculated at the control volume faces using interpolation and iterative techniques.

The magnitude of vertical velocities is of the order of 10^{-3}m/s and decrease to 0m/s across the depth. Also the change in vertical velocity for a variation in the time of, say 0.03 sec (time step for the simulations), is about 0.02 m/s. A small phase difference was also noted between the wave elevations in the simulations and the theortical calculations and, hence, it was very difficult to accurately match time at which the crest or a trough crosses in the numerical and theoritical calculations. A combination of all the above factors makes it very diffcult to predict the vertical velocities with a high degree of accuracy. The magnitude of horizontal velocities are much higher than the vertical velocities and their variation with a small change in time step is also not high. Hence, the agreement of horizontal velocities predicted by CFD against the theoritical calculations was better. Figure 4 shows the variation of pressure across depth for a crest and trough after 10 wave periods. Very good agreement is observed in the prediction of pressure when compared with the theory.

The time history of wave elevation for refined grids in y direction is shown in Figure 5. The results for medium and fine grids are denoted by Medium_y and Fine_y, respectively. Refer to Table 8, also note Fine_y is not as good as Medium_y. Wave simulation using coarse grids in y direction was also calculated using 10 cells per wave height. The results for this configuration showed that the wave height decreasing drastically and eventually dying out. A large phase difference was also observed after a few wave periods. Hence the results are not presented. There is very minimal decrease in wave height observed in the wave elevation simulated using the Star-CCM+, and the phase difference is almost negligible.

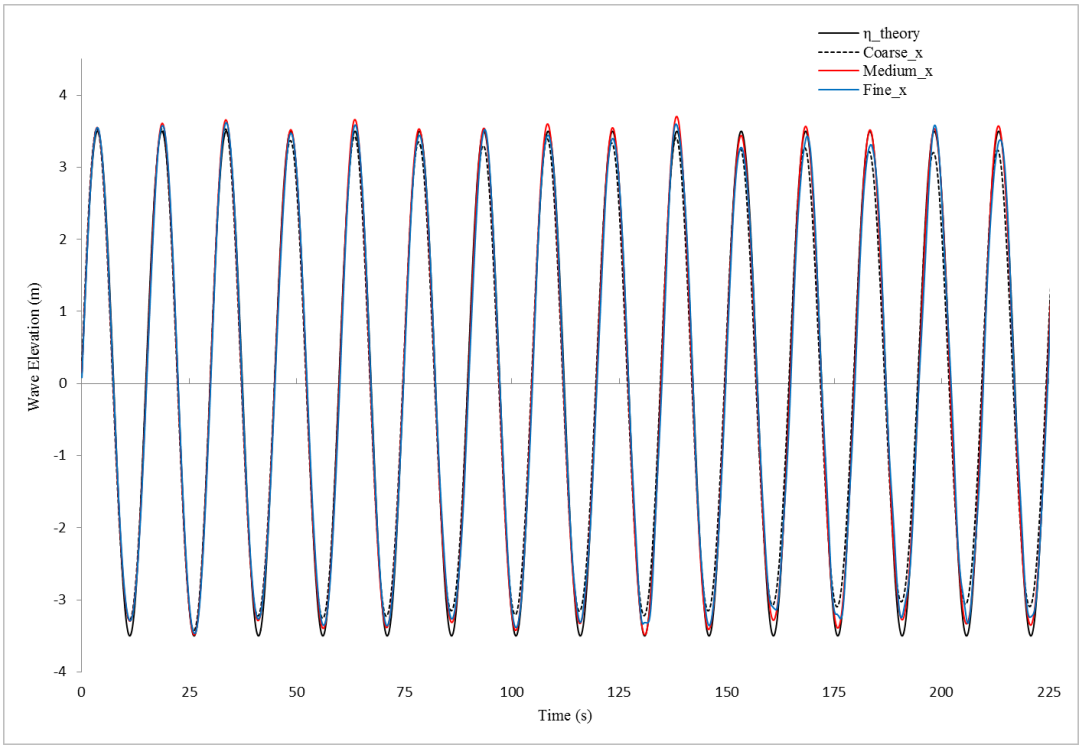

Figure 2: Time history of wave elevation for 350m wave for refinement in x direction

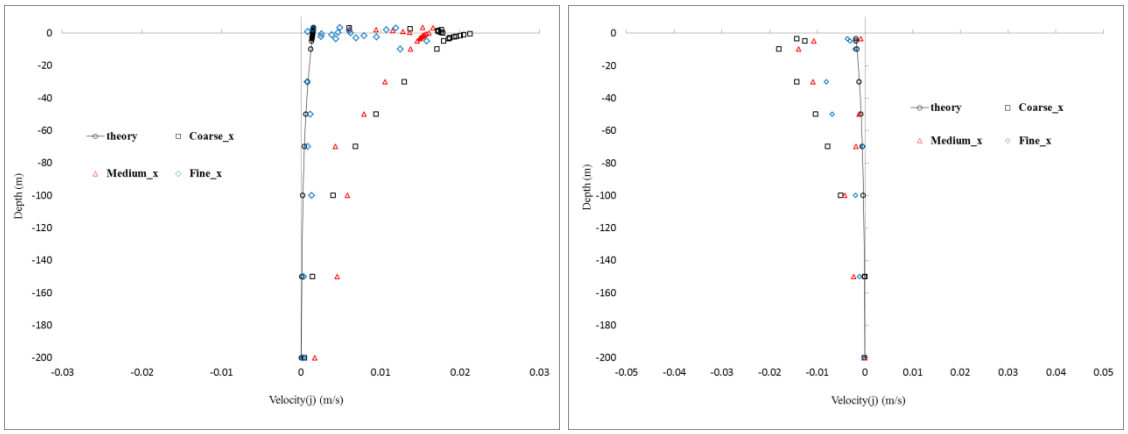

(a)

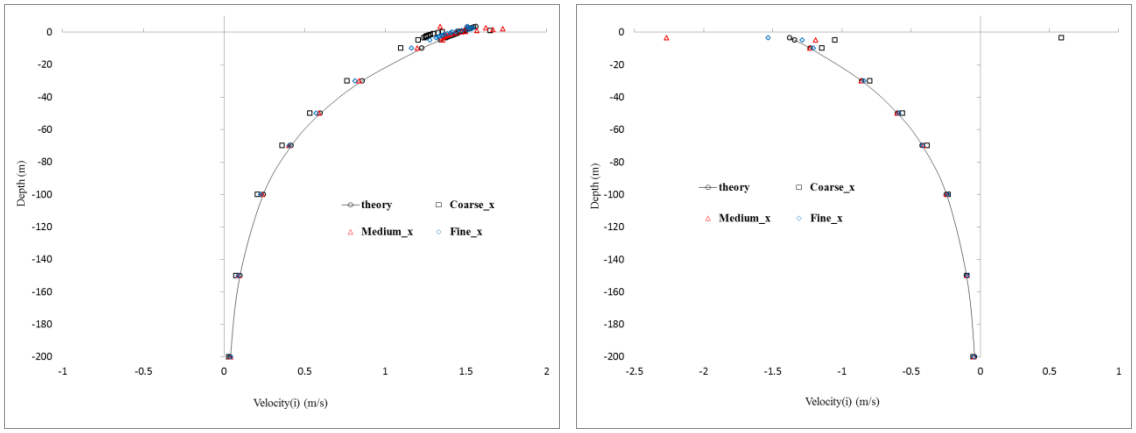

(b)

Figure 3: y (a) and x (b) orbital velocities for 350 m wave under wave crest (left) and trough (right) across depth for refinement in x direction

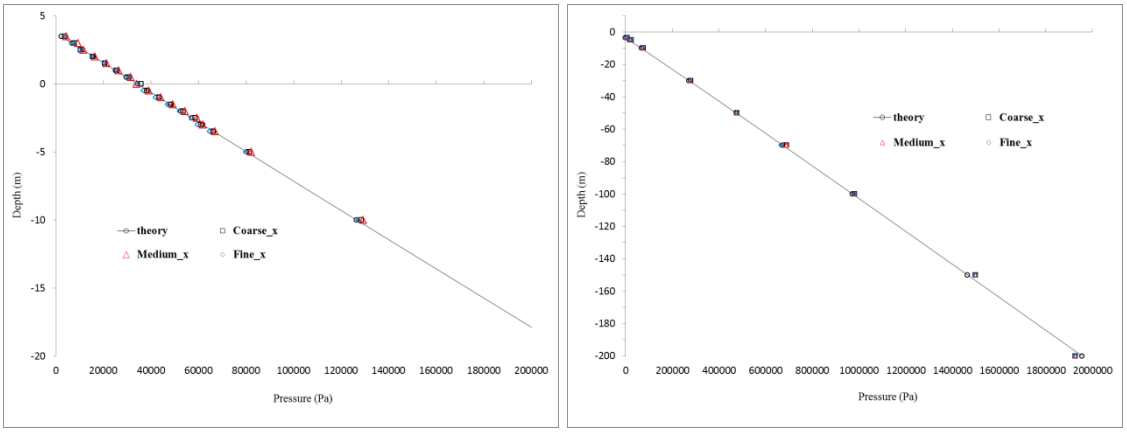

Figure 4: Pressure variation across depth for 350 m wave under wave crest (left) and trough (right) for refinement in x direction

The orbital velocities and pressure varying across the depth also show good agreement when compared with the theoretical values. The plots of orbital velocities and pressures across depth for the two mesh refinements calculated can be seen in Figure 6. The vertical (y) orbital velocities for medium and fine agree well with each other and the differences close to free surface are small. Again we observe that the horizontal velocities and the pressure match well with the theoretical trend.

The absolute maximum difference between the simulation and theory averaged over 10 wave periods, is shown in Table 8.

Table 8: Absolute maximum difference for cell refinement in y direction

Mesh Type	Total number of cells	Average wave height	Absolute maximum difference
Medium_y	94080	6.97	0.365 %
Fine_y	173440	6.85	2.2085 %

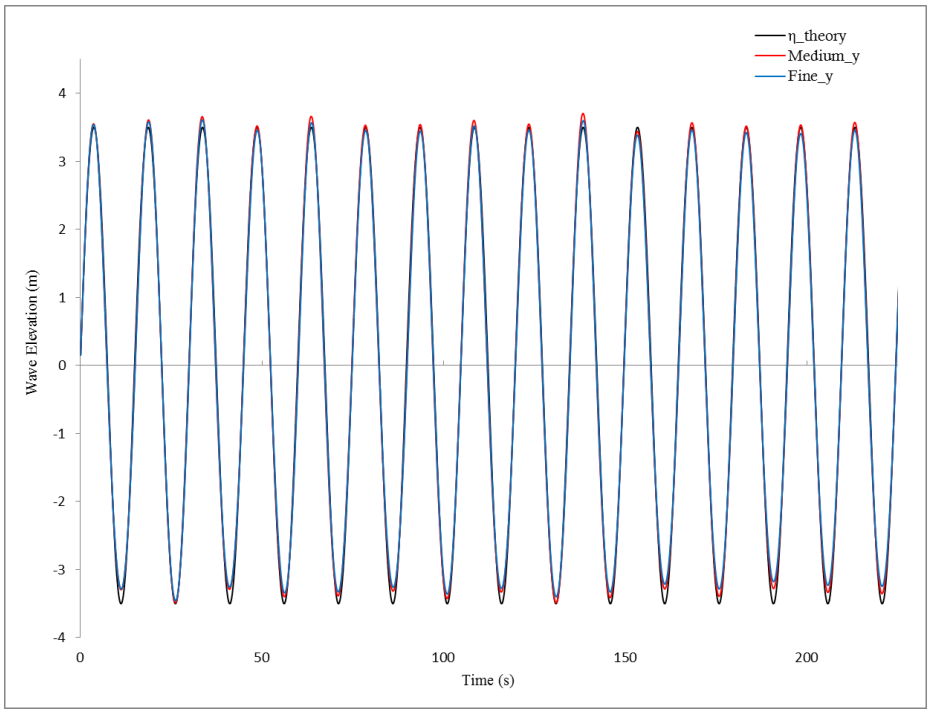

Figure 5: Time history of wave elevation for 350m wave for refinement in y direction

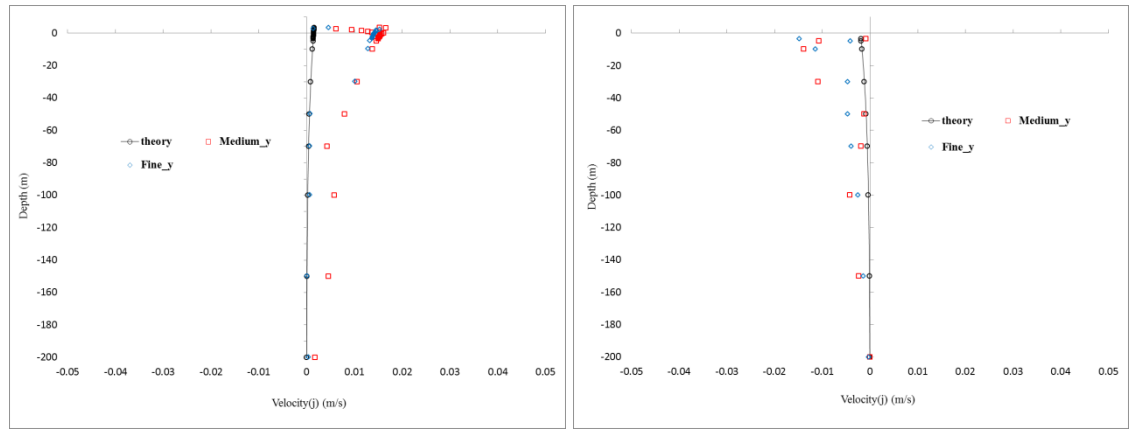

(a)

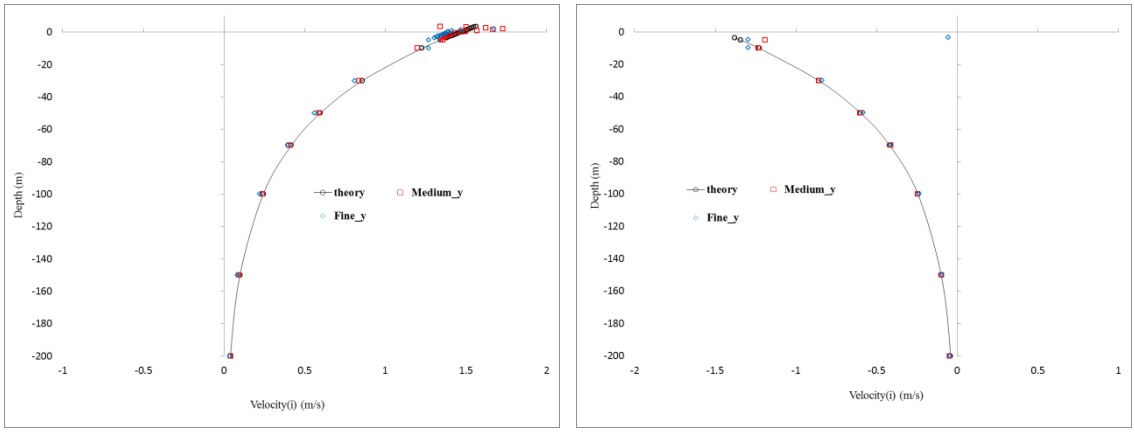

(b)

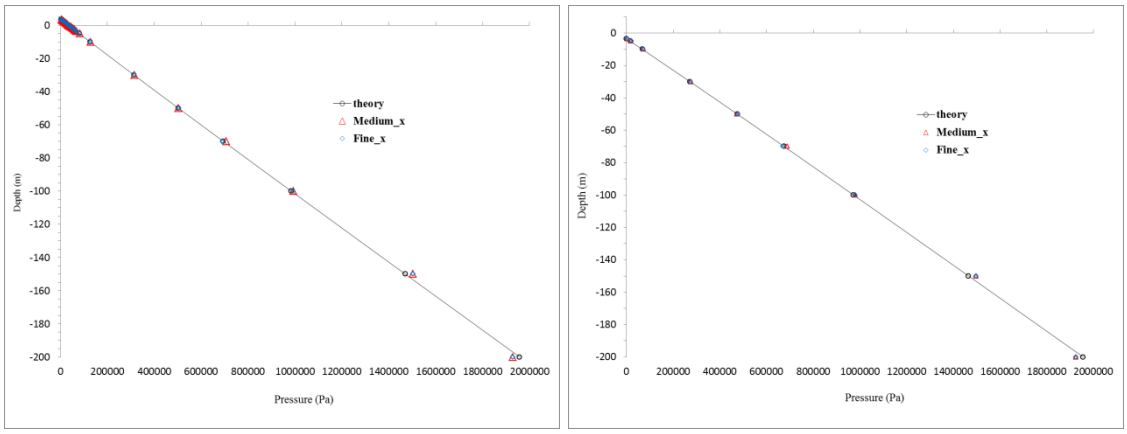

(c)

Figure 6 : y (a), x (b) orbital velocities and pressure variation (c) across depth for 350m wave under crest (left) and trough (right) for refinement in y direction

The wave elevations using two different time steps are shown in Figure 7. The results obtained from 1st order and 2nd order is denoted by 1st order and 2nd order, respectively. A considerable decrease in wave height can be seen in the 1st order solutions. Although a decrease of 15% is noted in the predictions using 1st order, the wave maintained the height after a few periods and did not decrease any further. Higher order schemes are relatively more accurate but can exhibit instabilities when simulating complex free surface flows or carrying out strong fluid-structure interactions problems. In these cases, using a 1st order scheme might give more stability to the simulations and errors in predictions can be quantified.

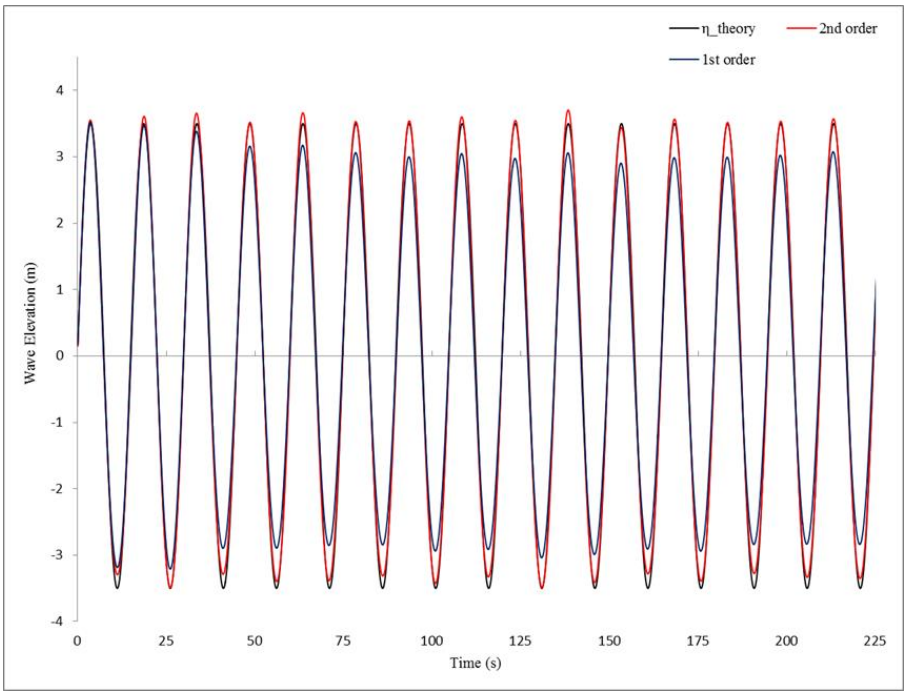

Figure 7 : Time history of wave elevation for 1st order and 2nd order time discretisation

4.1.2.2 Results for 700m wave

The wave height used to simulate a wave of length 700 m using a numerical wave tank was 7m. The time history of wave elevations obtained from Star-CCM+ using the medium mesh and denoted by Medium is compared with the theoretical calculations, denoted by η_theory, in Figure 8. The absolute maximum difference in the wave elevations between the simulation and the theoretical after 10 wave periods is about 2.5 %.

The variation of x and y orbital velocities and pressure across depth is shown in Figure 9. The trend is very similar to the previous cases, showing some scatter in the free surface region. The agreement in predictions improves across the depth of the domain.

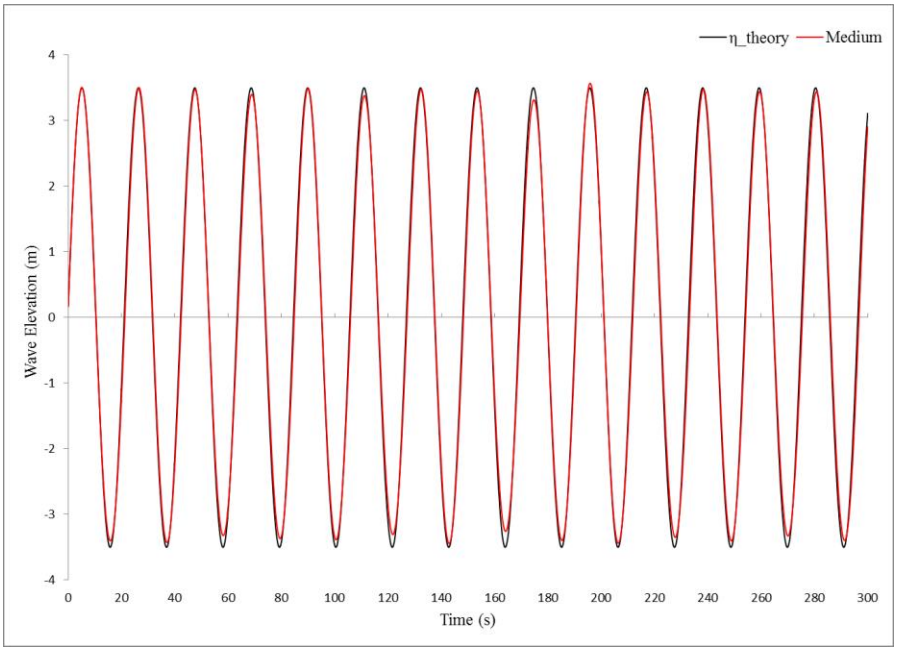

Figure 8 : Time history of wave elevation for 700m wave

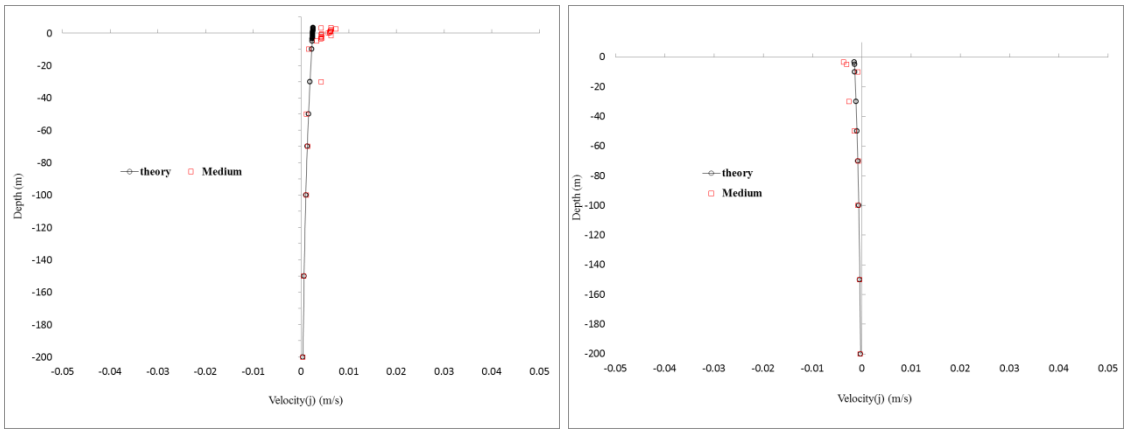

(a)

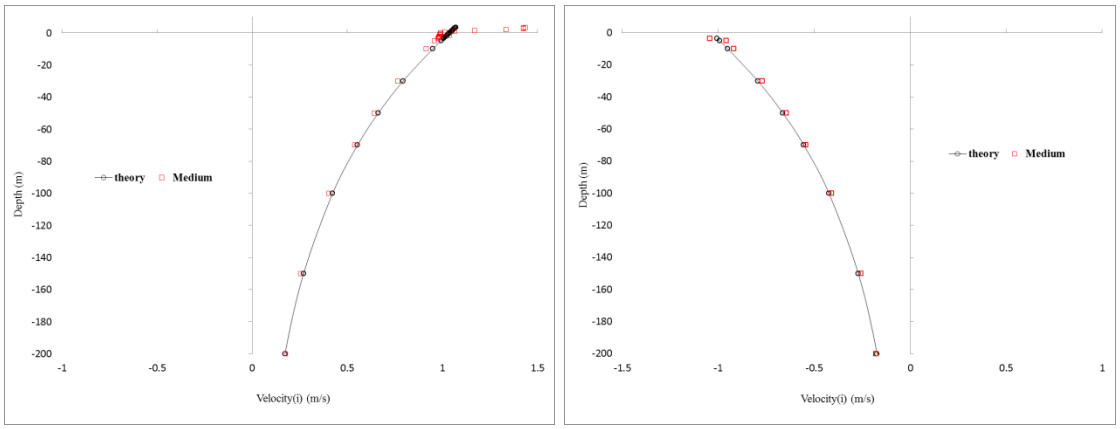

(b)

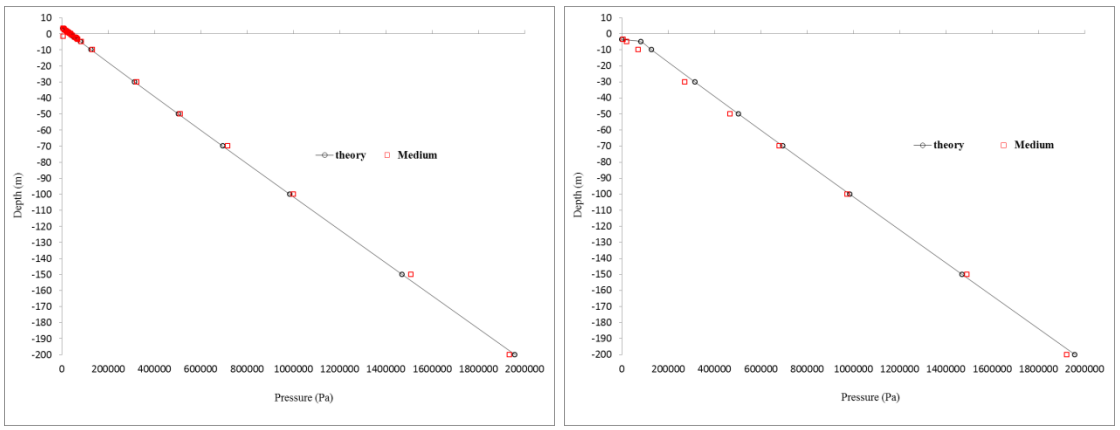

(c)

Figure 9: y (a), x (b) orbital velocities and pressure variation (c) across depth for 700 m wave under crest (left) and trough (right)

4.1.2.3 Results for 70m wave

For all simulations using this wave length only the medium mesh was used. Maintaining the maximum courant number below 1 is vital in numerical wave tank simulation to minimise diffusive errors. To compare the effect of higher courant number on the wave propagation, computations were performed using 2 time steps.

Numerical computations were carried out using a Δt of 0.03 and 0.01 seconds, with CFL between 1 and 2 and < 0.5 respectively, on the medium mesh configuration. The results of the wave elevation time history plots for the two time steps, denoted by Medium_0.03sec and Medium_0.01sec, are compared with the theoretical wave elevation, in Figure 10. The variation of orbital velocities across depth is shown in Figure 11.

Numerical predictions for a higher courant number deteriorate after 3-4 wave periods show a considerable decrease in wave height and a large phase difference as the simulation progresses. The results of simulation having a CFL of ≤ 0.5 showed good agreement with the theoretical solutions.

From these plots it can be inferred that the courant number is an important parameter for the numerical wave tank simulation and should be maintained below 0.5 (the lower courant number limit for HRIC) on the free surface. Good agreement is seen between numerical simulation and theoretical calculation for wave elevations and orbital velocities for time step of 0.01 sec.

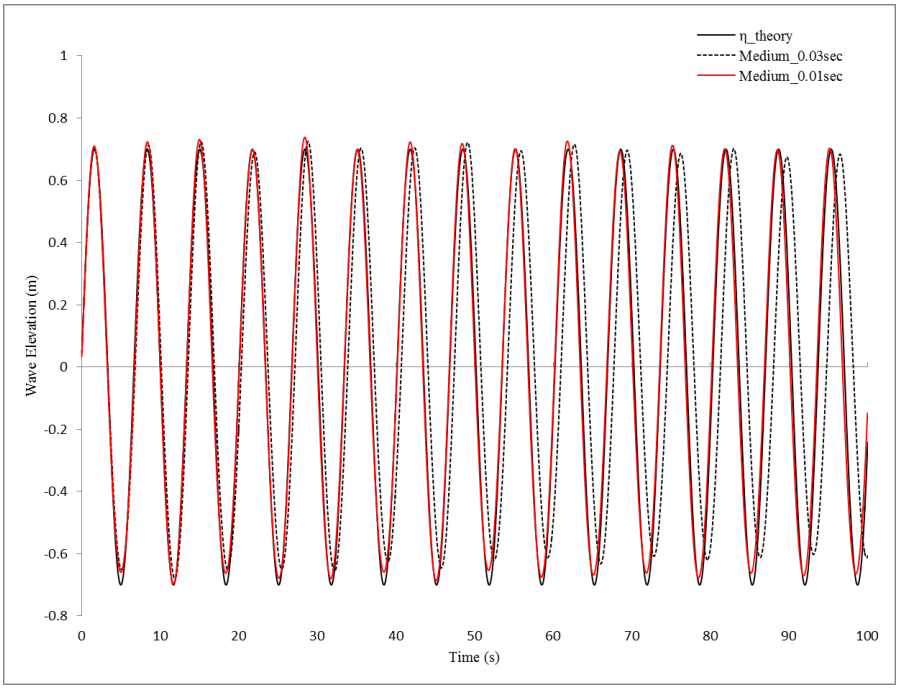

Figure 10: Time history of wave elevation for 70 m wave compared with theoretical wave elevation for 2 different time steps

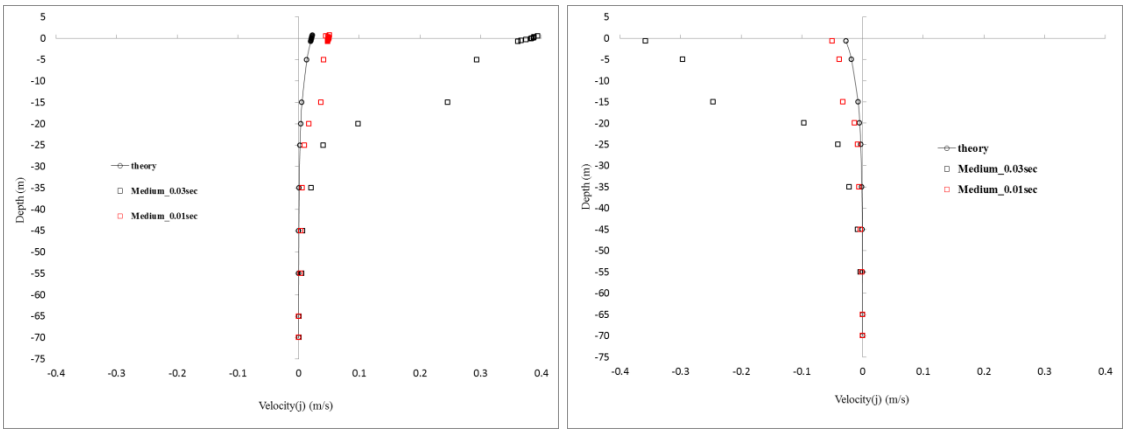

(a)

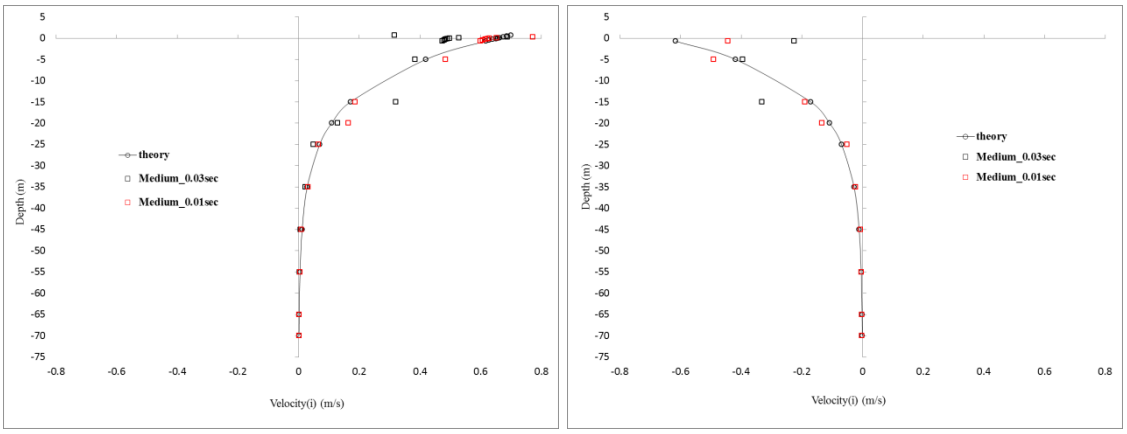

(b)

Figure 11: y (a), x (b) orbital velocities across depth for 70 m wave under crest (left) and trough (right)

4.1.2.4 3-D numerical wave tank

The previous investigations were carried out on a 2-D model and before proceeding to the hydroelastic coupling the same wave lengths described in Table 4 were simulated on a 3-D model. In this case only the elevations were recorded at a distance of 2L from the inlet and compared to the theoretical wave elevations. The medium mesh in Table 5 was used for the 3-D simulations of the linear wave. In addition to the domain sizes shown in Table 4, the side wall was extended to 4L (L=350 m) to create the 3-D computational domain. The elevations for five wave periods recorded for 700m, 350m and 70m is shown in Figure 12-14, respectively. For all the three wavelengths investigated the difference between the average amplitude for ten wave periods and the theoretical wave amplitude is less than 10%.

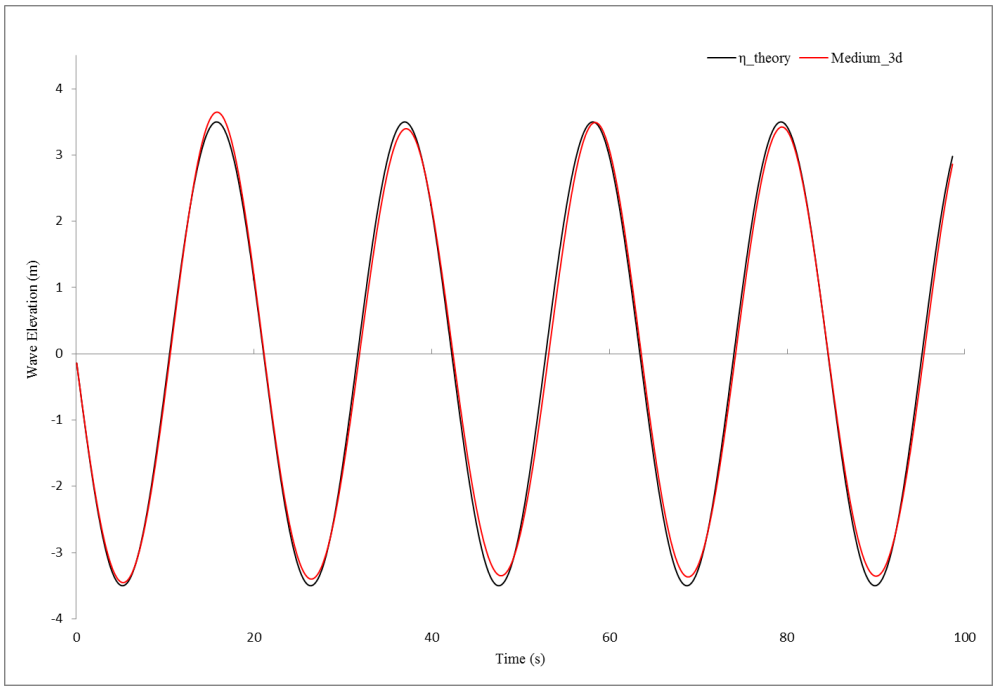

Figure 12: Time history of wave elevation for 700m wave for 3-D domain

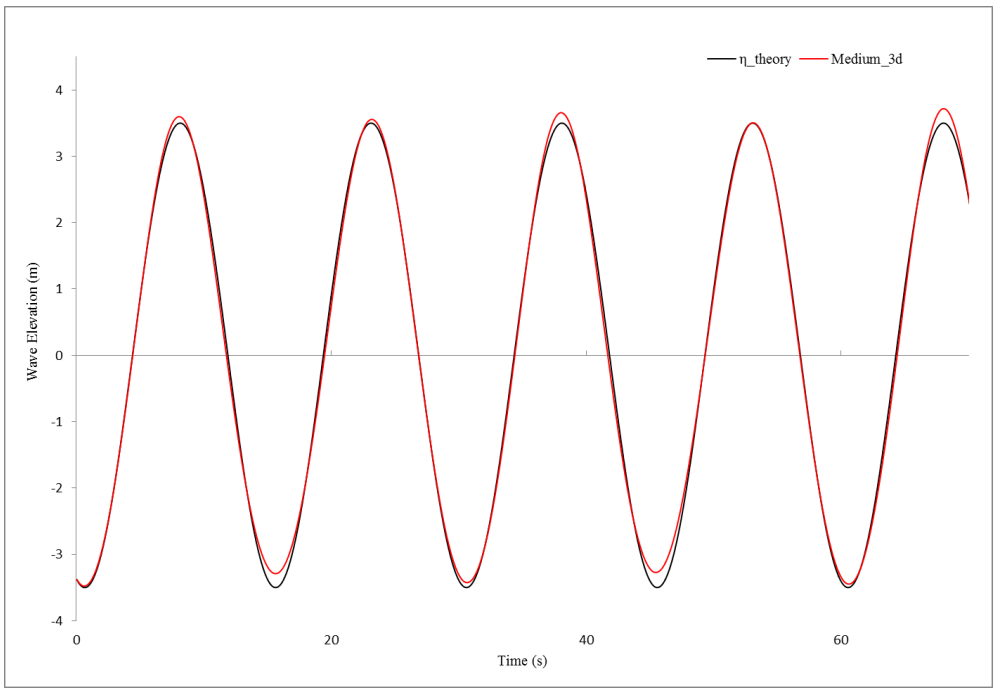

Figure 13: Time history of wave elevation for 350m wave for 3-D domain

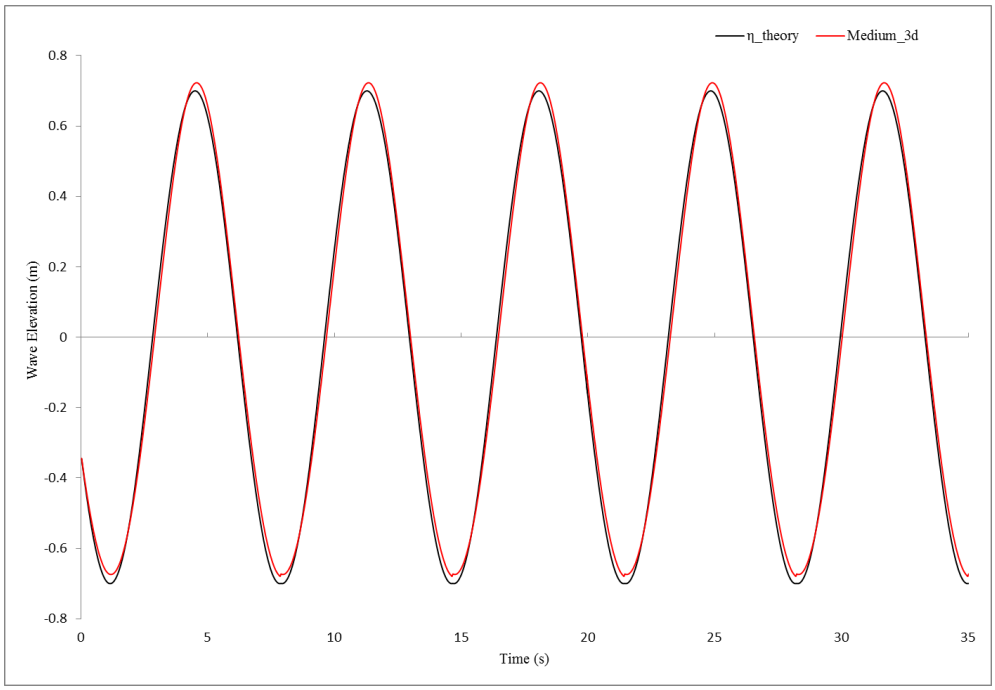

Figure 14: Time history of wave elevation for 70m wave for 3-D domain

4.2 Chapter Summary

This Chapter has investigated the accuracy of numerical wave tank simulations using Star-CCM+. The effect of mesh refinement at the free surface on the wave elevations, orbital velocities and pressure has been studied. It has been shown that for an accurate numerical wave simulation in Star-CCM+ the mesh refinement at the free surface, time step and the temporal discretisation scheme play an important role. The mesh refinement recommended by Star-CCM+ showed good accuracy when compared with the theoretical solution of first order wave. Little scatter was noted in the case of orbital velocities, especially at the free surface, which did not show much improvement when using fine grids. These discrepancies are mainly due to the inherent characteristic of the numerical method which is based on finite volume technique. Although, coarser meshes showed larger differences, the errors were within acceptable range. The next Chapter details the investigations carried out to study the motion response of a barge in head regular waves, treated as both rigid and flexible body. A two-way coupling is employed to model the flexible barge.

Chapter 5:

Response of Barge in waves

This Chapter presents the evaluation of motion and responses at various locations along a flexible barge (Remy et al. 2006) by applying the two-way coupling described in Section 3.7. Computations are carried out in regular head waves for a number of frequencies; hence the interest is only on symmetric motions and responses. This Chapter focuses on the method of application of the two-way coupling, modelling challenges, and accuracy of the method through results and discussion. The numerical instabilities experienced are also brought to light in the case of the very flexible barge. The results are validated against experimental measurements (displacements only) and 2-D linear hydroelastic predictions. A verification assessment involving grid convergence is carried out for the worst case scenarios. 3-D computations are first carried out treating the barge as a rigid body to establish the domain size and mesh refinement along the free surface and in the vicinity of the barge.

5.1 Barge Characteristics

The experimental model of a flexible barge consisting of 12 connected caissons is considered for validating the present numerical method (Remy et al. 2006). Each caisson is clamped to a steel rod which was placed at 57 mm above deck level. The rod has a square cross-section of 1 cm × 1 cm as shown in Figure 15. All the caissons were rectangular sections except for the bow caisson which has a bevelled shape. The caissons were separated with a gap of 15 mm to avoid contact when undergoing distortion in waves. The dimensions of the wave basin are 30m × 16m × 1m. The main characteristics of the barge and the flexible rod are given in Table 9. The model was secured using steel cables and springs to ensure that the natural periods of surge and sway were well above the wave periods.

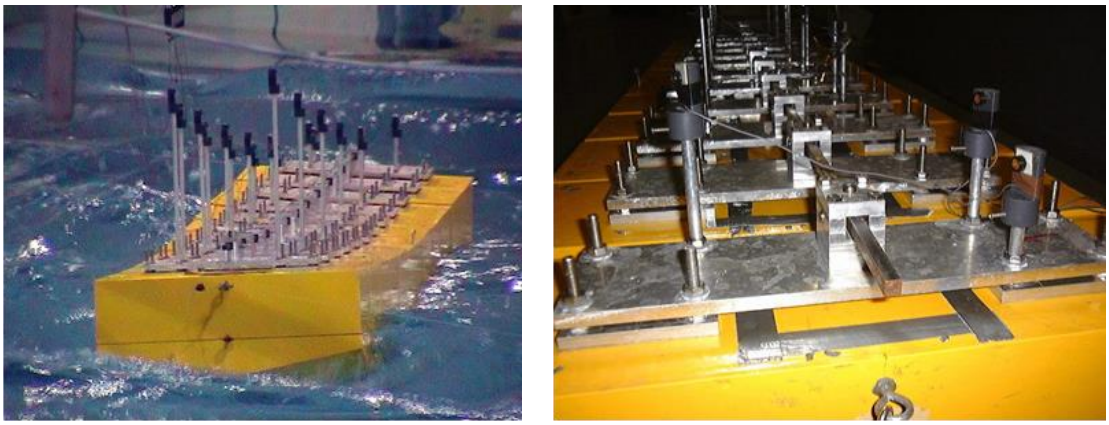

Figure 15: Hydroelastic model of the flexible barge used in the experiments

Vertical, horizontal and torsional bending was allowed for the model, and tests were conducted in regular waves, and irregular waves of varying headings. In the case of regular head waves, the barge was subjected to ten different wave periods (T_w) with two wave heights (H_w) for each wave period. The barge motions were measured at 6 different locations with the optical system RODYM DMM 6D (KRYPTON), consisting of three camcorders tracking six groups of three infrared LEDs attached to these locations, as shown in Table 10 (x, y and z measured from stern, centreline and the keel of the barge).

Table 9: Barge characteristics

Length of barge, L_{pp} (caissons + clearance)	2.445 m
Beam	0.6 m
Depth	0.25 m
Draft	0.12 m
KG	0.163 m
Total mass (caissons + equipment)	172.55 kg
Length of each caisson	0.19 m
Mass of each caisson (except bow)	13.7 kg
Mass of bow caisson	10 kg
Moment of inertia of rod	8.33×10^{-10} m ^{4}
Bending stiffness of rod	175 N m ^{2}
Young's modulus of rod	2.1×10^{11} N/ m ^{2}

Table 10: Measuring points from aft of barge

Location	x (m)	y (m)	z (m)	x/L
1	2.445	0.0	0.25	1.0
3	2.035	0.0	0.25	0.83
5	1.625	0.0	0.25	0.66
7	1.225	0.0	0.25	0.5
9	0.805	0.0	0.25	0.33
12	0.19	0.0	0.25	0.08

5.2 Test Cases

Two types of simulation were carried out in the present study.

- Response of the barge in head waves, treated as a rigid body, in head regular waves is calculated for five wave periods only, with details shown in Table 11. The objective is to obtain insight into domain sizes, damping zones, motion of rigid body and mesh refinement around the body for each wave period. The rigid body displacements calculated using CFD are compared against 2-D strip theory predictions.
- Response of the barge, treated as a flexible body, in regular head waves is calculated for the same wave periods. Simulations are conducted by applying the two-way coupling between Star-CCM+ and Abaqus. Total vertical displacements, vertical bending moments (VBM) and vertical shear forces (VSF) were calculated at the locations shown in Table 10. Calculated displacements were compared with experimental measurements and 2-D hydroelasticity. However, due to lack of experimental data, 2-D hydroelastic predictions served as the only comparator for the VBM and VSF calculated using co-simulation. Co-simulation was also performed using smaller wave heights for a few frequencies to study the effect of nonlinearity. The details are given in Section 5.7.

Table 11: Test Conditions

Wave Period (s)	Wave Frequency (rad/s)	Wave Length (m)	Wave Height	λ/L
1.8	3.490	5.058	100 mm	2.07
1.6	3.926	3.996	100 mm	1.63
1.2	5.235	2.248	100 mm	0.92
1.0	6.283	1.561	100 mm	0.64
0.9	6.981	1.264	50 mm	0.52

5.3 Computational Domain

The coordinate system of the 3-D domain used in the CFD computations has the x axis along the length of the barge and y and z in the athwartships and vertical directions, respectively. The length of the domain in the inlet-outlet and side wall directions are generally calculated based on L_{pp} or wave length (λ) for similar ship-wave interaction studies (Seng et al. 2012, Peric et al. 2007). The domain is considered sufficiently large in these directions to avoid any wave reflections. In the present study, the wavelength to barge length (λ/L) ratio varies from 2 to 0.4. For $\lambda/L \geq 1$, the inlet and wake regions are located at about 1.5 λ and 2λ from the barge, respectively. The length of inlet and wake regions for $\lambda/L \leq 1$ is 3.0 L_{pp} for both. In addition to this, a numerical beach is provided using VOF wave damping option in Star-CCM+ at the outlet to damp the waves and prevent reflections. The length of the damping region required from a specific boundary, in this case the outlet, is specified as an input. The VOF wave damping introduces a resistance to the vertical wave motion (Choi & Yoon 2009). The length of this damping region in all model is 2.0λ. The domain sizes for individual wave frequencies, for both rigid and coupled simulations, are shown in Table 12. The total distance from the body to outlet is sum of wake and the damping distance. (ITTC 2011) recommends that for ship simulations in waves, the inlet boundary should be located atleast 1-2 L_{pp}, whereas the outlet boundary should be positioned 3-5 L_{pp} to avoid wave reflections from the outlet. This criterion is satisfied in the present computational domain models, and in fact is surpassed in the cases of longer waves. The depth of the side wall (y-direction) is fixed as 8m (same as the tank) on one side of the barge for all cases. Initially, a reduced length of the side wall (6 meters) was tested for a few frequen-

cies but showed evidence of wave reflections from the side walls after 4-5 wave periods.

Symmetry condition is used for rigid body simulations, whereas full domain is modelled for the co-simulation cases(Lakshmynarayanana et al. 2015a). Although present investigations of co-simulations only concentrate on head waves, oblique wave conditions are also of interest for future investigations. To model oblique wave interactions on a body, symmetry condition can no longer be used. Hence, to get an idea of the mesh sizes and computational time, full domain is preferred for co-simulation case.

Table 12: Domain sizes for regular wave periods and lengths (*port side only)

Wave Period (s)	Wave Length (m)	Inlet zone L1 (m)	Wake Region L2 (m)	Damping Zone L3 (m)	Breadth of domain * (m)	Water Depth (m)
1.8	5.058	7.6	10	10.1	8.0	4.0
1.6	3.996	6.0	8.0	8.0	8.0	4.0
1.2	2.248	5.0	5.0	4.5	8.0	4.0
1.0	1.561	6.5	6.5	3.0	8.0	4.0
0.9	1.264	6.5	6.5	2.5	8.0	4.0

5.4 Meshing Strategy & Boundary Conditions

A combination of trimmed Cartesian mesh, extruder and overset mesh is used for all CFD simulations. The body and free surface grid refinement is identical for both rigid and flexible body simulations for identical frequencies. Cartesian grids aligned with the free surface are desirable for free surface applications using VOF multiphase flows (Prosperretti & Tryggvason 2009). Trimmed Cartesian mesh produces a base mesh of hexahedral cells aligned with the free surface and later trims the base mesh at the input hull surface creating polyhedrons. Once the core mesh is created, the side wall, in y-direction, and the outlet is extruded using user specified extrusion parameters (i.e. number of layers, stretching ratio and extrusion magnitude) to the required distance (as per Table 12). In Figure 16, the initial core mesh is differentiated by red lines which are then extended. Not only does the extruded grid aid in saving the global cell count but also dissipates the waves in the far field due to gradual coarsening of grid size. Nevertheless, the mesh growth rate in the extruder region was kept under 1.1 to prevent any numerical reflections

arising due to sudden change in grid sizes between adjacent cells (STAR-CCM+ 2012). The advantages of using overset grids for wave-body interaction problems are explained in Section 3.7.5.

The grid was refined along the free surface region, near the barge and in the wave radiation zone around the barge. A typical mesh, corresponding to T_w=1.8s is shown in Figure 16. The figure shows the fluid domain, the grid refinement around the body and the wave radiation zone on a plane section on the mean free surface level. Mesh refinement was carried out based on the disturbed wave contour around the body. After testing a few cases it was noted that the waves radiated out of the body in a circular pattern. The instantaneous wave contours for both rigid and flexible motions of the barge for two different frequencies (4.0 rad/s and 7.5 rad/s) also gave some insight into the radiated wave pattern (Kim & Kim 2009) and Figures 24 & 25. Hence, refinement around the body was also carried out in a manner so as to capture the circular disturbed wave pattern. In the free surface region, 45-60 cells are placed per wavelength and 12-15 cells per wave amplitude. Around 320 cells per wavelength and 160 cells per wavelength are clustered in the near body region (bow, stern and around body) and wave radiation zone, respectively. The global mesh count for the co-simulation cases varied from 2.3 million to 13.6 million and in the rigid body cases the mesh count was half of that in co-simulation cases. The simulations were run in parallel mode with single precision on the University of Southampton high power computing facility Iridis 4. It consists of a total of 12320 cores and each node is made up of 16 cores consisting of 2.6GHz and 4 GB RAM. The grids mentioned for the co-simulation cases were run with 128 processors and it took between 1.2 hours to 4 hours to run 1 second of real time simulation.

In CFD simulations, determining appropriate initial conditions and boundary conditions is critical not only to obtain accurate solutions for a particular problem but also to prevent unnecessary computational costs (Date & Turnock 1999). Boundary conditions for both rigid and flexible bodies were selected so that they mimic the conditions of a towing tank. At the velocity inlet boundary the kinematics of the wave, i.e. the position of the free surface and velocity of the first-order wave as field functions are prescribed. At the outlet boundary, the outlet pressure is set to the hydrostatic pressure of the wave and the position of free surface is specified. The top of the domain is set to velocity inlet as it prevents from fluid sticking to the

walls. Basically, it avoids a velocity gradient to happen between the fluid and the wall and in addition directs the flow parallel to the outlet boundary (Tezdogan et al. 2015). For the no-slip wall condition (Table 13) the fluid tangential velocity is set to zero.

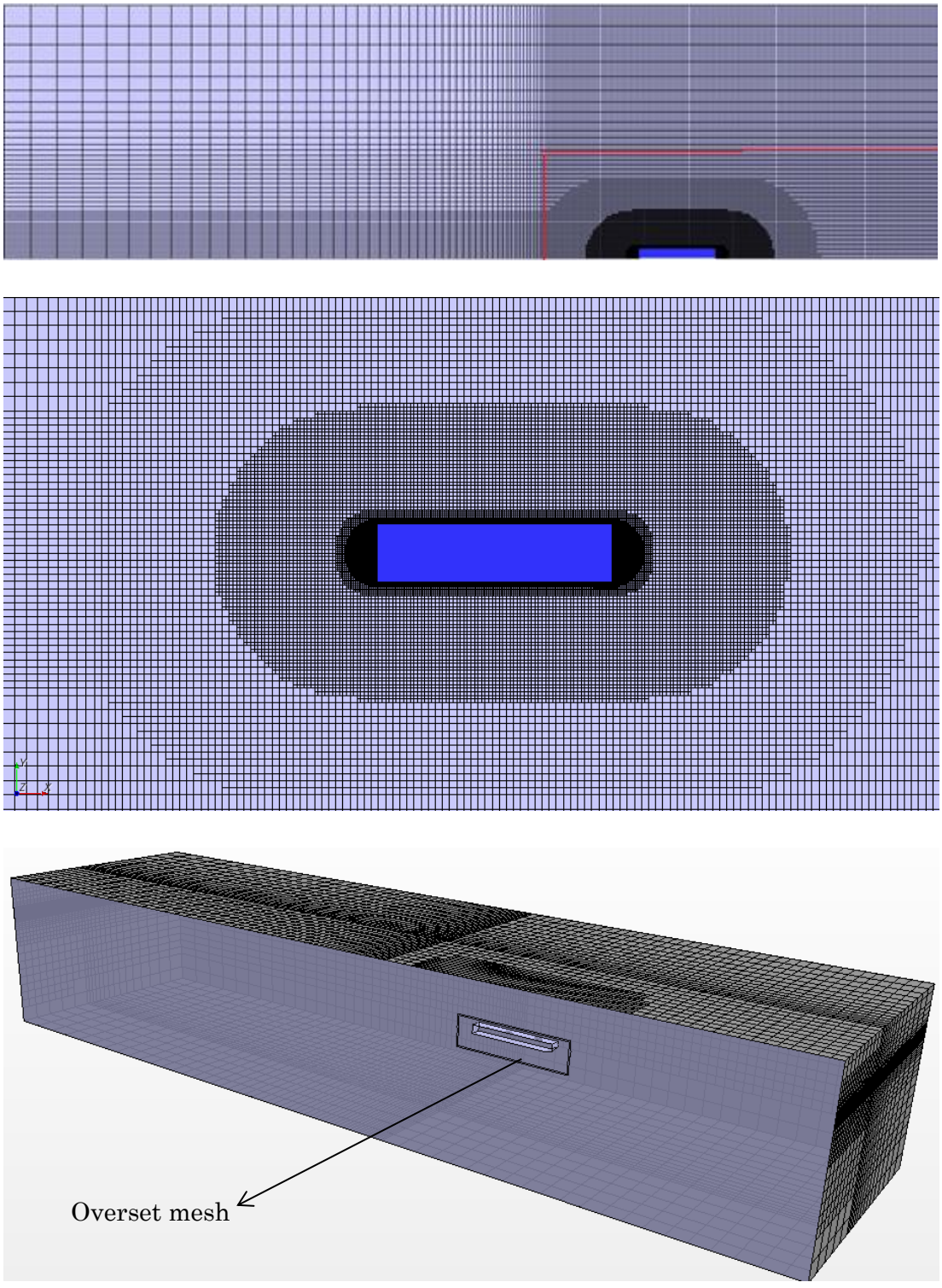

Figure 16: Mesh distribution and refinement on the free surface and body for wave period of 1.8 sec.

5.5 Rigid body Simulations

This section describes the numerical setup and settings specific to the rigid body barge simulations. Due to symmetry of this problem, the computational domain only extends to the port side of the barge.

5.5.1 Boundary Conditions, Motion & Solver settings

The fluid domain is split into two regions, namely the boundary and the overset. The boundary conditions selected for specific boundaries in the two regions is summarised in Table 13.

Table 13: Boundary condition for rigid body case

Region	Boundaries	Boundary Condition
Boundary	inlet	velocity inlet
	outlet	pressure outlet
	top	velocity inlet
	bottom	no-slipwall
	side (y extent)	no-slip wall
	symmetry	symmetry
Overset	barge	no-slip wall
	boundaries	overset boundary
	symmetry	symmetry

In order to simulate the rigid body motions of heave and pitch, a DFBI (Dynamic Fluid Body Interaction) Rotation and Translation motion is used. The DFBI motion enables the solver to compute the fluid forces and moments on the body surface due to the incident wave and solves the rigid body governing equations to reposition the body. A global earth fixed coordinate system and body local coordinate system is adopted to predict the rigid body motion of the barge. Initially, a user specified coordinate system, located at the centre of mass of the barge, is used to define the orientation of the barge relative to the global earth fixed coordinate system. The fluid forces and moments acting on the rigid body are calculated on the earth fixed coordinate system which is transformed to body local coordinate system. The rigid body equations are used to calculate the velocities of the body in the local coordinate system and again converted back to earth coordinate system. The new position of the body is updated with respect to the global earth fixed axes. The orienta-

tion of the overset grid is updated after each time step (STAR-CCM+ 2012). Body release and ramp time were specified for all simulations which is calculated on the basis of the time step. It is best to allow the fluid flow to initialise and become steady before the calculation of body motions begins. A typical value of 50 time steps is specified as a release time. At the release time, forces and moments are suddenly applied on the body, and can cause shock effect. To minimise this and facilitate a more robust solution by reducing oscillations, ramp time is specified. Ramp time of 10 times the release time is specified for all rigid body simulations.

The volume of fluid under relaxation factor is lowered from the default value of 0.7 to 0.6. This implies that only a fraction of the newly computed solution will be supplied to evaluate the new iterate, and has been done to increase stability. Consequently, the number of inner iterations must be raised to reach a convergent solution. The Maximum Inner iterations stopping criteria is the number of inner iterations that the solver performs during each time step. In general, when small time steps are used the solution changes very little from one time step to another, hence a fewer inner iterations would suffice. If the maximum number of inner iterations selected is too low, the solutions will not converge within a time step. Based on the knowledge gained from literature ten inner iterations were deemed sufficient to produce time-accurate simulations and ensure convergence (Wilson et al. 1998) (Wilson et al. 2001).

Computations were carried out using inviscid fluid model with an implicit unsteady solver. The choice of 1st order or 2nd order schemes for temporal discretisation and convection of segregated flow solver and VOF solver is completely dependent on the problem. The choice of these schemes for wave simulations can have a significant effect in the stability of wave and the amount of numerical dissipation. 1st order schemes were tested in numerical wave simulation presented in Chapter 4, and it was seen that after 10 wave periods the wave height decreases to about 15%. A better choice would be the second order schemes as they are more accurate than their counterpart. Hence, 2nd order scheme is chosen. For numerical stability, the value of local courant numbers given by $CFL = {U\Delta t}/{\Delta x}$, should be in general less than 1. Time step for each simulation was selected such that the Courant number on the free surface at all times is less than 1.0. A final summary of the solver setting is shown in Table 14.

Table 14: Solver settings for rigid body case

Property	Value
Gravity	Yes
Viscosity	No
Convection discretisation	2nd order
Temporal discretisation	2nd order
Velocity URF	0.9 (default)
Pressure URF	0.4 (default)
VOF URF	0.6
Maximum inner iterations	10
DFBI solver iterations	10

5.6 Co-Simulation of the barge

The interaction between the structure and the fluid taking into account the flexibility can be performed with the help of a coupled simulation between the fluid solver and the structural solver. As mentioned in Chapter 3, this can be done using a one-way coupling or two-way coupling. Responses of the barge, treated as a flexible body, is modelled in Star-CCM+ and Abaqus, using a two-way coupling. To obtain the response of the barge using a one-way coupling method, we need to save the fluid pressures on the rigid body at prescribed time steps for the complete simulation time, say 15 wave periods. The fluid pressures are then integrated on the FE model in Abaqus to calculate the responses. To perform one-way coupling between Star-CCM+ and Abaqus, it requires FORTRAN subroutines to run the load files obtained at each time step in Abaqus. Unfortunately, specific versions of C++ and FORTRAN compilers are required to be linked with Abaqus 6.13 so that the subroutines can be compiled and run successfully. The failure to obtain these specific commercial versions resulted in computations to be carried out only using two-way coupling. This section details the fluid solver settings specific to the coupled simulations. The details of mesh and properties of the finite element mesh in Abaqus are also described in detail. Firstly, the selection of the FSI scheme and instabilities surrounding the coupled simulations are presented with reference to the literature in Section 2.8.

5.6.1 Time discretisation of Flexible barge simulations

From the brief literature review of FSI methods and the associated instabilities, it was found that the explicit scheme can be unstable when the added mass effects are dominant. The numerical stability of a strongly coupled problem can be challenging when the density ratio between the fluid and the solid is close to one, for a very flexible structure, or high velocity impacts and subsequent high pressure peaks (Causin et al. 2005). There are restrictions to temporal discretisation and researchers have observed a limiting time step below which the loosely coupled scheme starts to become unstable. This deficiency can be overcome by employing strongly coupled schemes in compressible flows which ensures multiple exchanges performing subiterations between the fluidic and structural interfaces within a time step. In the case of the flexible barge an explicit scheme was tested. However, it resulted in quick pressure divergences for a range of time steps tested. Consequently, an implicit scheme was adopted for all the simulations presented in the thesis.

Reviewing the existing research there are no time step restrictions reported for strongly coupled problems when the flow is considered compressible. They are reported to be unconditionally stable with no restrictions in temporal or spatial discretisation. However, in the case of the very flexible barge test case it was found that the simulations are only stable for a $\Delta t \geq 0.005$ sec. This was the minimum time step size that could be used for all wave frequencies (Lakshmynarayanana et al. 2015a). This time step was consistent for all the wave frequencies investigated and had no effect on the spatial discretisation, meaning even when the grids were refined the coupled simulations were stable only for the 0.005 sec time step criteria. Simulations were attempted by gradually increasing the inner iterations and the subsequent exchanges between the solvers to see if the coupling stabilised for lower time steps, but even then the simulations diverged within 2-3 time steps. Pressure divergences occurring in such short time steps made the fault finding near to impossible. The fluid was considered compressible using the artificial compressibility method such that the density is made a function of pressure (STAR-CCM+ 2012). The speed of sound was set to 500 m/s to facilitate convergence. However, it showed no effect on the stability of the coupled simulations. This is contradictory to the reported fact that a strongly coupled scheme does not suffer from any convergence issues when artificial compressibility is introduced.

An observation that is intriguing from the test case of the very flexible barge is that the minimum time step size is independent of the grid refinement and speed of sound. Coupled simulations were tested by changing the cross-section of the beam to bring about variation in their stiffness. The stiffness was both increased and decreased from the original (see Table 9) to discover their link to minimum time step, and also figure out if there is a specific stiffness for this beam above which the simulations are unconditionally stable for any choice of time steps. The investigations were carried out on a single grid, and keeping the speed of sound constant. It is obvious from Table 15 that as the stiffness of the beam increases the time step in the simulation decreases. An attempt to draw relationship between the time step choice (Δt) and the dry natural frequency (f) was done using $\Delta t = {}^{1}\!/_{Cf}$. The constant C was calculated and compared for different beam cross-sections. The value of the constant for the different beam sections have to lower than the value showed in the Table 15. However, no definite relationship was identified between the stiffness and the time step.

Although, it was not possible to resolve the time stepping problem, the deformed FE model at the end of first few time steps led to some insight into the pressure divergence. The barge used in the simulations is very flexible, hence, as soon as it is left in water, in the first few time steps it is subjected to large deformations. This transient phase creates the restriction to the time step selection and makes it worse when the time step is decreased below a critical value. Basically when time step is decreased the fluid solver tries to balance the large deformation in a shorter time eventually causing an increase the pressure to an unrealistic value. Large grid deformations occurs rapidly causing negative volumes cells in the vicinity of the barge. Richter & Wick (2013) compares the time steps per oscillation required for a standalone CFD and FSI simulations on a flow around an elastic beam. It was reported that while the CFD simulations requires less than 10 time steps per oscillation the FSI problem required 100 time steps per period of the first flexible mode. The period of the first mode for the barge is about 1.05 seconds and the time step of 0.005 sec corresponds to 200 time steps per period. The time step is adequate to resolve the 2-node and even the 3-node frequencies. Hence, for all the simulations a constant fluid and structural time step of 0.005 sec is used as this was the minimum for carrying out a stable simulation.

Table 15: Relationship between the beam cross-section and critical time step

Cross-Section of Beam	Minimum time steps for stable simulation	Dry 2-node (Hz)	Constant 'C'
80 x 80 mm square rod	0.01 sec	0.61298	163.137
100 x 100 mm (original)	0.005 secs	0.95576	209.25
120 x 120 mm square rod	0.003 sec	1.3727	242.83

5.6.2 Boundary Conditions, Motion and Solver Settings

The boundary conditions are similar to those used in rigid body simulations (see Table 13). Discretisation of a full domain is carried out for the co-simulations and the boundary on the starboard side is also specified as wall. Lakshmynarayanana et al. (2015b) observed large longitudinal drift in the co-simulation of the barge as there was no boundary condition specified in the CFD or FE model to confine the motion. This motion cannot be categorised as a parasitic surge motion but was purely a large longitudinal drift. There are a few downsides of treating the barge model in this way. Firstly, due to the unphysical drift the overset mesh will fall out of the refinement in the background mesh permitting only to simulate about 8-10 wave periods. The grid sizes of the background mesh and the overset mesh must be similar to ensure they are coupled during the entire simulation. Secondly, for regular waves of $\lambda/L \leq 1$ strong bow and stern diffracted wave systems were existent. The large longitudinal displacement will result in the body generating weaker local end waves when compared with experiments where the barge was fixed. Consequently, this could result in discrepancies in motions, especially, towards the ends of the barge. In the present work the barge is restricted in the longitudinal direction by giving a boundary condition in the finite element model. The node close to LCG of the barge is prescribed with a longitudinal displacement (in x-axis) of zero which resulted in fixing the barge in place in response to the incoming waves. Grid adaptation to follow the deformation of body in waves is imparted using mesh morphing, which deforms the mesh based on the nodal displacements obtained from Abaqus. Abaqus exports absolute values of nodal displacements in the coupled simulations, implying that the displacement is relative to the initial position of the mesh at time zero. To ensure that the mesh morphing in CFD is also done with respect to the ini-

tial mesh configuration, “morph at zero” option is activated in the solver settings. The overset grid boundaries move in response to the interpolation field created by the morphing motion using the “floating boundary condition” in the morpher. The solver settings for co-simulation are shown in in Table 16.

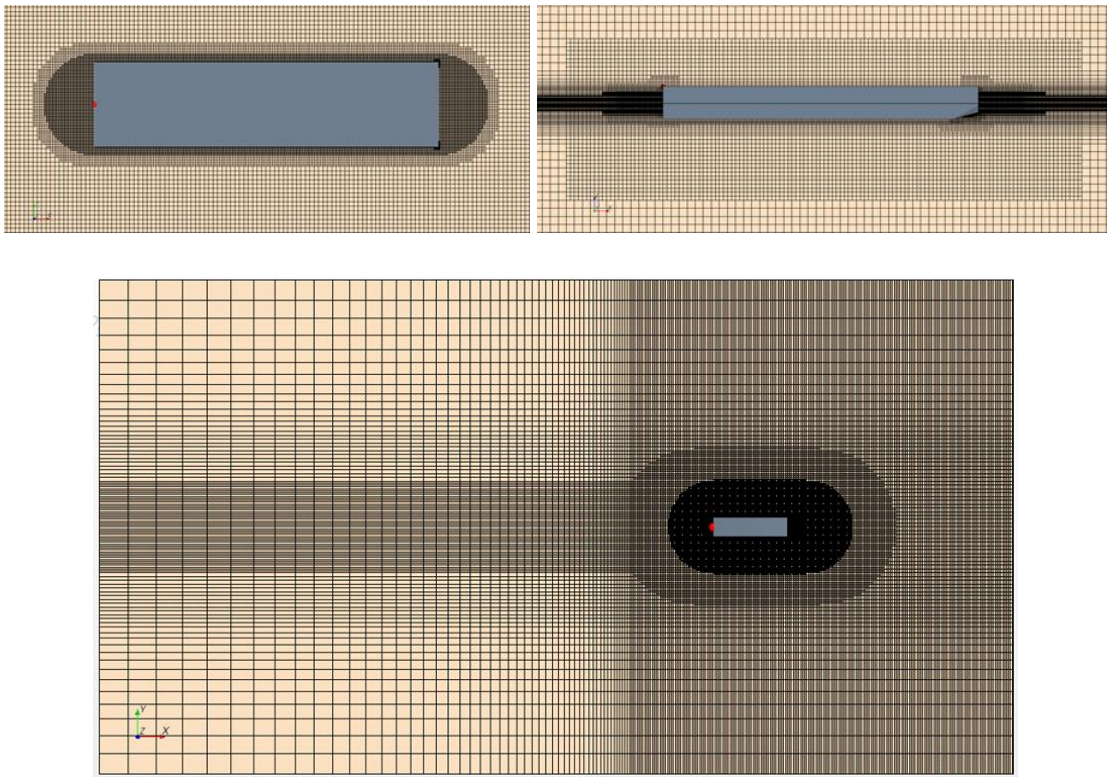

Figure 17: Mesh configurations for flexible barge for a wave frequency of 1.2 s

The fluid is assumed to be inviscid and time derivatives are discretised as implicit unsteady. The grid flux URF is lowered from a default value of 1.0 to 0.8, implying that the fluid response to structural response is slightly reduced by a fraction commensurate to the URF. This was done to provide stability as many attempts with a higher grid flux URF resulted in quick pressure divergence. For some cases, where pressure peaks were observed even when the morpher was running smoothly, the URF for pressure was lowered to 0.3 from a default value of 0.4. Similar to the rigid body cases, all simulations were run using a 2nd order temporal and convective scheme.

The field data is exchanged between CFD and FEA on the interface where the responses due to fluid-structure interactions are of interest. The barge surface is marked as FSI interface in the software.

Table 16: Solver settings for co-simulation

Property	Value
Gravity	Yes
Viscosity	No
Convection discretisation	2nd order
Temporal discretisation	2nd order
Velocity URF	0.9 (default)
Pressure URF	0.3-0.4
VOF URF	0.6
Grid Flux URF	0.8
Imported field URF	Adaptive 0.2-0.5
Maximum inner iterations	12-15
Time Step	0.005 s
Co-Simulation time	0.005 s

5.6.3 FE Model

The beam elements representing the structural flexibility are linked to dummy surface elements that define the actual wetted surface. The flexible barge is represented using a 3-D beam model consisting of 48 beam elements. The material and geometric properties of the beam elements are modelled in line with model test data. The material data and geometry specification is given in Table 17.

Table 17: Material and Geometric data of FE model

Property	Value
Material	Steel
Density	7850 kg/m^3
Young's Modulus	210×10^9 N/m^2
Poisson's ratio	0.3
Length	2.445 m
Cross-Section of beam	1cm × 1cm
Number of nodes	49 nodes

The elements chosen are the 2-node linear beam element B31 and 4-node quadrilateral (dummy) surface element SFM3D4, the latter representing the barge surface. The dummy surface elements are linked to the nodes on the beam elements using kinematic coupling constraints. A large number of nodes or surfaces can be

constrained to the rigid body motion of control nodes (in this case the beam element nodes) using kinematic coupling. All six degrees of freedom are constrained in the kinematic coupling of beam nodes and the dummy surface, in the sense that the beam deformations are imparted on to the barge hull. The total mass of the barge is distributed on the beam elements as lumped masses. The mass of each section of the barge, which encompasses the caisson, square rod and bracing equipment, is aggregated as the analogous beam section mass and the lumped mass.

The initial body coordinate axes of the FE model was such that the aft centreline of the barge was coincident with the origin (0, 0) and the positive x-axis was aligned towards the forward of the barge. The beam, carrying the masses, was located at a height 0.307 m from the base of the barge, thus creating an offset between the origin and centre of mass. Large differences were observed when the calculated responses (VBM and VSF) of the barge were compared with 2-D hydroelasticity (Lakshmynarayanana et al. 2015b). It was found that the differences originated due to the mass moment of inertia calculation in Abaqus, Section 3.5.2 provides a brief description of the beam formulation. To explain it in context, the exact formulation is by default used for the formulation of beam mass matrix and moment of inertia as opposed to isotropic formulation. The offset between the beam node and centre of mass is used for calculating the mass moment of inertia. As a result, the inertia is augmented by a value equal to mr^2, where r is the offset of beam coordinate from the origin. Hence, the finite element model was translated so that the first beam node, connected to the aft section, was placed at the origin. Figure 18 shows the finite element model and the datum coordinate axis at origin coinciding with the beam node. The results of motion and responses presented henceforth in this Chapter are using the new configuration of the CFD and finite element model. The results from the configuration with offset are available in the conference papers in Appendix B &C.

For the 2-D hydroelasticity analysis the barge is represented as a non-uniform beam element divided into 48 sections, to achieve consistency with the finite element model. The mass distribution, moment of inertia for each segment, is similar to the finite element model. No shear deformation or rotary inertia is specified for the beam elements. The response in waves is evaluated using modal analysis.

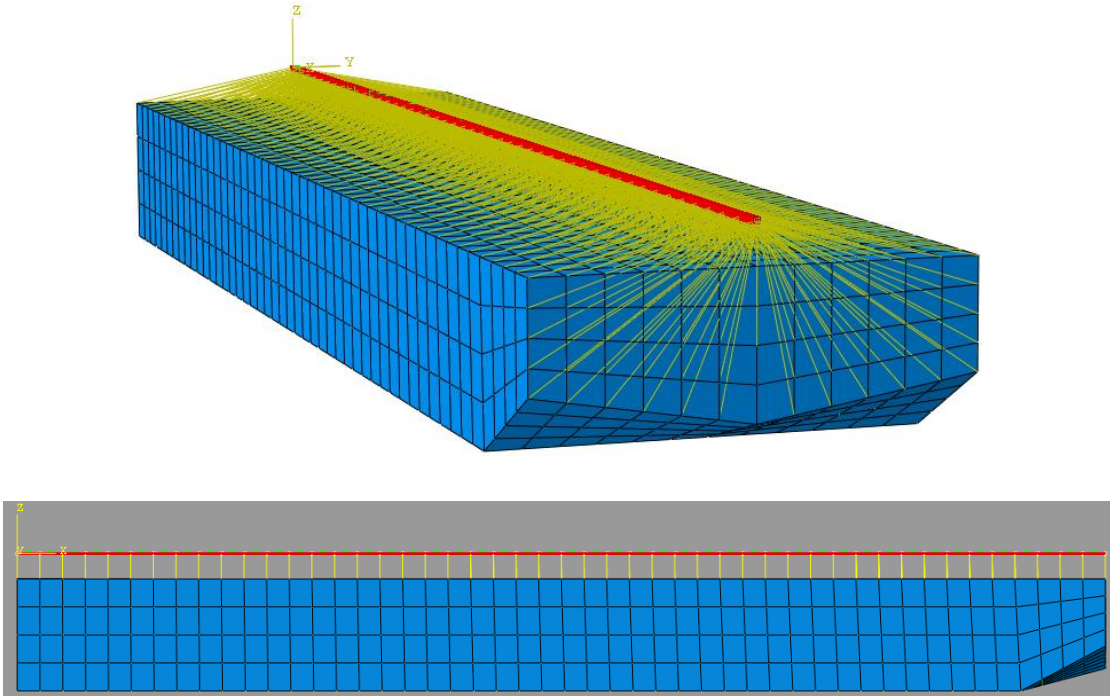

Figure 18: Finite Element mesh with beam and dummy surface linked using kinematic coupling

5.7 Results and Discussion

5.7.1 Modal Analysis

Modal analysis was performed in Abaqus using Block Lancozs (Dassault Systèmes 2013) eigen value extraction method. The dry (or *invacuo*) natural frequencies and mode shapes obtained in Abaqus were compared against calculations performed using finite difference method applied to a non-uniform beam (Bishop et al. 1977) (Seng et al. 2014), to ascertain the accuracy of structural modelling. The dry hull natural frequencies for the first 5 flexible modes are shown in Table 18. The dry mode shapes are shown in Figure 19 & 20.

Table 18: Symmetric Dry Hull natural frequencies (rad/s)

Mode	Abaqus	MARS(2-D strip theory)	% error
2-node	6.01	6.03	0.34
3-node	16.43	16.49	0.37
4-node	32.00	31.10	2.8
5-node	52.66	52.73	0.13
6-node	78.42	78.34	0.11

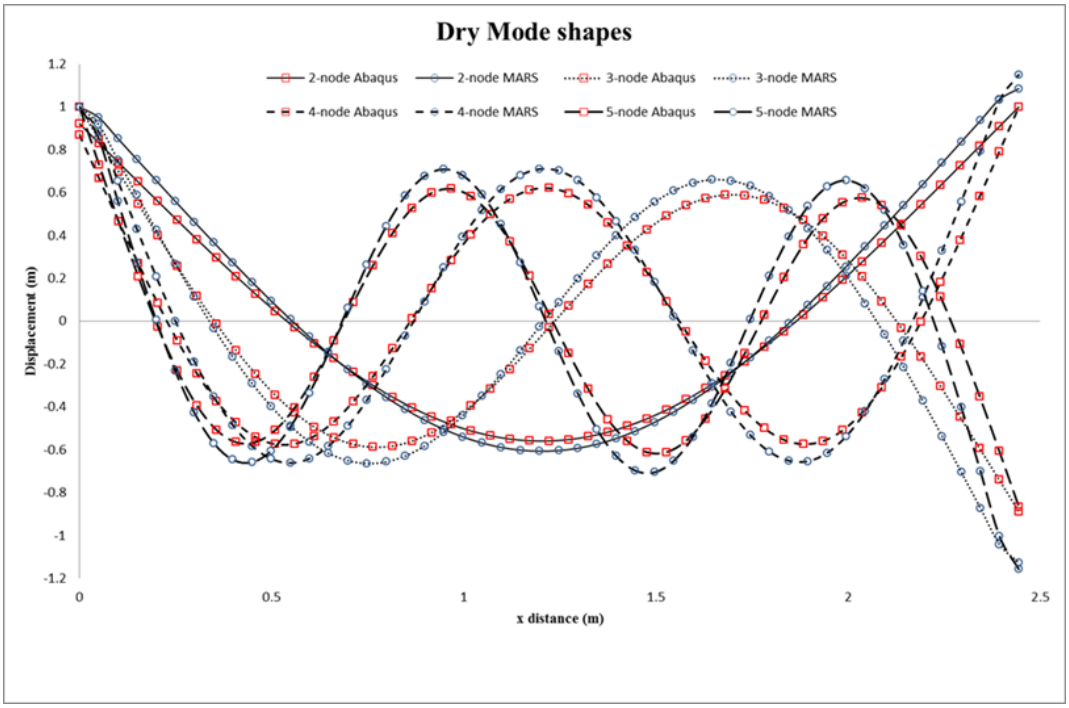

Figure 19: Plot of mode shape obtained from MARS and Abaqus

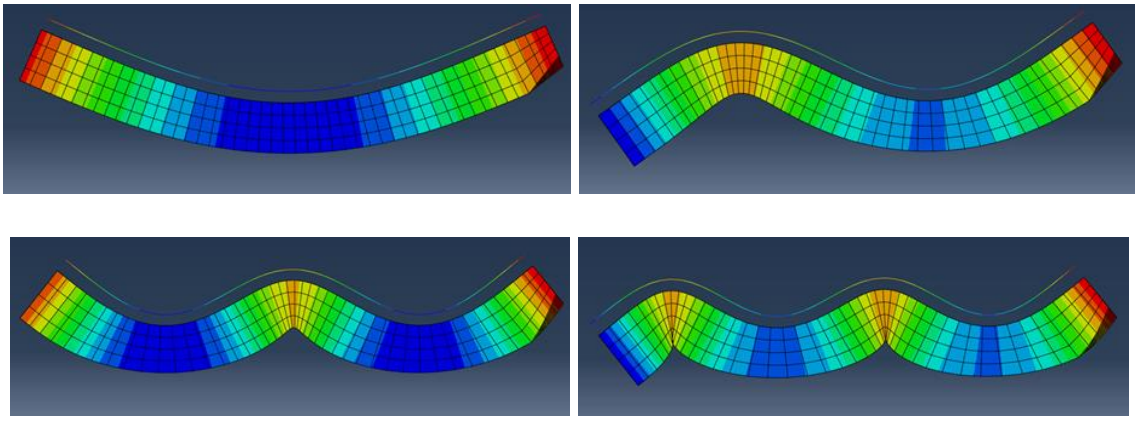

Figure 20: Contour plots of mode shapes obtained from Abaqus

5.7.2 Vertical Displacement in waves

The motion and responses calculated using the coupling technique is presented in the following sections. Vertical displacements predicted at various locations are compared against experimental measurements and 2-D hydroelastic predictions. Responses predicted include the vertical bending moments and vertical shear forces, are compared only with 2-D predictions. A discussion on the agreement and discrepancies is presented, and the possible reasons leading to these differences are

reviewed. The influence of nonlinearities on motion and responses is also studied in Section 5.7.4.

A detailed study on the spatial and temporal discretisation for numerical wave generation is presented in Chapter 4. The forcing function in the case of barge in waves is the incident wave and, hence, it is important to monitor the wave elevation in front of the barge. Assuming linearity, the motion and responses calculated are presented as transfer functions called Response Amplitude Operators (RAO). RAO's express the motion and responses of a structure with respect to a unit wave amplitude, thus requiring accurate monitoring of wave amplitude throughout the simulation. Wave elevations were recorded at one L_{pp} in front of the barge. The time history of the wave elevations revealed very little wave dissipation, and maximum decrease in wave height was around 5-6% as the simulation progressed. This slight reduction in wave height is considered acceptable for the current study. Average wave amplitude over 15 wave periods was used to calculate the RAOs noting that the simulation was run for 20 periods. Figure 21 shows the time history of wave elevation recorded for the 1.6 sec wave using a line probe plotted against the theoretical first order wave.

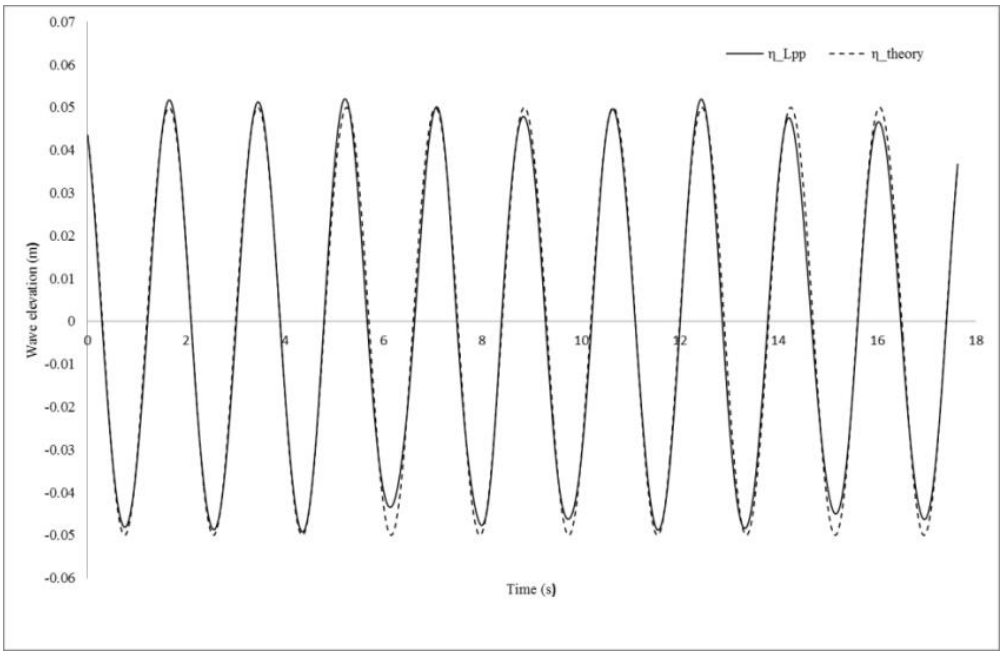

Figure 21: Wave elevation at L_{pp} in front of the barge for 1.6 secs wave.

Rigid body displacements of the barge were calculated at all six locations, as in Table 10, and plotted together with the flexible barge results shown in Figure 23. Results from the CFD simulations (rigid and flexible) and 2-D hydroelasticity are de-

noted as CFD and Mars, respectively. The rigid body results are distinguished from flexible in the plots as 'rigid'. The rigid body response from the 2-D hydroelastic code is calculated using the generalised coordinates of heave and pitch. Comparing the rigid body displacements, it can be seen that the numerical predictions at amidships (Pt.7) closely match each other for all frequencies. There is reasonable agreement between the predicted rigid body displacements at other locations with exception towards the forward end of the barge (points 1 and 3). The RAOs are larger in the CFD simulations than 2-D linear predictions towards the bow of the barge. At the forward section of the barge, strong bow waves were seen to develop in the CFD simulations from a wave frequency of 3.9 rad/s and upwards. With increase in frequency, diffraction becomes more dominant resulting in strong localized bow waves. This can be observed in the instantaneous wave contour around the rigid barge, for frequencies of 3.926 and 6.28 rad/s, is shown in Figures 24a and 25a, respectively.

In general, very good agreement is noted at all frequencies at locations from around amidships towards the stern of the barge. At point 12, close to the stern (0.19 m), the RAOs of the vertical displacement predicted by CFD_rigid at 3.926 rad/s are larger than 2-D linear predictions. The contour plot at this frequency shows strong bow and stern waves influenced by pitch motion, as seen in Figure 24a. The heave and pitch RAOs obtained from the rigid body CFD simulation, and the corresponding 2-D hydroelasticity rigid, as well as distortional principal coordinate amplitudes are shown in Figure 22. A peak in pitch response can be seen at around 4 rad/s in Figure 22. The reason for the discrepancy between CFD and 2-D linear analysis predictions at the bow and stern sections of the barge is largely due to the influence of strong localised wave systems, not very well predicted using a linear potential flow theory. The predictions using CFD is considered more reliable in this case since it accounts for the nonlinear interactions and 3-D effects between the wave and body; a drawback of 2-D linear strip theory.

The total vertical displacements for the flexible barge comprise of both rigid body and distortional displacements. RAOs from CFD/FEA co-simulation, also shown in Fig 23, compare well with the experimental measurements at most locations, albeit some differences were noted at higher frequencies. In general, the method underpredicts the displacements at higher frequencies, specifically towards the bow. Table 22 shows the relative percentage error between the measurements and the pre-

sent method at all locations for the frequencies investigated. The maximum percentage error is observed at Pt.5 (1.625m from aft) at 6.28 rad/s, about 36%, and between 2-D predictions and measurements is about 60% for the same condition. The relative percentage errors shown in Table 22 are highest at 6.28 rad/s and 6.98 rad/s. The wet natural frequency or 2-node natural frequency in water measured in experiments from decay tests was 6.7 rad/s. The maximum disagreement is also occurring at frequencies in the vicinity of the wet natural frequency. This indicates that the computations are sensitive around resonant region. Grid sensitivity analysis is conducted at this resonant frequency to study the influence of grid refinement on the RAOs and results are discussed in Section 5.7.5.

Table 19: Relative percentage error of vertical displacements between experiments and coupled simulations

Location	ω (wave frequency)				
	3.49 rad/s	3.93 rad/	5.24 rad/s	6.28 rad/s	6.98 rad/s
Pt. 1 (2.445m)	10.8%	6.6%	2%	9.7%	25%
Pt. 3 (2.035m)	3.6%	3.6%	9%	2.2%	16.7%
Pt. 5 (1.625m)	0.8%	3.9%	3.9 %	35.9%	24%
Pt. 7 (1.215m)	3.7%	1.9%	13.5%	18.5%	8%
Pt. 9 (0.825 m)	3.8%	4.2%	11%	10.7%	30%
Pt. 12 (0.19m)	4.8%	2.8%	5%	3.5%	6.9%

The gaps between the caisson in the experimental model is not considered in the CFD/FEA model. The absence of gaps in the numerical model could result in slightly different hydrodynamic properties, namely added mass and fluid damping, compared to the real situation. The absence of structural damping in the numerical model could also have an effect in the predictions, especially at the natural frequency. (Kim et al. 2013) had introduced artificial damping force on the outer surface on the barge and found significant difference in the vertical displacements end locations. They tuned the damping force to match the displacements at the ends of the barge with experiments.

Again with increase in frequency, the disparity between the two numerical predictions increases as we move towards the bow. Of the two numerical methods, the two-way coupling shows much better agreement with experimental data. Figure 24 and 25 illustrates strong diffraction effects in flexible body motions as the wave frequency increases. At 3.92 rad/s, there is a marked difference between the wave radiation contour of the rigid and flexible body simulations. In the case of rigid barge, strong localised bow and stern wave systems are prevalent; however, the flexible barge tends to deform following the wave, this results in very weak or rather no localised waves. Accordingly, the agreement between the numerical predictions is better at lower frequencies at the extremities of the barge. The motion of the barge, above 3.92 rad/s, creates significant disturbances on the free surface leading to strong free surface disturbances for both rigid and flexible case.

Comparing the present predictions on rigid and flexible barge (see Fig 23) at the bow and stern points (Pts. 1, 3, 12), we can observe an interesting trend. The influence of localised wave systems at 3.92 rad/s, absent in the flexible barge computations, results in larger rigid body displacements. As the wave frequency increases, the diffraction effect is existent in both rigid and flexible body simulations, although, flexibility starts to play a more dominant role producing higher distortions leading to large RAOs. This behaviour gets more prominent around the 2-node wet frequency exhibiting 34% difference between rigid and flexible displacements at the bow.

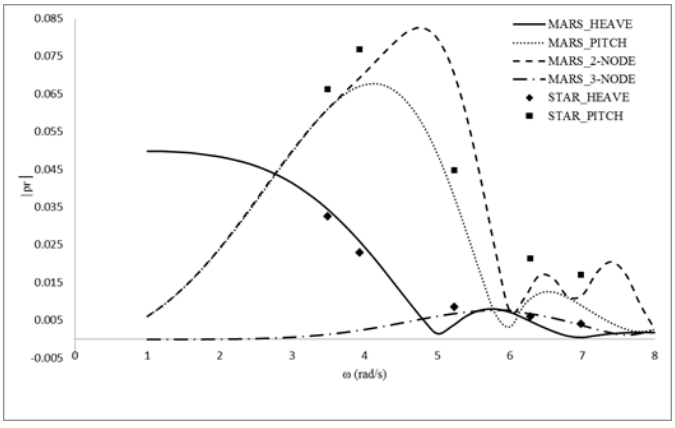

Figure 22: Heave, Pitch RAOs and principal coordinates of the barge

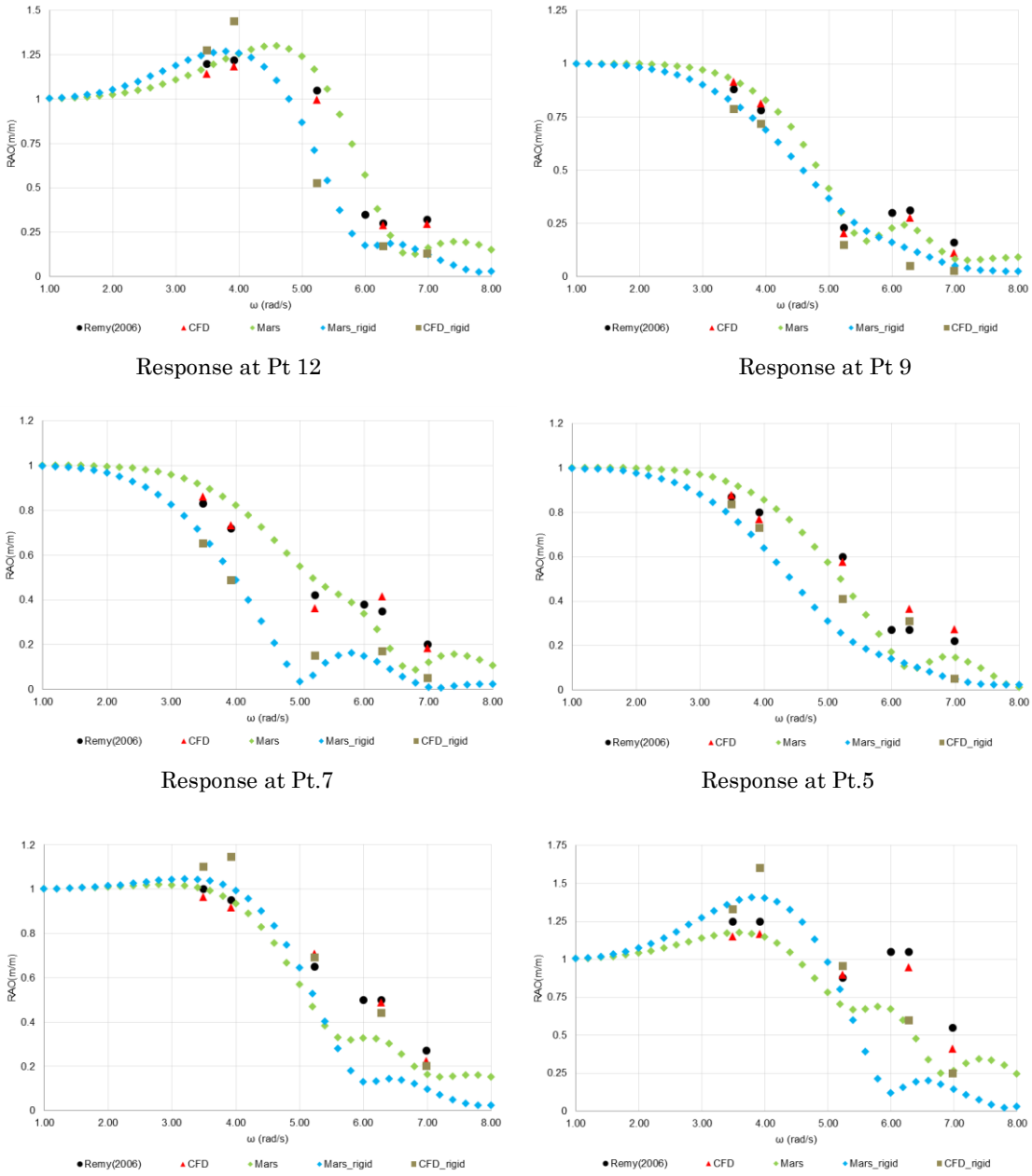

Response at Pt 12 | Response at Pt 9

Response at Pt.7 | Response at Pt.5

Response at Pt. 3 | Response at Pt. 1

Figure 23: RAOs of vertical displacements along the barge, point 12 near the stern and point 1 near the bow, for both rigid and flexible body analyses

It is clear from this validation exercise that the present method is capable of predicting the displacements of a very flexible structure to a good degree of accuracy. When compared to linear methods predictions taking into account the nonlinearities are well suited to such flexible structures which introduce significant free surface disturbances at certain frequencies. Omitting, such nonlinearities can result in under predictions when compared to actual measurements; hence, the CFD methods are more suited. The CFD simulation based methods also give insights into interesting flow features which aid in explaining the agreements and discrepancies

better. Finally, rigid body approximations are not well suited for a very flexible structure and can result in severe under prediction, especially in the vicinity of the natural frequencies.

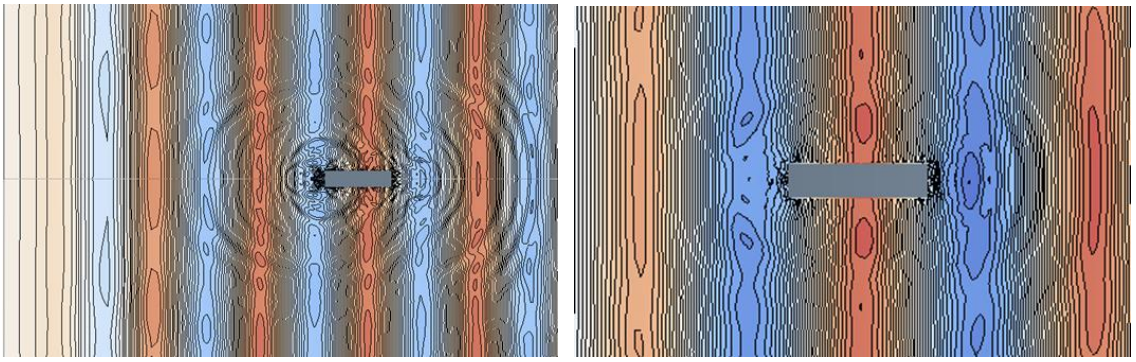

(a) (b)

Figure 24: Instantaneous wave contour around the rigid body (a) and flexible (b) at 11.5s wave frequency of 3.926 rad/s

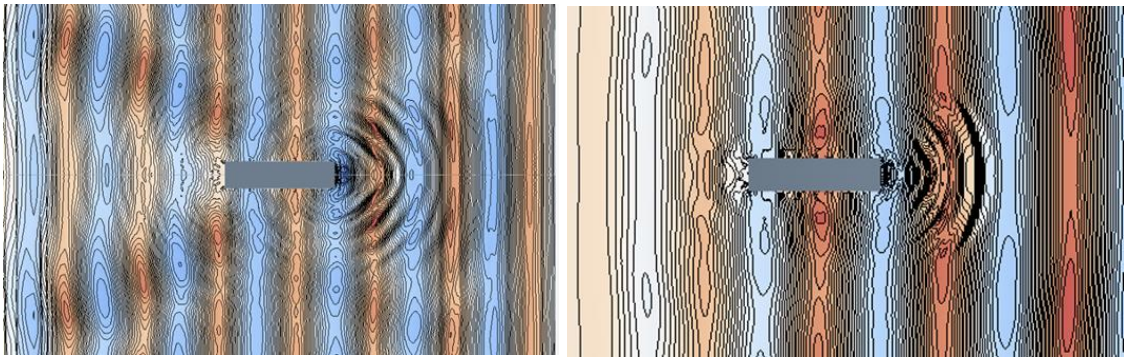

(a) (b)

Figure 25: Instantaneous wave contour around the rigid body (a) and flexible (b) at 9. 5s wave frequency of 6.28 rad/s

5.7.3 Vertical bending moments and shear forces in waves

RAOs of VBM are shown in Figure 26, at locations x/L = 0.33, 0.5, 0.66 and 0.83 together with comparisons from 2-D linear hydroelastic analysis. The displacements plots at the corresponding locations are also presented in the figure to draw relationships between displacements and bending moments for the barge. In the 2-D linear plots, the first resonant peak, which corresponds to ship-wave matching region (λ/L=1.0), is observed around 5.5 rad/s. At amidships, the CFD also shows a peak around this frequency. The occurrence of second peak is not clear in the 2-D linear simulations as it seems to be shifting depending on the location on the barge. At amidships it occurs around 7.5 rad/s and as the coupled simulations were car-

ried out only at discrete frequencies making it inconspicuous. The numerical investigations are carried out at two resonant frequencies, one corresponding to λ/L=1.0 (5.5 rad/s) and the 2-node wet frequency (6.2 rad/s). The RAOs are deduced by dividing the calculated responses by the wave amplitude. Comparing the RAOs of VBM predicted by the numerical methods, it is obvious that the general trend of the plots for the frequencies investigated is somewhat identical. Nevertheless, the relative magnitude of RAOs shows significant differences, especially in the vicinity of the resonant frequencies. Table 20 shows the relative percentage error between 2-D and coupled simulations. When expressed in this form, the contrast is immediately apparent exhibiting sporadic percentage errors in the range of 15-50% in majority of the cases. Firstly, let us study the effect of change in the location on the bending moment, at individual wave frequencies. A consistent and good agreement is discernible at the lowest frequency, ω=3.49 and 3.93 rad/s, where the diffracted waves in the coupled simulations were non-existent. There is also a good agreement in vertical displacements, see Figure 26, between the numerical predictions at this frequency. Aside from wave frequencies, ω= 5.25 rad/s and 6.28 rad/s, the relative differences at other wave frequencies are moderate, if not considerably low. When examining the percentages at these wave frequencies with respect to change in locations, the bending moments around amidships evinces minimum deviation.

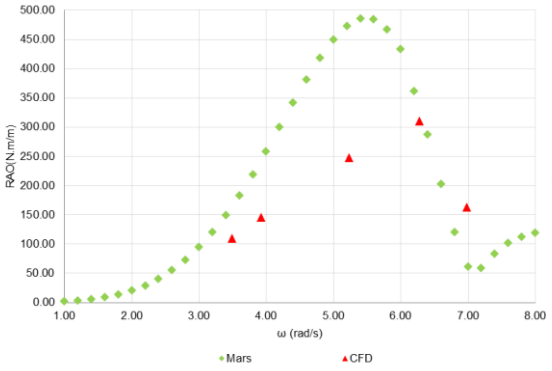

VBM at Pt 9 (x/L=0.33)

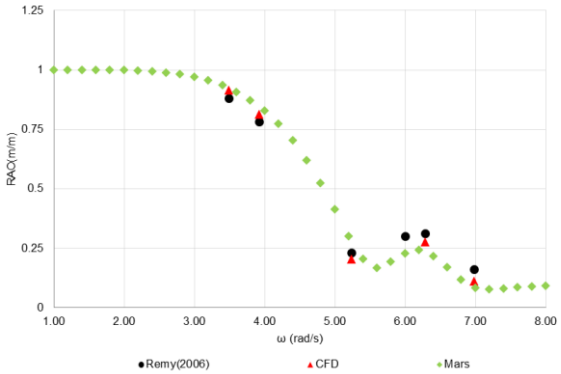

Displacement at Pt 9

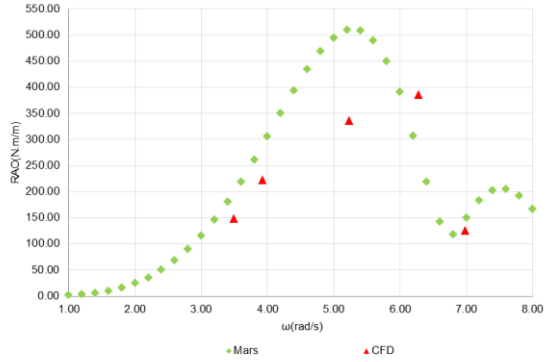

VBM at Pt.7 (x/L=0.5)

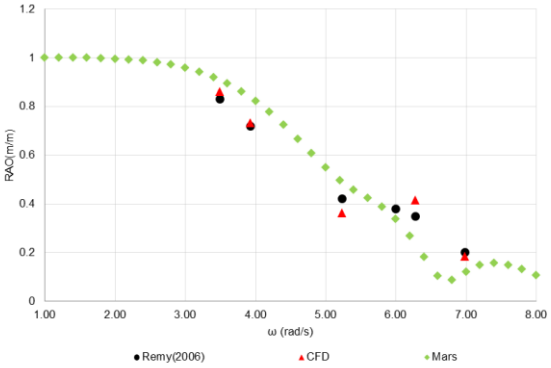

Displacement at Pt.7

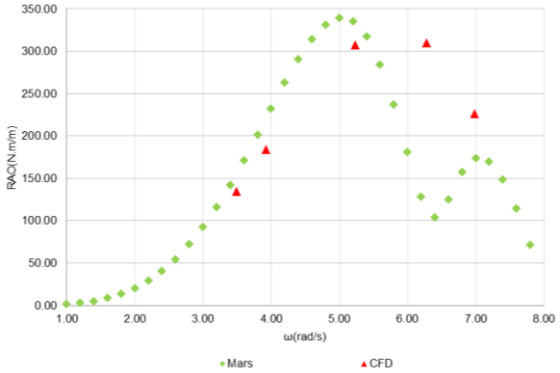

VBM at Pt. 5 (x/L=0.66)

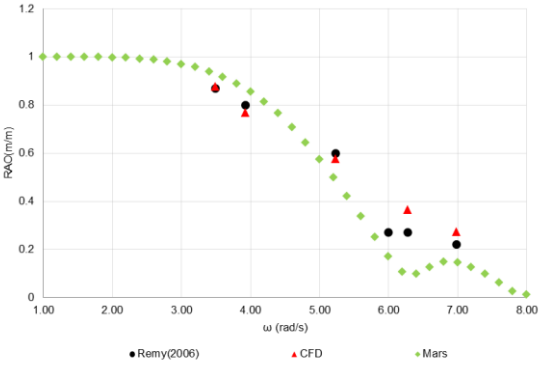

Displacement at Pt. 5

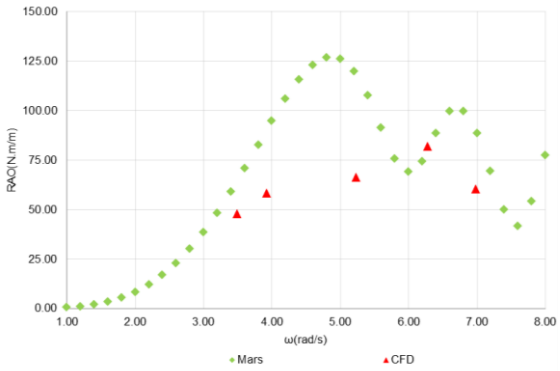

VBM at Pt. 3 (x/L=0.83)

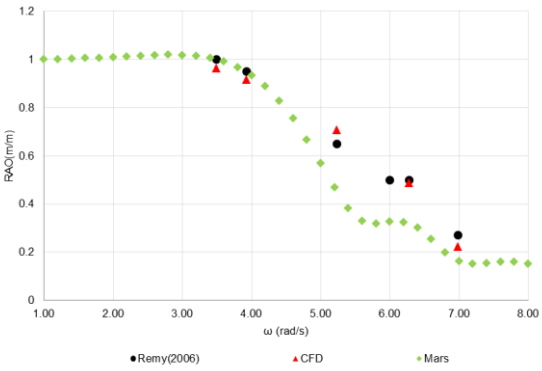

Displacement at Pt. 3

Figure 26: RAOs of VBM and vertical displacement along the barge at x/L=0.33, 0.5, 0.66, and 0.83

The RAOs of VBM amidships at the first resonant peak (5.5 rad/s) is lower in the coupled simulations by about 34% in comparison to 2-D hydroelastic predictions. In general, the VBM at this wave frequency is under-predicted by the present method at all locations. Referring to the vertical displacements, there is mismatch between the predictions of the two numerical methods; however, the predictions of the present method are closer to the experimental measurements. Although, this does not establish the fact that bending moment predicted by the coupled simulations are

closer to the true vertical bending moments, it is definitely encouraging since we observe a general relation between predicted displacements and bending moments. The main reason for the discrepancy is thought to be the influence of nonlinear hydrodynamic interaction between the divergent waves and the incoming waves. Another abnormality noted in Table 20 is for Pt.5 at ω=6.28 rad/s, where VBM predicted by coupled simulations is nearly 1.4 times more than the 2-D predictions. A slump occurs in the 2-D prediction at this location and frequency which is not captured by the coupled simulations. The difference in vertical displacements is also about 160% between the numerical predictions, with the coupled CFD/FEA method larger than 2-D linear and closer to experiments.

Table 20: Relative percentage error of VBM amidships between 2-D and coupled simulations

Location	ω (wave frequency)				
	3.49 rad/s	3.93 rad/	5.24 rad/s	6.28 rad/s	6.98 rad/s
Pt. 3 (2.035m)	19%	29%	49%	10.8%	31%
Pt. 5 (1.625m)	5%	20.6%	8.3 %	140%	29%
Pt. 7 (1.215m)	17.6%	14.8%	33.8%	25%	16.5%
Pt. 9 (0.825 m)	26.3%	35%	45%	13.9%	36%

The RAOs of VSF, shown in Figure 27, show slightly better correspondence with the 2-D linear predictions than the VBM plots, the only exception being the bow location x/L=0.83. At the bow location the shear forces are over predicted by nearly 4 times at the wet resonant frequency when compared to the linear predictions. When compared to the VBM plots, the RAOs of VSF show minor differences, even at the resonant peaks. At x/L=0.66, there is a dip in the shear force predicted by coupled simulation at 7.0 rad/s. When we compare the plots of VBM and VSF, at corresponding locations, there is the contrasting tendency, i.e. when RAO of VBM is larger than 2-D predictions, the VSF is smaller and vice versa.

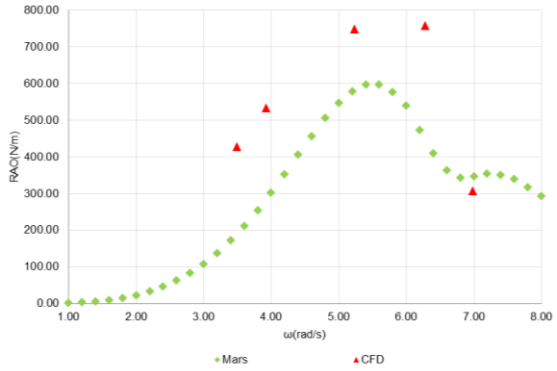

VSF at Pt.9 (x/L=0.33)

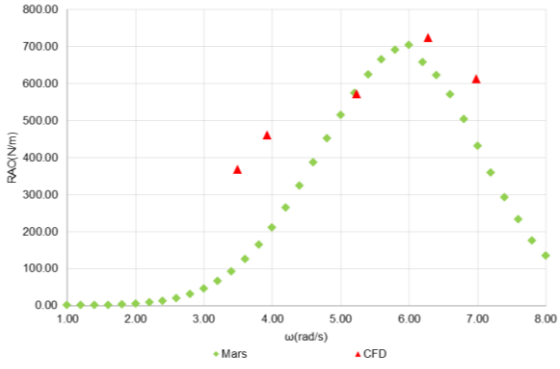

VSF at Pt.7(x/L=0.5)

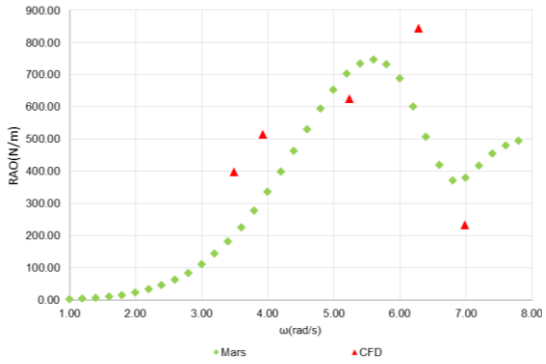

VSF at Pt.5 (x/L=0.66)

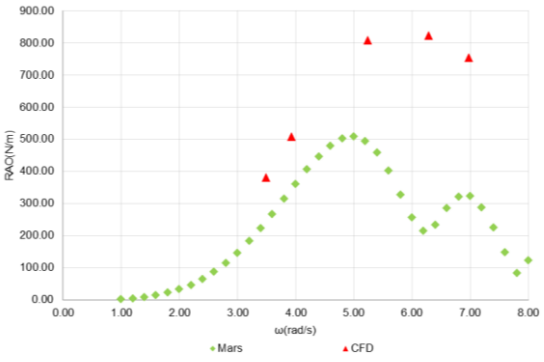

VSF at Pt. 3 (x/L=0.83)

Figure 27: RAOs of VSF along the barge at x/L=0.33, 0.5, 0.66, and 0.83

From these responses, it can be noted that although qualitatively the agreement between the numerical predictions is good, there are large quantitative discrepancies. The above investigations unveil the possibility of effect of nonlinearities in motions and responses due to the hydrodynamic interactions. The wave heights used in the above investigations are considerably high to induce large motions, and consequent free surface disturbances. Having linear predictions as the only comparator in circumstances where we expect nonlinear contributions is unreasonable. There are also considerable differences in the vertical displacements, particularly at resonance, between the numerical methods. These differences also manifest in the predicted responses of the barge. Lack of experimental measurements or other references make it difficult to reliably conclude as to which method is more accurate. The coupled problem of the barge using the present method can be assumed to be linear by carrying out computations in smaller wave heights. Comparisons with linear potential flow using such an assumption can be considered more proximate. The next section describes the computations for a less steep wave (ratio of H/L) and subsequent comparisons with linear predictions.

5.7.4 Influence of nonlinearities

To get a better insight into the dissimilarities and make the comparisons more consistent, the best option in hand is to linearise the problem. This can be done by simulating the two-way coupling using very small wave heights, say of H/L≥100. RAOs of motion and responses at x/L=0.33, 0.5, 0.66 and 0.83 are shown in Figure. A wave height of 20mm (H/L=122) was tested for ω= 3.49, 3.93, 5.24 rad/s in the coupled CFD/FEM simulations.

Figure 30 shows the RAOs of VBM and displacements for smaller wave height, denoted as CFD_0.02. The simulation results for different wave heights at lower frequencies show small differences. At lower frequencies, the free surface disturbances are practically non-existent for the two wave heights; see Figure 28, showing wave contour plots at same time instances. However, at the resonant condition, see Figure 29, the divergent waves disappears as the wave height decreases. This is also reflected in the RAOs of responses, as we notice a better agreement between Mars and CFD_0.02. Table 21 shows the relative difference in bending moment predicted by the numerical methods. There is a good improvement in the bending moment predicted by the CFD/FEA coupling at the ship-wave matching region. This is an indication that the nonlinear interactions on the free surface do have an impact on the motions and responses of the barge.

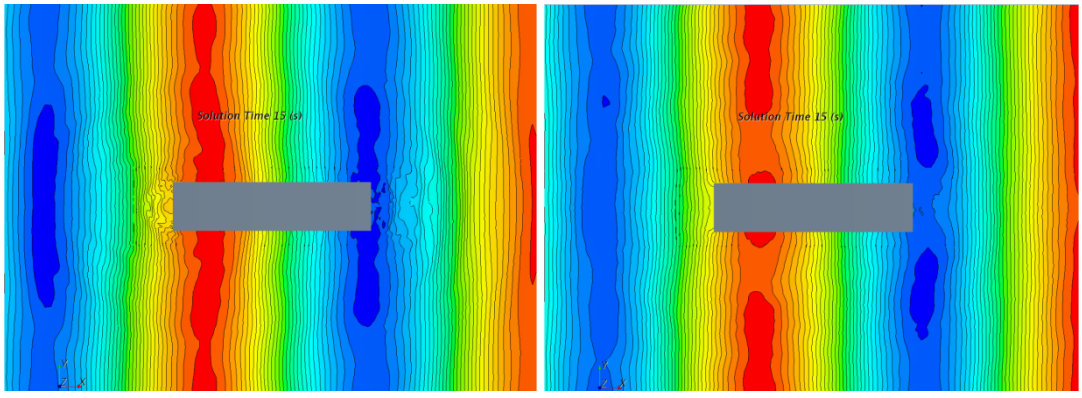

(a) (b)

Figure 28: Instantaneous wave contour around the flexible body for wave height (a) 0.1m and (b) 0.02m at 15s wave frequency of 3.926 rad/s

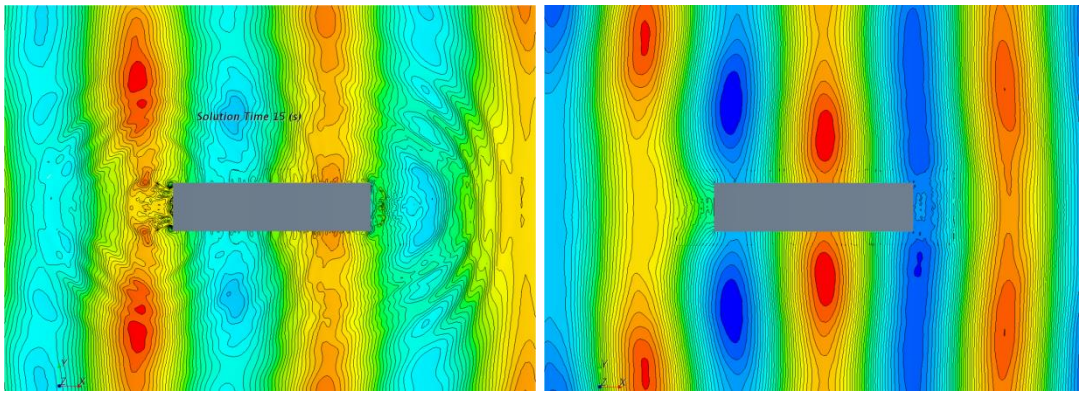

(a) (b)

Figure 29: Instantaneous wave contour around the flexible body for wave height (a) 0.1m and (b) 0.02m at 15s wave frequency of 5.235 rad/s

Table 21: Relative percentage error in VBM between 2-D and coupled simulations for smaller wave height (0.02m)

Location	ω (wave frequency)		
	3.49 rad/s	3.93 rad/	5.24 rad/s
Pt. 3 (2.035m)	38%	35%	16.6%
Pt. 5 (1.625m)	11%	22.9%	4.1 %
Pt. 7 (1.215m)	21%	15.9%	18.8%
Pt. 9 (0.825 m)	26%	38%	23.2%

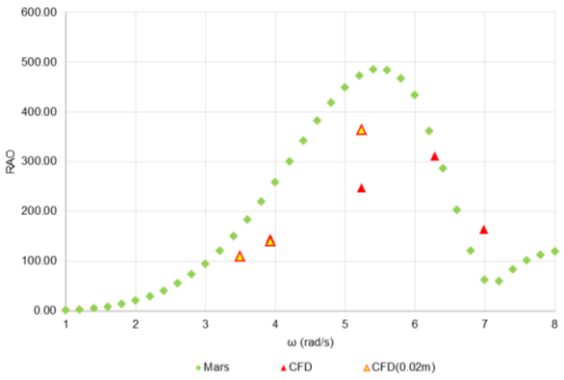

VBM at Pt.9 (x/L=0.33)

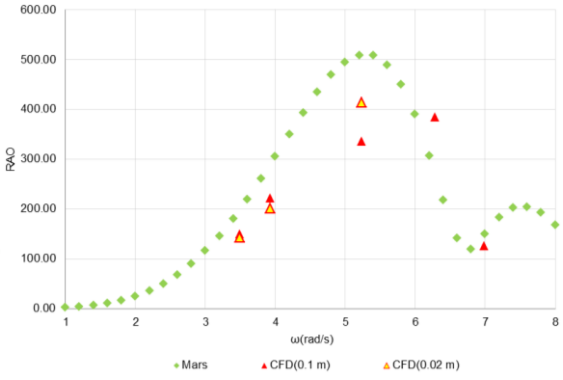

VBM at Pt.7(x/L=0.5)

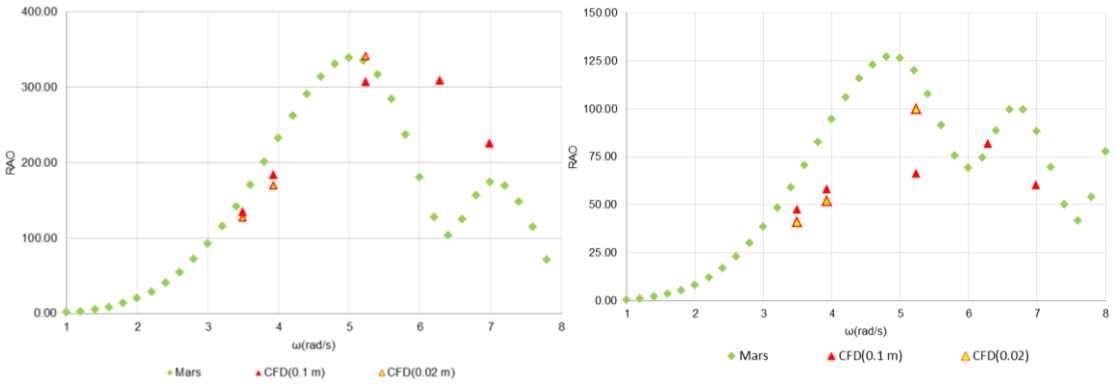

VBM at Pt.5 (x/L=0.66) VBM at Pt. 3 (x/L=0.83)

Figure 30: RAOs of VBM for two wave heights (0.1 m & 0.02 m) compared with 2-D linear.

5.7.5 Verification assessment

Grid and iterative convergence examined for the flexible barge is presented in this section. Grid convergence was carried out using 3 grids for two wave frequencies. CFD methods use iterative schemes to simulate the fluid flow problem. In the case of unsteady simulations, the real time is broken down into smaller time steps and the solution at each time step is obtained using number of iterations. After the solution attains convergence at a particular time step it proceeds to the next time step. The accuracy of the solution at a particular time step depends on the number of iterations and the convergence of conservation equations and various scalar quantities that affect the flow. Iterative convergence can be examined by monitoring residuals. One can also monitor scalar quantities like lift, drag, pressure etc. ensuring that they have attained convergence in a time step and remain unchanged by the end of the time step.

The behaviour of the residuals was acceptable for all frequencies, and additionally the co-simulations residual which is a function of the imported nodal displacements reduced by an order of four-five in the simulations performed. Pressure on the barge was also monitored at every time step. Figure 31 shows the pressure plot on the barge for 10 time steps. Basically the pressure attains a steady value in about 8-10 iterations and remains steady till the end of each time step.

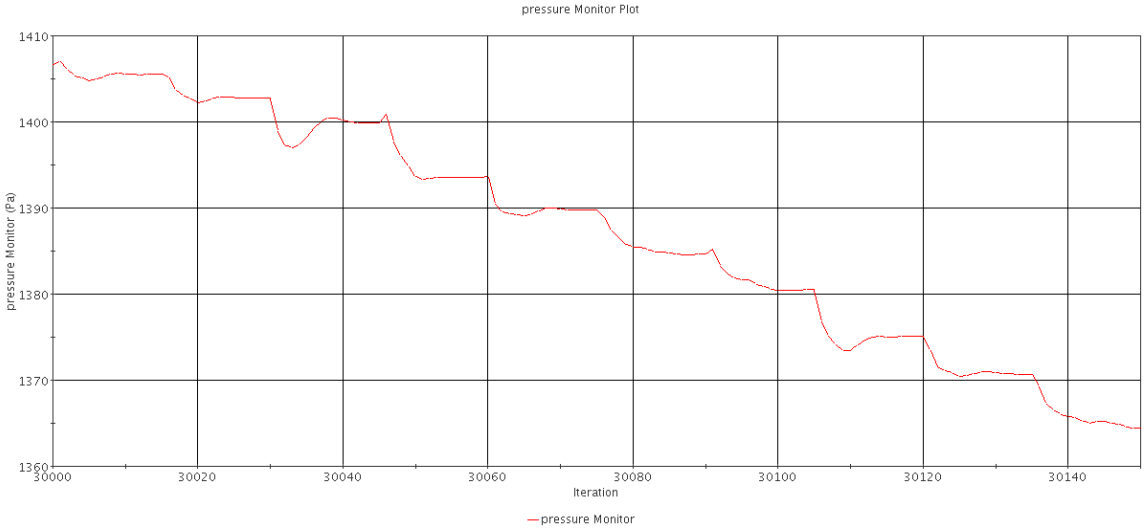

Figure 31: Convergence of pressure on the barge for twelve arbitrary time steps in the coupled simulation for wave frequency of 5.235 rad/s

Grid convergence is examined by using at least a minimum of 3 grids with a particular refinement ratio (r). A minimum of r_k >=1.3 should be maintained so that discretisation error can be differentiated from other sources of error like iterative error, round-off error etc. ASME (2008) . Roache (1998) suggested a grid convergence index (GCI) which is derived from the generalised Richardson's extrapolation theory to report the error estimation of different grids used for convergence studies. We would observe a monotonic asymptotic convergence as the grid is refined and should ideally reach an asymptotic value when the grid refinement reached zero. The GCI indicates a measure of error between the solutions from the asymptotic value. A small value of GCI would indicate that the numerical simulation is close to the actual solution. This should not be confused with the true value as the asymptotic result could have differences with the true value.

Spatial/Grid convergence studies were undertaken to assess the numerical errors and uncertainties in the flexible barge simulations. The grid used in the simulations presented in Section 5.4 is considered as coarse grid. Medium and fine grids were generated from the coarse grid using a constant refinement ratio (r_k) of 1.3. The mesh sizes for refined grids are shown in Table 22. Stern et al. (2001) reports that while commonly recommended r_k=2 may be too large for industrial CFD purposes, a good alternative may be to use r_k=√2 which is close to the value used in the present assessment. ASME (2008) describes a systematic step-by-step procedure to conduct error and uncertainty study due to discretization in CFD computations. Two frequencies (ω=5.24, 6.28 rad/s, H_w=100mm) were chosen to conduct conver-

gence studies using the GCI method proposed by Roache (1998). Large motions and responses were observed in these two resonant conditions which in-turn is likely to induce highest numerical errors, making it the worst case scenarios. In the grid study, the time steps were kept constant equivalent to 240 time steps per wave period for ω=5.2 rad/s and 200 time steps per wave period for ω=6.28 rad/s. As prescribed by ASME (2008) the apparent order of accuracy, approximate and extrapolated relative error and the GCI are reported for the simulations. Two integral variables (first harmonic of vertical force on the barge F_z and bending moment amidships VBM) and a point variable (vertical displacement amidships u_z) is used in the verification studies. The average of the variable over 8-10 wave periods were used in the calculations involving relative errors and GCI. The verification parameters for the variables are given in Table 23. The medium and fine grids mentioned in Table 22 were run with 160 processors and it took about 2 hours on the medium grid and 3.5 hours on the fine grid to run 1 second of real time simulation.

Table 22: Three different grid levels used for verification studies and the total grid count.

Grid Level	**Global Cell count**
Coarse	3.15 million
Medium	6.62 million
Fine	12.2 million

Monotonic grid convergence was achieved for the variables at the two frequencies. The apparent orders for ω=5.24 rad/s were close to the order of the unsteady solver, however, ω=6.28 rad/s show higher orders of accuracy. Higher orders of accuracy do not necessarily imply higher numerical accuracy, but indicate that finer meshes converged rapidly when compared to the coarse mesh. Nevertheless, such sporadic orders are not unrealistic and the values presented here are reasonable when compared with similar unsteady problems investigated by Weymouth et al. (2005), Wilson et al. (2001), Carrica et al. (2006). The relative errors and GCI fine for ω=6.28 rad/s are small and results are deemed reliable. A low percentage of GCI for both fine and medium indicate that the numerical results are close to the asymptotic value. The errors and GCI index is larger in the case of ω=5.24 rad/s, which

demonstrates that the unsteady problem for this wave frequency is especially sensitive to the grid size. Regardless, the values are small and within acceptable limits for such complex wave body interaction problems. For both wave frequencies the percentage of errors and uncertainties are much lower for the VBM when compared to the first harmonic vertical force acting on the barge. VBM is post-processed in Abaqus using the pressures imported at each time step during the coupled simulations. The difference in pressure at around amidships for all the three grids is relatively small; consequently the differences calculated in the bending moment are small. However, refinement of grid around the body changes the diffracted wave profile around the barge which results in variations in pressure, especially towards the ends of the barge. The vertical force is calculated by integrating the total pressure on the body which could vary moderately in magnitude for different grids, if not significantly. This could be one of the main reasons why the verification parameters are comparatively higher for the vertical force.

Table 23: Grid Convergence verifications parameters for three variables namely the vertical displacements amidships, vertical force and the vertical bending moment amidships

ω	**φ**	**Approximate relative error** e_a^{21}	**Extrapolated relative error** e_{ext}^{21}	GCI_{fine}^{21}	GCI_{medium}^{32}	**Apparent order p**
5.24rad/s	u_z	2.613%	3.762%	4.532%	5.846%	2.069
	F_z	5.559%	9.344%	10.6%	6.131%	1.91
	VBM	0.923%	1.88%	2.307%	1.524%	1.5
6.28 rad/s	u_z	1.713%	0.433%	0.539%	2.635%	6.1
	F_z	5.56%	2.191%	2.68%	0.708%	4.866
	VBM	1.163%	0.127%	0.159%	1.59%	8.8

5.8 Conclusions

The time domain hydroelastic investigation is carried out using commercially available software Star-CCM+ and Abaqus. The field equations are coupled using an iterative implicit scheme, and a Full Newton solution technique is used for solv-

ing the structural dynamics. The numerical solution is compared to experimental measurements and 2-D linear hydroelastic predictions. Calculations are carried out for both rigid body and flexible structural idealisations. Very good agreement is achieved between time domain predictions and experimental measurements in most cases, with some exceptions especially at the forward section of the barge.

Although the comparisons for rigid body motions between the two numerical methods agreed well overall, large differences were observed in the bow and stern regions of the barge at lower frequencies. This is believed to be due to strong bow and stern waves systems mainly influenced by the pitch, which are captured in CFD. CFD solves nonlinear Navier-Stokes equations, even when an inviscid flow model is selected which makes it more realistic than the linear potential flow code. Nevertheless, it should be noted that the rigid body approximation is not suitable for this very flexible barge.

Comparisons made between the present coupling technique and the experimental measurements showed very few discrepancies. Very good agreement was observed at relatively low frequencies, but slight differences were noted at higher frequencies. Of the two numerical methods, predictions using the coupled CFD method showed a far better agreement with experiments as it allows for nonlinearities.

Influence of flexibility is clearly seen in the relatively low frequencies as the body deforms with the wave resulting in weak stern and bow waves, hence; lower vertical displacements when compared to the rigid body approach. The results show that the coupling technique investigated is reliable and compares well with experimental measurements.

Kim & Kim (2009), Taghipour et al. (2008) time domain hydroelastic predictions showed discrepancies in the aft and fore end of the barge at higher frequencies (close to 2-node resonance) when compared with experiments. The differences were attributed to nonlinearities resulting from strong wave systems that are not well predicted using their numerical methods.

The next Chapter will investigate the coupling on a realistic flexible containership in regular head waves. The focus will be on calculating the wave loads with particular attention to nonlinear wave loads and 2-node springing component.

Chapter 6:

Wave loads on a flexible containership

This chapter concerns the numerical investigations of motions and wave induced loads on a flexible containership (S-175) advancing with a forward speed in regular head waves. The main emphasis is on the prediction of linear and non-linear wave loads. The nonlinearities are expressed as the higher order harmonics of the time series signals, high frequency 2-node flexible mode or so to say the springing component, and the asymmetry in sagging and hogging loads. The two-way coupling is applied to investigate the dynamic behaviour of the vessel for a range of wave frequencies in two regular wave heights. The numerical results are compared with a number of experimental measurements and other published numerical predictions showing an ability to reproduce the nonlinear effects even in relatively severe wave conditions. The main focus is on the ability of the coupled procedure to capture the nonlinear effects in the wave loads and identify the areas of discrepancies.

6.1 Review of Experiments

The data available from model tests of flexible or backbone models are few as compared to rigid body seakeeping measurements. Extensive model tests were conducted by some researchers on a modern containership, as stated in the Literature review. It would be intriguing to carry out validation of the two-way coupling against measurements on large flexible modern containership where the higher order harmonics higher than the second or third become important, because they might coincide with the 2-node natural frequency of the hull (Drummen et al. 2009) (Hong et al. 2008). Furthermore, nonlinear springing could have a strong influence on the wave loads at particular wave frequencies. Unfortunately, the hull forms were not available due to confidentiality agreement. Comparative studies on the experimental results of S-175 containership have been carried out for several decades. 16th ITTC presented the model tests results on S-175 containership, and furthermore in the 18th ITTC, 23 organisations participated in the model tests of S-175. They reported the test procedures and detailed data analysis techniques. The above experiments have provided exhaustive database covering various wave con-

ditions and the corresponding responses of S-175 which can be used for comparative study of linear methods. O'Dea et al. (1992) investigated the variation of heave and pitch of S-175 model with respect to varying wave steepness, and showed presence of nonlinearities in motion.

When we review the wave load measurements of S-175, the following three experiments are considered as a benchmark and vast majority of numerical validations utilise them. Watanabe et al. (1989) measured the of effects bow flare on deck wetness and the asymmetry in vertical bending moment on an elastic S-175 model built using synthetic resin and foam urethane. The first and second harmonics of wave loads were reported in their paper. To study the influence of different wave heights on the nonlinear characteristic of responses, Fonseca & Guedes Soares (2004b) tested a three segmented S-175 model in regular waves of varying frequencies. The amplitude and phase of the first, second and third harmonics of bending moments were obtained at amidships and 1/4 Lpp from the forward perpendicular. Nonlinear effects were detected in both vertical motions and wave loads, although it was proclaimed that they emerge stronger in the loads than in the motions. Focusing more on the nonlinear wave loads, Chen et al. (2001) also carried out a model test of a self-propelled S-175 container ship, but using an elastic ship model. Four different wave steepness were tested, for a number of wave frequencies, with the model advancing at one speed. The vertical bending moment due to 2-node flexible mode or the springing component were also detected in the bending moment records. The model properties and experimental conditions from Chen et al. (2001) are used to construct the numerical models for the application to the current two-way coupled simulation.

A comparative study between the two-way coupled analysis and their experiments is carried out for two wave heights to assess the accuracy of the current numerical method. Examining the results between the above three experimental measurements unveiled some differences in the measurements, especially in the higher order harmonics. While Watanabe et al. (1989) and Chen et al. (2001) used elastic self-propelled S-175 model, Fonseca & Guedes Soares (2004b) used a towed segmented model. The treatment of the model and the forward speed boundary conditions could be contributing to the emerging differences. Although, the experiments by Chen et al. (2001) are used as a primary comparator, the measurements of Fonseca & Guedes Soares (2004b) and Watanabe et al. (1989) are also used to vali-

date the numerical predictions. The expectation is that comparisons with different experiments will give a better awareness into the numerical uncertainties and aid in making recommendations on how they can be alleviated so that the coupled analyses could be applied with confidence to solve such complex ship-wave interaction problems involving flexibility.

6.2 Experimental Measurements

6.2.1 Model Particulars

The model tests were conducted in the towing tank of CSSRC having a dimension of 474m (L) x 14m (B) x 7m (D) (Chen et al. 2001). The elastic model of S-175 was made using ABS material ABS702. The thickness of ABS plate for deck, bottom and side hull is 2mm and for the bulkheads is 4mm. Due to the limitation in the choice of plate thickness, the structural similitude was not exactly held and the rigidity of the model amidships is approximately 18% higher than intended. 21 transverse bulkheads (0~20 stations) were used to reinforce the model in transverse direction. The 2-node frequency in water was 9.45 Hz, rather than 8.57Hz calculated by the law of similitude. Conversely, the model tested by Watanabe et al. (1989) was made of synthetic resins and the similitude bending rigidity was matched to that of the full ship making the model slightly more flexible than the above. The self-propelled model was free to surge, heave and pitch, but was constrained in sway, yaw and roll axis. The vertical bending moments were measured at five locations, shown in Table 26, along the model using strain gauges placed on the starboard side-deck plate. In addition to the wave loads, vertical accelerations at the FP, heave and pitch motions were also measured. Ballast blocks were arranged along the length to satisfy the exact weight distribution and location of the centre of gravity of ship. The particulars of the model and some structural characteristics are shown in Table 24. The 2-node frequency and damping ratio in water were estimated from hammer tests. It should be noted that the model length used by Watanabe et al. (1989) and Fonseca & Guedes Soares (2004b) were 4.5 m and 4.4 m, respectively.

Table 24: Principal particulars of S-175 containership (Wu et al. 2003) in full scale and model scale. * denotes the values calculated as per the law of similitude.

Particulars	**Ship**	**Model**
Length (L)	175 m	3.6 m
Beam (B)	25.4 m	0.523
Depth (D)	15.4 m	0.317
Draught (T)	9.5 m	0.195
Displacement (Δ)	24742 t	215.4 kg
Centre of Gravity (CG)		
X_G(from aft perpendicular)	85.0 m	1.75
Z_G (above the baseline)	9.52 m	0.196
$_b$ (block coefficient)	0.5787	0.5787
EI (amidships)	2.28 x 10^{18} kg.mm^2	* 8.4 x10^9 kg.mm^2 10.18 x 10^9 kg.mm^2
2-node frequency (dry)	1.6 Hz	* 11.15 Hz 12.27 Hz
2-node frequency (wet)		* 8.57 Hz 9.45 Hz
δ (2-node damping ratio in water)		0.067

6.2.2 Test Matrix and Measurements

Experiments were conducted by Chen et al. (2001) in the wave basin of CSSRC in regular and irregular waves with the model advancing at a Froude number of 0.275, which corresponds to a model speed of 1.6342 m/s. Watanabe et al. (1989) and Fonseca & Guedes Soares (2004b) tested the model at a slightly lower speed of advance corresponding to a Froude number of 0.25. Please note that some primary differences between the experiments and the coupled analysis are listed in Table 25. The numerical setup for the coupled analysis will be discussed in the following sections. Table 26 shows the regular head wave conditions that were used for comparisons with the coupled analysis. Even in the case of H/λ=1/50 a significant amount of green water and severe spray were observed in the model tests around the resonant frequency region.

Table 25: Summary of certain key model and boundary conditions from the experiments and coupled analysis.

Cases	Model	Fwd Speed	H/L	Froude No:	EI(scaled)
1.Chen (2001)	3.6 m	Self-Propelled	1/50, 1/30	0.275	20% stiffer
2.Watanabe (1989)	4.5 m	Self-Propelled	1/30	0.25	Similar to scaled
3.Fonseca (2004)	4.4 m	Towed	1/50	0.25	Similar to scaled
4. 2-way coupling	3.6 m	Fixed in position and velocity input to wave	1/50	0.275	Similar to scaled

Table 26: S-175 test cases simulated using the coupling technique.

Condition	**Wave Height**	**λ/Lpp**
1	H=L/50=72 mm	0.6, 0.7, 0.8, 0.9, 1.0, 1.1, 1.2, 1.3, 1.5, 2.0
2	H=L/30=120 mm	1.1, 1.2, 1.3

Table 27: Model locations where the motions and responses are calculated H=L/30 only amidships data available in literature

Location	Station	Longitude
1	Station 5	0.95 m from AP
2	Station 7.5	1.35 m from AP
3	Station 10 (amidships)	1.85 m from AP
4	Station 12.5	2.25 m from AP
5	Station 15	2.65 m from AP

The vertical bending moments were calculated from the strain measurements (Chen et al. 2001). The location of measurement points are given in Table 27 and illustrated in Figure 32.

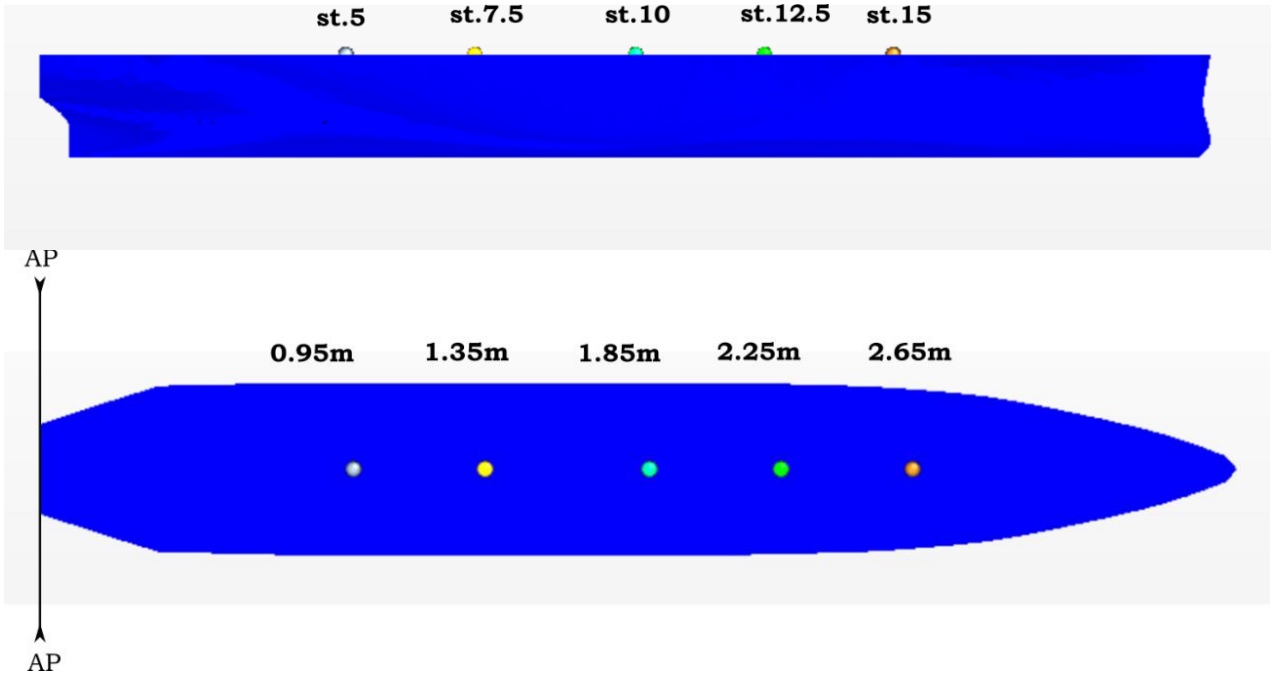

Figure 32: Pictorial representation depicting the side and top view of the point probes placed on the model to calculate responses (Chen et al. 2001).

Locations 1 and 5 are close to 1/4 L_{pp} from the aft and forward of the model, respectively. To distinguish the asymmetry between hogging and sagging moments, the strain gauges were set to zero before each test after the model was at rest in water. Hence, the measured bending moments excluded the still water bending moment.

To investigate the effect of higher order harmonics and springing component in the wave-induced loads, the time series signal of the vertical bending moment must be separated into the corresponding frequency components. In the regular wave measurements, ten complete stable wave periods were analysed for each wave frequency and steepness (Chen et al. 2001). The time series signal was then decomposed into its sinusoidal frequency components using a Fourier transform. The transformed signal were identified as first, second, third harmonics of the wave encounter frequency, as well as the springing component near the 2-node wet resonant frequency. An inverse Fourier transformation on these frequency components produced the time domain expressions. Moreover, the amplitude of the corresponding frequency components was non-dimensionalised with respect to the wave

heights. A similar approach is adopted in the numerical predictions to separate and non-dimensionalise the harmonic components of the vertical bending moment. The non-dimensional amplitudes of heave, pitch, vertical accelerations and bending moment are given as.

$$C_z = \frac{Z}{a_w},\ C_\theta = \frac{\theta}{ka_w},\ C_A = \frac{L\ddot{Z}}{ga_w},\ C_M = \frac{M^{(i)}}{D}$$

where L denotes the length of the model; g, acceleration due to gravity; k, wave number; Z, heave amplitude; θ, pitch amplitude, $\ddot{Z}$, vertical acceleration amplitude; a_w, wave amplitude. $M^{(i)}$ denotes the frequency component of bending moment which is differentiated by the index i and denominator D is the parameter for non-dimensionalisation of the corresponding wave-load component.

$D = \rho g L^2 BH$ for $M^{(i)} = M^{(1)}$ (double amplitude of first harmonic bending moment)

$D = \rho g L^2 B a_w$ for $M^{(i)} = M^{(2,3,2-node)}$ (amplitude of 2nd, 3rd and 2-node bending moment. $M^{(sag,hog)}$ is also non-dimensionalised using the latter denominator.

In addition the 2-D linear hydroelasticity is used to obtain predictions numerical results (Bishop et al. 1977) for heave, pitch, acceleration at bow and the first harmonic of bending moment.

6.2.3 Computational Domain and Grid Design

The coordinate system of the computational domain is designed such that the longitudinal direction of the ship is aligned with the x-axis with the stern located at x=0 and the side wall extended in the y-axis. The mean free surface of wave lies at z=0. The domain was designed based on the minimum requirements prescribed by (ITTC 2011). The computational domain extends to 2.0 L_{pp}, 4.0 L_{pp} (includes 2.0 L_{pp} damping zone) and 2.5 L_{pp} towards the inlet, outlet and side wall direction, respectively. Since the problem is symmetric with respect to the y-axis (only vertical motions and responses are calculated), the coupled analyses were carried out on one-half of the solution domain, unlike the barge. A constant damping distance of 2.0 L_{pp} is set for all wave models. The extension of the computational domain in all directions is shown in Figure 33 & 34. The red line in Figure 33 indicates the extent

of the overset boundaries. The domain for all wave simulations were constant calculated on the basis of L_{pp}, unlike the case of the barge where it was based both on λ and L_{pp}. Table 28 shows the distances of the boundaries of the computational domain measured from the ship.

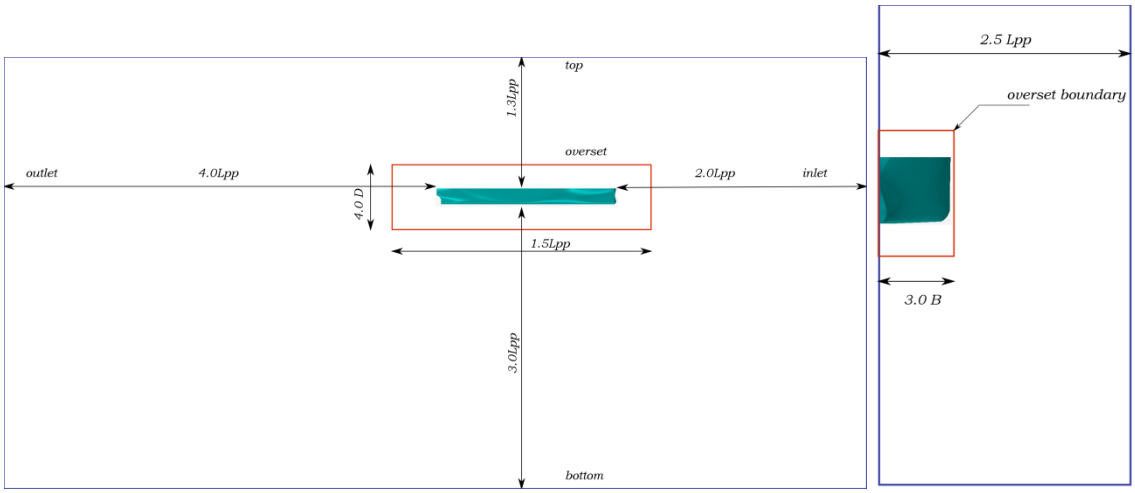

Figure 33: Overview of the computational domain and the distances towards the boundaries from the body. The extent of the overset boundaries in the three-dimensions is also shown.

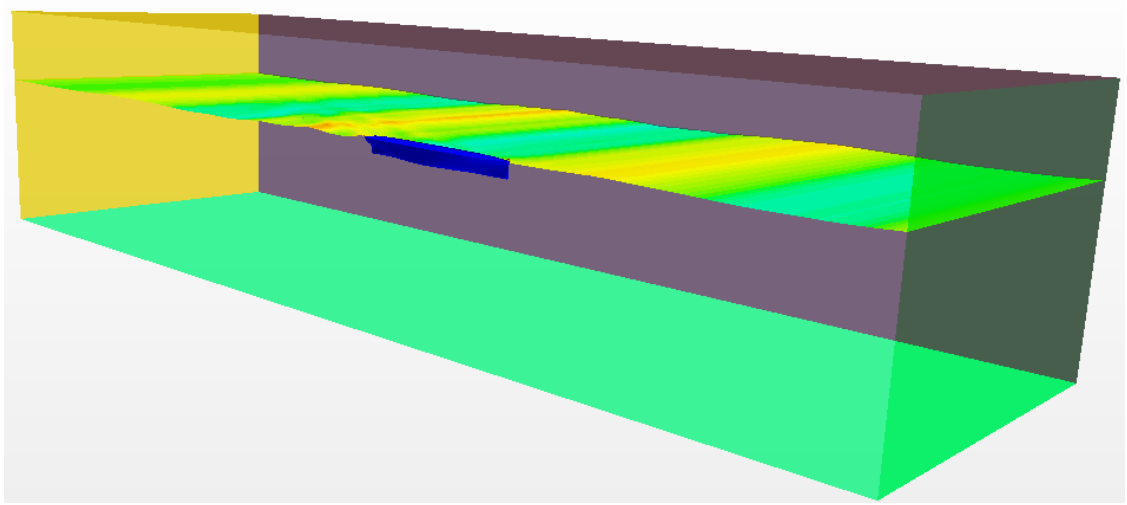

Figure 34: Three-dimensional representation of the fluid domain used for S-175 computations. The boundary on the far right corresponds to the inlet boundary.

Table 28: Distances in meters and with respect to the length between perpendiculars (L_{pp}) of various boundaries in the CFD model from the ship.

Boundary	Distance from the body	Distance in terms of L_{pp}
Inlet	7.2 m	2.0 L_{pp}
Outlet	14.4 m	4.0 L_{pp}
Side-wall	9 m	2.5 L_{pp}
Bottom	10.8 m	3.0 L_{pp}
Top	4.6 m	1.3 L_{pp}

From a detailed review of the CFD simulations of ships with forward speed, undergoing rigorous motions including green water, it is expected that fine grid and time step sizes will be required to capture the flow physics around the hull and the wake field. The meshing models used in this case are identical as described in Section 5.4 of the previous Chapter. A trimmed Cartesian grid is used for the discretising the 3-D domain. The ensuing mesh was made up effectively of unstructured hexahedral cells with trimmed cells adjacent to the ship model. This means that the hexahedral cells have one or more edges cut off to fit the surface. Further, the outlet and the side-wall boundaries are extruded using user specified stretching parameters keeping into consideration that there is not any massive change in the grid sizes of the adjacent layers that could result in numerical issues.

Taking into consideration the number of test cases that needs to be simulated for the validation of S-175 in waves, it is not really practical to design individual grids for each wave frequency as done in the case of the barge. However, with a bit of care it is possible to design one computational grid so that the minimum grid sizes requirement on the free surface for stable wave propagation is satisfied in all cases. In the present study, grid refinements were carried out around the hull surface, the bow and the stern region, as well as the wake region to produce one single mesh, suitable for all the wave frequencies, that closely satisfies the recommendations in the literature. Firstly, the grid sizes on the free surface, along the wave length and the wave height, were calculated for $\lambda/L_{pp}=1.0$ so that the recommendations by STAR-CCM+ (2012) is satisfied (80 cells per wave length and 20 cells per

wave height). The experience gathered from the numerical wave tank and the coupled barge simulations indicate that a minimum of 40 cells per wave length and 20 cells per wave height would suffice to produce a stable wave with acceptable dissipation. Following the above design about 50 cells per wave length is available for λ/L=0.6 which is the shortest wavelength case investigated. This means that for the longest wave length λ/L=2.0 there are approximately 160 cells per wave length. About 22 cells per wave height were available in the free surface refinement region for both the wave heights investigated. The only difference between the meshes for the two wave heights is that for H=L/30 the refinement block was larger to make sure that the wave is within the refinement at all times.

Thereafter the refinements adjacent to the model surface and in the wake region were calculated to adequately capture the severe free surface flows arising due to the green water effects and the wake field of the advancing ship. Kim & Lee (2011) suggest a minimum of 150 grid cells per wave length near the hull surface in both upstream and downstream directions when severe motions inducing slamming and green water effects are present. Tezdogan et al. (2015) and Piro (2013) also followed this grid configuration for their ship-wave CFD simulations, and reported to produce reliable comparisons with experiments. Piro (2013) sought an efficient refinement method taking into advantage the speed of coarse grid simulations while providing refined grids to capture slamming and green water induced fluid behaviour. Volumetric blocks were used to sufficiently refine the grids at the bow region; approximately 29 grid points along the depth to resolve the impact flow and water shipped on the deck.

In the coupled simulations, for λ/L =1, 160 cells per wave length are placed in the vicinity of the hull which translates to about 100 grid points for the shortest wave length (λ/L=0.6). Additionally, about 50 grid points along the depth in the bow and stern region to capture the violent free surface flow is available. Table 29 shows the global cell count of the background and the overset mesh. The above refinements around the hull remained within the overset boundaries to eliminate any interpolation error between the overset boundaries and the background mesh during the simulation. The refinements at the bow and in the wake region are shown in Figure 35.

Table 29: Total cell count of the fluid grid showing the distribution in the boundary and overset regions.

Case Study	Cell count		Total
	Background	Overset	
S-175 in waves	1,889,262	1,667,020	3,556,282

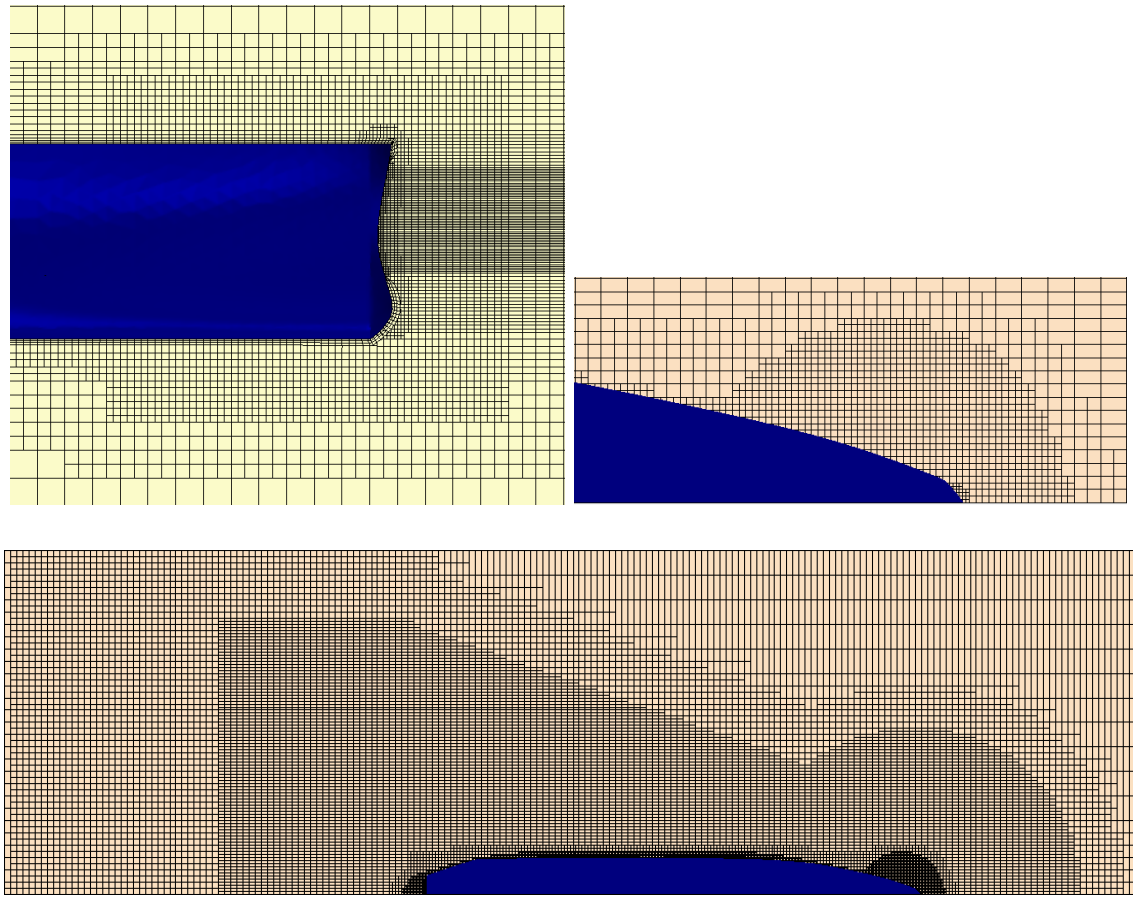

Figure 35: Grid refinement provided in the bow and wake region to capture the violent deck flows and the diffracted and radiated waves.

It is evident from the snapshots in Figure 36 from the CFD simulations that the containership model experienced severe green water effects. This phenomenon occurred at λ/L=0.9~1.5, but no bow slamming events were detected in the conditions of Table 25. This was also observed in the experiments of Chen et al. (2001).The above grid design is capable of capturing the violent free surface flows. The simulations were run in parallel mode with single precision on the University of Southampton high power computing facility Iridis 4. The test cases were run with 256 processors and it took between 8-10 hours to run 1 second of real time simulation.

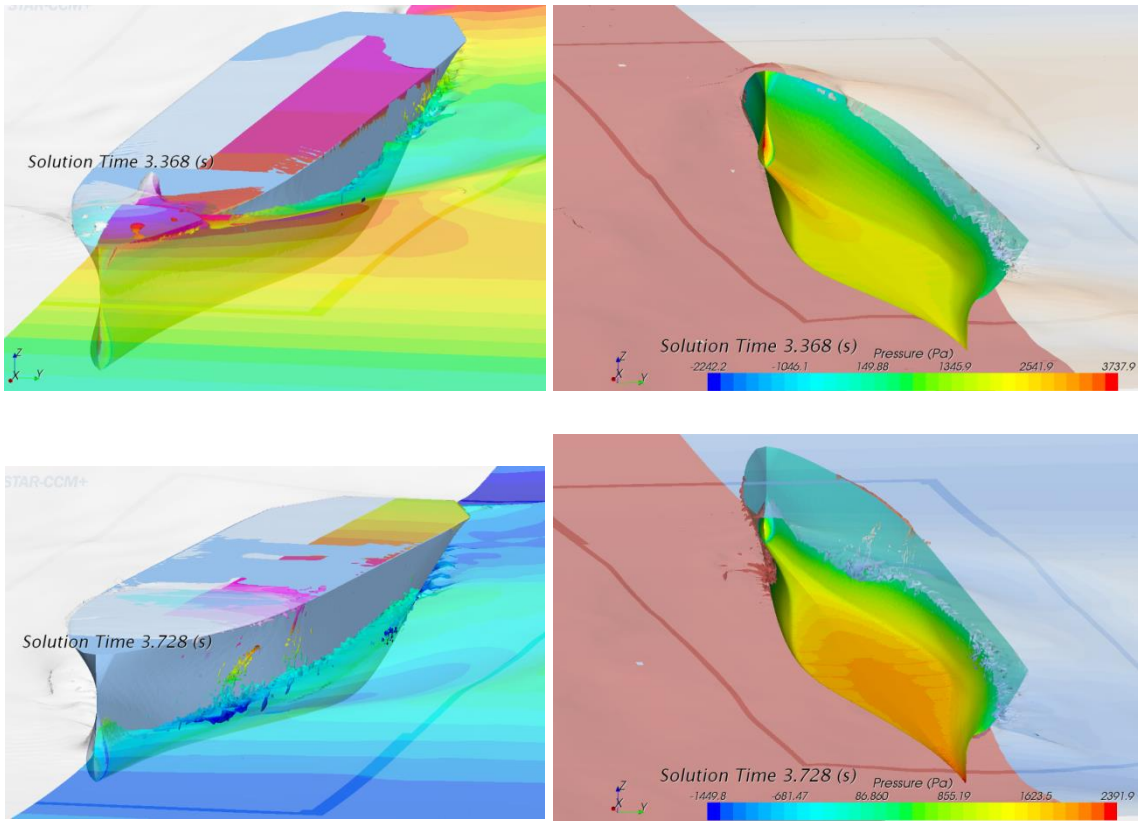

Figure 36: Contour plots of the CFD simulations for λ/L=1.3 showing significant amount of water on deck.

6.2.4 F E model of S-175

The model tested by Chen et al. (2001) has a scaling coefficient α= 1/48.6. The experimenters had used a single plate of uniform thickness to construct the hull; hence the model was more or less a uniformly elastic. The FE model of S-175 used in the coupling procedure consists of beam elements which takes into account the flexibility of the ship in a global sense. The nodes of the beam elements are connected to dummy surface elements which represent the hull surface. Thus, the modelling procedure followed is similar to the flexible barge described in Chapter 5. The model properties were calculated using scaling laws from the full scale mass and structural properties published by Wu & Hermundstad (2002). The 3-D beam elements are defined in Abaqus using a general cross-section where in the geometric quantities required to define the section is specified. Table 30 shows the list of mass and structural inputs for the full ship. Due to the symmetry condition used in the coupled simulations, only one-half model is considered. The generalised beam sections can only take into account linear material behaviour, although the section

response can be linear or nonlinear. The structural model consists of 100 3-D quadratic Timoshenko beam elements. The length of each beam element L_{beam} is 0.036m, and five beam elements are assigned the properties of the corresponding section in Table 30. The material properties of the beam elements are defined as that of Aluminium. The area of the beam sections and transverse shear areas are calculated as described in the Equations below.

$$A = M / (\rho L)$$

A is the area of the cross-section, M is the mass of each section, ρ is the density of aluminium (2712 kg/m^3), L = 5*L_{beam} =0.18m. The effective shear area was available from the experiments in the case of S-175 and was taken into account in the F E model in the following way.

The transverse shear area of a section of a shear flexible beam is:

$$\frac{K_a''}{f_a} = K_a$$

where K_a'' is the effective shear stiffness in the α-direction, f_a is a dimensionless coefficient to prevent large shear stiffness for slender beam elements, K_a is the actual transverse shear stiffness which is the input that Abaqus requires to define the generalised beam section properties.

The shear stiffness has the units of force (Newton) and is equal to kAG. kA is the effective shear area and G is the shear modulus, in this case of Aluminium (2.6*10^9 N/m^2). The station wise effective shear areas are given by Wu & Hermundstad (2002).

The dimensionless factor is defined as

$$f_a = \frac{1}{(1 + \xi * SCF \frac{L^2_{beam} A)}{12(I_a)}}$$

ξ is 10^{-4} for quadratic elements, SCF is the slenderness compensation factor which takes a default value of 0.25.

Table 30: S-175 F E model sectional properties

Section	Mass (Kg)	2nd moment of area (m^4)	Cross-section area (m^2)	Transverse shear stiffness(N)
1	5.94243868	9.95824E-08	0.0121731	106929.4885
2	7.4280048	3.87E-07	0.0152163	389897.4787
3	8.91365802	6.63882E-07	0.0182597	885427.4501
4	11.88488774	8.85177E-07	0.0243463	1239598.43
5	11.88488774	9.95824E-07	0.0243463	1310162.807
6	11.88488774	1.10647E-06	0.0243463	1380754.895
7	11.88488774	1.21712E-06	0.0243463	1415967.938
8	13.3704435	1.32776E-06	0.0273895	1415027.597
9	13.3704435	1.32776E-06	0.0273895	1416027.597
10	14.8560096	1.43841E-06	0.0304327	1416078.077
11	14.8560096	1.32776E-06	0.0304327	1416246.363
12	14.8560096	1.21712E-06	0.0304327	1416445.245
13	13.3704435	1.21712E-06	0.0273895	1416206.592
14	11.8848774	1.106427E-06	0.0243463	1516158.866
15	11.8848774	9.95824E-07	0.0243463	1416392.224
16	10.3992241	7.74529E-07	0.0213029	1381266.811
17	8.9135802	6.63882E-07	0.0182597	1310432.626
18	7.4280048	6.08559E-07	0.0152163	10622333.934
19	5.94243868	5.97494E-07	0.0121731	531001.2356
20	4.45678545	5.69832E-07	0.0091298	106169.0939

The hull surface is modelled using dummy surface elements (SFM3D4) and these are connected to the beam nodes using kinematic coupling constrains. The beam is shown in red colour in the FE model assembly shown in Figure 37. The hull is cut arbitrarily to show the beam which is positioned at a height corresponding to the VCG from the base of the hull.

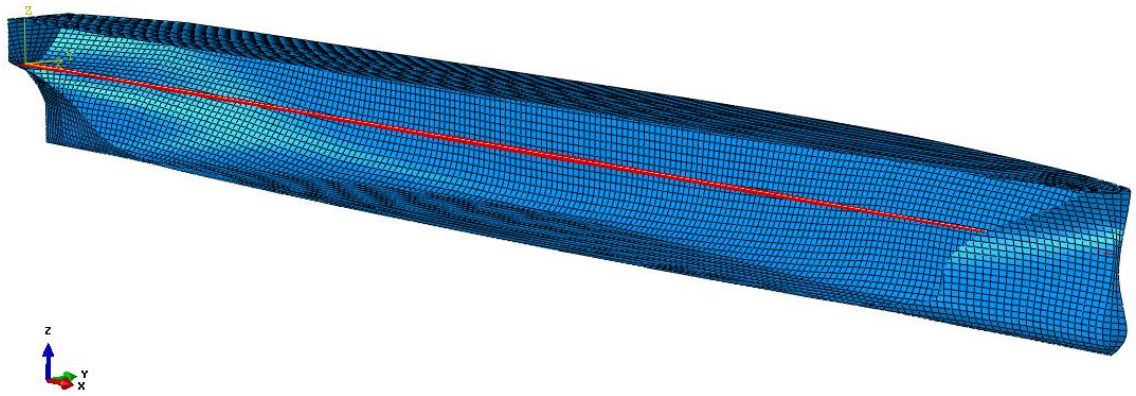

Figure 37: Perspective of S-175 FE model. The red coloured line is the beam model whose inputs are specified as per Table 29.

The FE model is restricted to translate in the y-axis (no sway) and rotate in the x and z-axis (no roll and yaw). The forward velocity of the S-175 containership in the coupled analyses is simulated by assigning an additional velocity of propagation, equal to the model velocity, to the regular wave. If the model is not restricted in the longitudinal direction in either the CFD or FE model it experiences a drift in direction of wave propagation due to longitudinal force. The numerical issues surrounding this unphysical drift when the model is not restrained in any way is described is similar to the description in Section 5.6.3. Additionally, the time history of bending moment (BM_without_BC), shown in Figure 38, revealed a progressive decrease in the magnitude as the simulation proceeded and a subsequent increase in the wave encounter period. This was suspected due to the lack of restriction of motion in the longitudinal direction. The possible solution to nullify this effect is to define an additional boundary condition in the FE model to restrict the unphysical drift in the longitudinal direction. The cheapest and simplest option to realise is by defining zero translation in the x direction to one beam node close to the LCG of the model. Figure 38 also shows the comparison between the time history of bending moments with and without the aforementioned boundary condition. The magnitude and period of bending moment with the boundary condition (BM_with_BC) is now steady and period of the response is also fairly constant.

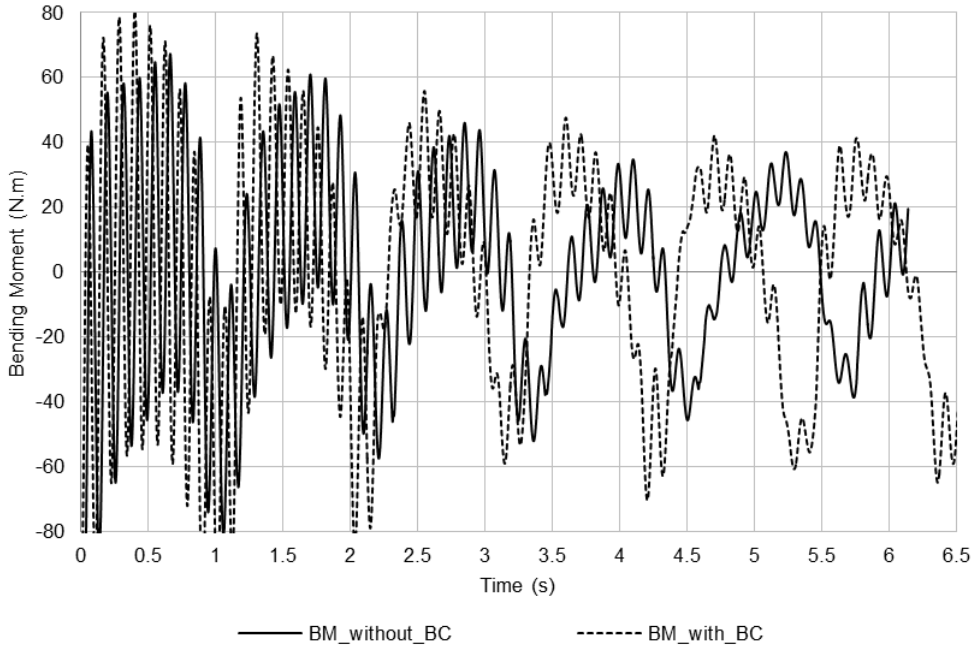

Figure 38: The time history of VBM amidships with and without the boundary condition to restrict the unphysical drift in longitudinal axis. H=L/50 and λ/L= 1.0.

6.2.5 Boundary Conditions and Solver Settings

The boundary conditions used in the CFD model of S-175 is given in Table 31. The boundaries and the boundary conditions are similar to the barge simulations.

Table 31: The boundary conditions used in the CFD model

Region	**Boundaries**	**Boundary Condition**
Domain	Inlet	velocity inlet
	Outlet	pressure outlet
	top	velocity inlet
	Bottom	no-slip wall
	side (y extent)	no-slip wall
	Symmetry	symmetry
Overset	S-175	no-slip wall
	Boundaries	overset boundary
	Symmetry	symmetry

The total number of inner iterations per time step is chosen to be twelve with four exchanges in one time step. The containership is stiffer compared to the flexible barge. The containership co-simulations were stable when the time steps were de-

creased and did not exhibit any instability issues as observed in the previous case. This was also evident from Table 15 that when the stiffness of the barge beam was increased the critical time step decreased. However, due to the violent free surface flows there was a restriction on the maximum time step, especially in the region of λ/L=0.9~1.5. In this region a constant time step of 0.0008 seconds, which resolves the first natural frequency of the model into 145 time steps per period, was essential. Above this time step, the simulations suffered from negative volume cells at the overset boundary eventually leading to divergence. When the body experiences violent flows and rigorous motions, finer time steps are required for the overset boundary to be coupled at all times with the background region. With respect to the encounter wave period, for λ/L=0.6~2.0, the time step chosen varied between 1100~1600 time steps per wave period which is considered fine when referred to the literature for similar computations (Peric et al. 2007) (Paik et al. 2009) (Seng 2012). The solver settings are given in Table 32.

Table 32: The solver settings and parameters in the CFD model

Property	**Value**
Gravity	Yes
Viscosity	No
Artificial compressibility	Yes
Convection discretisation	2nd order
Temporal discretisation	2nd order
Velocity URF	0.9 (default)
Pressure URF	0.3
VOF URF	0.6
Grid Flux URF	0.8
Imported field URF	Adaptive 0.2-0.5
Maximum inner iterations	12
Number of exchanges per time step	4
Time Step	0.0008/0.001 s
Co-Simulation time	0.00080.001 s

6.3 Results and Discussion

6.3.1 Modal Analysis

The first five dry natural frequencies of the model were evaluated using Block Laconzs eigen value extraction method. The full scale S-175 has a 2-node dry frequency of 1.6Hz. The scaled natural frequency is 11.15 Hz, however, due to the restriction in choice of plates the frequency of model investigated by Wu et al. (2003) Chen et al. (2001) is 12.27 Hz. Table 33 presents the natural frequency of the FE model compared with calculations performed by 2-D finite difference method(MARS) Bishop et al. (1977). The values given in brackets correspond to the natural frequency ω in rad/s.

Table 33: Dry natural symmetric frequencies (Hz/rad/s) of the S-175 FE model compared with 2-D finite difference

Mode	Abaqus	MARS
2-node	11.12 (69.92)	10.90 (68.493)
3-node	25.22 (158.49)	24.31 (152.76)
4-node	41.19 (259.86)	39.59 (248.80)
5-node	58.773 (369.28)	56.24 (353.39)
6-node	77.832 (489.03)	73.473 (461.64)

The 2-node dry frequency of the FE model is close to the requirement as per the law of similitude. There is good agreement between the FE models and the 2-D finite difference results. The mode shapes are shown in Figure 39.

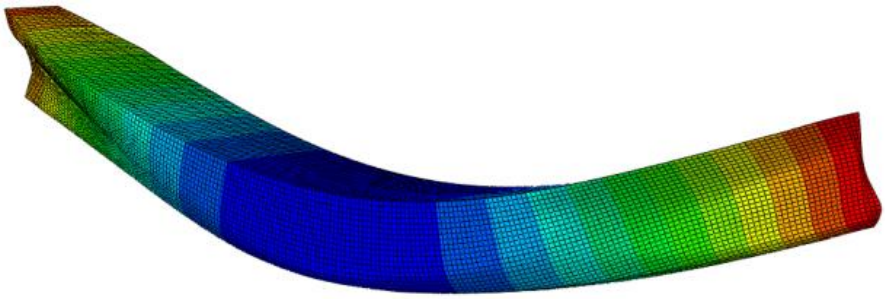

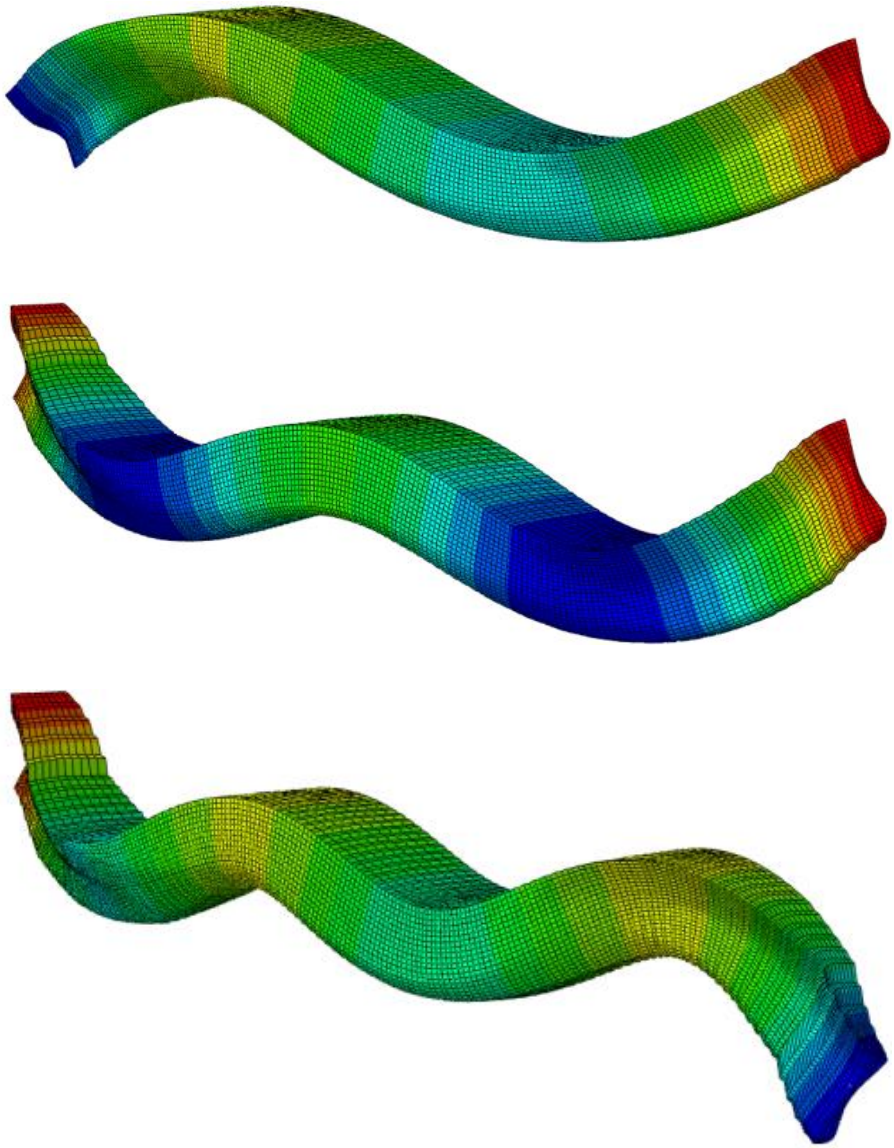

Figure 39: The first four symmetric modes shapes of the FE model.

6.3.2 Regular wave measurements

Accurate monitoring of the incoming wave field is the core of a seakeeping analysis. In the numerical analysis and in experiment, the incoming wave is monitored at one ship length (3.6m) in front of the model. The waves generated in the towing tank may themselves have nonlinear effects, appearing as higher harmonics of the wave frequency. O'Dea et al. (1992) and Fonseca & Guedes Soares (2004b) had analysed the incoming waves and separated them into the first and higher order harmonics. The ratio of second order/first order and third order/first order for varying frequencies were less than 10% and 1%, respectively. When measuring the higher order harmonic responses, quantifying the harmonic components in the incoming

wave is a useful first step. This will aid in distinguishing the nonlinear contribution of the incoming wave to the responses.

The non-dimensional transfer functions in Section 6.2.2 require accurate estimation of the wave height. The transfer functions are expressed in an average sense, meaning the responses for each wave frequency are analysed over a nearly ten complete cycles. Table 34 shows the average wave height obtained from simulations which is calculated as the average of peak-to-trough for ten complete cycles. The deviation from the input wave height (H_w= L/50= 0.072 m) is expressed as percentages and are larger in shorter waves. From the observed results we can conclude that the incoming wave is stable and the decrease in amplitude is negligible.

Table 34: Average wave heights from the simulations for 10 wave periods and the deviation from nominal wave height.

λ/L	CFD	Deviation (%)
0.6	0.065316	6.7
0.7	0.067836	3.1
0.8	0.06866	4.6
0.9	0.069446	3.6
1.0	0.069893	2.9
1.1	0.071	1.39
1.2	0.07	2.8
1.3	0.070509	2.07
1.5	0.071227	1.07
2.0	0.072177	0.25

In the numerical simulations the incoming wave is generated using a first-order regular wave. Consequently, it is expected that the higher-order component will be negligible in the wave records, nonetheless, the time history of the incoming wave was Fourier analysed and transformed to second and third order harmonics.

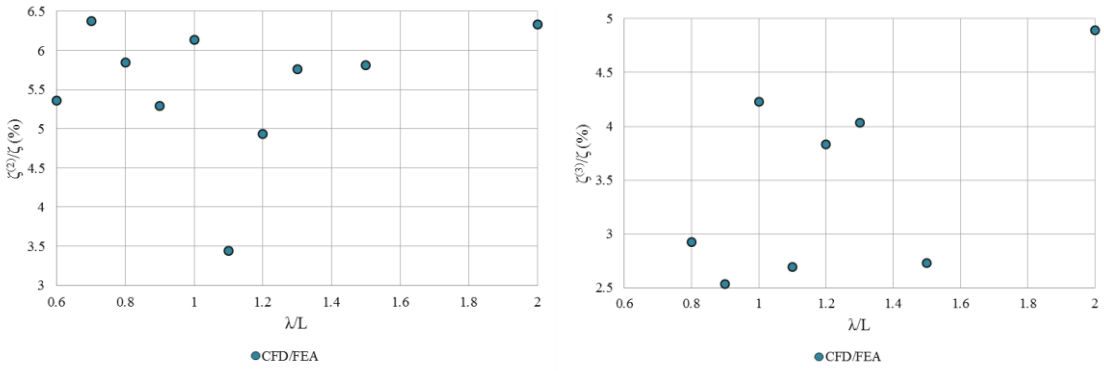

Figure 40: Non-dimensional amplitudes of second and third harmonics of the tested regular waves (H=L/50)

The results are shown in Figure 40 as a percentage ratio of amplitude of the harmonic component to the amplitude of the first harmonic. The second harmonic wave amplitudes are less than 6.5% of the first harmonic. With regard to the third harmonics, the amplitudes are less than 5% of the first harmonics. In model scale, this implies that for all cases the second harmonic amplitude is less than 5mm, and the third harmonic less than 3.5mm. In conclusion, one may say that the incident waves are predominately linear, and the higher order harmonics measured in the simulations are due mainly to nonlinear behaviour in linear waves.

6.3.3 Heave, Pitch and Vertical Acceleration in waves

In this section the heave and pitch responses along with the vertical acceleration at the bow is presented for the test matrix in Table 25. The CFD calculations are carried out using two wave heights and for a range of frequencies. The results are compared against three sets experiments and linear 2-D potential flow method. To make the interpretation of the results easier for the reader the naming convention in the plots are stated first. In all the graphs, henceforth, the 2-way coupled and linear predictions are denoted as CFD/FEA and 2-D Linear, respectively. The experimental measurements of Chen et al. (2001) is denoted as Chen(2001). The measurements from Watanabe et al. (1989) and Fonseca & Guedes Soares (2004b) is differentiated as Watanabe (1989) and Fonseca (2004).

The responses in this section are plotted again the non-dimensionlised wave frequency $\omega\sqrt{(L/g)}$, where ω is the incident wave frequency. So, as we progress towards the right hand side of the x-axis the waves are getting shorter. The numerical predictions are compared with experimental measurements Chen et al. (2001) and 2-D

linear predictions Bishop et al. (1977). The 2-D linear results were also used as a comparator in Chen et al. (2001). Additionally, when available the numerical predictions are compared with the experimental measurements of Fonseca & Guedes Soares (2004b) and Watanabe et al. (1989).

The heave response as a function of the non-dimensionlised wave frequency is shown in Figure 41. Although, the term heave is used in this context, it should be considered as the total vertical displacement at CG which includes rigid body displacements and distortion of the flexible model. In the experiment, heave and pitch were measured by means of a 4-component motion measuring device placed at amidships. In the numerical simulations, the total displacement of a point probe on the deck of the ship at LCG is used to record the time histories and the average amplitude is used to calculate the RAO.

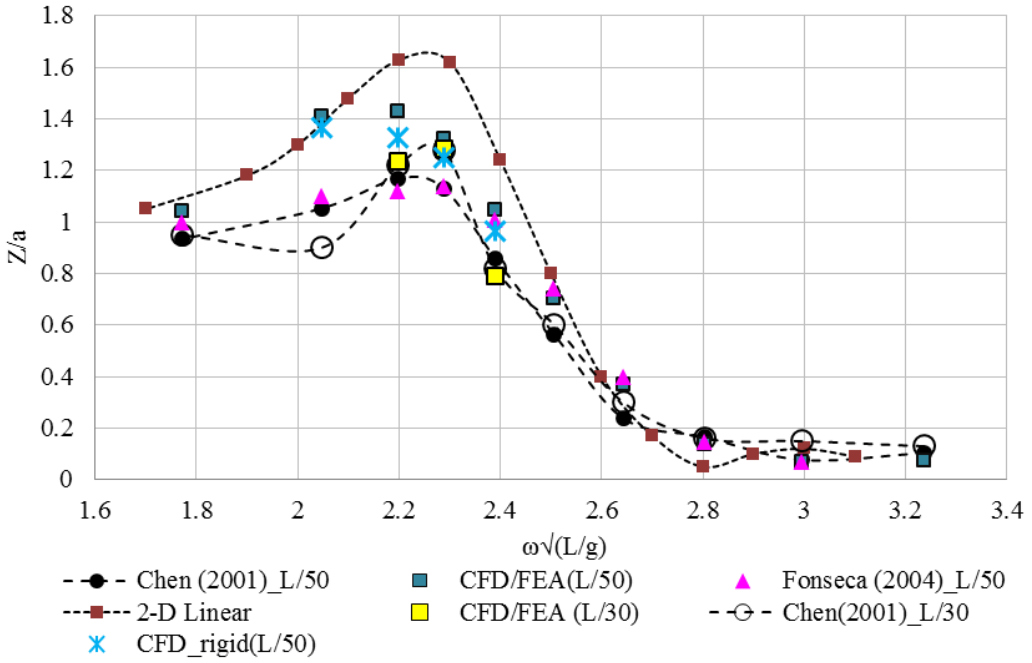

Figure 41: Non-dimensional heave amplitudes predicted from coupled simulations with other numerical and experimental measurements.

To study the effect of distortion the rigid body heave calculated using CFD (CFD_rigid) is compared with the flexible body. The difference in heave increases with increase in the frequency (decrease in wave length) from 3.5 % to 8.6 %. This means that the effect of distortion becomes more prominent with the increase in the amount of green water shipped on the deck. At $\omega\sqrt{(L/g)}=2.04$ the flexible containership very much behaves like a rigid body.

In the case of the flexible body, the heave response (H=L/50) measured by the two experiments is more or less close to each other at most frequencies. The resonant peak occurs in the frequency range of 2.2~2.4 which corresponds to a $\lambda/L = 1.1\sim1.3$. Indeed, severe green water effects and water spray were observed around this range in the CFD simulations. The linear predictions largely over-estimate the heave response in the non-dimensionalised frequency of 1.7~2.5 by about 40% when compared to the experiments. The coupled analyses, for H= L/50, produce slightly better results in this frequency range, but they are still greater than the measurements by about 15-25%. This difference can be noticed in the frequency of 2.0~2.6, wherein the bow of the model was immersed in the simulations shipping large amount of water on deck. Besides, the agreement is better in the frequency region where no deck water was shipped. The heave response for the larger wave height show better agreement when compared to measurements.

Chen et al. (2001) indicates that a possible reason for the differences between measurements and 2-D linear predictions is due to the omission of viscous and non-linear effects in the numerical model. Iijima et al. (2008) employed a 3-D linear potential flow method and found that the heave response in long waves (H=L/120) of S-175 containership was over-predicted by nearly 30% in the non-dimensional frequency range 1.7~2.4 when compared to the measurements by Fonseca & Guedes Soares (2004b). Alternatively, Fonseca & Soares (2005) state that the heave response in waves (H= L/40) using the nonlinear time domain code developed by Fonseca & Soares (1998) overestimate the measurements in the range of 2.2~2.5. With introduction of viscous effects, the heave amplitudes were reduced and the predictions improved when compared to experiments.

Following the above recommendations, two cases were simulated using a k-ω SST turbulence model. The heave response after including viscosity is shown in Table 35 and is now slightly lower than the inviscid case; nevertheless the difference was still 15 % at this frequency when compared to experiments.

Table 35: Heave calculated for two wave frequencies with and without viscosity compared with experimental measurements and 2-D linear

λ/L	ω√(L/g)	CFD (inviscid)	CFD (Turbulence)	Chen (2001)	Fonseca (2004)	2-D Linear
1.3	2.19	1.428	1.35	1.17	1.1	1.4
1.5	2.04	1.412	1.3	1.05	1.12	1.63

With increase in wave height, the disparity between measurements and linear predictions were higher due to highly nonlinear behaviour induced due to flare impact and green water effects. The reason for the decrease in the heave response as the wave height increases is also due to the above nonlinearity. The contour plots at the non-dimensional frequency 2.19 (λ/L=1.3) is shown in Figure 42 for the two wave heights. Two time instances of the motion of the vessel are shown. In Figure 42 a & b the vessel is at its highest point and immersing back into the water and in figure 42 c & d the vessel is accelerating upwards from its lowest immersion point in water.

The amount of green water on deck and violent free surface flows for the two wave heights are significantly different. At higher wave heights, although the absolute motion of the vessel increases, the larger mass of water on deck is damping the vessel motion causing lower RAOs. The effect of these nonlinearities on loads will be discussed in the following sections. The experimental RAOs at wave frequencies where there was low or no flare impact or green water showed negligible differences with change in wave height.

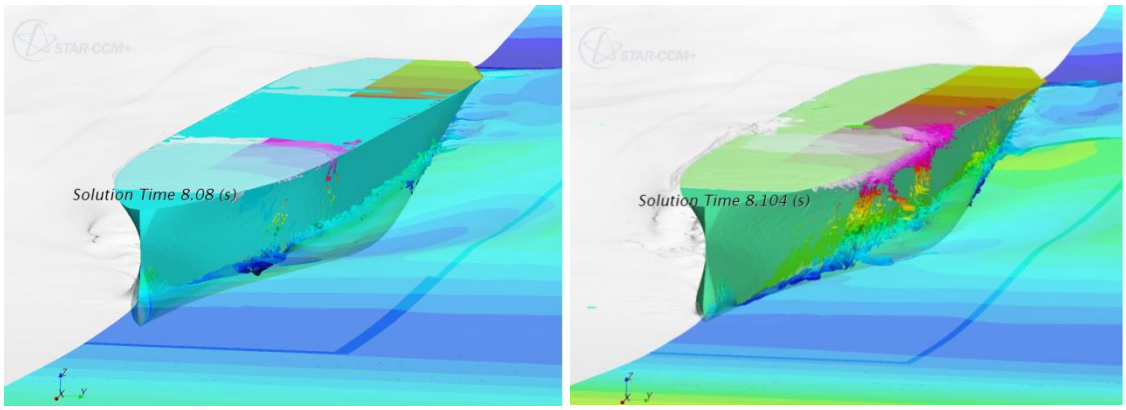

(a) (b)

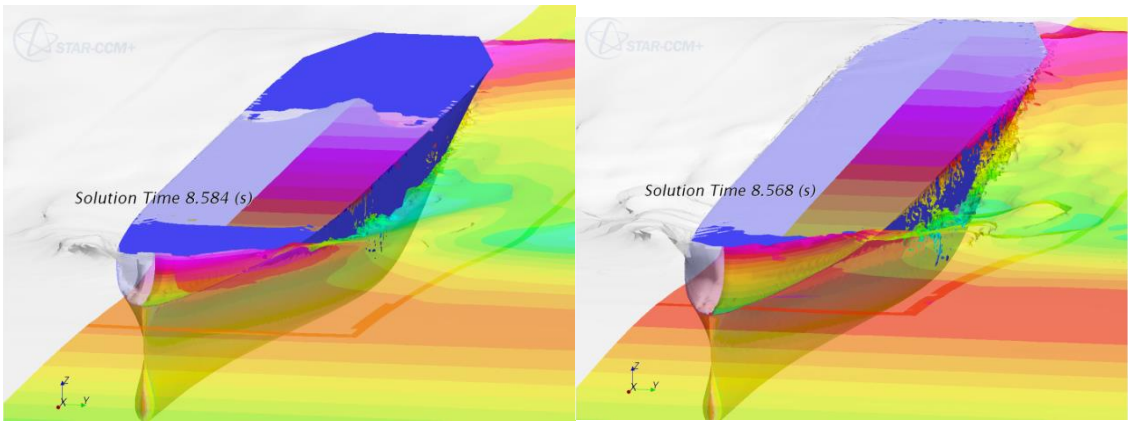

(c) (d)

Figure 42: Comparison between the green water and flare impacts from the two wave heights investigated for λ/L=1.3. Contour plots a & c are for H/L=1/50 and b & d are for H/L=1/30.

The numerical predictions of the pitch (in Figure 43) show good agreement with the experiments except in the frequency range of 2.0~2.2 where the pitch is highly over predicted. Please note that the pitch angle is non-dimensionalised using the ka (product of wave number (k) and wave amplitude (a)) due to which the differences are amplified in Figure 43. The magnitude of pitch angle is very small for this model in the range of 0.6~4.0 degrees. The predictions in this region (2.0~2.2) are closer to the measurements conducted by Fonseca & Guedes Soares (2004b). O'Dea et al. (1992) noted that the pitch motion for varying wave steepness was virtually linear. The CFD pitch RAO decreases by about 15% with increases in wave height. The measurements by Chen et al. (2001) exhibit a sharp descent in the non-dimensionalised frequency region 2.0~2.2; not noted by other experimentalists. There is no specific reasoning offered in their paper about this odd behaviour. This nonlinearity was not captured in the CFD/FEA simulations and the prediction at this frequency is twice than the measurements. No specific reason could be identified for the difference at this one frequency. The effect of distortion on pitch is very small when we compare the coupled (CFD/FEA) and rigid body (CFD_rigid) simulations.

The vertical accelerations predicted by the 2-D linear theory are greater than the measurements, and the maximum difference of 38% is observed at the resonant non-dimensional frequency 2.3. The 2-way coupled result in Figure 44 shows remarkably good agreement with the measurements in the frequency range, with a maximum difference below 10%. This indicates that the bow vertical acceleration

which is sensitive to the nonlinearities arising in the cases is well captured in the simulations.

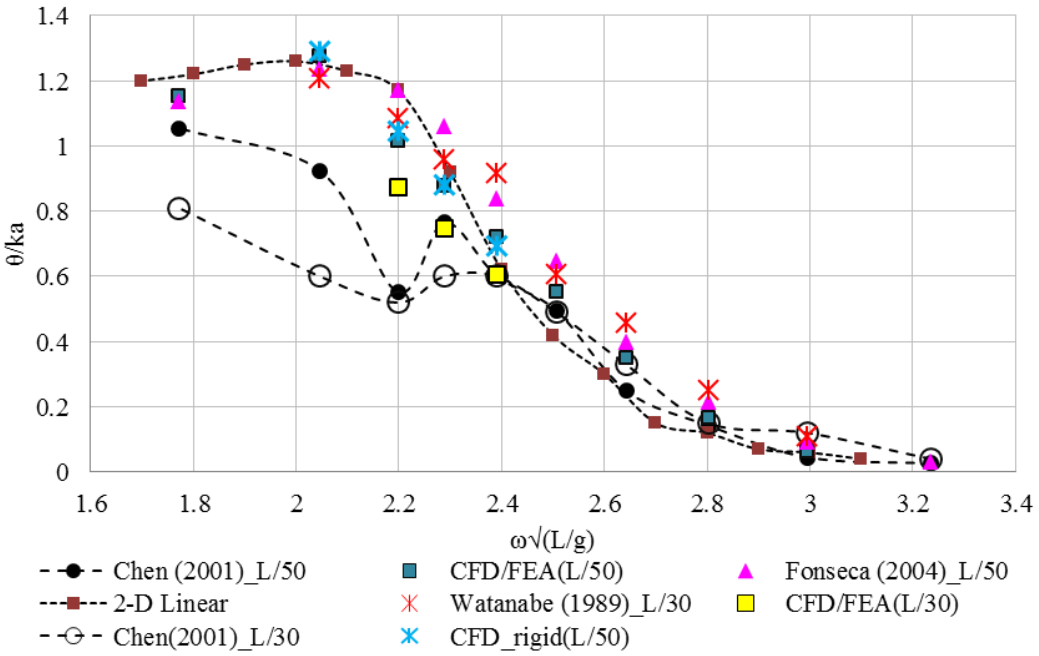

Figure 43: Non-dimensional pitch amplitudes predicted from coupled simulations with other numerical and experimental measurements.

If we consider a simple sinusoidal equation of motion, say displacement $X = A\sin(\omega t)$ where A is the amplitude of motion, ω is the frequency and t is the time, the second time derivative of this motion $\ddot{X}$ will equate to the acceleration. Therefore, we can say that the bow acceleration is a more sensitive indication of the higher order harmonics as the first, second and third harmonics will be proportional to ω^2, $4\omega^2$ and $9\omega^2$, respectively. The time histories of vertical bow accelerations clearly displayed nonlinear influences. The second and third harmonic component of the bow acceleration is displayed in Figure 45. The magnitude of the second harmonic component is in the range of about 5-12% of the first harmonic. The third harmonic component is much smaller and is less than 2% of the first harmonic.

Even when the ship undergoes extreme motions in waves, apparently, the motions in vertical plane exhibit sinusoidal fidelity in contrast to the vertical accelerations. This can be interpreted as the heave and pitch will be predominantly sinusoidal with the same frequency as the incoming wave which accelerations are more sensitive to the nonlinearities.

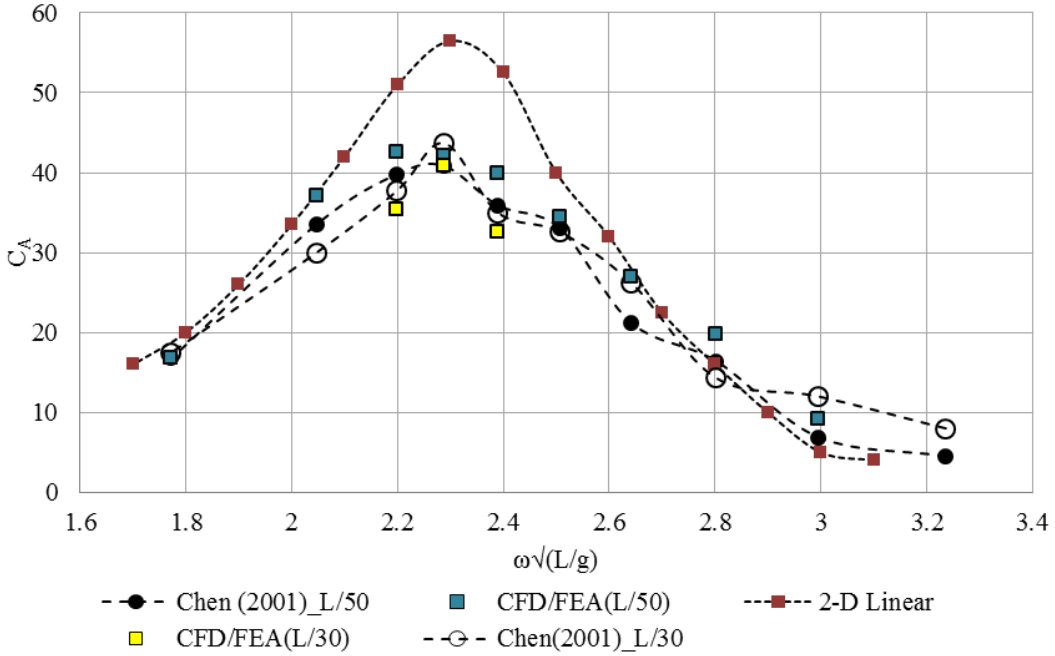

Figure 44: Non-dimensional vertical acceleration predicted from coupled simulations with other numerical and experimental measurements.

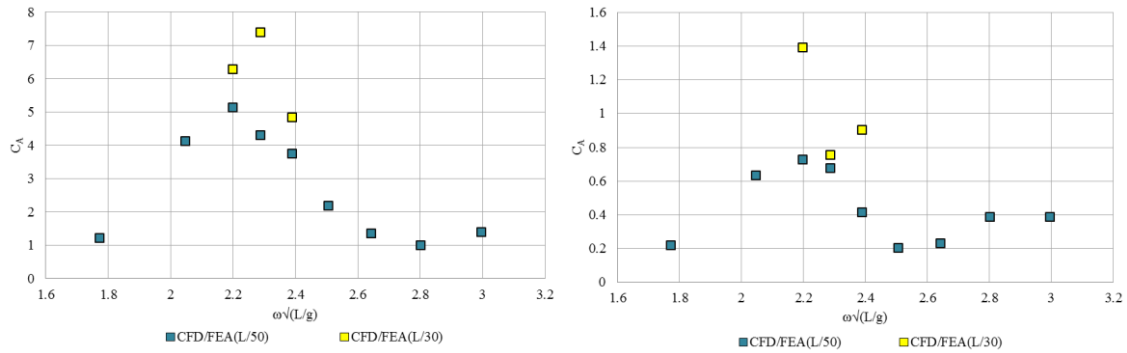

Figure 45: Non-dimensional second and third harmonics of vertical accelerations for the two wave heights investigated.

6.3.4 Vertical Bending Moments in waves

The first harmonic of wave bending moment estimated using the coupling method is compared with 2-D linear and experimental measurements. The first harmonic of bending moment amidships and at the forward location is also compared with the nonlinear strip theory results from Wu & Hermundstad (2002). Before discussing the 2-way coupling predictions, a brief insight is provided on the different experimental measurements. For numerical validations, Chen et al. (2001) is treated as the primary comparator. Nevertheless, the results from other experiments (given in Table 34) are also used to discuss the validity of numerical predictions. This

is because the differences in the model and boundary conditions produce different experimental results given in Table 25. The linear bending moment amidships for the wave steepness H/L=1/30 measured by Chen et al. (2001) is greater than Watanabe et al. (1989) in the range of λ/L= 0.9~1.5 by a maximum of about 20% (Fig 47) considering a small change in speed and also the difference between (Fonseca & Guedes Soares 2004b) and (Chen et al. 2001) in the range of 1.0~1.3 is about 10-15% . Please refer to Table 25 for some primary differences between the experimental models. It was not possible to exactly replicate the experimental conditions, for example, the numerical model is closer to a towed model than a self-propelled model. In spite of the differences it is worthwhile to compare the results in general terms.

First let us examine the bending moments amidships predicted using the 2-D linear and the 2-way coupling method. The 2-D linear method Bishop et al. (1977) has been shown to predict the wave loads in the linear range with sufficient engineering accuracy (Aksu et al. 1991) (Bishop et al. 1984). Therefore, before proceeding to the forward velocity problem, the 2-way coupling was investigated for zero speed condition at two wave frequencies corresponding to a ratio of λ/L = 1.3 and 2.0, and compared with zero speed 2-D linear predictions. This exercise is to check the consistency between the two numerical methods by eliminating the steady forward speed effects. The non-dimensional values of the first harmonic of bending moment amidships shown in Table 36 are in close agreement at these two frequencies.

Table 36: VBM amidships for two wave conditions (H/L=1/50) in zero speed condition.

λ/L	2-D Linear	CFD/FEA	Difference (%)
2.0	0.006145	0.0064752	5.4 %
1.3	0.0119477	0.0112794	5.5%

Comparing the predictions with forward speed in Figure 46, the agreement between the two methods is seemingly good, but in the range of λ/L =1.0~2.0 the 2-D linear predictions are larger. The nonlinear strip theory also follows a similar trend to the 2-D linear predictions in this region. With increase in wavelength, the difference between the non-dimensionalised bending moments also increases, approaching a maximum of about 18-20% in the region of 1.5~2.0. The bending moments predicted by the 2-way coupling in this region is under-predicted when com-

pared to 2-D linear and even the experiments. Examining the zero speed and forward speed condition unveils an unfamiliar behaviour in the coupled simulations which is that at λ/L=2.0 the bending moment calculated decreases by 16% with forward speed. Simultaneously, there is a significant increase of about 55% at λ/L=1.3 with introduction of forward speed, and the agreement with 2-D linear also turns out to be better. In relatively shorter wave length, i.e. λ/L =0.6~0.9, the agreement between the two-way coupling and the two numerical methods is excellent.

The inlet boundary is placed at a distance of 2L from the model which means for λ/L= 2.0 there is only one wavelength in front of the body. Hence, one possibility triggering the problem could be the effect of reflected waves, but there was no evidence of such in the CFD simulation. The heave for this case was steady sinusoidal and the velocity vectors on the domain and the wave surface indicated no reflections. To be certain the distance of the inlet from the body is not causing the issue; the distance is increased to 4.0L. Inadequate spatial discretisation could also lead to erroneous pressures to be exported to the FE model resulting in inaccurate responses. To ascertain that the problem is not related to grid refinement, the initial mesh was globally refined by a factor of 1.4. The predictions for the above grid configurations are compared with the original mesh in Table 37. The results showed relatively small changes (about 1-2% for first harmonic) when compared to the original mesh. In fact it is reassuring that the numerical error emerging from grid refinement is quite negligible for both linear and the nonlinear responses for this wave length. A detailed grid refinement study is not carried out in the coupled simulations of S-175 due to the computational time required to run very fine meshes. All the results presented are on a coarse grid but Table 37 suggests that error in responses calculated is within acceptable limits.

Table 37: Comparison between various grid configurations used to estimate the responses for λ/L=2.0

Grid	1st harmonic	2nd harmonic	3rd harmonic	2-node	Heave	Cell count
Original mesh	0.005567	0.0006266	0.0002924	0.0005940	1.042	3.75 million
Extended inlet	0.00555	0.0005122	0.0003440	0.0006915	1.059	4.2 million
Refined mesh	0.005686	0.000657033	0.0003689	0.000589645	1.0455	6.2 million

For H=L/50 the bending moments comparisons between the present method and the experiment amidships produce small differences in the resonant region, however, there is over prediction in the shorter waves by a maximum of about 35% and under prediction by the same amount in the longer waves. In the longer wave length region (1.5~2.0) the CFD/FEA coupling under-predicts the bending moment. The cause for this under prediction is undetermined. In absolute magnitude the bending moment predicted by CFD/FEA is 26 Nm and this value is smaller by 16 Nm compared to the measurements. The correspondence between the two-way coupling and the three experiments is excellent in the region of λ/L= 1.0~1.3. Some differences can also be noticed between the different experiments but these are under 15%.

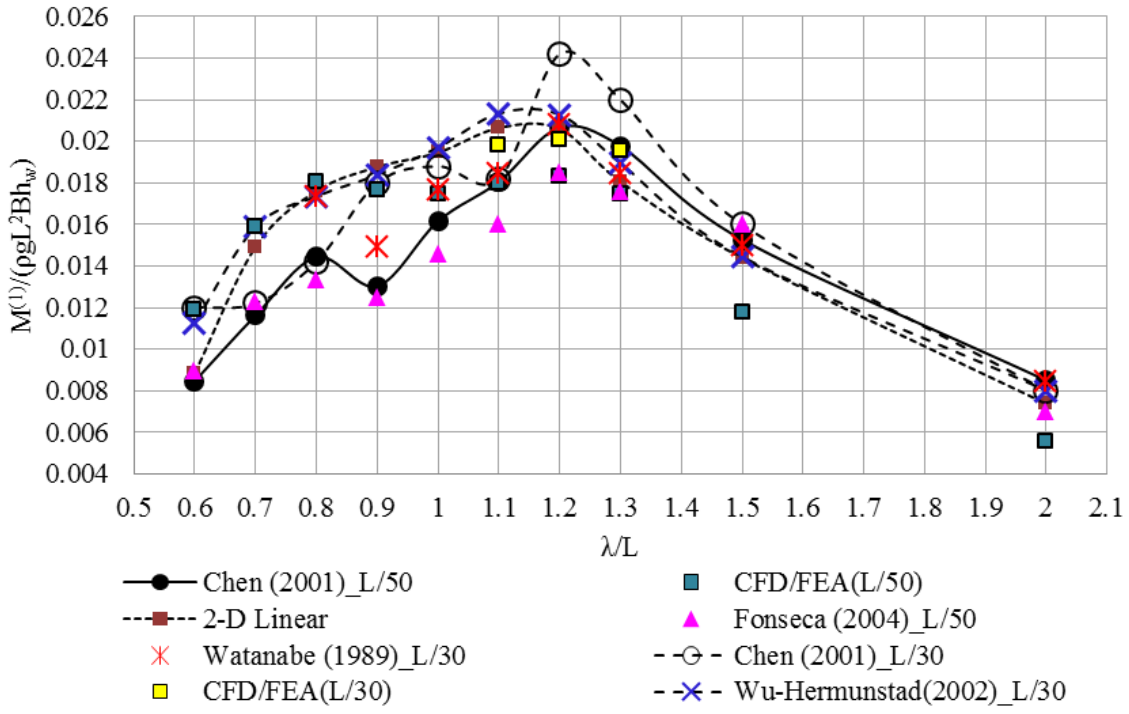

Figure 46: Non-dimensional amplitude of first harmonic VBM amidships calculated using coupling method and numerical and experimental measurements for two wave heights.

Increase in wave height causes an increase in the amidship bending moment by 10% in the coupled simualtions. A definite peak is noted in Chen et al. (2001) at λ/L = 1.2. The bending moment is 15% greater than the simulations and the other experiment at this wavelength. Another observation from the coupled simulations in the region of λ/L = 0.8~1.3 is that the first harmonic of bending moment is constant. Although, in this range the experiments do not exhibit such behavior and

the peak is clearly perceivable at λ/L = 1.2 (ω√(L/g)= 2.28). In fact the RAOs of VBM predicted by 2-D linear in this range differ by only about 12% and a sharp peak is absent. Figure 47 shows the frequency components of bending moment amidships vs encounter frequency for two wavelengths. The first harmonic occuring at the encounter frequency of the incoming wave is practically same. The differences emerge in the higher order frequency components.

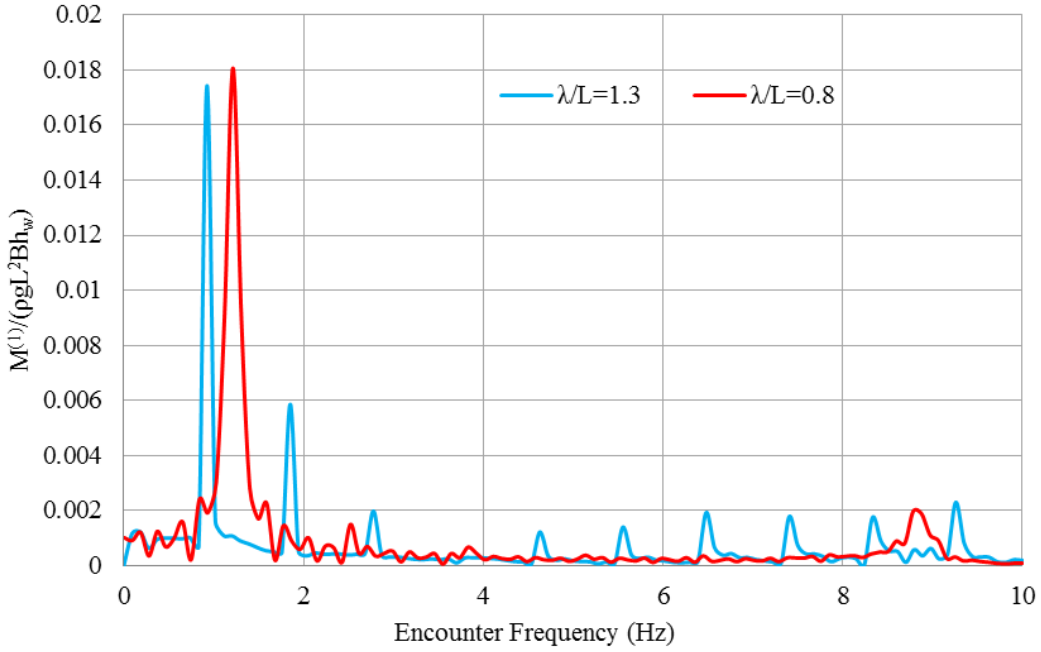

Figure 47: FFT signal for two wave frequencies (H/L=1/50). The non-dimensional first harmonic VBM amplitudes are plotted against the encounter frequency. The first peak is the wave frequency and subsequent ones are the higher harmonics

A comparative study using various established partially non-linear methods and the model tests of S-175 was undertaken by ISSC (2000). The objectives of the systematic validation were to demonstrate the consistency of the non-linear seakeeping methods in the prediction of wave loads, motions and structural responses. The brief summary of the capabilities of the codes is shown in Table 38; fundamentally they are modifications of linear strip theory to account for the non-linear effects when a ship is sailing in moderate or rough seas.

The results from their study are presented in Figure 48, together with the predictions using the present method. The first harmonics calculated by the various 2-D non-linear methods do not show a consistent comparison and displays different trends across the frequencies investigated. Majority of the methods over-predict

the amidships bending moment in the region of λ/L 0.7~1.2. The idea behind comparing the validation studies conducted by ISSC with the coupled method is to get an outlook of the quality of present method when compared with more established methods used in the industry and by researchers. Apart from the inevitable uncertainties in measurements, it can be definitely stated that the coupled analyses is capable of predicting the linear wave loads to a similar degree of accuracy, if not better. Nevertheless, the drawback of the CFD/FE method is the computational time required to carry out these predictions which makes the 2-D linear methods better for the first harmonic wave loads. Another salient feature from the plots is that the 2-D linear prediction which is the cheapest and quickest of all methods is able to give a good estimation of the first harmonic bending moment when compared to other methods of varying complexity. It is, therefore, a very useful tool to evaluate the bending moments amidships and decide the scantlings in the initial design phase of the vessel.

Table 38: Non-linear strip theory methods (ISSC. 2000) used for comparison with the coupled analysis

Methods	Time domain SHIPSTAR	Time domain SRSLAM	Time domain IST	2nd order frequency domain SOST
Non-linear restoring and Froude-Krylov forces	Yes	Yes	Yes	Yes
Non-linear hydrodynamic coefficients	Yes, using a higher order differential equation	Yes, at fixed frequency	No	Yes, by 2nd order expansions
Slamming load by 'momentum' slamming	Yes	Yes	No	Yes
Green water on deck	Yes, by momentum approach	Yes, at static water height	Yes, by momentum approach	No
Steady state forward speed potential	No	No	No	No
Degrees of freedom	Vertical, elastic hull	Vertical, elastic hull	Vertical, elastic hull	Vertical, elastic hull
Publications	(Xia et al. 1998)	(Watanabe & Sawada 1986)	(Fonseca & Soares 1998)	(Jensen & Pedersen 1979)

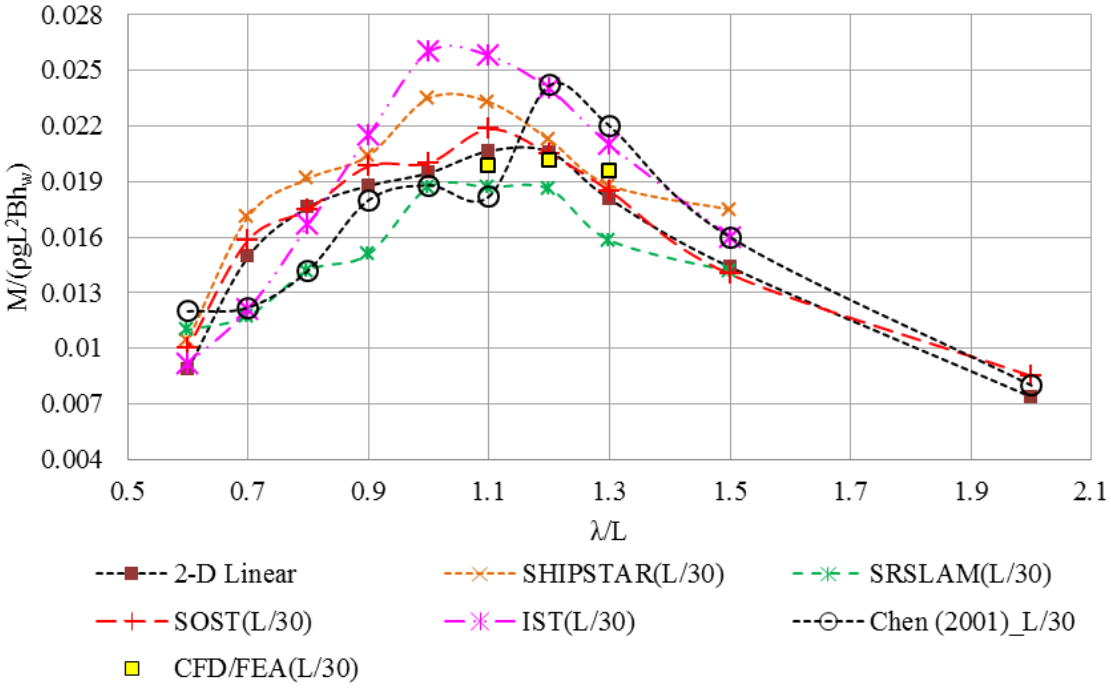

Figure 48: Non-dimensional amplitudes of first harmonic VBM amidships calculated by the coupled method and the weakly nonlinear methods by ISSC (2000). Measurements from Chen (2001) also shown.

The bending moments at other locations, however, display larger dissimilarities when compared with the experiments. Table 39 shows the percentage difference between the predictions and Chen et al. (2001) at various locations for the range of frequencies for H=L/50. The plots are displayed in Figure 49-52. The experimental measurements at all locations were only available for one wave height (L/50) Wu et al. (2003). Comparing the aft and forward locations, the CFD/FEA predictions are better towards the aft of amidships and deteriorates towards the forward; the most inferior of them being the forward most location at about 1/4 L from the forward. At this location, 2-D linear greatly under-predicts the bending moments at all wave frequencies by a maximum of about 80% around the ship-wave matching region. The difference between measurements vary between 24%-82% for the 2-D linear. Except at λ/L=1.5~2.0, the maximum difference in Table 39 at Pt. 5 is about 44%. It is noteworthy that generally the CFD method at all points in shorter wavelength λ/L=0.6~0.9 calculate the linear bending moments accurately. In addition to that, in the region of λ/L=1.0~1.3 the differences are below 25%, omitting a couple of them towards the forward of the vessel.

Measurements using the self-propelled flexible model are more alike than the towed model. The results from the towed model at the forward location are lower than the coupled predictions and the two experiments. Fonseca & Guedes Soares (2004b) reasoned that the vertical bending moment at the forward station is strongly dependent on the longitudinal inertia about the pitch axis, and that it was higher in the experimental model. However, using the proper inertia Fonseca & Soares (2005) performed numerical calculations using the non-linear time-domain code IST Fonseca & Soares (1998) and found that at the forward station the first harmonic of bending moments is well represented in longer wave lengths(λ/L=1.2~2.0) but largely overestimate as they get shorter. The numerical codes in ISSC. (2000) validation also very much behaved liked the present CFD/FEA coupled method.

Table 39: Relative percentage difference of VBM amidships between the experiments and present predictions at all locations and wave frequencies investigated for H=L/50. The values in brackets are for H=L/30.

Location (from A.P)	**λ/L (H/L=1/50)**									
	0.6	**0.7**	**0.8**	**0.9**	**1.0**	**1.1**	**1.2**	**1.3**	**1.5**	**2.0**
Pt.1 (0.95m)	8.2%	13%	4.2%	15.2	3.7%	11.2%	18.9%	16.5%	35.8%	53.8%
Pt.2 (1.35m)	14.1%	17.3%	8.8%	22%	7.8%	9.7%	18.6%	15.8%	29.89%	44.65%
Pt.3-amidships (1.85m)	40.8%	36.6%	25.14%	35.3%	8.1%	0.5% (9%)	11.4% (16%)	11.8% (10%)	23.0%	34.4%
Pt.4 (2.25 m)	11.2%	12.5%	4.1%	11.4%	7.3%	9.6%	24.5%	25%	39%	43%
Pt.5 (2.65 m)	12.7%	8.5%	13.1%	10%	26%	26.4%	40%	43.5%	61%	66%

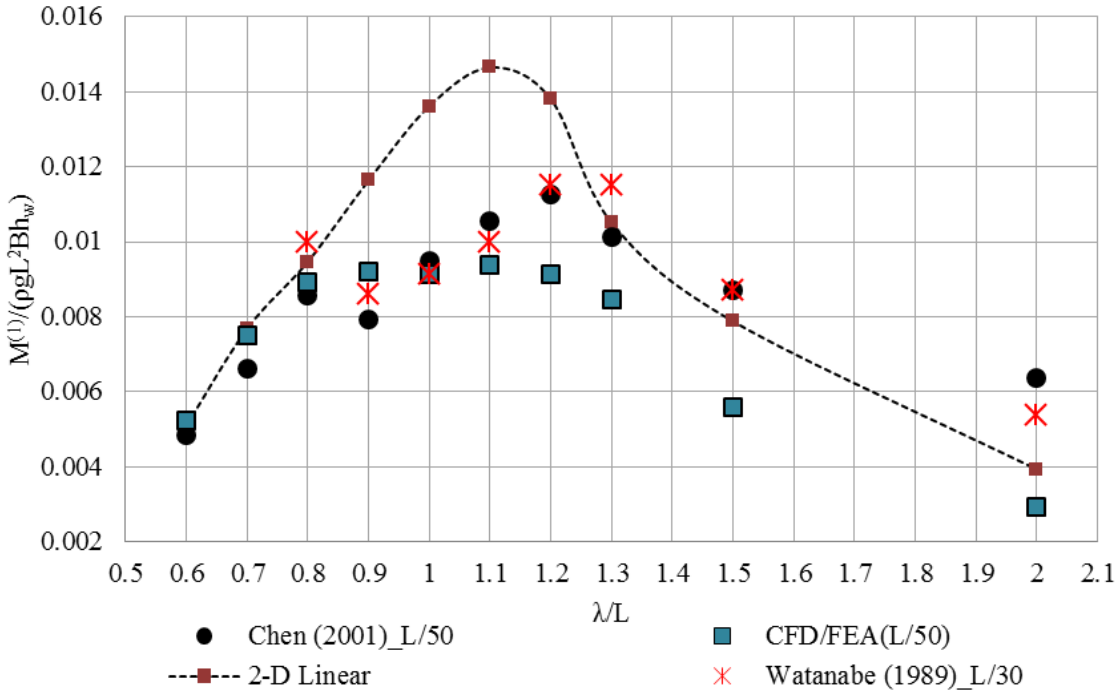

. Figure 49: Non-dimensional amplitude of first harmonic VBM at Pt.1 (0.95 m from aft Lpp) calculated using coupling method and numerical and experimental measurements.

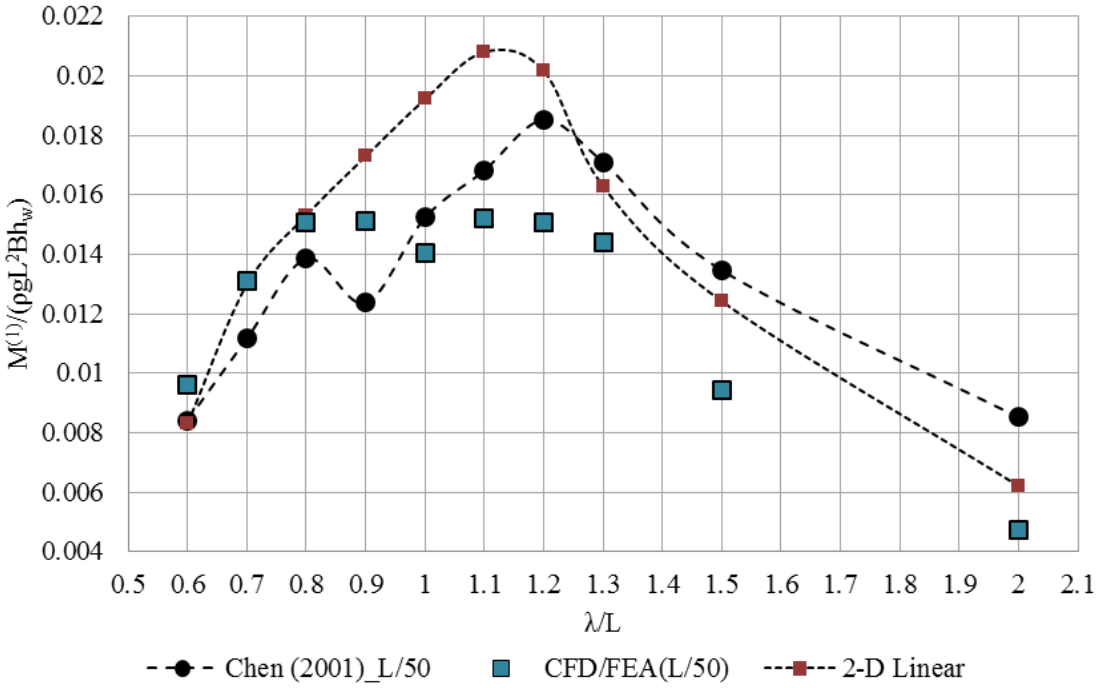

Figure 50: Non-dimensional amplitude of first harmonic VBM at Pt.2 (1.35.m from aft Lpp) calculated using coupling method and numerical and experimental measurements.

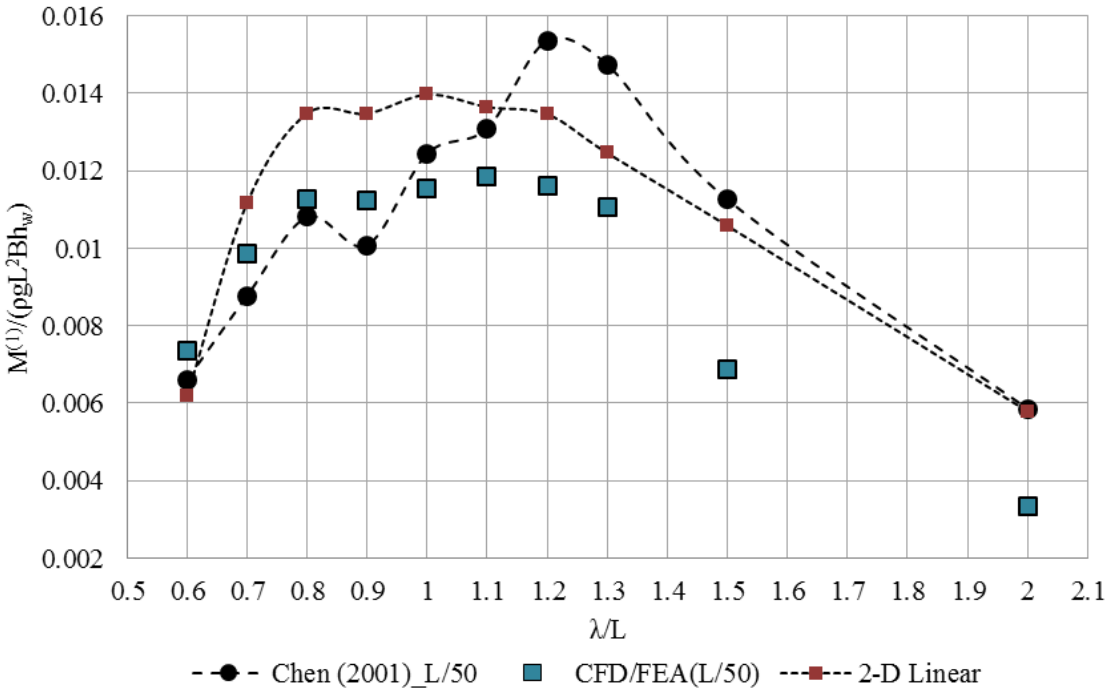

Figure 51: Non-dimensional amplitude of first harmonic VBM at Pt.4 (2.25 m from aft Lpp) calculated using coupling method and numerical and experimental measurements.

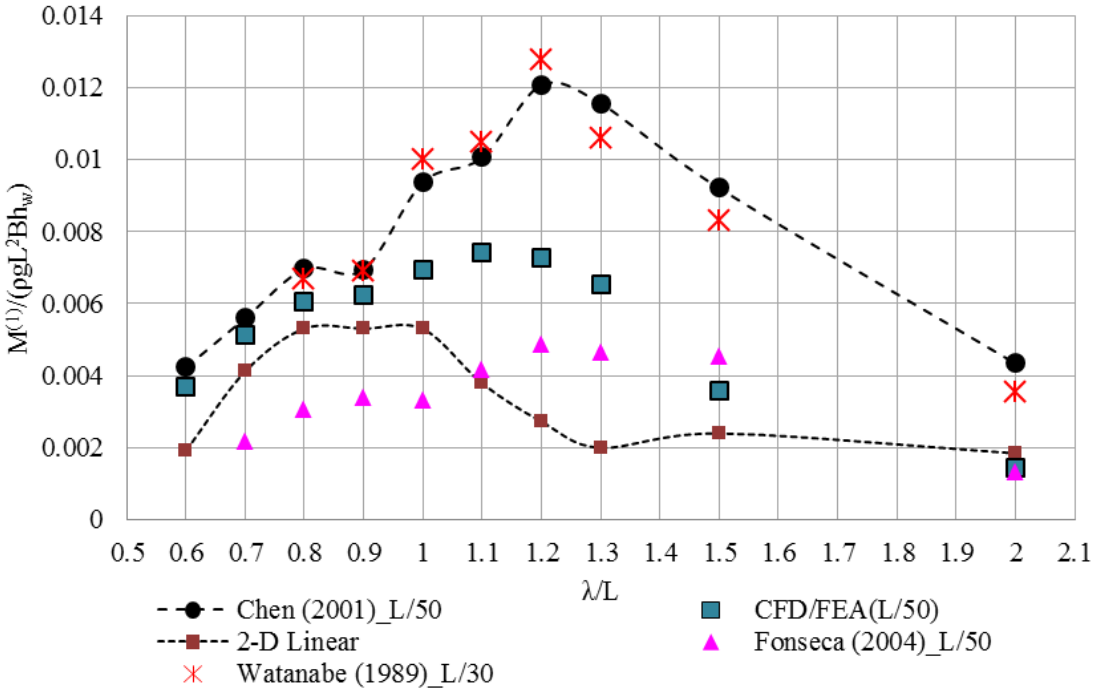

Figure 52: Non-dimensional amplitude of first harmonic VBM at Pt.5 (2.65 m from aft Lpp) calculated using coupling method and numerical and experimental measurements.

Wu & Hermundstad (2002) used nonlinear time domain code and presented results on S-175. The results from their paper are presented in Figure 53 & 54. The

differences are smaller at the bow location than the aft location. At the aft location their predictions are in good agreement with the 2-D linear. In summary we can say that at the fore and aft locations the two self-propelled flexible models are able to exactly reproduce the bending moments measured. On the other hand, the loads estimated using various numerical methods show deviations from the measurements. Additionally, the measurements using a towed model are nearly three times lower than the self-propelled. Hence, one possible reason for the disparity could be due to the treatment of boundary condition in the model. Presently, this is not possible to check in the CFD/FEA calculations as it would require a massive computational resource.

Aside the uncertainties, the first harmonic of bending moment calculated using the present method compares well with the measurements and other benchmark numerical calculations, and on an average the difference is about 25-30%, omitting a few points in the test matrix. Furthermore, in the resonant region the predictions on an average present even smaller percentage error of the order of about 15-20%.

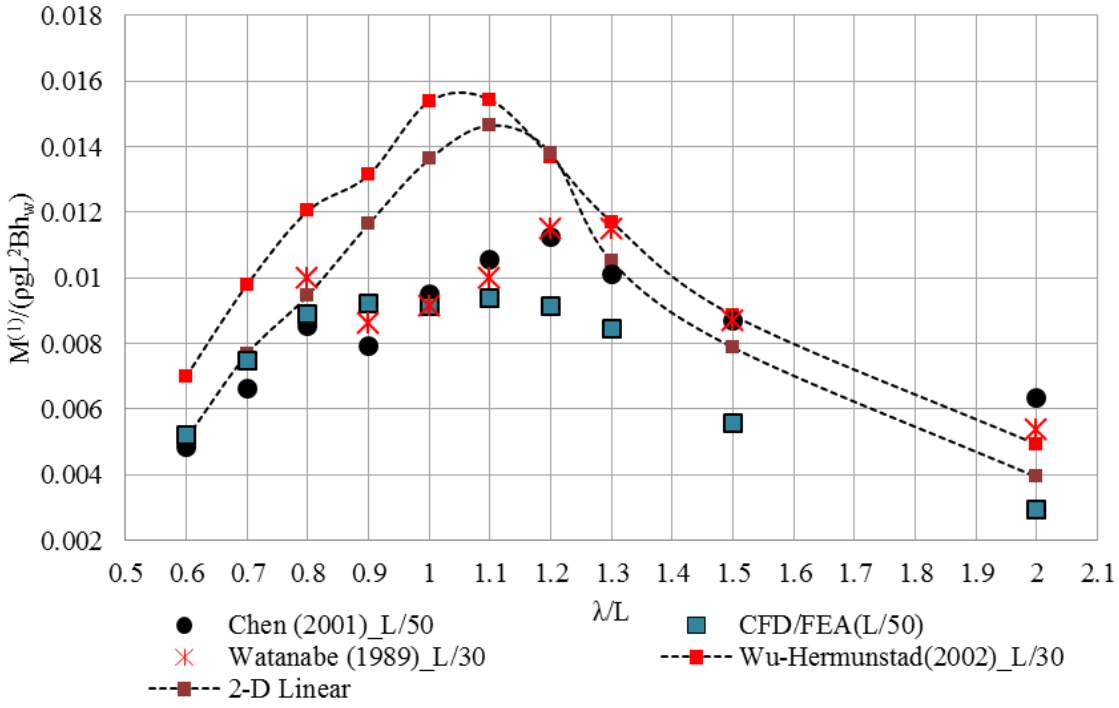

Figure 53: Non-dimensional amplitude of first harmonic VBM at Pt.1 (0.95 m from aft Lpp) calculated using coupling method and Wu & Hermunstad (2002). Experimental measurements of Chen (2001) & Watanabe (1989) also plotted for comparison

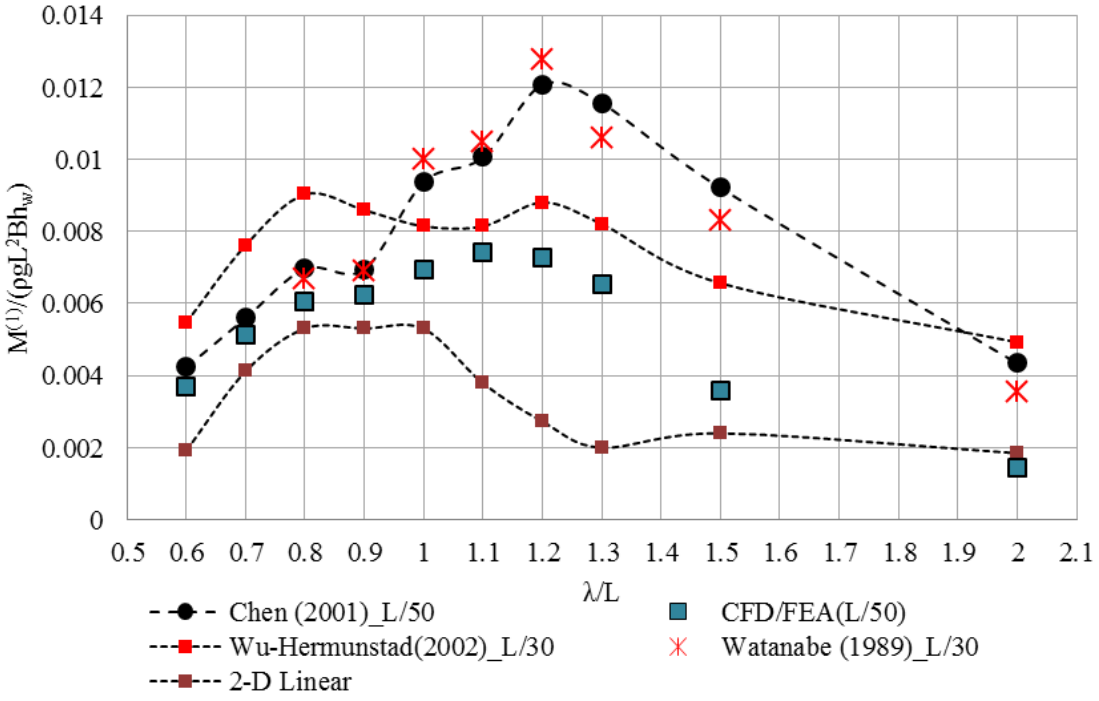

Figure 54: Non-dimensional amplitude of first harmonic VBM at Pt.5 (2.65 m from aft Lpp) calculated using coupling method and Wu & Hermunstad (2002). Experimental measurements of Chen (2001) & Watanabe (1989) also plotted for comparison.

6.3.5 Nonlinear effects in wave load of S-175 in head waves

The nonlinearities in the wave loads are expressed in the form of higher order harmonics of wave bending moments, 2-node flexible mode, and the asymmetry in hogging and sagging bending moment. The higher order components are essentially the higher harmonics of the wave encounter frequency. The second and third harmonics in the vertical bending moment time histories measured were found to be a significant percentage of the first harmonics.

The 2nd harmonic of bending moment amidships calculated using CFD/FEA and measured from experiments are shown in Figure 55. The numerical predictions at amidships have maximum values that vary between 15% and 30% of the first-harmonic amplitudes, whereas in the experiments by Chen et al. (2001) it varies between 2%-10% of the first harmonic. The numerical predictions estimate higher second harmonics (λ/L=1~1.5) compared to Chen et al. (2001), but produce good agreement with the measurements by Watanabe et al. (1989). The nonlinearity in the wave loads becomes weaker as the wave gets shorter, further, displaying good congruency with the measurements. In steep waves, the above two experiments

record large differences, considering the fact that a flexible self-propelled models is used in both. With increase in wave height the predicted second harmonics get stronger in the numerical predictions to about 11-30% of the first harmonic in the range of λ/L=1.1~1.3.

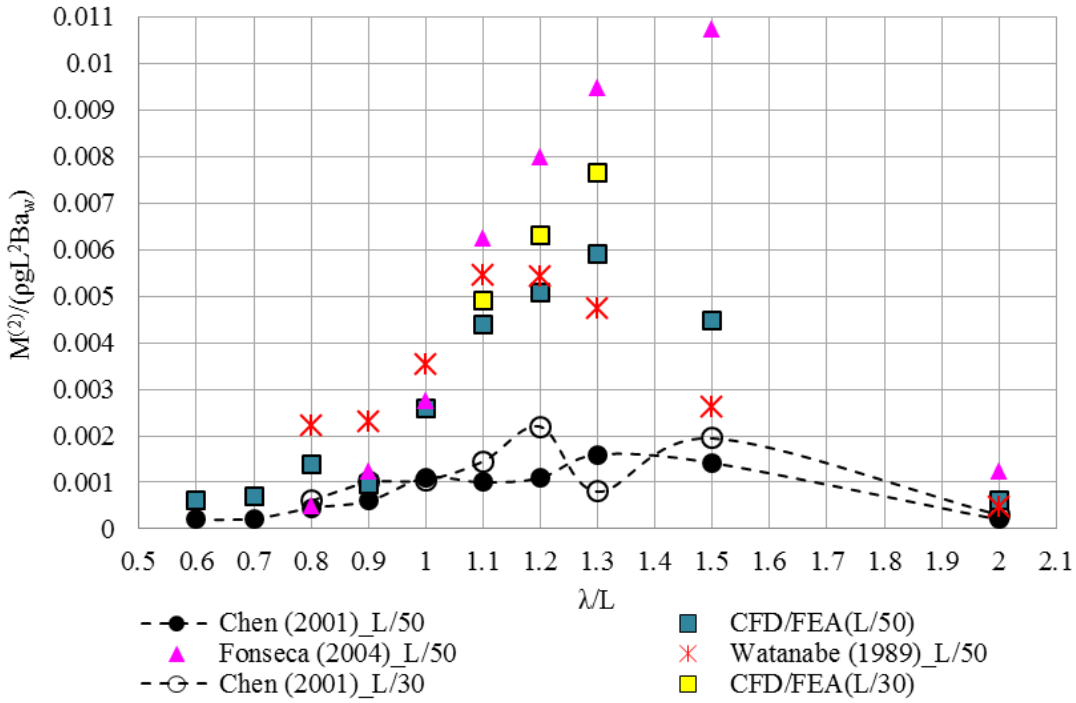

Figure 55: Non-dimensional amplitudes of second harmonic component of VBM amidships.

The influence of nonlinearities induced due to green water effects and bow immersion reflects in the second harmonics of bending moment towards the forward of the vessel, shown in Figure 56. This location (pt.5) is at 1/4 L_{pp} from the F.P of the model. The maximum values at this location attain about 50-60% of the first harmonics in the region of λ/L =1.0~1.5. The comparison between Fonseca & Guedes Soares (2004b) as well as Watanabe et al. (1989) and the present method is excellent at the forward location, but not at amidships.

The impact pressure at the FP on the deck is shown in Figure 58 & 59 for the two wave heights (1.1 ≤ λ/L ≤ 1.3). Only three frequencies are compared since for these conditions severe deck water and flare impact was observed in the simulations. Consequently, they produce strong nonlinear components in the wave loads. The trend of the peak impact pressure follows the behaviour we observe in the nonlinear load components. The second harmonic attains a maximum value at λ/L=1.3 for both wave heights and the impact pressures are larger at this condition. With in-

crease in wave steepness, the impact pressure nearly doubles at all three wavelengths presented. Clearly, the higher harmonics in the bending moment arise from the nonlinear motions and conditions experienced by the vessel. In Figure 57, the magnitude varies between 15-20% of the first harmonics at 1/4 L_{pp} from the aft and is nearly half when compared to amidships and the forward location. It is expected that the corresponding nonlinearities will be smaller as most water would have drained off the deck.

An advantage of the CFD simulations is that it can provide insights into the flow field and other scalar quantities in the solution domain. The snapshots of motion of the model (λ/L=1.3) for the two wave steepnesses investigated are shown in Figure 60; steeper wave plots on the right-side. The time instances in Figure 60 demonstrate the vessel emerging in and out of the water shipping large quantities of water and producing violent free surface flows. Not only does the green water impact on deck increase for the larger wave height but also larger quantity of water remain on the deck when the vessel is at an instance where it is starting to pitch by the bow. The higher harmonics of the wave load directly relate to the amount of severity in the wave condition.

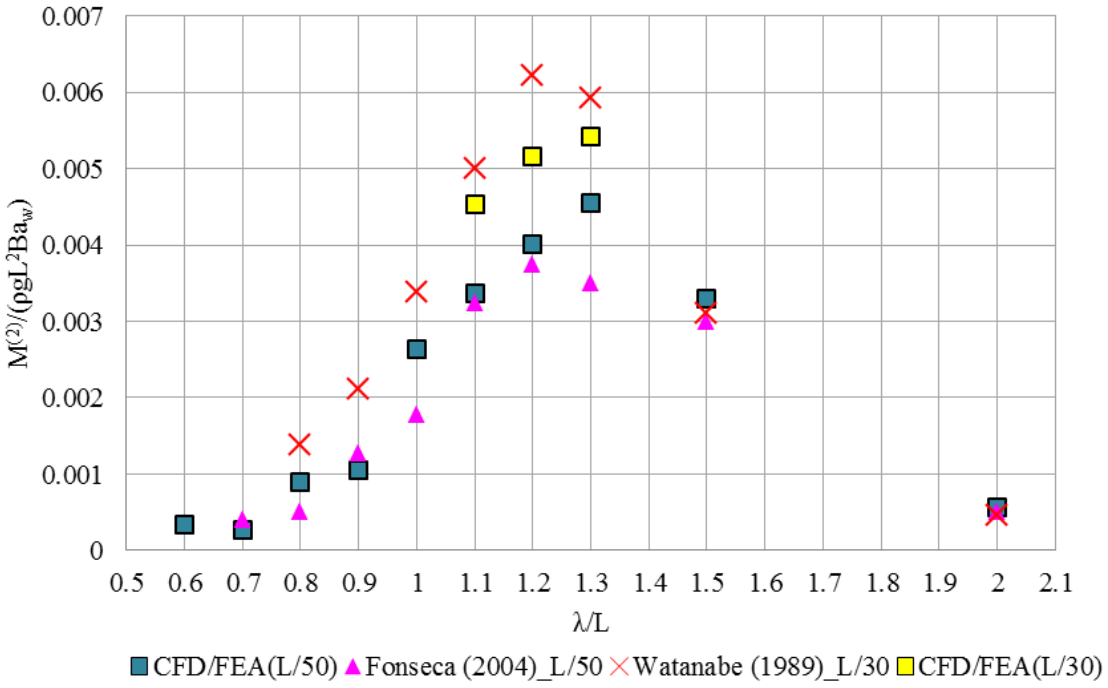

Figure 56: Non-dimensional amplitudes of second harmonic component at Pt.5 (2.65 m from aft Lpp).

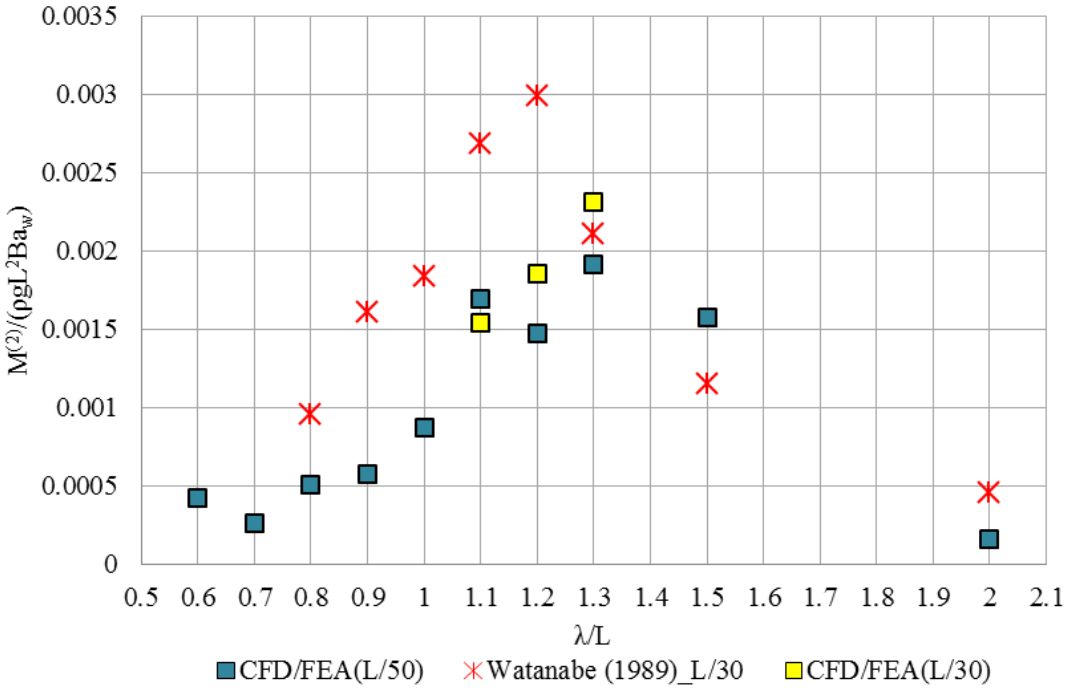

Figure 57: Non-dimensional amplitudes of second harmonic component at Pt.1 (0.95 m from aft Lpp).

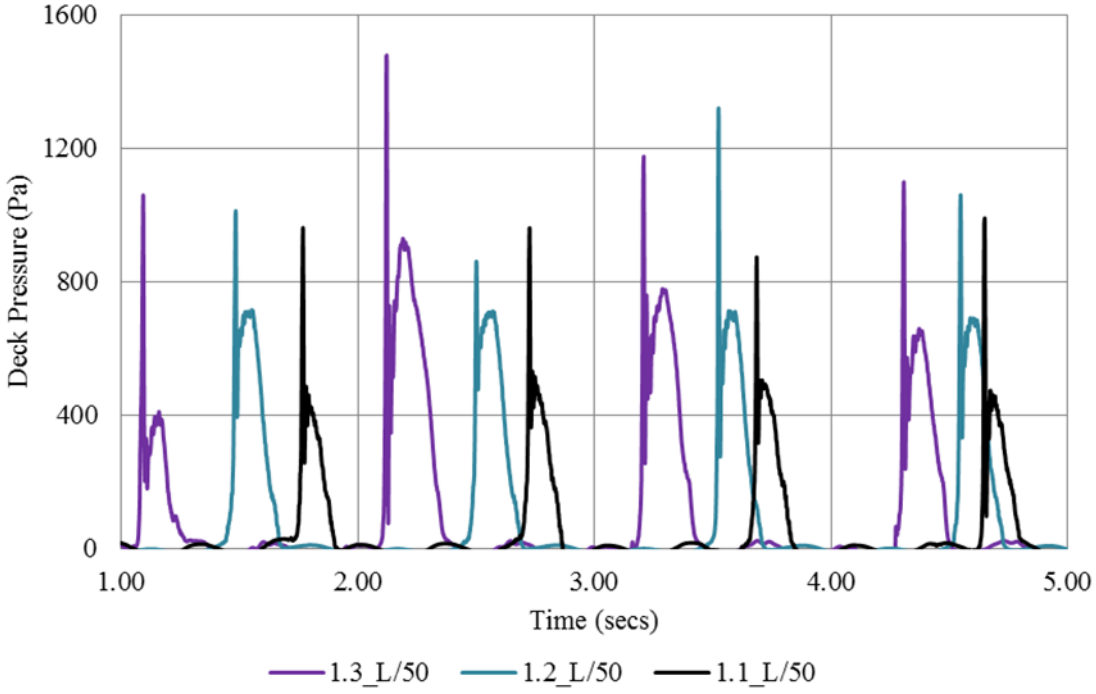

Figure 58: Deck impact pressure at forward perpendicular for H/L=1/50

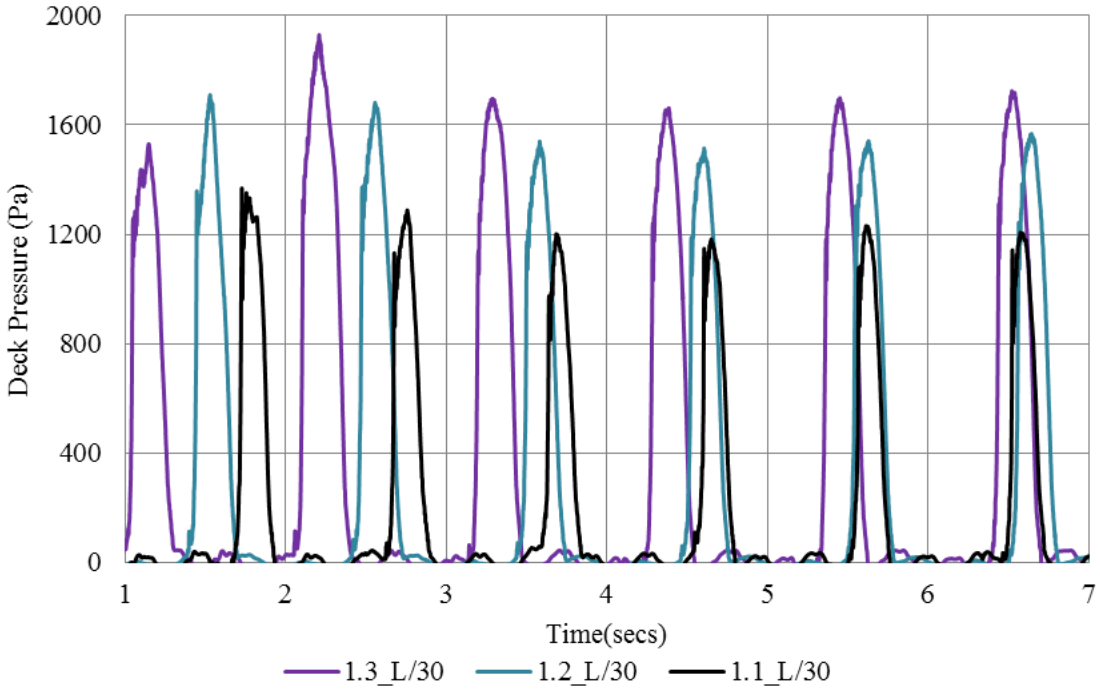

Figure 59: Deck impact pressure at forward perpendicular for H/L=1/30

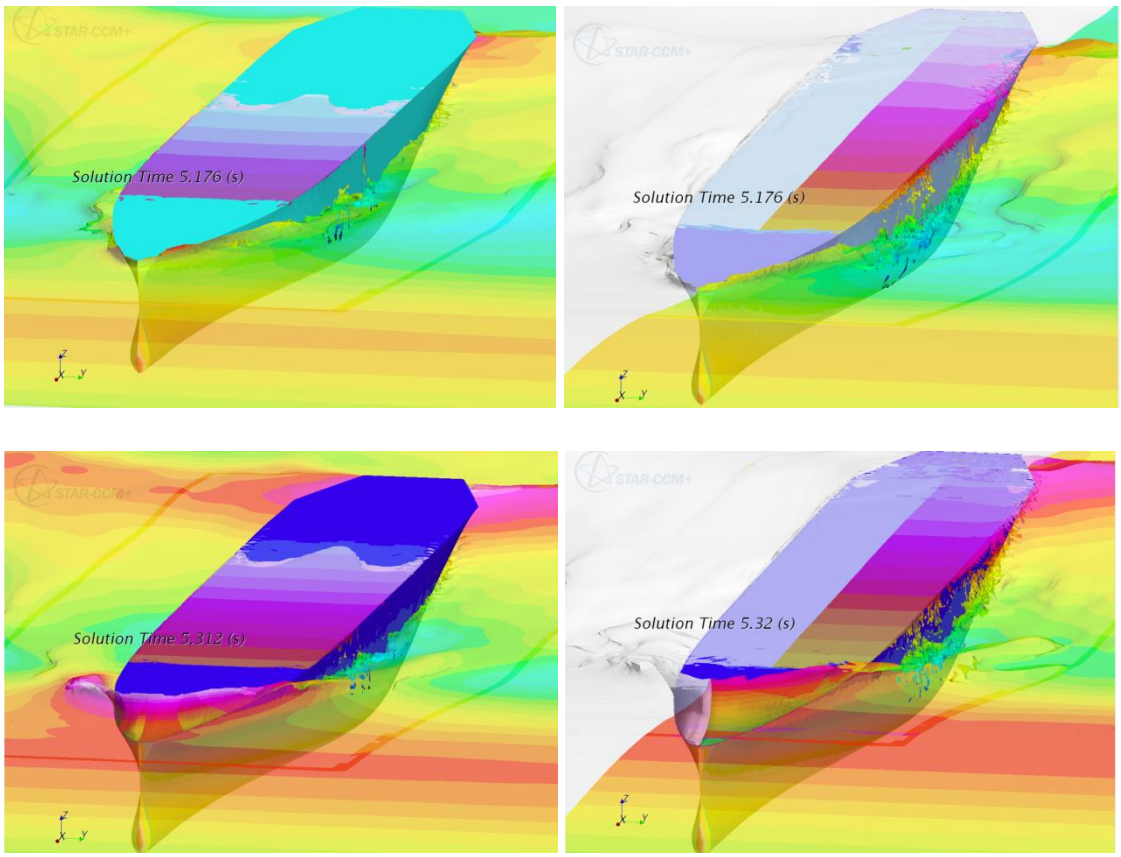

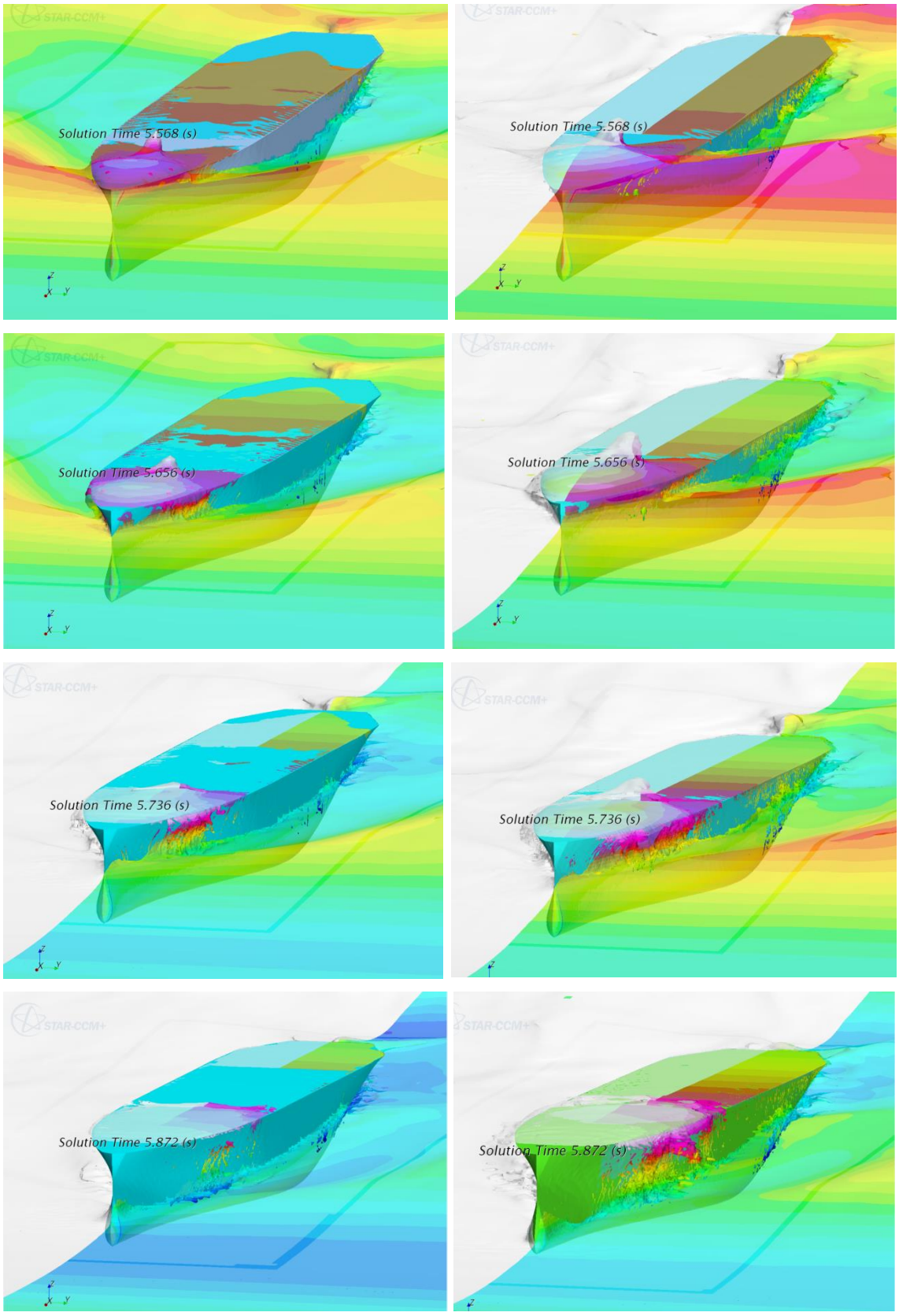

Figure 60: Time instances of the coupled CFD simulations showing the bow emerging in and out of water surface. The left- side is for H/L=1/50 and right-side for H/L=1/30

The second harmonics calculated amidships agree really well with the measurements on a steeper wave of Watanabe et al. (1989), but are larger than Chen et al. (2001) mainly around the ship-wave matching region. The second harmonics recorded for the steeper wave (H/L=1/30) by Chen et al. (2001) did not vary much compared to the longer waves (H/L= 1/50), although measurements by Watanabe et al. (1989) exhibit stronger nonlinearities. Fonseca & Guedes Soares (2004b) recorded sizeable second harmonic component for H=L/50 in comparison to the other two experiments and attributed it to the differences in experimental conditions. Compared to a self-propelled model that is free to surge, the towed model, restrained in surge motion is subjected to higher accelerations in the surge directions resulting in higher magnitudes of harmonic components.

It is obvious from the plots (Figure 55-57) that the uncertainties in measurements are larger in the case of the nonlinear components than the first harmonics. The measurements show significant scatter and it makes it difficult to comment on the accuracy of the CFD/FEA method. The absolute magnitude of second harmonics is nearly about 3-5 times the measurements in this region, however, the order of magnitude of the second harmonics are very similar. Furthermore, the numerical predictions are consistent with Watanabe's experimental measurements at all three different locations. The conclusion from the predictions using nonlinear time-domain codes was that care must be taken when adopting them for design load calculations, particularly for ships with unconventional hull forms where the nonlinearities can attain significant magnitude (ISSC 2000). The present predictions are better when compared to the nonlinear strip theory procedures reinforcing the fact that CFD is capable of capturing the nonlinearities to a good degree of accuracy.

The third harmonics of vertical bending moment at amidships and fore quarter are shown in Figure 61 & 62. Once again the CFD/FEA tend to overestimate the nonlinear effects by about twice in the region of $\lambda/L=1.1\sim1.3$, nevertheless the comparison is better than the second harmonic predictions. In general, a good agreement is achieved in the case of the third harmonics. The numerical predictions reveal that the third harmonics are of the order of 5-10% of the first harmonics. It is noteworthy that the two-way coupled method is able to capture even the weakest nonlinear effects in the wave loads to acceptable level of accuracy. This would mean that, in cases where the nonlinear effects could be stronger, the coupled method could be used to make estimations with good engineering accuracy.

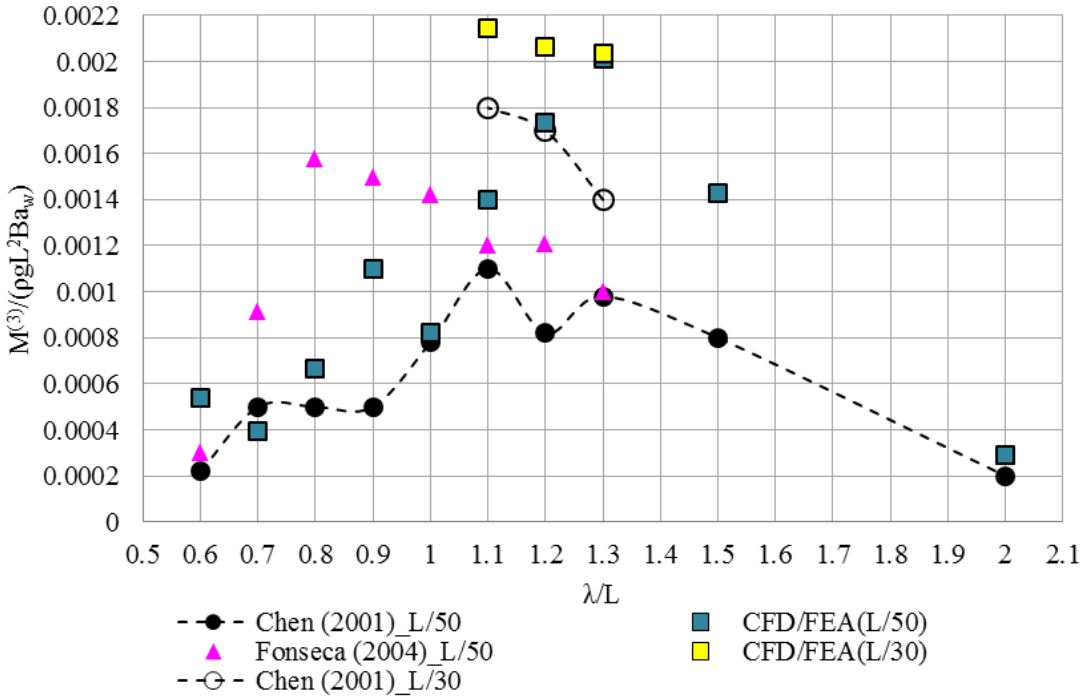

Figure 61: Non-dimensional amplitudes of the third harmonics in VBM amidships.

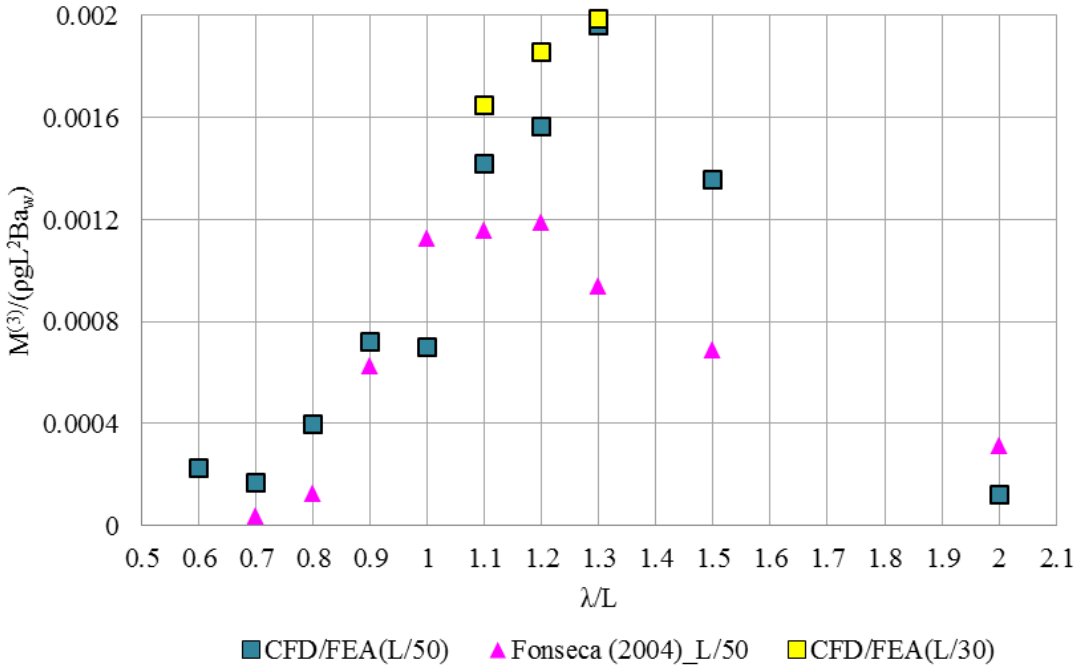

Figure 62: Non-dimensional amplitudes of the third harmonics in VBM at Pt.5 (2.65 m from the aft perpendicular)

The 2-node flexible mode of the vertical bending moment amidships is shown in Figure 63. In the experimental measurements, the contribution of the 2-node component to the total vertical bending moment is relatively low, of about 5-15 % which is shown in Figure 64. The peak occurs in the region of λ/L=1.0~1.5. The numerical predictions agree well at some wave frequencies, although there is substantial deviation at certain frequencies. The order of magnitude of the 2-node component is similar to the experiments, except at λ/L=1.0 and 1.2. For the low wave height (H/L=1/50), in long waves (λ/L=2.0 and 1.5), the numerical predictions severely under-predict the 2-node flexible component by about 3 times the absolute magnitude measured in the experiments. In this region, the first harmonic of bending moment also deviates from the measured. The predictions show an anomaly at λ/L=1.0 and 1.2 and the response is larger by nearly 6 times the measurements. The time history of non-dimensionalised vertical bending moment for a few wave cycles in the region of λ/L =1.0~1.3 is shown in Figure 65. The presence of higher frequency components is clearly noticeable in the time traces and the magnitude is considerably higher for λ/L=1.0 and 1.2 when compared to the other wavelengths shown in the figure. The predictions for H/L=1.30 is good when compared to experimental measurements for the three wave lengths investigated.

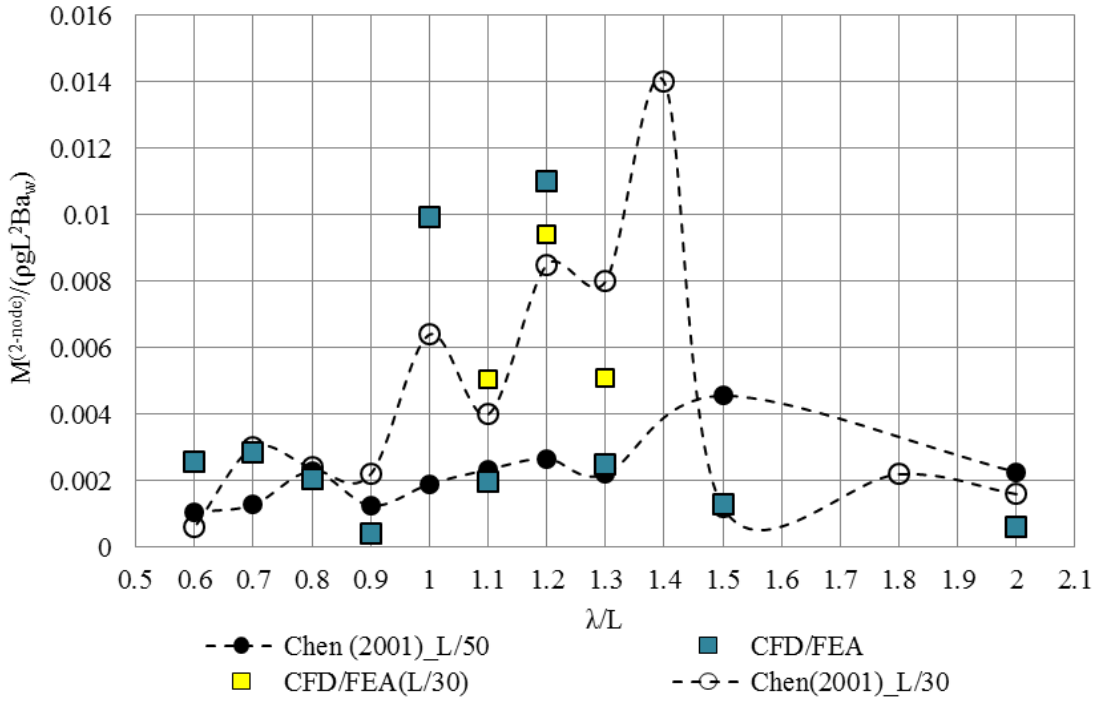

Figure 63: Non-dimensional amplitudes of the 2-node in VBM amidships

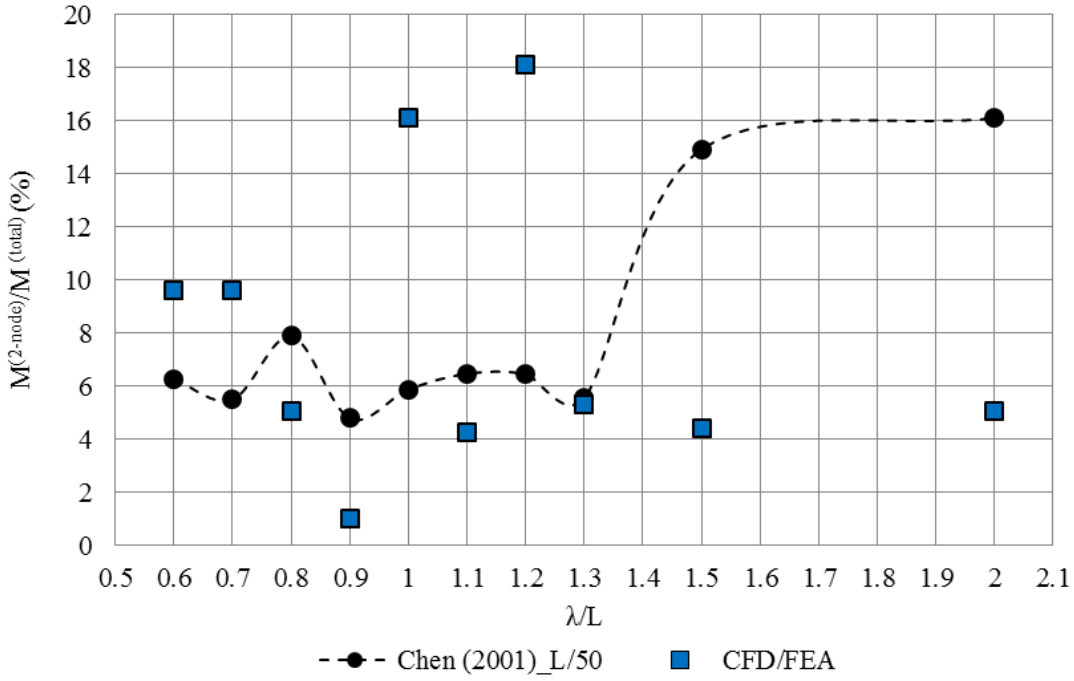

Figure 64: Percentage contribution of 2-node to total vertical bending moment in experiments (Chen et al. 2001)

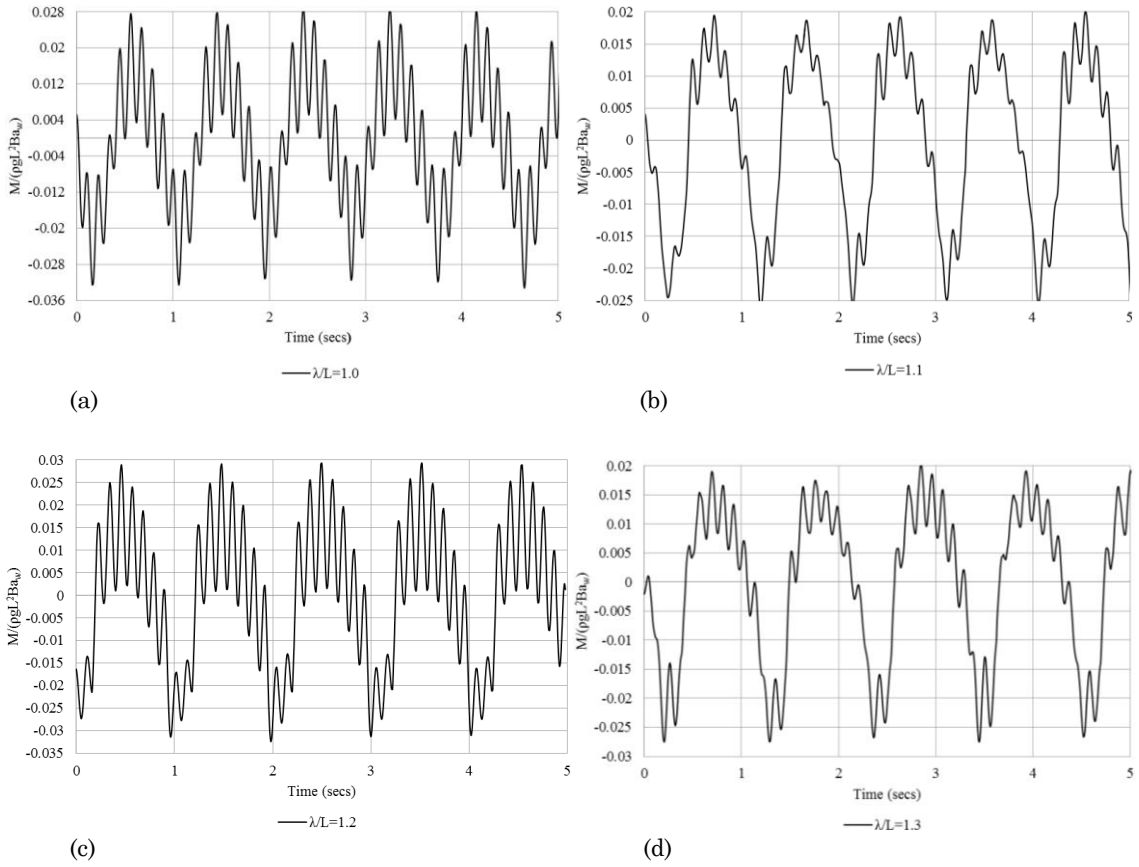

(a) (b) (c) (d)

Figure 65: Time histories of total VBM amidships from coupled simulations for four wave frequencies (H/L=1/50) (a) λ/L=1.0 (b) λ/L=1.1 (c) λ/L=1.2 (d) λ/L=1.3

Wang et al. (2015) showed that the springing behaviour of a bulk carrier is influenced by the forward speed. The study using a 3-D hydroelastic frequency domain code verified that the high frequency component is influenced by high speeds. This is even noticeable in the present investigations where the high frequency component was practically non-existent in zero speed case. Figure 66 shows the time history of total VBM for one regular wave length (λ/L=1.3) with no forward speed and the harmonic analysis is shown in Figure 67. We can see that the nonlinear contributions in the time history are negligible and it is mainly dominated by the first harmonic of the wave frequency. Apart from the effect of forward speed, the shipping of water also contributes to the high frequency component. No water was shipped on the deck in the zero speed case resulting in very small nonlinear contributions to the wave loads.

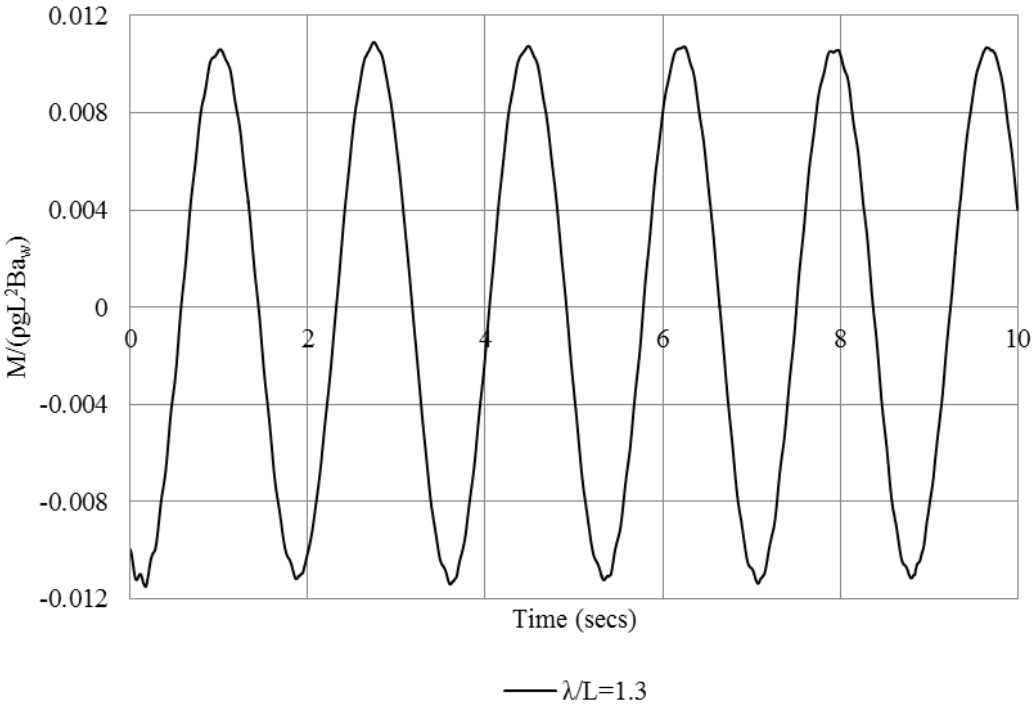

Figure 66: Time history of total VBM from coupled simulation for λ/L=1.3 with no forward velocity

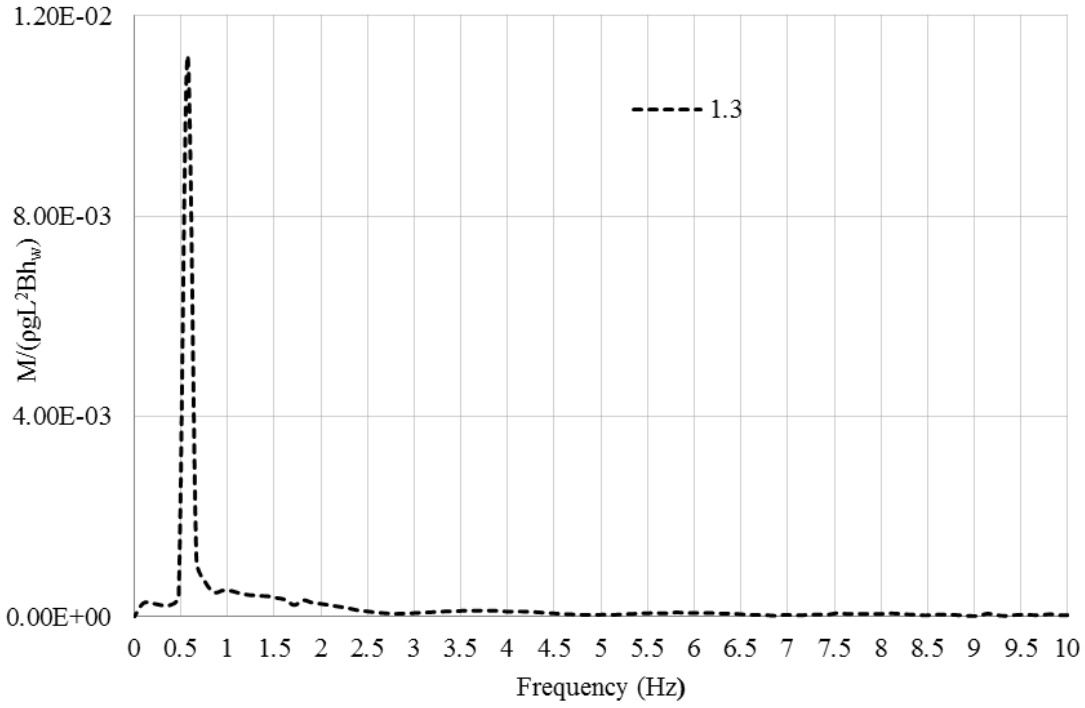

Figure 67: FFT of the VBM amidships for λ/L=1.3 with no forward velocity

Nonlinear springing component has been observed in hydroelastic model tests when the encounter frequency can be expressed as:

$f_e = f / N$, where f_e is the wave encounter frequency, f is the 2-node structural wet frequency and N is an integer from 2 to n. The order N indicates the nonlinear order of springing i.e. second-order, third-order etc. A similar phenomenon seems to be occurring for the containership in waves, and the reason for large high frequency component at 2 discrete frequencies becomes obvious by observing the FFT signal of the bending moments amidships (Figure 68) and Table 40. The smaller wave height is used to explain the observations due to the same number of test cases simulated as the experiments. Please note that the discussions are pertaining to the present numerical model with no structural damping, however the findings might prove to be important when carrying out predictions for large containerships whose 2-node frequency response may be lower than the present ship.

Table 40 shows the wave encounter frequency and the frequency at which the 2-node responses are located in the FFT signal. The information is used to discuss certain chief aspects of the high frequency response. The harmonic order is calculated as per equation $N = f / f_e$.

1. At λ/L =1.2 and 1.0 the harmonic order N is a perfect integer corresponding to the 9th and 8th order harmonic component, respectively. Even though the wet frequency is not estimated for the numerical model, Table 40 reveals that it is apparently 8.88 Hz which appears at several wave conditions. The 2-node frequency of the model shown in Table 24 is also close to this value. When the encounter wave frequency is a higher-order of the wet natural frequency (f/N), nonlinear resonant/springing condition occurs resulting in large amplitude of high frequency response (Miyake et al. 2009). Assuming no structural damping in numerical model, the magnitude of the high frequency response is about 40% of the first harmonic of the bending moment; alarming for a relatively rigid ship as S-175.

2. In shorter waves (0.6~0.8), the high frequency component coincides with the apparent wet natural frequency (8.88 Hz) producing considerable magnitudes. Even though, the order N is not a perfect higher-order of the wet natural frequency the response coinciding with the wet natural frequency creates a resonant condition leading to relatively strong responses.

3. In contrast to that, at λ/L=1.1 and 1.3, the 2-node responses are of the same magnitude as the shorter wavelengths but this should not be confused as a resonant behaviour. Although, it is termed as 2-node following the same conventions as Chen et al. (2001), it is distinctly a higher harmonic effect, namely the ninth and tenth harmonic, respectively (see Table 40). The term 'higher order harmonic effect' means that it is a higher order of the wave encounter frequency which is not coinciding with the 2-node wet frequency of the model (8.88 Hz). The responses occur at a higher frequency than the wet frequency, see Figure 68, but producing strong nonlinear behaviour. In fact, at λ/L=1.3, the sixth to tenth higher harmonics are nearly of a constant value. The nonlinear behaviour in this case is caused by the nonlinearities due to the green water and flare impact only and not due to nonlinear springing. The evidence is revealed in the time instances shown in Figure 60.

4. The eleventh-order of the wet natural frequency (8.88 Hz) is equal to 0.88 Hz and the corresponding λ/L is equal to 1.4. According to the explanation in point 1, the model should be experiencing a nonlinear resonant behaviour at this wave frequency. Chen et al. (2001) had carried out model tests using four wave heights, and except for H/L=1/50, measurements were done at λ/L=1.4. The resonant behaviour was undoubtedly occurring at this frequency which strengthens with increase in

wave height. As a matter of fact, for ratios of λ/L (1.0, 1.2, and 1.4) equating to higher-order (8^{th}, 9^{th} and 10^{th}) of the wet natural frequency the nonlinear resonant behaviour occurs resulting in clear-cut peaks in the graph (Chen et al. 2001).

5. To investigate the occurrence of nonlinear higher order springing at a couple of other wave frequencies, two simulations were performed corresponding to the 7^{th} and 10^{th} order of the 2-node wet frequency of the model (λ/L=1.4 & 0.833). In Table 39 these two frequencies are distinguished using bold blue colour. It must be noted that at λ/L=0.833, corresponding to the 7^{th} harmonic order, no green water on deck was observed in the CFD simulations. The FFT of VBM amidships is shown in Figure 69 along with the λ/L=1.2 & 1.0. Even though the magnitude of 2-node is not high as the wave lengths investigated originally, they still exhibit strong 2-node responses. The magnitude of 2-node response for these two frequencies is nearly 2.5-3.0 times higher than responses at other wave frequencies in Table 40. The water shipped on the deck also has a dominant effect on the nonlinear higher order harmonic springing, and hence, the responses are smaller than λ/L=1.2 & 1.0. Again the 2-node response occurs at around 8.88 Hz for the new wave frequencies investigated.

6. The peaks in 2-node measured in experiments also occur at λ/L=1.5, 1.3 and 1.1 which are as discussed in point 3 due to the nonlinear behaviour translating to comparatively strong higher harmonic components of the wave encounter frequency.

From the above, we understand that when a flexible model with forward speed encounters regular waves, the higher-order springing and the higher-order harmonics of the wave encounter frequency can become extremely important. Moreover, these two are separate nonlinear behaviour, and must be carefully considered when planning experiments or even in numerical calculations using other nonlinear codes to calculate wave loads. It is paramount that while conducting measurements or numerical calculations one should include the discrete frequencies where the occurrence of a nonlinear resonant behaviour is suspected. According to the CFD predictions on a numerical model without structural damping for a comparatively rigid ship such as the S-175, this effect is nearly of the same order of the first harmonic bending moment. For a modern flexible containership these nonlinear reso-

nant effects could become extremely important since their contribution to the wave loads could be large.

Table 40: Relationship between the wave encounter frequency and the 2-node component calculated in the VBM amidships using FFT and their respective higher-order.

λ/L	Encounter frequency (Hz)	2-Node component (Hz)	Harmonic Order 'N'
0.6	1.6067	8.88	5.5
0.7	1.4356	8.88	6.2
0.8	1.3037	8.88	6.8
0.833	**1.266**	**8.88**	**7.0**
0.9	1.1985	8.42	7.0
1.0	1.1125	8.88	8.0
1.1	1.0405	9.33	8.9
1.2	0.9794	8.88	9.0
1.3	0.9267	9.25	10.0
1.4	**0.888**	**8.88**	**10.0**
1.5	0.8403	9.25	11
2.0	0.6926	8.91	12.8

The two-way coupled simulations have demonstrated the capability of capturing the above nonlinear behaviour to a good degree of accuracy. It has also aided in revealing the effect of higher-order behaviour, greater than second-order or third-order which would otherwise not be possible with weakly nonlinear potential flow codes. The absence of structural damping in the FE model could be leading to the erroneous magnitude of nonlinear high frequency component at λ/L =1.0 and 1.2. The higher order harmonics in the same wave frequency region were also noted to be larger than the experimental measurements. Therefore, at this point it is important to investigate the effect of structural damping on the higher order harmonics and the springing contribution to the vertical bending moment of the vessel.

The next section deal with the effect of structural damping on the linear and non-linear wave loads.

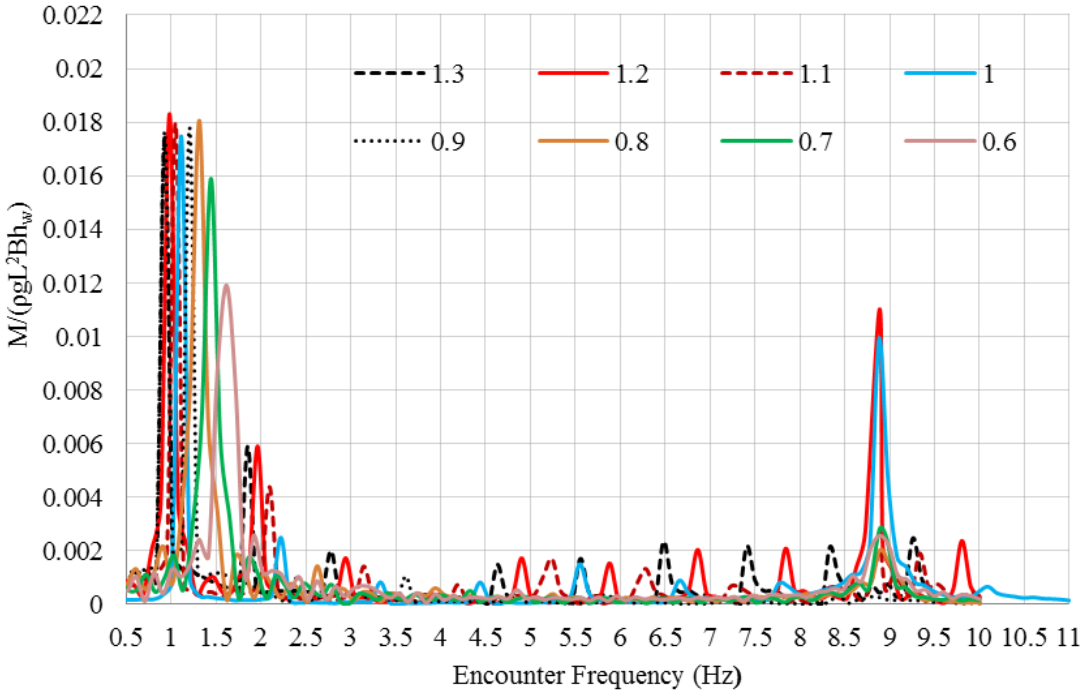

Figure 68: FFT signals of the VBM amidships at certain frequencies emphasizing on the 2-node high frequency component.

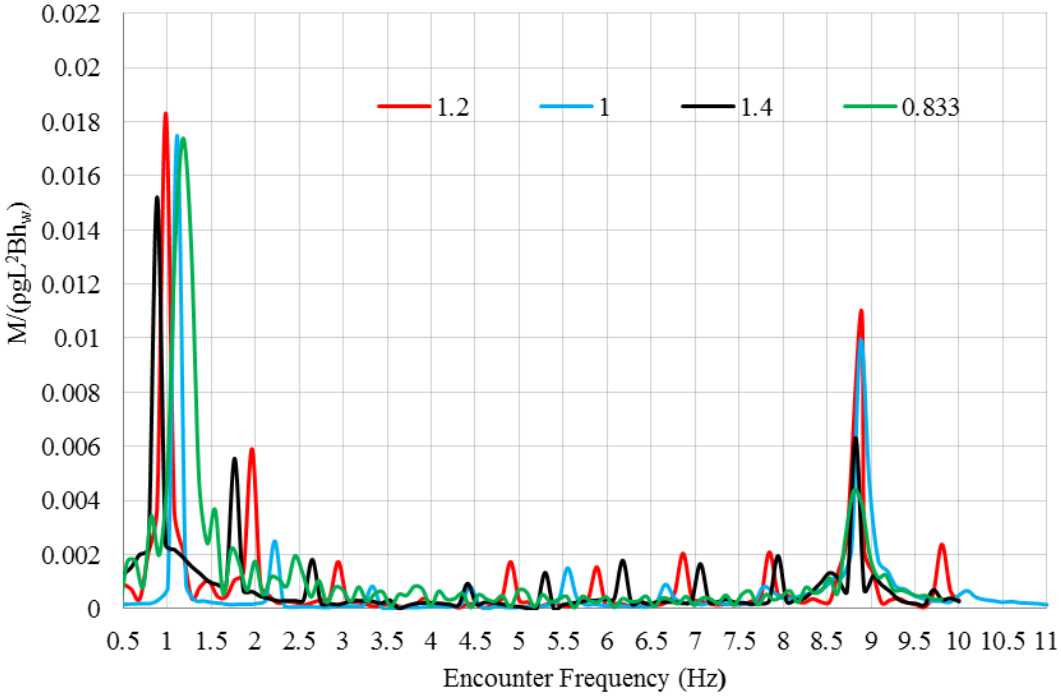

Figure 69: FFT signals of the VBM amidships at wave frequencies exhibiting nonlinear higher order.

6.3.6 Effect of structural damping on the wave loads

Wu et al. (2003) estimated the 2-node damping ratio of S-175 model in still water from the time history of impulse-exciting responses amidships to be 0.067. This damping ratio is a combination of hydrodynamic and structural damping. In this case it is found to be approximately 1% of critical damping factor. Rayleigh's damping is used to assign structural damping to the beam model using only the mass proportional damping ratio α. The damping provided is approximately 1% of the critical damping. This value is calculated from the case studies of ships in Bishop & Price (1979) which gives an approximate structural damping vs hydrodynamic damping comparison.

The wave loads are recalculated using structural damping for λ/L=1.0~1.3. When examining the time traces of the mid-ship bending moment, an instant observation is that the transient phase settled quite quickly, nearly within 2 wave periods in simulations with structural damping as opposed to the no damping where it took nearly 4-5 wave periods. The numerical predictions of the first and higher harmonic contributions and the 2- node component is shown in Figure 70-73. The structural damping in the numerical model should not have any effect on the first harmonic of the VBM. Figure 70 also shows only a marginal variation in the first harmonic of the bending moment; basically it decreases slightly by about 3-4% with structural damping. Regarding the higher order harmonics, the numerical predictions either move closer towards the experiments or exhibit negligible change. An interesting observation here is that the improvements takes place at λ/L= 1.0 and1.2, where in the previous case without damping had significant deviations from experiments. The gap closes between the predictions and measurements with damping.

There is an overwhelming change in the 2-node flexible mode in the aforementioned frequencies and decreases by about 60-70% compared to the undamped case. The agreement is excellent when compared with measurements. Besides, the 2-node component does not change much at λ/L=1.1 and 1.3. Again referring to the Table 40, the 2-node component in this case occurs not at the wet natural frequency for which the Rayleigh's damping is calculated. The high frequency damping in the time history of bending moment for λ/L=1.2 can be seen in Figure 74. For the damped case there is a massive change in the magnitude of the 2-node component.

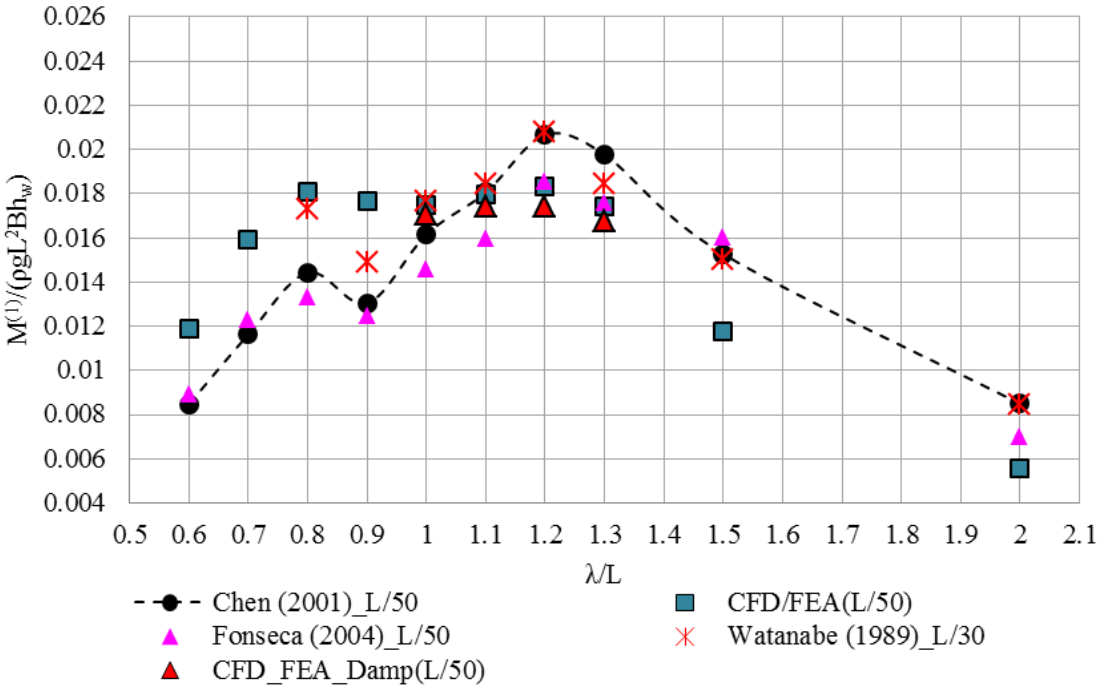

Figure 70: Non-dimensional amplitudes of first harmonic of VBM amidships compared with and without Rayleigh's structural damping in the FE model of S-175.

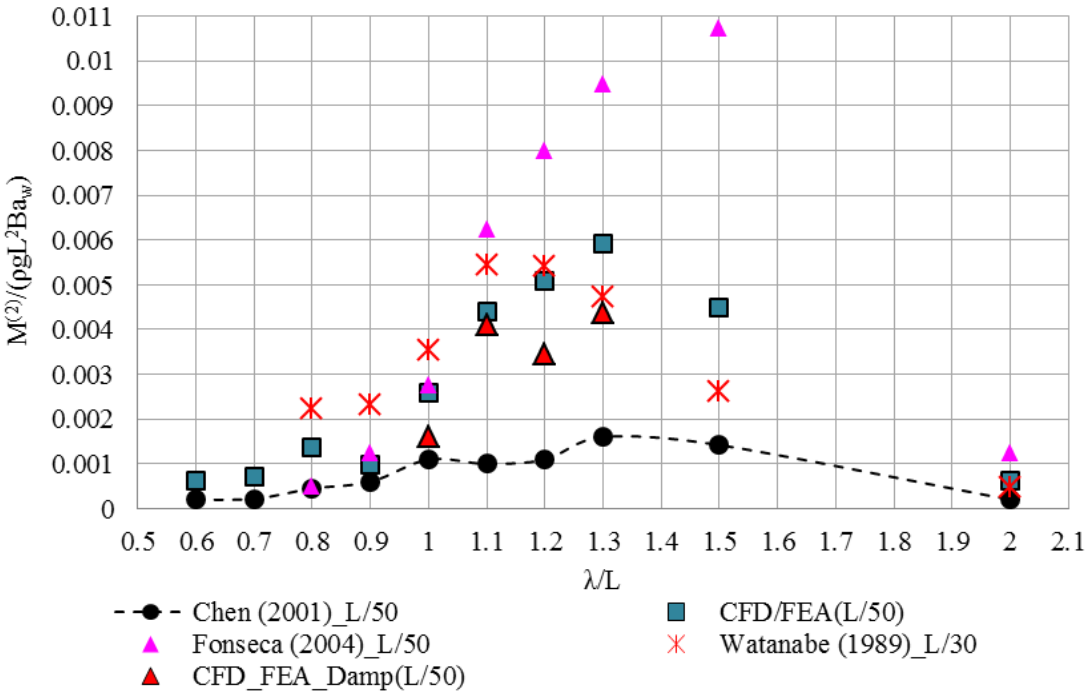

Figure 71: Non-dimensional amplitudes of second harmonic of VBM amidships compared with and without Rayleigh's structural damping in the FE model of S-175.

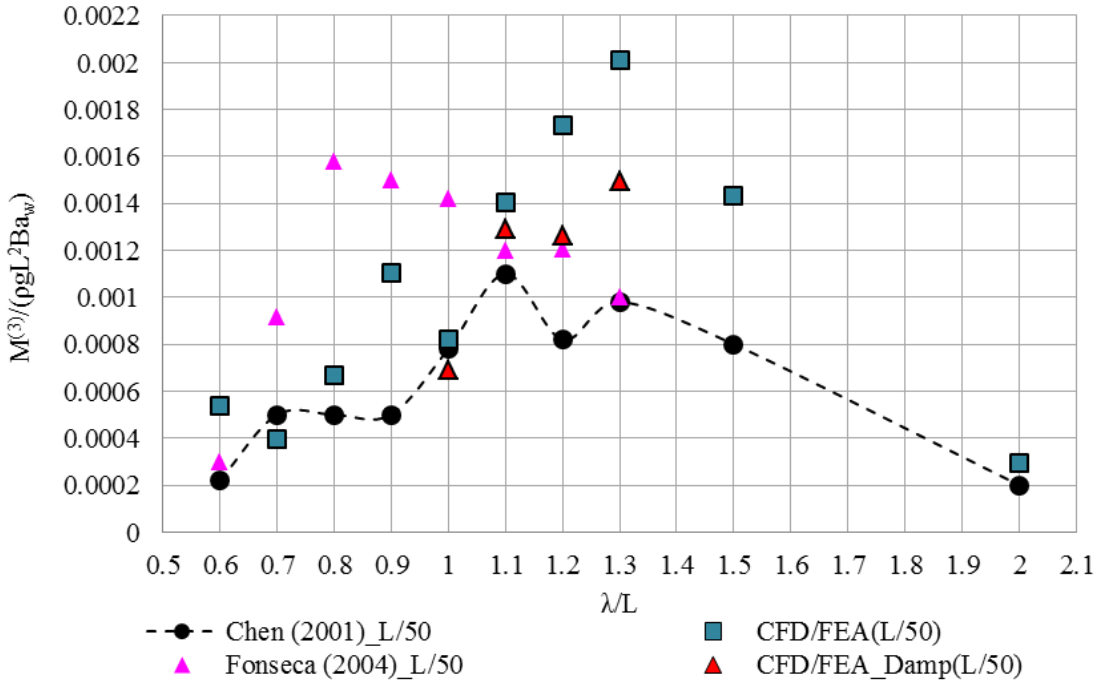

Figure 72: Non-dimensional amplitudes of third harmonic of VBM amidships compared with and without Rayleigh's structural damping in the FE model of S-175.

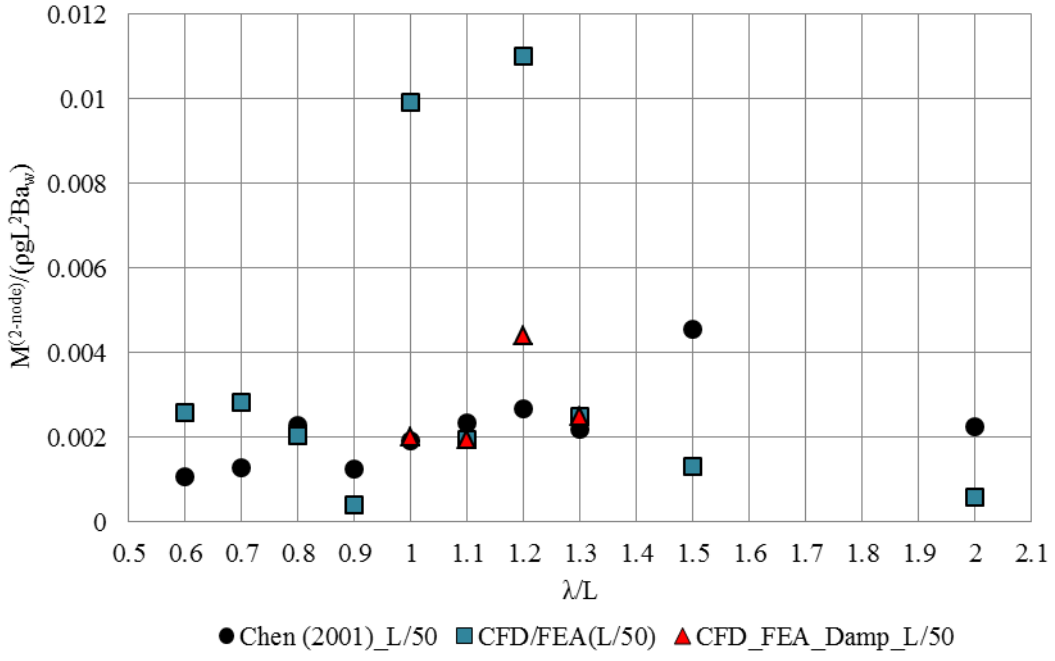

Figure 73: Non-dimensional amplitudes of 2-node flexible component of VBM amidships comparison with and without Rayleigh's structural damping in the FE model of S-175.

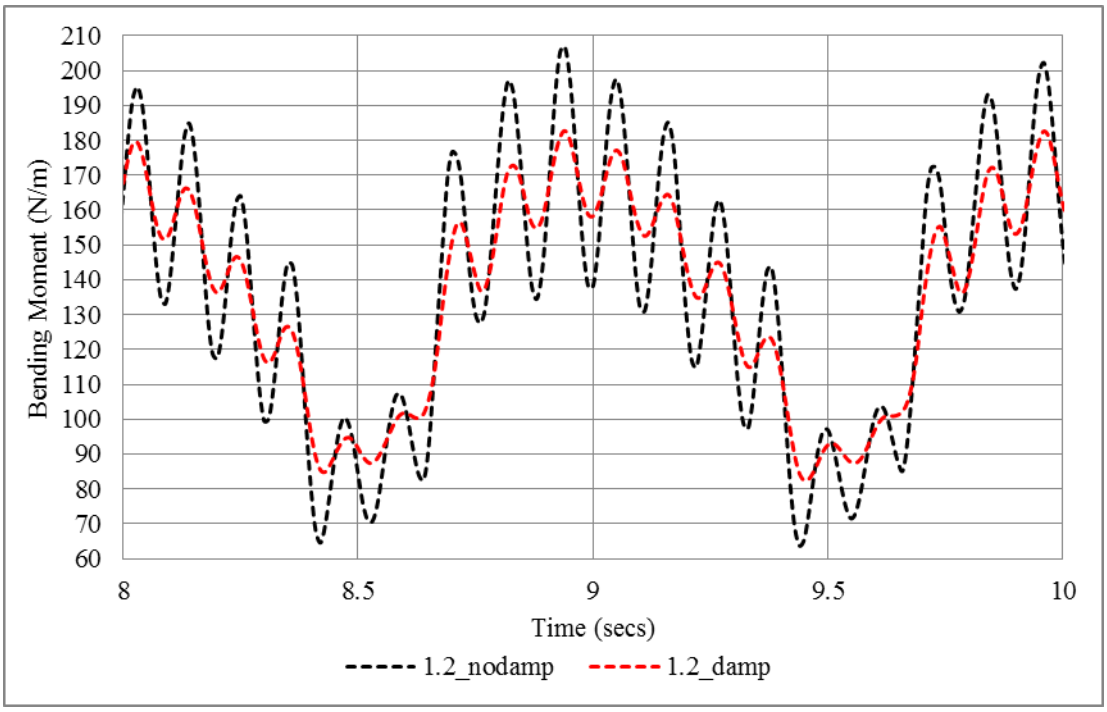

Figure 74: Time history of VBM amidships with and without damping in the FE model of S-175

There is some influence of the structural damping on the higher order harmonics but the effect is much stronger in the 2-node component. Only four frequencies were investigated with one damping coefficient. The results raises an important question as to what will be the change if say the computations were done using 5% critical damping factor. Figures 75-78 shows the 2- node flexible component with and without structural damping at other locations. The responses behave very similar to the amidships and the agreement improves with inclusion of structural damping. The general agreement is better from amidships to aft and shows moderate discrepancies towards the bow of the ship, especially at Pt. 5. From the plots we understand that, it is important to study the influence of damping not only at these frequencies but on the range of frequencies investigated. This is not undertaken presently for this thesis. Finally, the coupled method is capable of capturing the 2-node contribution to a good degree of accuracy when compared to the experiments not only at amidships but also at other locations.

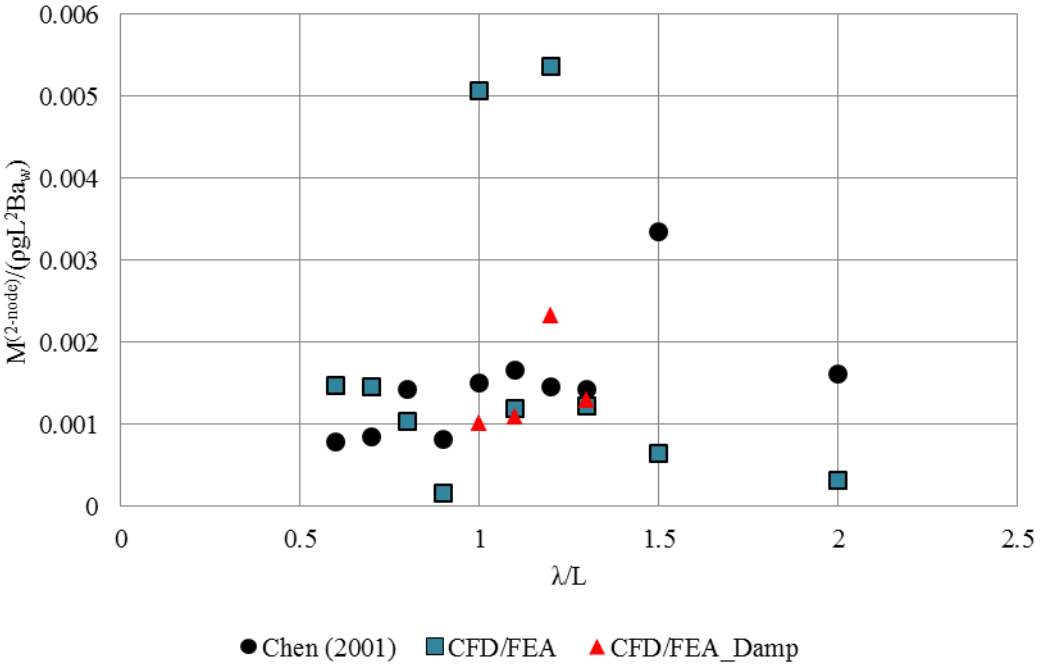

Figure 75: Non-dimensional amplitude of 2-node flexible component of VBM at Pt.1 (0.95 m from aft Lpp) with and without Rayleigh's structural damping in the FE model of S-175.

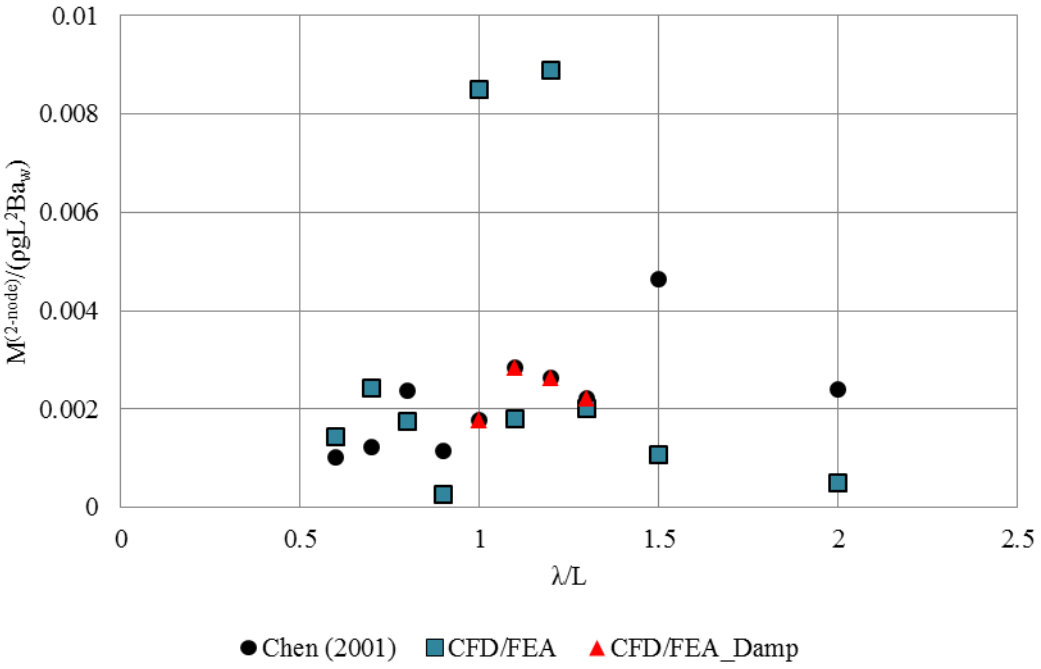

Figure 76: Non-dimensional amplitude of 2-node flexible component of VBM at Pt.2 (1.35 m from aft Lpp) with and without Rayleigh's structural damping in the FE model of S-175.

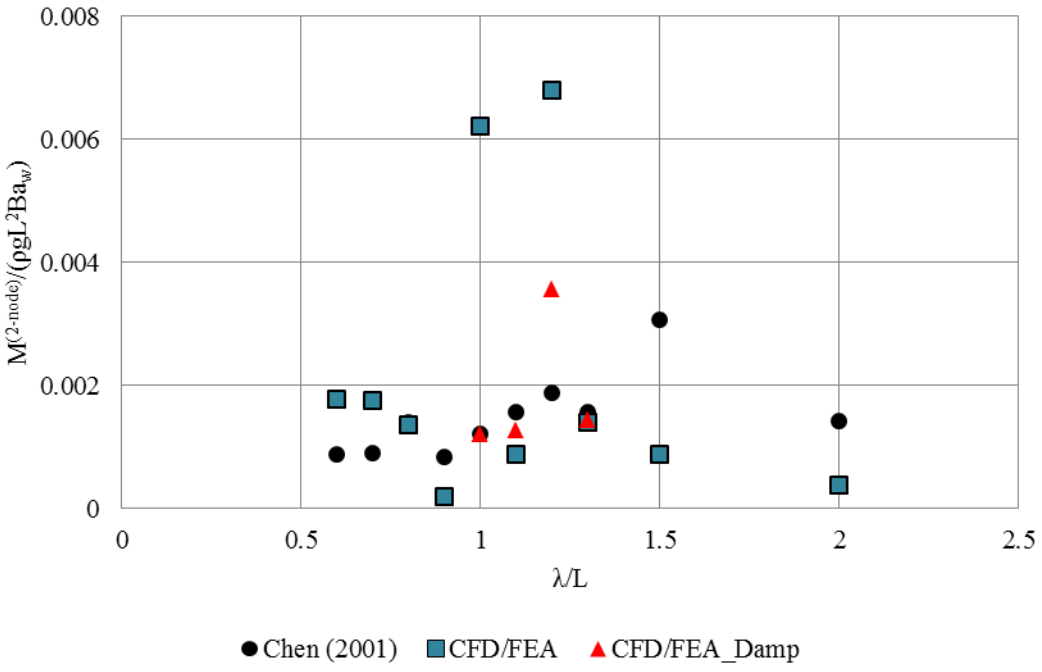

Figure 77: Non-dimensional amplitude of 2-node flexible component of VBM at Pt.4 (2.25 m from aft Lpp) with and without Rayleigh's structural damping in the FE model of S-175.

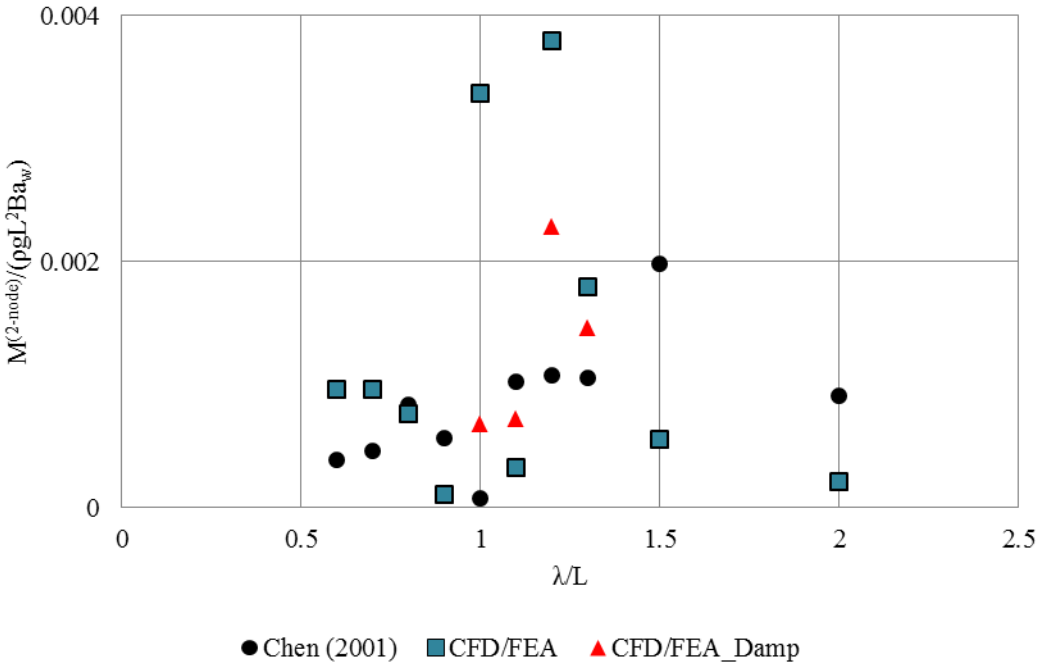

Figure 78: Non-dimensional amplitude of 2-node flexible component of VBM at Pt.5 (2.65 m from aft Lpp) with and without Rayleigh's structural damping in the FE model of S-175.

6.3.7 Asymmetry in Hogging and Sagging wave loads

The non-dimensionalised hogging and sagging loads measured showed appreciable asymmetry in the relatively long wave considered for comparison coupling. The nonlinearity in the hogging and sagging loads increases with increase in wave height. In the region of λ/L= 1.0~1.3 the measurements show a maximum divergence of the non-dimensionalised sagging moments is 0.01, with the peak sagging occurring at a ratio of 1.2. The numerical prediction with and without damping shown in Figure 79 signifies that the structural damping provides improvements in the predictions. Around the ship-wave matching region, the hog/sag asymmetry is evident in the numerical predictions. For the steeper wave the sagging loads are about 40-55% higher than the hogging wave loads. The asymmetry in wave loads is well captured by the coupling and there is a good convergence with experiments. Linear potential flow methods are incapable of calculating the asymmetry in the wave loads and predict equal magnitudes for the hogging and sagging.

Table 41 shows the ratio of sagging/hogging ratio for different wave condition and wave heights. The sagging loads are larger than the hogging once again in the region where the ship experience extreme motions and green water loads.

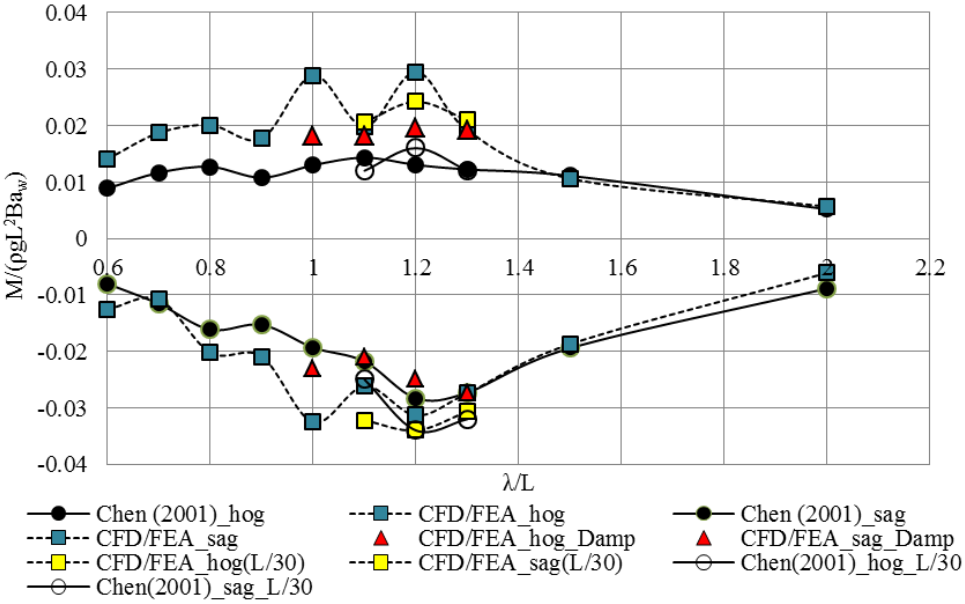

Figure 79: Non-dimensional amplitudes of hogging and sagging VBM amidships with and without Rayleigh's structural damping is vs measurements from Chen (2001)

Table 41: Ratio of sagging/hogging for different wave frequencies. * corresponds to H/L=1/30

λ/L	Sagging/Hogging Ratio
0.6	0.89
0.7	0.58
0.8	1.0
0.9	1.18
1.0	1.27
1.1	1.16
1.2	1.27
1.3	1.43
1.5	1.76
2.0	1.08
1.1 *	1.56
1.2 *	1.40
1.3 *	1.46

6.4 Conclusions

A flexible S-175 containership model with forward speed is used to validate the CFD/FE coupling by comparing the motions and the wave loads in regular head waves predictions with experimental measurements of Chen et al. (2001) and 2-D linear hydroelastic code. The simulations were carried out using an inviscid flow model and with no structural damping in the FE model. The wave load measurements clearly indicate the presence of nonlinear behaviour in the vertical accelerations at the bow and the structural responses of the model. The nonlinearity is not only reflected in the asymmetry of the sagging and hogging vertical bending moments but also appeared as the higher order harmonics of the wave encounter fre-

quency and the 2-node flexible wet frequency. The numerical predictions were also compared with the measurements from two other experimenters. The predictions were carried out for two different wave heights H=L/50 and L/30, however, only three wave frequencies were compared with measurements for the latter case.

Chapter 7:

Conclusions and Recommendations

A validation exercise is undertaken into the prediction of motion and wave loads on flexible floating bodies in regular waves. A two-way coupling between the CFD and FE software is carried out to perform this validation. The software employed for this study is commercially available and the coupling is also carried out using the inbuilt libraries in the software. The objective is to apply an available method to evaluate the difficulties and shortcomings of the method rather than developing the coupling algorithm from scratch. The predictions are compared with experimental results when available and also with 2-D linear hydroelastic predictions. The numerical method employed can be categorised as a 'strong' coupling since data is exchanged multiple number of times in a time step. This chapter aims at summarising the general conclusions arrived from the investigations carried out using the two-way coupling method to predict the hydroelastic behaviour of ships in waves and providing recommendation for future work.

7.1 Motion and responses of S-175 containership

Heave and Pitch motions

The motions, namely heave and pitch predicted generally agreed well with the measurements except at a few wave lengths (λ/L=1.1~1.5) where they were over predicted by a maximum of about 30% for the smaller wave height. The 2-D linear hydroelastic code also over predicted the motion in this region by a maximum of about 40%. Even though only three wave frequencies were investigated, the heave agreed better with the measurements for the larger wave height. It is clear that the differences are not arising due to the boundary conditions used in the FE model which replicates a towed condition and not a self-propelled model, since the motions of a towed model (Fonseca & Guedes Soares 2004b) agrees well with self-propelled model (Chen et al. 2001). Simulations carried out using k-ω SST turbulence model for two wave frequencies for H=L/50 to include the viscous effects

showed improvements but there were still differences between the predictions and measurements by about 15-20%.

Vertical Accelerations at the bow

The vertical accelerations at the bow for the two wave heights showed excellent agreement with the measurements for all wave frequencies investigated. The presence of second and third harmonic of the wave encounter frequency was traced in the vertical acceleration at the bow and showed an increase with increase in wave height. The nonlinear behaviour is induced mainly due to the flare impact and green water on deck which increases with increase in wave height.

Linear wave loads

The time traces of vertical bending moment using CFD/FE coupling were separated into the first, second and third harmonics of wave encounter frequency and the 2-node flexible mode using Fourier analysis. The agreement of the first harmonic of bending moment amidships predicted around the resonant region (ship-wave matching region) agreed well with measurements. In longer wave, the first harmonic amidships was under predicted by about 30-35% when compared with measurements and 2-D linear hydroelasticity. The two numerical methods agreed well in the longer wave for the zero speed case. Grid refinement or domain size showed negligible improvement to the first harmonic in this region. An over prediction of about 30-35 % was observed for the first harmonic in relatively short wave lengths for both the coupling and 2-D linear predictions. The predictions at other locations were also compared with measurements and showed a similar order of difference. When the measurements were compared with various nonlinear strip theory based codes a similar trend was observed. It can be concluded that the CFD/FE coupling predicts the first harmonic bending moments amidships to a similar degree of accuracy of the linear and nonlinear strip theories, however, it is computationally very expensive.

Second and third harmonic of wave encounter frequency

The second and third harmonics of bending moments when compared with three experimental measurements revealed that the present method is capable of capturing the nonlinearities in wave loads at amidships and fore and aft of the model to a good degree of accuracy. The present method predicts stronger second harmonic

component when compared with Chen et al. (2001) but agrees well with Watanabe et al. (1989). The nonlinear loads measured by the experiments showed more scatter than the linear wave loads. The absolute magnitude of these components is very small and the nondimensionalised values changes significantly for a small change in their magnitude. The nonlinear wave loads are mainly influenced by the effect of green water on deck and the flare impact and showed larger magnitudes in wave lengths where they were larger. Also, with increase in wave height the nonlinearities in wave loads were also larger.

2-node flexible mode

The 2-node flexible mode of the vertical bending moment amidships predicted for two wave heights using the coupling techniques showed excellent agreement with the experimental measurements except at two frequencies for H/L=1/50. At these two frequencies the predictions were nearly 6 times higher than the measurements. The predictions were carried out using a model which had no structural damping and it was seen that inclusion of 1% of critical damping as the structural damping to the FE model improved the predictions. The 2-node agreed well with the measurements, and furthermore, the inclusion of structural damping had negligible influence on the first, second and third harmonics.

Higher-order springing and higher-order harmonics

The CFD/FE coupling of S-175 with no structural damping showed the presence of nonlinear springing of the 7^{th} to 10^{th} harmonic order. It was noted that the relatively high frequency component in the wave load is due to occurrence of two different nonlinear phenomena, namely higher-order springing and higher-order harmonic of wave encounter frequency, which is stated together as 2-node flexible mode in the experiments as they both occur in the vicinity of the 2-node wet frequency. In general, the contribution of nonlinear or higher-order springing to the wave load is stronger than the higher-order harmonic contribution. It is important to identify these conditions and evaluate when carrying out a detailed hydroelastic investigation of a vessel. Although, these inferences were made with a model without any structural damping for a relatively rigid ship, it will become very important for a modern flexible containership. The magnitude of these nonlinear effects could be large and the CFD/FE coupling could be a useful tool to predict the wave loads in severe wave conditions.

7.2 Numerical wave simulations

The numerical wave simulations carried out in Chapter 4 showed that the CFD software Star-CCM+ is capable of simulating stable regular wave even for a wave steepness of 1/50 for over ten wave periods using a linear wave formulation. Although, the recommendations for the number of cells / wave length and wave height is given to be 80 cells/wavelength and 20 cells/wavelength, respectively, it was seen that even with 40 cells/wavelength a stable wave can be generated, but requires at least 20 cells/wave height. ITTC (2011) also recommends a minimum of 40 cells/wavelength and 20 cells/wave height. The decrease in wave height after ten wave periods in the all the cases investigated in this thesis is about 5-6% of the nominal wave height. The vertical velocities show a large scatter from the theoretical calculations and the horizontal velocities agree well with the theoretical calculations, except very close to free surface. The reason for this is because the numerical method involved is volume of fluid and attempting to predict the particle velocities at cell centres and comparing with particle velocities would definitely show differences. The pressure variation across the depth show very good agreement with the calculations for all the wave lengths investigated. Nevertheless, when investigating fluid-structure interaction of bodies in waves we need a stable wave for a long period of time and it is assumed that the orbital velocities will not heavily influence the motions and loads. The 2nd order temporal discretisation is the only choice we have to attain a stable wave with very minimal numerical diffusion in the software. The time step used in the wave simulations also needs careful consideration since it depends on the local courant number. It is recommended to alter the lower and higher courant number HRIC setting to larger values as described in Section 3.3 to ensure that the HRIC scheme is always selected.

7.3 Fluid and structural meshing strategy

For the barge simulations conducted in Chapter 5, individual meshes were created for different wave lengths. Although, it is preferred to design individual meshes for different wave frequencies it is tedious and time consuming. Hence, a more efficient approach was adopted for the containership in Chapter 6 to design the mesh in such a way that the minimum cell requirement for the wave simulations and in the wake region is satisfied for majority of wave frequencies. Grid sensitivity can

later be performed considering this mesh for selected frequencies where the deviations from the minimum cell requirements are large. Additionally, if the vessel experiences severe motions causing slamming and green water on deck, it is advised to refine the mesh in the bow and stern region to capture the violent flows accurately. For the containership simulations a total of 50 grid points along the depth of the ship was used to spatially resolve the green water and flare impact. It is observed that when predicting motions and wave loads on a flexible ship with zero forward speed, a relatively coarse mesh is sufficient and the differences in predicted bending moment between the refined meshes and coarse meshes is quite small. The one case simulated for the forward speed case also showed that the linear wave loads showed negligible changes on a refined mesh.

When symmetric motions and distortions are of interest, only a half of the hull needs to be modelled which can reduce computational demand. The length of the computational domain can be calculated based on the length between the perpendiculars of the vessel (L_{pp}) and the recommendations given by ITTC (2011) are deemed sufficient for the computational domain in the coupling simulations. To prevent reflections from the side wall should be located at least 2.5-3.0 L_{pp} from the centre plane of the vessel. There are no particular recommendations in the literature regarding the dimensions of an overset for ship simulations. The inference from the present investigations, especially when dealing with violent free surface flows like the containership, is to design the overset dimensions such that the significant flow features, for example wave breaking, green water, slamming, bow emergence, occur inside the overset boundaries. Additionally, the overset boundaries should not be very close to these violent phenomena since it will result in large gradients causing an overset mesh error and the solution to diverge. From the containership simulations a minimum length of the overset domain to be 1.5 L_{pp} and a breadth of 3.0 B and depth of 4.0 D is recommended and the same was used for the barge simulations too.

It is not possible to directly couple a beam in Abaqus with the fluid model in Star-CCM+. The approach used in this work can be adopted to couple the 3-D fluid model to the structural model where the flexibility is idealised using beam elements. The 3-D wetted surface can be modelled using dummy surface elements in Abaqus and coupled to the beam nodes using kinematic coupling. This is a very useful approach since the wave loads can be predicted to a good accuracy using beam ideali-

sation unless we are interested in condition where it is required to model a complete 3-D FE model, for example, to investigate the local stresses on the hatch corners of a ship subjected to torsional loads.

7.4 FSI coupling settings

A partitioned scheme is used to coupling the fluid and structural solver where the data is exchanged multiple times in a time step depending on user defined exchange settings. The computational time increases depending on the number of exchanges performed and limiting the number of exchanges to attain a stable and accurate coupled simulation would be computationally beneficial. It is seen from the literature that in general about 20 inner iterations and a maximum of 4 exchanges within a time step is sufficient for a very flexible seal (Bloxom 2014). In this study a maximum of 3 exchanges and 15 inner iterations were used and the co-simulation displacement residuals converged for these settings. The investigations carried out on the flexible barge using the CFD/FE coupling showed that there might be particular numerical issues when simulating very flexible floating structures. The issue is mainly when dealing with the time step adopted for the coupled simulations. It is shown that below a particular time step value the coupling becomes unstable resulting in high pressure peaks and finally the solution diverges. The problem is due to strong added mass effects occurring due to the flexibility resulting in large deformations very early in the simulation causing negative volume cells.

It is worth noting that in the present study a direct integration FE method is used rather than modal analysis. Investigations to predict global responses can be performed by coupling a CFD and a solver based on modal analysis and it can be computationally cheaper than direct integration FE technique. However, the coupling between CFD and direct integration FE could be more accurate when relatively higher frequencies become dominant, such as in the case of slamming or for a slender monopile fixed wind turbines.

When studying the hydroelastic reponse on a ship in waves, the boundary conditions of the FE model is considered as a free-free beam. This causes an additional problem of an unphysical drift in the simulations after a few wave periods due to the wave translating the body in the direction of wave propagation. It can be over-

come by restricting the longitudinal translation of a beam node close to the LCG of the body. From the investigations carried out it is clear that this is the simplest option and does not affect the deformation and structural responses. A more realistic option might be to calculate the wave resistance of the body from the CFD simulations and applying that as a longitudinal force on the beam nodes in the FE model.

7.5 Wave Loads

The coupling technique produces a reliable estimate of the wave loads on flexible bodies. It was shown that there are some differences in the calculated wave bending moment and they are of the order of 30-35% at few wave encounter frequencies for a containership. The 2-D linear and nonlinear strip codes also predict the bending moment to a similar degree of accuracy when compared with experiments. The higher order harmonics of wave bending moments are well predicted by the coupling technique when a ship is experiencing severe green water and water spray. The 2-D linear hydroelastic theory is a very powerful and quicker tool to estimate the linear wave loads, and hence, a better choice than the coupling technique for the initial design stage of the vessel. Reviewing the studies carried out by ISSC. (2000) and the present investigations it is recommended that for conditions where the nonlinearities are not so strong even a nonlinear strip theory could provide reasonable estimate of the nonlinear wave loads. However, when the wave conditions induce strong nonlinear behaviour the CFD/FE coupling used could be a better choice among the available numerical methods. Considering the computational power available at present, the coupling technique is not going to be practical to evaluate the bending moments and shear forces for the entire spectrum of wave conditions given in class rules but it can be quite functional to simulate certain important severe wave conditions and provide accurate predictions. For flexible modern day containerships where the nonlinear springing or higher order nonlinear loads provide significant contribution to the bending moment the coupling technique could be very beneficial.

The investigations on S-175 containership revealed that the higher-order springing and higher-order harmonics are well predicted by the coupling technique and while designing the test matrix for simulations or model testing these conditions should

be located and included in the test matrix. More validations on flexible ships are also required to have complete confidence on the accuracy of the coupling technique. A reliable estimate of the structural damping is prudent in hydroelastic simulations particularly when the vessel is experiencing nonlinear springing phenomenon.

It must be kept in mind that there are certain issues with the time step in the coupled simulations when dealing with very flexible structures and needs attention. Nevertheless, if the minimum time step used in the simulations is sufficient to resolve the dominant resonant frequencies, say by at least 100 time steps per period of oscillation, the results can be considered reliable.

7.6 Future work

The two-way coupling technique described in this thesis is applied to predict the motions and loads on two distinct structures; a very flexible barge and a realistic containership. The loads on the flexible barge are only compared using 2-D linear potential flow predictions due to lack of measurements and some discrepancies were also noted. It is important in the future to apply and validate the coupling technique on a similar flexible structure where measurements are available and also with a nonlinear time domain hydroelastic code. Comparisons need to be carried out between two-way and one-way coupling for the barge and the containership to identify conditions where the one-way coupling can predict the motions and responses to similar degree of accuracy as the two-way coupling. Then it would be more practical to apply a one-way coupling to these conditions because the computational cost for the two-way coupling is nearly double that of the one-way coupling.

Only symmetric motions and responses are considered in this thesis and the coupling technique needs to be validated for oblique sea conditions. Numerical modelling of oblique seas is feasible in Star-CCM+ and even the computational setup will not require many changes than what is described in Chapter 5 & 6, except that a full CFD domain will be required when investigating oblique seas. In reality, a ship as hip seldom, or even never, experiences a regular head wave in its life time. The real seas are irregular and the coupling needs to be applied to predict wave loads on irregular seas. Chen et al. (2001) had carried out model tests of S-175 container-

ship in irregular waves and the measurements can be used to validate the present coupling without many changes to the numerical models. In Star-CCM+, irregular waves can be simulated using Pierson-Moskowitz and JONSWAP wave spectrum that are frequently applied to model irregular waves.

A limited, but not detailed, spatial and temporal discretisation study is undertaken in this thesis as majority of the work concentrated on successfully applying the coupling and carrying out a number of wave conditions and wave heights on different structures. A more detailed analysis of the effects of these requires attention in the future to ensure that the predictions on a relatively coarse mesh give accurate estimates for all the cases. It could be possible that the global wave loads can be predicted on a coarser mesh than the one used in this study. The grid sensitivity on the predicted motions and wave loads can then be investigated in detail.

Faltinsen (2014b) stated that we still do not understand the physics behind the linear, and particularly, the nonlinear springing phenomenon but the most probable reason could be the nonlinear hydrodynamic interaction of the diffracted and radiated waves with the incident waves. Although, attempts were carried out to identify the reasons for the occurrence of the nonlinear springing in the containership by studying the flow field, no inferences could be made. The coupling should be investigated on a large flexible containership like the one tested by Miyake et al. (2009) where the nonlinear springing were evident and a detailed analysis on the flow field and pressure contours might give us more insight into the actual physics behind these nonlinearities.

References

Aagaard, O., 2013. *Hydroelastic Analysis of Flexible Wedges*. NTNU. Available at: http://www.diva-portal.org/smash/get/diva2:649589/FULLTEXT01.pdf.

Aksu, S., Price, W.G., Suhrbier, K.R. & Temarel, P., 1991. A comparitive study of dynamic behaviour of fast patrol boat travelling in rough seas. *Mar.Structs*, 6, pp.421–441.

Andersen, I.M. V & Jensen, J.J., 2014. Measurements in container ship of wave-induced hull girder stresses in excess of design values. *Mar.Structs*, 37, pp.54–85.

ASME, 2008. Procedure for Estimation and Reporting of Uncertainity due to Discretization in CFD Applications. *Journal of Fluids Engineering*, 130(7).

Bailey, P.A., Hudson, D.A., Price, W.G. & Temarel, P., 1998. A unified mathematical model describing the manoevring of a ship travelling in a seaway. *Trans. R. Inst Nav. Architects*, 140, pp.131–149.

Baso, S., Matsuda, H., Kurihara, T., Kurokawa, T., Doi, Y. & Sji, J., 2010. An Eulerian scheme with lagrangian particles for evaluation of seakeeping performance of a ship in nonlinear wave. In *ISOPE*.

Bathe, K.J., 2007. *Finite Element Procedures*, New Jersey: Prentice Hall.

Benra, F.K., Dohmen, H.J., Pei, J., Schister, S. & Wan, B., 2011. A comparison of one-way and two-way coupling methods for numerical analysis of fluid-structure interactions. *Journal of Applied Mathematics*, p.16 pages.

Bereznistki, A., 2001. Slamming: The role of hydroelasticity. *International Shipbuilding Progress*, 48(4), pp.333–351.

Bishop, R.E.D., Clarke, J.D. & Price, W.G., 1984. Comparison of full scale and predicted responses of two frigates in severe weather trial. *Trans. R. Inst Nav. Architects*, 127, pp.153–166.

Bishop, R.E.D. & Price, W.G., 1979. *Hydroelasticiy of Ships*, Cambridge University Press.

Bishop, R.E.D., Price, W.G. & Tam, P.K.Y., 1977. A unified dynamic analysis of ship response to waves. *Trans. R. Inst Nav. Architects*, 119, pp.363–390.

Bishop, R.E.D., Price, W.G. & Temarel, P., 1980. A unified dynamic analysis of antisymmetric ship response to waves. *Trans. R. Inst Nav. Architects*, 27, pp.54–65.

Bishop, R.E.D., Price, W.G. & Wu.Y, 1986. A general linear hydroelasticity theory of floating structures moving in a seaway. *Phil. Trans. R. Soc. Lond*, A316, pp.375–426.

Bloxom, A.L., 2014. *Numerical simulation of the fluid-structure interaction of a surafce effect ship bow seal*. Virginia Polytechnic Institue and State University.

Brizzolara, S., County, N., Hermundstad, O., Kukkanen, T., Viviani, M. & Temarel, P., 2008. Comparison of experimental and numerical loads on an impact bow section. *Ships and Offshore Structures*, 3(4), pp.305–324.

Brummelen, van E.H., 2009. Added mass effects of compressible and incompressible flows in fluid-structure interaction. *Journal of Applied*

Mechanics, 76, pp.021206–1–021206–7.

Cabos, C., Dilba, B., Kromer, M. & Schwenkenberg, A., 2011. Modal approach to fluid structure interaction applied to a ship in waves. In *MARSTRUCT*. Hamburg, Germany, pp. 9–11.

Camilleri, J., Temarel, P. & Taunton, D., 2015. Two-dimensional numerical modelling of slamming impact loads on high-speed craft. In *7th International Conference on HYEL*. Split, Croatia, pp. 43–54.

Carrica, P.M., Wilson, R. V & Stern, F., 2006. Unsteady RANS simulation of the ship forward speed diffraction problem. *Computers & Fluids*, 35(6), pp.545–570.

Causin, P., Gerbeau, J. & Nobile, F., 2005. Added-mass effect in the design of partitioned algorithms for fluid-structure problems. *Computer methods in applied mechanics and engioneering*, 194, pp.4506–4527.

Chang, M.S., 1977. Computations of three-dimensional ship-motions with forward speed. In *International Conference on Numerical Ship Hydrodynamics*. Berkeley, USA, pp. 124–135.

Chapchap, A., Ahmed, T.M., Hudson, D.A., Temarel, P. & Hirdaris, S.E., 2011. The influence of forward speed and nonlinearities on the dynamic behaviour of a container ship in regular waves. *Trans. R. Inst Nav. Architects Part A: InternationalJournal of MEritime Engineering*, 153(2), pp.137–148.

Chen, C.C., Huang, C.H., Chen, K.C. & Wang, P.W., 2014. Slamming loads calculation for an oil tanker. In *OAME*.

Chen, R.Z., Du, S.X., Wu, Y.S., Lin, J.R., Hu, J.J. & Yue, Y.L., 2001. Experiment on extreme wave loads of a flexible ship model. In *PRADS*. pp. 871–878.

Chen, X.J., Wu, Y.S., Cui, W.C. & Jensen, J.J., 2006. Review of hydroelasticity theories of global response of marine structures. *Ocean Engng*, 33, pp.439–457.

Choi, J. & Yoon, S.B., 2009. Numerical simulations using momentum source wave-maker applied to RANS equation model. *Coastal Engineering*, 56(10), pp.1043–1060.

Chorin, A.J., 1967. A numerical method for solving incompressible viscous flow problems. *Journal of Computational Physics*, 2, pp.12–26.

Clough, R.W. & Penzien, J., 1993. *Dynamics of Structures*, Berkely, CA: McGraw-Hill.

Dai, Y.Z. & Wu, G.X., 2008. Time domain computation of large amplitude body motion with mixed source formulation. In *Proc. 8th International Conference on Hydrodynamics*. pp. 441–452.

Dassault Systèmes, 2013. *Abaqus 6.13-1 Manual*, Providence, RI, USA.

Date, J.C. & Turnock, S.R., 1999. *A study into the techniques needed to accurately predict skin friction using RANS solvers with validation against Froude's historical flat plate experimental data*, University of Southampton, Southampton, U.K (Ship Science Reports(114)).

Degroote, J., Souto-Iglesias, A., Van Paperpegem, A., Annerel, S., Bruggeman, P. & Vierendeels, J., 2010. Partitioned simulation of the interaction between an elastic structure and free surafce flow. *Computer Methods in Applied Mechanics and Engineering*, 199, pp.2085–2098.

Demirdzic, I. & Peric, M., 1988. Space conservation law in finite volume calculations of fluid flow. *International Journal for Numerical Methods in Fluids*, 8, pp.1037–1050.

Dhavalikar, S., Awasare, S., Joga, R. & Kar, A.R., 2015. Whipping response analysis by one way fluid structure interaction-A case study. *Ocean Engineering*, 103, pp.10–20.

Drummen, I., Wu, M. & Moan, T., 2009. Experimental and numerical study of containership responses in severe head seas. *Marine Structures*, 22(2), pp.172–193.

Du, S.X., Hudson, D.A., Price, W.G. & Temarel, P., 2011. The occurrence of irregular frequencies in forward speed ship seakeeping numerical calculations. *Ocean Engineering*, 38(1), pp.235–247.

Du, S.X., Wu, Y.S. & Price, W.G., 1998. Forward speed effect on structural responses of a ship travelling in waves. In *In Proceedings of the 2nd International Conference on Hydroelasticity in MArine Technology*. Fukuoka, Japan, pp. 401–410.

Dvorkin, E.N., D, C., Cuitino, A. & Gioia, G., 1988. A Vlassov beam element. *Computers and Structures*, 33(1).

Faltinsen, O., Zhao, R. & Umeda, N., 1991. Numerical Predictions of Ship Motions at High Forward Speed [and Discussion]. *Philosophical Transactions: Physical Sciences and Engineering*, 334(1634), pp.241–252.

Faltinsen, O.M., 2014a. Hydrodynamics of marine and offshore structures. In *Proc. 11th International Conference on Hydrodynamics*. pp. 1–14.

Faltinsen, O.M., 2014b. Hydrodyanmics aof mrine and offshore structures. In *Proceedings of 11th International Conference on Hydrodynamics*. Singapore.

Ferziger, J. & Peric, M., 2003. *Computational Methods for Fluid Dynamics* 3rd Editio., Springer, Berlin.

Fonseca, N. & Guedes Soares, C., 2004a. Experimental Investigation of the Nonlinear Effects on the Statistics of Vertical Motions and Loads of a Containership in Irregular Waves. *J. Ship Res.*, 48(2), pp.148–167.

Fonseca, N. & Guedes Soares, C., 2004b. Experimental Investigation of the Nonlinear Effects on the Vertical Motions and Loads of a Containership in Regular Waves. *J. Ship Res.*, 48(2), pp.118–147.

Fonseca, N. & Soares, C.G., 1998. Time-Domain analysis of large-amplitude vertical motions and wave loads. *Journal of Ship Research*, 42(2), pp.100–113.

Fonseca, N. & Soares, C.G., 2005. Comparison between experimental and numerical results of the nonlinear vertical ship motions and loads on a containership in regualr waves. *International Shipbuilding Progress*, 52(1), pp.57–89.

Förster, C., Wall, W.A. & Ramm, E., 2007. Artificial added mass instabilities in sequential staggered coupling of nonlinear structures and incompressible viscous flows. *Computer Methods in Applied Mechanics and Engineering*, 196(7), pp.1278–1293. Available at: http://www.sciencedirect.com/science/article/pii/S0045782506002544 [Accessed February 16, 2016].

Frank, W., 1967. *Oscillation of cylinders in or below the free surface of deep liquids*,

Bethesda,MD,USA.

Froude, W., 1861. On the rolling of ships. *Trans. R. Inst Nav. Architects*, 2, pp.180–229.

Gao, R., Ren, B. & Wang, Y., 2012. Numerical modelling of regular wave slamming on subface of open-piled structures with the corrected SPH method. *Appl. Ocean Res.*, 34, pp.173–186.

Havelock, T.H., 1929. LIX. Forced surface-waves on water. *Philosophical Magazine Series 7*, 8(51), pp.569–576.

Havelock, T.H., 1945. Notes on the theory of heaving and pitching. *Trans. R. Inst Nav. Architects*, pp.109–122.

Havelock, T.H., 1958. The effect of speed of advance upon the damping of heave and pitch. *Trans. R. Inst Nav. Architects*, 100, pp.131–135.

Hirdaris, S.E. & Temarel, P., 2009. Hydroelasticity of ships: Recent advances and future trends. *In Proceedings of the Institution of Mechanical Engineers, Part M: J. Engng Maritime Environment*, 223, pp.305–330.

Hirdaris, S.E., White, N.J., Angoshtari, N., Johson, M.C., Lee, Y. & Bakkers, N., 2010. Wave loads and flexible fluid-strutcure interactions: current developments and future directions. *Ships and Offshore Structures*, 5(4), pp.307–325. Available at: http://dx.doi.org/10.1080/17445301003626263.

Hirt, C.W., Amsden, A.A. & L, C.J., 1974. An arbitary Lagrangian-Eulerian computing method for all flow speeds. *Journal of Computational Physics*, 14(3), pp.227–253.

Hirt, C.W. & Nichols, B.D., 1981. Volume of Fluid (VOF) method for the dynamics of free boundaries. *Journal of Computational Physics*, 39, pp.201–225.

Hong, S., Kyoung, J., Kim, Y., Kim, S. & Malencia, S., 2008. Validation of wave loads of a containership in oblique waves. In *6th Osaka Colloquim on Seakeeping and Stability of ships*. pp. 10–117.

Hou, G., Wang, J. & Layton, A., 2012. Numerical methods for fluid-structure interaction-A Review. *Commum.Comput.Phys*, 12, pp.337–377.

Huang, Y. & Sclavonous, P.D., 1998. Nonlinear ship motions. *Journal of Ship Research*, 42, pp.120–130.

Idelsohn, S.R., Pin, D.F., Rossi, R. & Onate, E., 2009. Fluid-structure interaction problems with strong added-mass effect. *International Journal for Numerical Methods in Engineering*, 80, pp.1261–1294.

Iijima, K., Yao, T. & Moan, T., 2008. Strutural response of a ship in severe seas considering global hydroelastic vibrations. *Marine Structures*, 21, pp.420–445.

Inglis, R.B. & Price, W.G., 1980. Motions of ships in shallow water. *Trans. R. Inst Nav. Architects*, 122, pp.269–294.

Inglis, R.B. & Price, W.G., 1981a. Calculation of the velocity potential of a translating, pulsating source. *Trans. R. Inst Nav. Architects*, 123, pp.163–175.

Inglis, R.B. & Price, W.G., 1981b. Irregular frequencies in three dimensional source distribution techniques. *International Shipbuilding Progress*, 28, pp.57–62.

Inglis, R.B. & Price, W.G., 1981c. The influence of speed dependent boundary conditions in three dimensional ship motion problems. *International Shipbuilding Progress*, 28(318), pp.22–29.

Inglis, R.B. & Price, W.G., 1982. A three dimensional ship motion theory: Calculation of wave loading and responses with forward speed. *Trans. R. Inst Nav. Architects*, 124, pp.183–192.

ISSC., 2000. Committee VI.1. Extreme Hull Girder Loading. *Proceedings of the 14th International Ship and Offshore Structures Congress 2000, Vol. 2 (Eds. Ohtsubo, H. and Sumi, Y.)*, pp.263–320.

ISSC., 2009. Report of Committee I.2: Loads. In Proceedings of the 17th International Ship and Offshore Structures Congress,Seoul,Korea. , 1, pp.127–210.

ISSC., 2012. Report of Committee I.2: Loads. In Proceedings of the 18th International Ship and Offshore Structures Congress, Rostock, Germany. , 1, pp.79–150.

ITTC, 2011. Practical Guidelines for Ship CFD Applications. In *International Towing Tank Conference*. pp. 1–18.

ITTC., 2011. The Seakeeping Committe final report and recommendations. In the Proceedings of 26th ITTC, Rio de Janerio, Brazil. , pp.183–245.

Jameson, A., 1991. Time dependent calcualtions using multigrid, with applications to unsteady flows past airfoils and wings. In *AIAA 10th Computational Fluid Dynamics Conference*. Honolulu, USA.

Jensen, J.J. & Pedersen, P.T., 1979. Wave-induced bending moments in ship-a quadriatic theory. *Trans. R. Inst Nav. Architects*, 121, pp.151–165.

Jensen, J.J. & Pedersen, P.T., 1981. Bending Moments and Shear Forces in ships sailing in irregular waves. *Journal of Ship Research*, 25(4), pp.243–251.

Joppich, W. & Kürschner, M., 2006. MpCCI-a tool for the simualtion of coupled simualtions. *Concurrency and Computation:Practice and Experience*, 18, pp.183–192.

Kim, J.H., Kim, Y., Yuck, R.H. & Lee, Y.D., 2015. Comaprison of slamming and whipping loads by fully coupled hydroelastic analysis and experimental measurement. *Journal of Fluids and Structures*, 52, pp.145–165.

Kim, K., Shin, Y.S. & Wang, W., 2008. A Stern slamming analysis using Three-Dimensional CFD simulation. In *Proc. 27th Int. Conf. on Offshore Mechanics and Arctic Engineering*. Estoril, Portugal, pp. 929–934.

Kim, K.H., Bang, J.H., Kim, Y. & Kim, S.J., 2013. Fully coupled bem-fem analysis of ship hydroelasticity in waves. In *Marine Structures*. pp. 71–99.

Kim, K.H. & Kim, Y., 2014. Numerical analysis of sprining and whipping using fully-coupled FSI models. *Ocean Engineering*, 91, pp.28–50.

Kim, S. & Yu, H., 2010. Segmented model testing and numerical analysis of wave-induced extreme and springing loads on large container carriers. In *Proc. 20th Int. Conf. on Offshore and Polar Engineering Conference*. pp. 385–392.

Kim, S.P. & Lee, H., 2011. Fully nonlinear seakeeping analysis based on CFD simualtions. In *In Proceedings of the 21st International Offshore and Polar Engineering Conference*. Hawaii, U.S.A, pp. 970–974.

Kim, Y. & Kim, K.H., 2009. Analysis of Hydroelasticity of Floating Shiplike Structure in Time Domain Using a Fully Coupled Hybrid BEM-FEM. *J. Ship Res.*, 50(1), pp.31–47.

Kim, Y., Malencia, S., Bigot, F. & Senjanovic, I., 2009. Linear Sprining model-Comparisons of different numerical models. In *Hydroelasticity in Marine Technology*. pp. 361–371.

Korvin-Kroukovsky, B. V, 1955. Investigation of Ship Motions in Regular Waves. *Trans. SNAME*, 63, pp.386–435.

Korvin-Kroukovsky, B. V & Jacobs, W.R., 1957. Pitching and heaving motions of a ship in regular waves. *Trans. SNAME*, 65, pp.590–631.

Kriloff, A., 1898. A general theory of the oscillations of a ship on waves. *Trans. R. Inst Nav. Architects*, 40, pp.135–196.

Lakshmynarayanana, P., Temarel, P. & Chen, Z., 2015a. Hydroelastic analysis of flexible barge in regular waves using coupled CFD-FEM modelling. In *MARSTRUCT*. pp. 95–103.

Lakshmynarayanana, P., Temarel, P. & Chen, Z., 2015b. Coupled Fluid-Structure Interaction to model Three-Dimensional Dynamic Behaviour of Ship in Waves. In *7th International Conference on HYEL*. pp. 623–637.

Lewis, F.M., 1929. The inertia of water surrounding a vibrating ship. *Trans. SNAME*, 37, pp.1–20.

Lin, W.M., Meinhold, M., Salvesen, N. & Yue, D.K.P., 1994. Large-amplitude motions and wave loads for ship design. In *Proc, 20th Symp. on Naval Hydrodynamics*. Santa Barabara, California, USA.

Lin, W.M. & Yue, D.K.P., 1990. Numerical solutions for large-amplitude ship motions in time domain. In *Proc. 18th Symposium on Naval Hydrodynamics*. pp. 41–66.

Madsen, P.A. & Schäffer, H.A., 2006. A discussion of artifical compressibility. *International Journal for Coastal , Harbour and Offshore Engineers*, 53, pp.93–98.

Maki, K.J., Lee, D., Piro, D.J. & Colletter, M., 2010. Hydroelastic impact of stern structure using CFD and FEA. In *Proceedings of the 2010 Conference on Grand challenges in modelling and simulation*. pp. 231–238.

Malenica, S., Moan, B., Remy, F. & Senjanovic, I., 2003. Hydrelastic reponse of a barge to impulsice and non-impulsive wave loads. In *Hydroelasticity in Marine Technology*. pp. 107–115.

Mikami, T. & Kashiwagi, M., 2008. Time-domain strip method with memory-effect function considering body nonlinearity of ships in large waves (2nd report). *Journal of Marine Science and Technology*, 13(3), pp.139–149.

Miyake, R., Matsumoto, T., Yamamoto, N. & Toyoda, K., 2010. On the estimation of hydroelastic reponse acting on a Ultra-Large Container ship. In *Proc. 20th Int. Conf. on Offshore and Polar Engineering Conference*. pp. 849–856.

Miyake, R., Matsumoto, T., Zhu, T., Usami, A. & Dobashi, H., 2009. Experimental studies on the hydroelastic response using a flexible Mega-Container ship model. In *Hydroelasticity in Marine Technology*. pp. 161–171.

El Moctar, O., Oberhagemann, J. & Schellin, T.E., 2011. Free-surface RANS method for hull girder sprining and whipping. In *In Proc. SNAME*. pp. 286–300.

Mukhopadhyay, M., 1989. *Vibration, Dynamics and Structural Systems*, Oxford & IBH Publishing Co Pvt Ltd.

Muzaferija, S., Peric, M., Sames, P. & Schellin, T., 1998. A Two-Fluid Navier-Stokes Solver to Simulate Water Entry. In *In Proceedings of the 22nd symposium on naval hydrodynamics*. Washinton, DC, pp. 277–289.

Nakos, D.E., Kring, D.C. & Sclavonous, P.D., 1993. Rankine Panel methods for time-domain free surface flows. In *6th International Conference on on Numerical ship hydrodynamics*.

Nakos, D.E. & Sclavonous, P.D., 1990. Ship motions by a three-dimensional Rankine panel method. In *18th Symposium on naval hydrodynamics*. pp. 21–39.

Newman, J.N., 1964. A slender-body theory for ship oscillations in waves. *Journal of Fluid Mechanics*, 18, pp.602–618.

Newman, J.N., 1977. *Marine Hydrodynamics*, Cambridge, MA: The MIT Press.

Newman, J.N., 1980. The unified theory of ship motions. *In Proceeding of the 13th Symposium on Naval Hydrodynamics,Tokyo,Japan*, pp.373–394.

Noor, A.K. & Dwoyer, D.L., 1988. *Computational Structural Mechanics & Fluid Dynamics: Advances and Trends*, Pergamon Press, Oxford. Available at: http://www.sciencedirect.com/science/article/pii/B9780080371979500012.

O'Dea, J., Powers, E. & Zselecsky, J., 1992. Experimental determination of nonlieanrities in vertical plane ship motions. In *Proc. 19th Symposium on Naval Hydrodynamics*. pp. 73–91.

Oberhagemann, J., Holtmann, M., El Moctar, O., Schellin, T.E. & Kim, D., 2009. Stern slamming of a LNG carrier. *Journal of Offshore Mechanics and Artic Engineering*, 131:013303.

Oberhagemann, J., Kromer, M., Cabos, C. & El Moctar, O., 2012. A fluid-structure coupling method based on field methods and a structural mode decomposition. In *Hydroelasticity in Marine Technology*. pp. 267–276.

Oberhagemann, J., Shigunov, V. & El Moctar, O., 2012. Application of CFD in long-term extreme value analyses of wave loads. *Ship Technology Research*, 59(3), pp.4–22.

Ogilvie, T.F. & Tuck, E.O., 1969. A rational strip theory for ship motions. *Technical Report 013, University of Michigan, Ann Harbor, USA*.

Ozisik, M.N., 1994. *Finite difference methods in hear transfer*, CRC Press.

Paik, K.J., Carrica, P.M., Lee, D. & Maki, 2009. Strongly coupled fluid–structure interaction method for structural loads on surface ships. *Ocean Engng*, 36, pp.1346–1357.

Park, J.H. & Temarel, P., 2007. The Influence of Nonlinearities on Wave-induced Motions and Loads Predicted by Two-dimensional Hydroelasticity Analysis. *In Proceeding of the 10th International Symposium on Practical Design of Ships and Other Floating Structures,Houston, Texas*, 1, pp.27–34.

Patankar, S. V & Spalding, D.B., 1972. A calculation procedure for hear, mass and momentum transfer in three-dimensional parabolic flows. *Int. Journal of Heat and Mass Transfer*, 15(10), pp.1787–1806.

Peric, M., 2012. Wave impact, body motion and overset grids in Star-CCM+. In *South East Asian Conference*. Available at: http://www.cd-adapco.com/sites/default/files/Presentation/WavesBodyOverset_MP.pdf.

Peric, M., Zorn, T., El Moctar, O., Schellin, T. & Kim, Y.S., 2007. Simulation of Sloshing in LNG-Tanks. In *OAME*.

Piro, D.J., 2013. *A Hydroelastic method for the analysis of global response due to slamming events*. The University of Michigan.

Piro, D.J. & Maki, K.J., 2013. Hydroealstic analysis of bodies that enter and exit water. *Journal of Fluids and Structures*, 37, pp.134–150.

Prosperretti, A. & Tryggvason, G., 2009. *Computational Methods for Multiphase Flow*, Cambridge University Press.

Querard, A.B.G., Temarel, P. & Turnock, S.R., 2008. A RANS approach to hydrodynamic and hydroelastic responses of a flexible barge. In *Proceedings of 8th International Conference on Hydrodynamics (ICHD'08)*. pp. 493–504. Available at: http://eprints.soton.ac.uk/63482/.

Ramos, J., Incecik, A. & Guedes Soares, C., 2000. Experimental study of slam-induced stresses in a containership. *Marine Structures*, 13, pp.25–51.

Remy, F., Moilin, B. & Ledoux, A., 2006. Experimental and numerical study of wave response of a flexible barge. In *4th International Conference on Hydroelasticity in Marine Technology*. pp. 255–264.

Richter, T. & Wick, T., 2013. *On time discretizations of Fluid-structure interactions*, Spinger.

Riemslagh, K., Vierendeels, J. & Dick, E., 2000. An efficient coupling procedure for flexible wall fluid-structure interaction. In *European Congree on Computational Methods in Applied Sciences and Engineering*. Barcelona, pp. 1–13.

Roache, P.J., 1998. *Verification and Validation in Computational Science and Engineering*, Albuquerque, New Mexico: Hermosa Publishers.

Salvesen, N., Tuck, E.O. & Faltinsen, O., 1970. {Ship motions and sea loads}. *Trans. SNAME*, 78, pp.250–287.

Sclavonous, P.D., Kring, D.C., Huang, Y., Mantzaris, D.A., Kim, S. & Kim, Y., 1997. A computational methos as an advanced tool of ship hydrodynamic design. *Trans. SNAME*, 105, pp.375–397.

Seng, S., 2012. *Slamming and whipping analysis of ships*. Denmark Technical University.

Seng, S., Andersen, I.M. V & Jensen, J.J., 2012. On the influence of hull girder flexibility on the wave induce bending moments. In *6th International Conference on Hydroelasticity in Marine Technology*.

Seng, S., Jensen, J.J. & Malenica, S., 2014. Global hydroelastic model for springing and whipping based on a free-surafce CFD code (OpenFoam). *International Jornal of Naval Architecture and Ocean Engineering*, 6, pp.1024–1040.

Senjanovic, I., Malenica, S. & Tomasevic, S., 2008. Investigation of ship hydroelasticity. *Ocean Engng*, 35, pp.523–535.

Senjanovic, I., Malenica, S. & Tomasevic, S., 2009. Hydroelasticity of large container ships. *Marine Structures*, 22, pp.287–314.

Senjanovic, I., Tomasevic, S. & Valdimir, N., 2009. An advanced theory of thin wall girders. *Marine Structures*.

Shao, Y.L. & Faltinsen, O.M., 2012. A numerical study of of the second-order wave

excitation of ship sprining in infinite water depth. *Journal of Engineering for the Maritime Environment*, 226(2), pp.103–119.

Shin, Y.S., Chung, J.S., Lin, W.M., Zhang, S. & Engle, A., 1997. Dynamic loadings for structural analysis of fine form ships based on non-linear large amplitude motions and loads method. *Trans. SNAME*, 105, pp.127–154.

Sneed, A., 2015. Moore's Law Keeps Going, Defying Expectations. *Scientific American*.

Song, M., Kim, K.H. & Kim, Y., 2010. Analysis of linear and nonlinear structural loads on a 6500 TEU containership by a time-domain rankine panel method. In *Proc. 20th Int. Conf. on Offshore and Polar Engineering Conference*. pp. 379–384.

St.Denis, M.S. & Pierson, W.J., 1953. On the Motion of Ships in Confused Seas. *Trans. SNAME*, 61, pp.280–357.

STAR-CCM+, 2012. STAR-CCM+ version 8.04 manual.

Stern, F., Wilson, R. V, Coleman, H.W. & Paterson, E.G., 2001. Comprehensive Approach to Verification and Validation of CFD Simulations-Part 1: Methodology and Procedures. *Journal of Fluids Engineering*, 123, pp.793–802.

Storhaug, G., Choi, B.K., Moan, T. & Hermundstad, O.A., 2010. Consequence of whipping and springing on fatigue for a 8600TEU container vessel in different trades based on model tests. In *11th International Symposium on a practical design of ships and other floating structures*. pp. 1180–1189.

Taghipour, R., Perez, T. & Moan, T., 2008. Time-Domain Hydroelatic Analysis of a Flexible Marine Structure using State-Space Models. *J. Offshore Mech. Arct. Eng*, 131(1).

Tang, H.S., Jobes, S.C. & Sotiropoulos, F., 2003. An overset-grid method for 3D unsteady incompressible flows. *Journal of Computational Physics*, 191, pp.567–600.

Tasai, F., 1960. *Formula for calculating hydrodynamic force of a cylinder heaving on a free surface*,

Tezdogan, T., Demirel, Y.K., Khoransanchi, M., Incecik, A. & Turan, O., 2015. Full scale unsteady RANS CFD simulations of ship behaviour and perforamnce in head seas due to slow steaming. *Ocean Engineering*, 97, pp.186–206.

Thomas, G., Davis, M., Holloway, D. & Roberts, T., 2003. Transient dynamic slam response of large high speed catamarans. In *In: The 7th International Conference on Fast Sea Transportation*. Ischia, Italy.

Thomas, P.D. & Lombard, C.K., 1979. Geometric conservation law and its application toflow computations on moving grids. *American Institute of Aeronautics and Astronautics*, 17(10), pp.1030–1037.

Tu, J., Inthavong, K. & Wong, K.K.L., 2015. *Computational Hemodynamics – Theory, Modelling and Applications*, Springer Netherlands.

Ursell, F., 1949. On the heaving of a circular cylinder on the surface of liquid. *Quaterly Journal of Mechanics and Applied Mathematics*, 2(2), pp.218–231.

Wang, X.L., Liu, R.M. & Hu, J.J., 2015. Wave-induced responses of a bulk carrier in heading and following seas. In *MARSTRUCT*. pp. 53–60.

Wang, Z.J., 1995. A fully conservative interface algorithm for overlapping grids.

Journal of Computational Physics, 122, pp.96–106.

Watanabe, I. & Guedes Soares, C., 1999. Comparative study on the time-domain analysis of non-linear ship motions and loads. *Mar.Structs*, 12, pp.153–170.

Watanabe, I., Keno, M. & Sawada, H., 1989. Effects of bow flare shape on wave loads of a container ship. *Journal of the Society of Naval Architects of Japan*, 166, pp.259–299.

Watanabe, I. & Sawada, H., 1986. Effects of Elastic Responses to the Longitudinal Bending Moment in Two-Directional Irregular Waves. *Naval Architecture and Ocean Engineering*, 24, pp.91–102.

Weems, K., Zhang, S., Lin, W.M., Bennet, J. & Shin, Y.S., 1998. Structural dynamic loadings due to impact and whipping. In *Proc. Practical Design of Ships and Mobile Units*. pp. 79–85.

Wehausen, J.Y. & Laitone, E. V, 1960. Surface Waves. *Encyclopedia of Physics*, 9(Springer Verlag), pp.446–778.

Westphalen, J., Greaves, D., Williams, C., Zang, J. & Taylor, P., 2008. Numerical simulation of extreme free surface waves. In *Proc. 8th International Offshore and Polar Engineering Conference*. pp. 55–61.

Weymouth, G., Wilson, R. & Stern, F., 2005. RANS Computational Fluid Dynamics Predictions of Pitch and Heave Ship Motions in Head Seas. *Journal of Ship Research*, 49(2), pp.80–97.

Wilson, R., Paterson, E. & Stern, F., 1998. Unsteady RANS CFD method for naval combatants in waves. In *Proc, 22th Symp. on Naval Hydrodynamics*. pp. 532–549.

Wilson, R. V, Stern, F., Coleman, H.W. & Paterson, E.G., 2001. Comprehensive Approach to Verification and Validation of CFD Simulations- Part 2: Application of Rans Simulation of a Cargo/Container Ship. *Journal of Fluids Engineering*, 123, pp.803–810.

Wu, M. & Hermundstad, O.A., 2002. Time-domain simulation of wave-induced nonlinear motions and loads and its applications in ship design. *Marine Structures*, 15(6), pp.561–597.

Wu, M. & Moan, T., 1996. Liner and nonlinear hydroelastic analysis of high-speed vessels. *Journal of Ship Research*, 40, pp.149–163.

Wu, M. & Moan, T., 2006. Statistical analysis of wave-induced extreme nonlinear load effects using time-domain simulations. *Applied Ocean Research*, 28(6), pp.386–397.

Wu, Y., Chen, R. & Lin, J., 2003. Experimental Technique of Hydroelastic Ship Model. In *Hydroelasticity in Marine Technology*. pp. 131–142.

Wu, Y.S. & Cui, W.C., 2009. Advances in the three dimensional hydroelasticity of ships. *In Proceedings of the Institution of Mechanical Engineers, Part M: J. Engng Maritime Environment*, 223, pp.331–348.

Wu, Y.S., Maeda, H. & Kinoshita, T., 1997. The second order hydrodynamic actions on a flexible body. *Journal of Institue of Industrial Science, University of Tokyo*, 49, pp.8–19.

Xia, J., Wang, Z. & Jensen, J.J., 1998. Non-linear wave loads and ship responses by a time-domain strip theory. *Mar.Structs*, 11, pp.101–123.

Yan, H. & Liu, Y., 2010. Efficient computations of fully-nonlinear wave interactions with floating structures. In *In Proceedings of the 20th International Offshore and Polar Engineering Conference*. pp. 645–655.

Zhao, R. & Faltinsen, O.M., 1993. Water entry of two-dimensional bodies. *Journal of Fluid Mechanics*, 246, pp.593–612.

Zhu, S., Wu, M. & Moan, T., 2011. Experimental investigation of hull girder vibrations of a flexible backbone model in bending and torsion. *Appl. Ocean Res.*, 33(4), pp.252–274.

Zienkiewicz, O.C., Taylor, R.L. & Nitharasu, P., 2014. *The Finite Element Method for Fluid Dynamics* Seventh., Oxford: Butterworth-Heinemann.

Appendix A

ADDED MASS AND DAMPING COEFFICIENTS FOR A UNIFORM FLEXIBLE BARGE USING VOF

J.H.KIM

Department of Naval Architecture and Ocean Engineering, Seoul National University
Gwanak-gu, Seoul, South Korea

P.A.LAKSHMYNARAYANANA, P.TEMAREL

Fluid Structure Interactions Group, University of Southampton
Southampton, Hampshire, United Kingdom

11th International Conference on Hydrodynamics, 19th-24th October 2014, Singapore

ADDED MASS AND DAMPING COEFFICIENTS FOR A UNIFORM FLEXIBLE BARGE USING VOF

J.H.KIM

Department of Naval Architecture and Ocean Engineering, Seoul National University
Gwanak-gu, Seoul, South Korea

P.A.LAKSHMYNARAYANANA, P.TEMAREL

Fluid Structure Interactions Group, University of Southampton
Southampton, Hampshire, United Kingdom

The main aim of this paper is the numerical investigation of the effect of domain size and mesh density on modeling the three-dimensional (3-D) the radiation problem using RANS CFD software. The solution for the radiation forces and moments, namely the added mass and damping coefficients, is obtained by imposing a simple harmonic oscillation to a marine structure floating in still water at the relevant mode shape. A uniform barge is used to illustrate the investigation, with the relevant symmetric mode shapes provided from the Euler beam theory. The hydrodynamic coefficients for symmetric oscillations of the barge are evaluated using an inviscid flow model in STAR-CCM+. These include the rigid body motions of heave and pitch and the 2- and 3-node distortion mode shapes. A range of mesh densities, between 1.1M and 9.6 M, are used to examine their effects with particular reference to low and high frequencies and the cross-coupling hydrodynamic coefficients between rigid and distortion modes. The influence of the damping zone on the solution is also examined. The RANS CFD predictions are compared with the results from a three-dimensional potential flow boundary element method, allowing for hull distortions.

1 Introduction

Substantial progress has been made during the last few years in dealing with the nonlinear response of a rigid ship travelling in regular waves, using potential flow analysis and Reynolds Averaged Navier-Stokes (RANS) methods [1]. Prediction of the nonlinear behaviour of a flexible hull in waves using 3-D flow analysis, on the other hand, has not received much attention. Dealing with hydroelasticity is of vital importance considering the increasing size ships and offshore structures, as rigid body assumptions to evaluate the wave-induced motions and loads of real ships will, inherently, omit important dynamic features [2, 3]. Use of RANS method, either through commercially available or in-house software, has been relatively widespread in modelling violent flows associated with, for example, slamming and sloshing [4, 5]. However, their application to model the problems of seakeeping and wave-induced loads has been relatively limited. For example, there are applications for the two-dimensional radiation problem of obtaining the hydrodynamic coefficients in sway, heave and roll [6] and the 3-D problem presented by Paik et al. involving CFD and FEM codes and different ways of coupling [7].

In this paper we present the computations of hydrodynamic coefficients of a stationary uniform rectangular barge, in still water, undergoing forced simple harmonic oscillations in symmetric rigid body and distortion modes, for a range of frequencies between 0.2 and 2.0 rad/s. These computations were carried out using the STAR-CCM+ software, using the inviscid flow option, and 3-D modelling. The predictions were compared against three-dimensional potential flow results using the Green's function for pulsating source. The eigen vectors for the distortion modes were calculated using polynomial approximations fitting the Euler beam idealisation. The main aim of this paper is to highlight the effects of domain size, mesh density and the influence of damping zone on the predicted hydrodynamic coefficients, in the range of frequencies investigated. Particular attention is paid to the cross coupling coefficients and satisfaction of relevant symmetry conditions.

2 Numerical Modelling

2.1 *The Numerical Method*

The RANS equations form the mathematical background of the methodology in the STAR-CCM+ software used in this paper [8]. For the case of inviscid flow these reduce to the well-known Euler

equations. In this software a finite volume method is used to discretize the fluid domain with control volumes (CVs) corresponding to the size of computational cells. The integral form of conservation equations is discretized and applied to each cell centre. Each equation is a function of pressure and velocity at the cell centre and in the neighbouring cells. FOR nonlinear equations iterative techniques are applied for linearization. The mid-point method is used to compute the space integrals, implying that the surface integrals are a product of the integrand at the cell face centre and the area of the face and the volume integrals are the product of mean integrand value and the CV. Both are 2^{nd} order accurate if the integrand is also calculated to 2^{nd} order accuracy. The Hybrid Gauss-Least Square gradient method is used to solve the transport equations.

2.2 *The Numerical Model of the Barge*

The geometry under consideration is a uniform rectangular barge, whose main particulars are given in Table 1. Both the geometry and fluid domain were modelled using the inbuilt CAD modelling option in STAR-CCM+ which provides various volume meshing models [8]. In this study, a combination of trimmer and extruder mesh was used. Trimmer cell mesher is a robust and efficient method of producing high quality hexahedral meshing with minimal cell skewness. Once a core mesh is identified and generated, extruder mesher produces orthogonal extruded cells for specific boundaries. Based on the extrusion parameters (i.e. number of layers, stretching ratio, extrusion magnitude) the mesh is extruded from the specific boundary in normal direction. Extruder meshing not only aids in saving the global cell count of the model but also assists in efficiently refining the cells in regions where the flow features have to be accurately captured. The mesh growth rate was kept under 1.1 to prevent any wave reflections arising due to sudden change in mesh sizes of adjacent cells.

Table 1. Main particulars of the Rectangular Barge.

Main Particulars	Barge
Length	120 m
Breadth	7 m
Depth	11.15 m
Draft	5.575 m

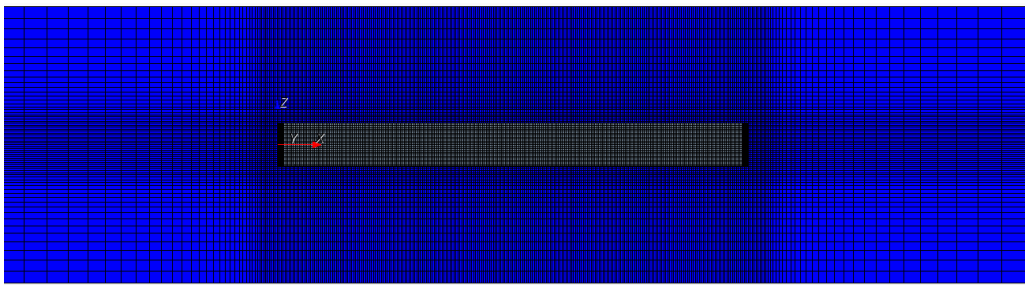

Figure 1. Core mesh of barge (xz plane) and the extrusion of inlet and outlet

The domain is modelled in three dimensions, with x along the barge and y and z in athwarthships and vertical directions, respectively. The generated core mesh (xz plane) for a particular case, corresponding to 2.6 million cells, is shown in Figure 1. The size of the domain was decided based on the wave lengths of individual frequencies. The length of the inlet, outlet and the domain breadth were divided into two zones, namely wave propagation zone and the damping zone. The lengths of both these zones were equal to the wavelength of the radiated wave. The Star-CCM+ inbuilt volume of fluid damping (VOF) option, introducing resistance to the vertical motion, was activated in the damping zone. The water and air depth (z direction) was 0.5*wavelength for deep water condition. The range of frequen-

cies investigated was from 0.2 rad/s to 2.0 rad/s in steps of 0.2 rad/s, as illustrated in Table 2 with their respective domain sizes. Additional meshes used are discussed in Section 4.

Table 2. Summary of frequencies investigated and their respective domain sizes.

Frequency	0.2 rad/s	0.4 rad/s	0.6rad/s	0.8 to 2.0 rad/s
Wavelength	1539.658 m	384.914 m	246.345 m	61.583 m
Wave Propagation Zone	1539.658 m	384.914 m	246.345 m	61.583 m
Damping Zone	1539.658 m	384.914 m	246.345 m	61.583 m
Water & Air Depth	769.829 m	192.457 m	123.1725 m	30.79 m
Number of Cells	4.4 million	2.6 million	2.2 million	1.1 million

2.3 *Boundary Conditions, Motions and Solution*

The boundary conditions were selected so that they mimic the conditions of a towing tank. Since the body used in this study is symmetrical about its longitudinal axis, symmetry plane boundary condition was used and only one half of the rectangular barge was modeled. STAR-CCM+ provides various options to assign motion to a body. Morphing motion was used in this study to assign motion to the barge. Morphing is a dynamic mesh technique where the points and their associated displacements are interpolated by the morpher throughout the region to displace the actual vertices of the discretized domain. Deformation of morpher control points was specified using grid velocities. The regions and their respective boundary conditions and morpher motion is summarized in Table 3.

Table 3. Regions and their corresponding boundary conditions morpher motion and damping

Region Name	Boundary Condition	Morpher Motion	Damping Condition
barge (body)	wall	Grid velocity	
inlet	wall	fixed	VOF damping
outlet	wall	fixed	VOF damping
sym_wall	symmetry plane	NA	
top	wall	fixed	
bottom	wall	fixed	
wall (y extent)	wall	fixed	VOF damping

The velocity of a body undergoing simple harmonic motion is given by:

$$\dot{y} = \omega y_a \cos \omega t \qquad (1)$$

where $\dot{y}$ is the velocity, ω is the frequency of oscillation (rad/s), y_a the amplitude and t time (s). Morphing motion is imposed using grid velocities computed using Equation (1). In this study we are interested in the rigid body motions of heave and pitch and the vertical 2- (2VB) and 3- node (3VB) distortions. The grid velocity for each morphing motion was imposed as a vector multiplying the velocity in Equation (1) with the eigen vector for individual rigid body motions or distortions. For example the grid velocity vector for heave is:

$$gridvelocity = \omega y_a \cos \omega t * eigenvector \qquad (2)$$

where [0, 0, 1] is the eigen vector for heave.

The eigen vectors for the distortion modes were calculated using Euler Beam theory approximated using polynomials. VOF wave model was used to initialise the air-water interface. That is to say a first order wave with zero amplitude was initialised to model the still water condition. The inviscid computations were performed with the help of an implicit unsteady solver and 2nd order discretization scheme. For numerical stability, local Courant numbers given by $CFL = U\Delta t / \Delta x$, should in general be less than

1. CFL relates to the cell dimension Δx, time step Δt and the flow velocity U. The time step for each simulation was calculated ensuring the Courant number is approximately 0.4. The phase velocity of the radiated wave was used as the flow velocity U. The excitation amplitude was 1 m for frequencies less than 1 rad/s and 0.2m for frequencies equal to or greater than 1 rad/s.

2.4 *Hydrodynamic Coefficients of the Barge*

To obtain the added mass and damping coefficients of the barge undergoing oscillations given by Equation (1), the dynamic force component in the direction of motion is required. In morphing motion the body is considered massless, i.e. at static condition the vertical force on the body is the initial buoyancy. The dynamic force is the difference of the static force from the total force experienced by the barge. Static and total forces for rigid body motion and distortions were successfully calculated in STAR-CCM+ with user-defined field functions. The static force on the body was calculated on the mean free surface. The vertical dynamic force distribution along the barge was then transformed into a generalised force F_{rs}(t), by multiplying with the s^{th} eigenvector and integrating along the barge [3]. Here r denotes the index of the mode at which the barge is oscillated. Instantaneous values of the hydrodynamic coefficient are obtained by Fourier analysis of the dynamic force F_{rs}(t) time history using discrete windows approach for one period, $T=2\pi/\omega$, of oscillation, namely

$$A_{rs} = \frac{2}{T\omega^2} \int_{t-T/2}^{t+T/2} F_{rs}(t) \sin(\omega t) dt \tag{3}$$

$$B_{rs} = -\frac{2}{T\omega} \int_{t-T/2}^{t+T/2} F_{rs}(\mathrm{t}) \cos(\omega t) dt \cdot \tag{4}$$

3 Results and Discussion

The results of a stationary uniform barge harmonically oscillating, at the relevant mode shapes, at a free surface are presented in this section. Predictions using inviscid flow with STAR-CCM+ for the diagonal and off-diagonal terms were compared against three-dimensional potential flow results using the pulsating source Green's function [3]. Good agreement was seen in the diagonal terms but discrepancies were noted in the off-diagonal terms, especially in relatively low frequencies.

To investigate these discrepancies (a) extended domain and (b) refined grids. The size of the extended domain was based on a wavelength corresponding to the frequency of 0.1 rad/s and had a total cell count of about 6.8 million. In this case the refinement on the body and free surfaces was similar to other, coarse, meshes used (see Table 2). As it is not practical to eliminate reflected waves, and their effects on the predictions at lower frequencies, the extended domain was used to run computations in cases where the predictions deviated largely from the 3-D potential flow results. For refined grids, for the sake of simplicity, a refinement ratio (fine mesh size/coarse mesh size) of 2 is used around the body in the core mesh and the adjacent cell size in the extruder mesh is maintained as 1.1 for all directions. The refinement ratio on the free surface was a little more than $\sqrt{(2)}$. Use of refinement resulted in an increase in the total grid size by a factor of about 4. For example, in the case of 0.4 rad/s the refined grid has a total cell count of 9.6 million.

The hydrodynamic coefficients calculated for the rigid body motions of heave and pitch are presented in Figure 2. A very good agreement with potential theory predictions can be observed. A sudden slump is seen at ω=1.6 rad/s in the hydrodynamic coefficients calculated using potential theory in all cases, corresponding to an irregular frequency. In the case of pitch the discrepancies noted at 0.4 and 0.8 rad/s in Figures 2(c) and (d), respectively, were further investigated. Use of the extended (6.8M) mesh did not change the predictions significantly. However, use of the refined grids (fine) resulted in closer agreement with potential flow results.

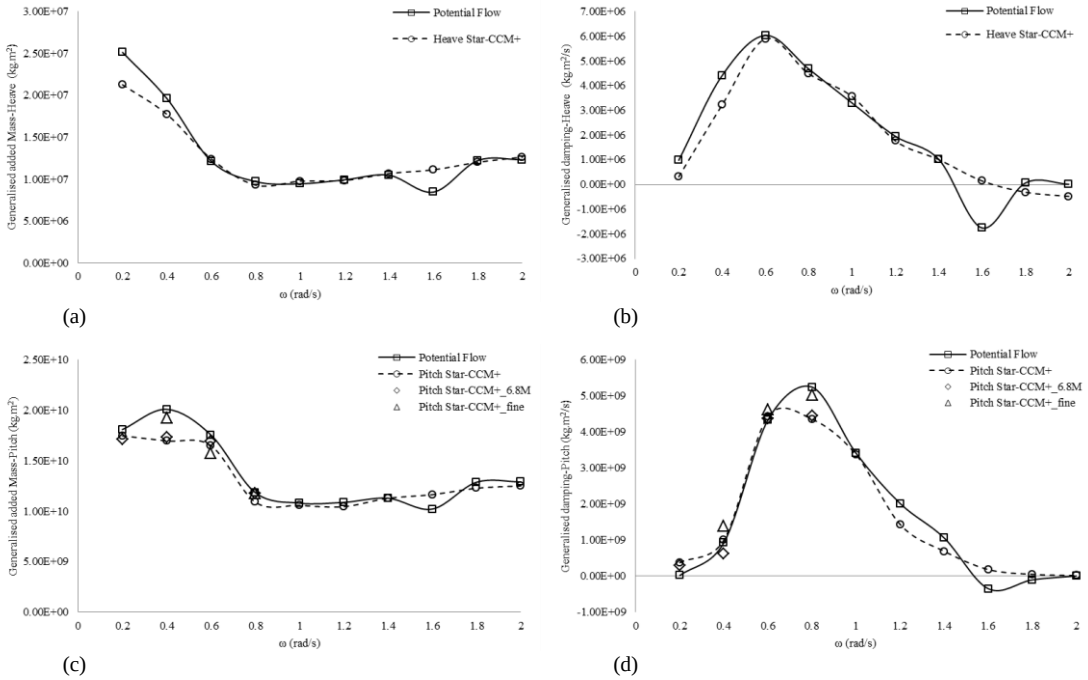

Figure 2. Comparison between generalized added mass and damping coefficients obtained from 3-D potential flow analysis and CFD analysis (inviscid): (a) & (b) Heave motion, (c) & (d) Pitch motion

The comparisons of hydrodynamic coefficients for the distortion modes are shown in Figure 3. The agreement with potential flow results is better for the added mass than the fluid damping coefficients. Differences in fluid damping were observed in the lower frequencies and the numerical results showed slight over prediction when compared to potential flow results. Further investigations were carried out for the 3VB hydrodynamic coefficients with additional meshes for 0.4 to 0.8 rad/s. Neither an improvement nor any deterioration was seen in the predictions using the extended domain (6.8M). In the case of refined grids (fine), slightly better agreement was observed compared to the potential flow.

The predictions for cross-coupling coefficients between Heave and 2-node (2VB) distortion mode and Pitch and 3-node (3VB) distortion are presented in Figures 4 and 5, respectively. It is expected that the upper diagonal and lower diagonal terms will be same for a stationary symmetrical body, such as the barge use in this study.

The off-diagonal terms of Heave-2VB and 2VB-Heave compare well with potential flow results, except for significant differences observed at low frequencies. Computations using the extended domain (6.8M) show some improvement for the added mass at 0.2 rad/s, but no improvement for the damping. The calculated off-diagonal terms improved using the refined grid (fine) at 0.4 rad/s. Although a small difference is observed when compared to potential flow, the CFD-predicted cross-coupling damping coefficients are close to each other.

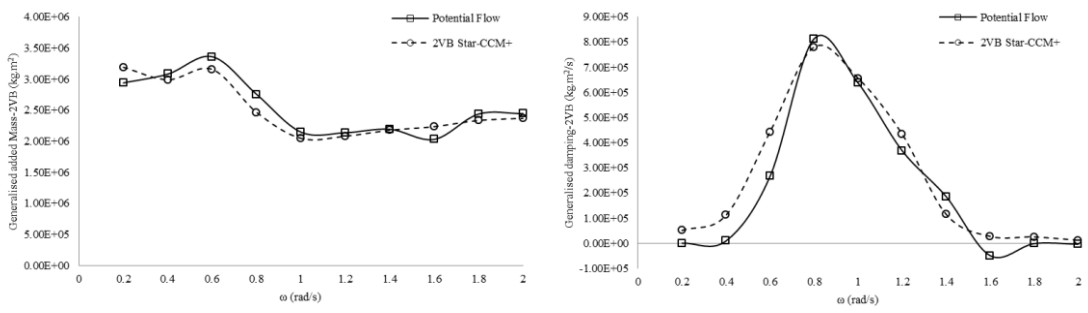

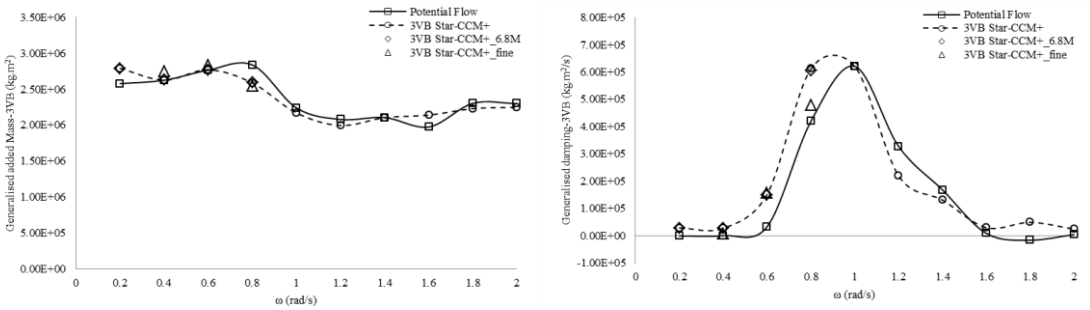

Figure 3. Comparison between generalized added mass and damping coefficients obtained from 3-D potential flow analysis and CFD analysis (inviscid) : (a) & (b) 2-node distortion mode, (c) & (d) 3-node distortion mode

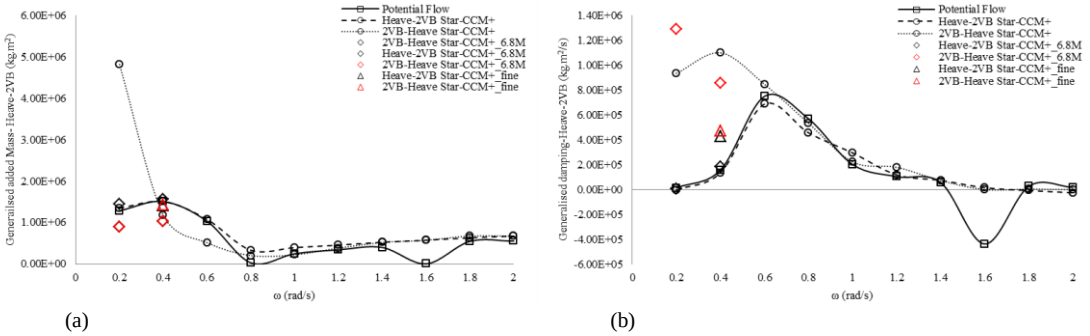

Figure 4. Comparison between generalized added mass and damping cross coupling coefficients obtained from 3-D potential flow analysis and CFD analysis : (a) & (b) coupling coefficients of Heave in 2-node distortion and 2-node distortion in Heave.

CFD predictions presented for Pitch-3VB and 3VB-Pitch terms show least agreement with potential flow results. Except for a few frequencies Pitch-3VB shows better agreement than 3VB-Pitch coefficients. Furthermore, the CFD predictions show large deviations when compared with each other. Omitting the relatively lower frequencies, added mass coefficients showed better symmetry than the damping coefficients which showed large deviations for all frequencies investigated.

As observed in the previous cases, use of extended fluid domain model (6.8M), by and large, made only small improvements to the agreement of inviscid CFD predictions with potential flow, and no improvement to the symmetry relationships. There is a substantial improvement in the predicted coefficients when using the refine grids (fine). The asymmetry in the magnitude of the off-diagonal coefficients is much less for the refined grids. Differences in the level of agreement with potential flow can be partially explained by the fact that although the computations are done using an inviscid model, CFD solves Navier-Stokes equations which account for non-linearity.

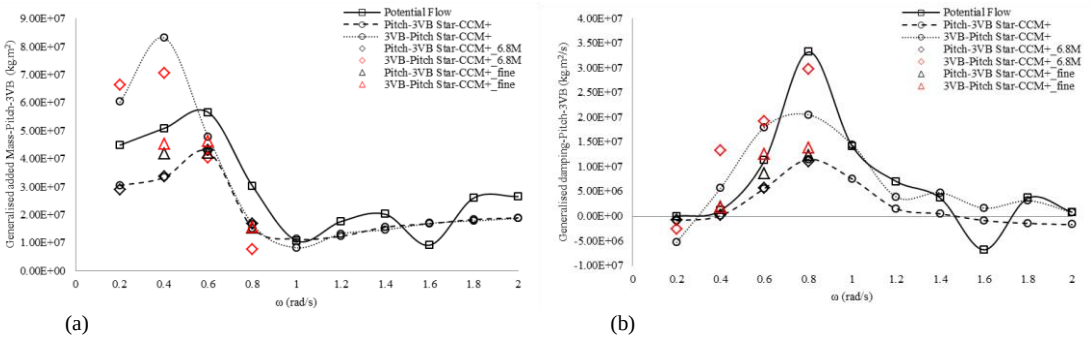

Figure 5. Comparison between generalized added mass and damping cross coupling coefficients obtained from 3-D potential flow analysis and CFD analysis : (a) & (b) coupling coefficients of pitch in 3-node distortion and 3-node distortion in pitch.

The difference in the calculated coefficients for the 3VB-Pitch term for the refined grids is highest among all mesh densities, compared to the Pitch-3VB term. This could be attributed to the complexity involved in calculating the generalized forces in the 3-node distortional mode when compared to the rigid body motion. The magnitude of dynamic forces are quite small in relatively lower frequencies and the accuracy in calculating the forces is very sensitive to the mesh refinement on the body. The mesh refinement on the free surface also contributes largely to the radiated wave pattern and flow field, and thus the hydrodynamic coefficients.

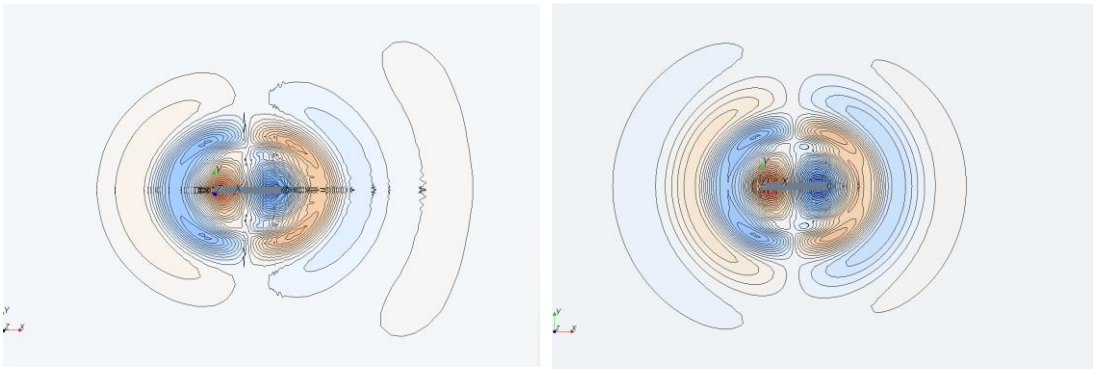

(a) (b)

Figure 6. Contour lines of radiated waves for pitch mode at 0.8 rad/s taken at t=10.0s : (a) extended domain; (b) refined grid.

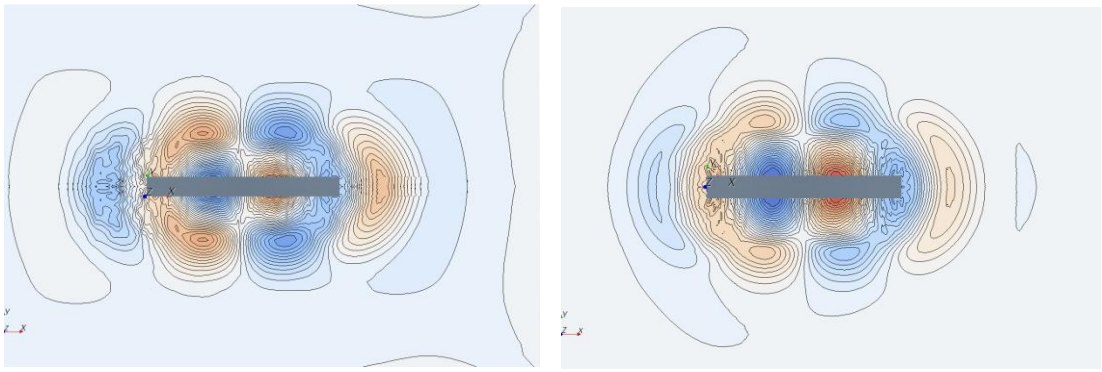

(a) (b)

Figure 7. Contour lines of radiated waves for 3VB mode at 0.8 rad/s taken at t=10.0s : (a) extended domain; (b) refined grid.

Figure 6 and 7 show the contour lines of the waves radiated away from the body for the extended domain (6.8M) and refined grid. The wave contours in the pitch motion, shown in Figure 6, are not significantly different from each other for either model. Except for a few numerical noises in the far field, the radiated waves for the rigid body motion do not change much for the refined grid as compared to the coarse mesh of the extended domain. However differences can be spotted in the case of the 3-node distortional mode, shown in Figure 7. The waves radiated from the body dampen out very close to the body in the coarser mesh of the extended domain, whereas, in the refine grid there is less numerical noise around the body, and better defined wave crests and troughs are developed. Along with the symmetry in the calculated coefficients, the flow field contours also contribute in predicting the hydrodynamic coefficients with a good degree of accuracy.

4 Conclusions

In this work, hydrodynamic coefficients of a stationary barge harmonically oscillating in still water was successfully calculated using STAR-CCM+, with inviscid flow option, for symmetric rigid body and

distortional modes, and compared to results from a 3-D potential flow method. Good agreement was achieved in most cases investigated, with some exceptions for the cross-coupling coefficients. Computations in lower frequencies were particularly difficult due to the large length of the radiated wave which calls for large domains and damping zones to prevent any wave reflections. The discrete time window for the calculation of hydrodynamic coefficients is also large in the case of low frequencies, which is likely to introduce errors in calculations. The dynamic force in the low frequencies is very small when compared to the static component; hence the results are very sensitive to mesh densities. Extended domain and damping zones did not improve the quality of solution in relatively lower frequencies. Major discrepancies were observed in the case of cross coupling between 3VB and Pitch modes which can be eliminated to a large extent using refined grids. It is concluded that by comparing the symmetry in the cross-coupling coefficients and observing the radiated wave contour, the radiation problem of a symmetric body can be solved with confidence and accuracy.

The next stage of the investigation will involve the coupled antisymmetric (horizontal bending and twisting) hydrodynamic coefficients, likely to introduce further complexities in terms of radiated waves.

Although this investigation was limited to the radiation problem, namely added mass and damping coefficients, the conclusions drawn are applicable to the modelling of the behaviour of ship in regular waves, a problem currently being investigated.

Acknowledgements

The authors from University of Southampton would like to gratefully acknowledge the support from Lloyd's Register and the Lloyd's Register Foundation through its University Technology Centre.

References

1. ISSC, Report of Committee I.2: Loads. **1** 79–150 (2012).
2. Bishop, R.E.D. and Price, W.G., *Hydroelasticiy of Ships*, Cambridge University Press (1979).
3. Bishop, R.E.D., Price, W.G. and Wu, Y., A general linear hydroelasticity theory of floating structures moving in a seaway. *Phil. Trans. R. Soc. Lond.* **A316** 375–426 (1986).
4. Brizzolara, S., Couty, N., Hermundstad, O., Kukkanen, T., Ioan, A., Kukkanen, T., Viviani, M. and Temarel, P., Comparison of experimental and numerical loads on an impacting bow section. *Ships and Offshore Structures* **3(4)** 305-324 (2008).
5. Brizzolara, S., Savio, L., Viviani, M., Chen, Y.G., Temarel, P., Couty, N., Hoflack, S., Diebold, L., Moirod, N. and Souto Iglesias, A., Comparison of experimental and numerical sloshing loads in partially filled tanks. *Ships and Offshore Structures* **6(1-2)** 15-43 (2011).
6. Querard, A.B.G., Temarel, P. and Turnock, S.R., Application of RANS to hydrodynamics of bilge keels and baffles. *William Froude Conference on Advances in theoretical and applied hydrodynamics* – Past and Future, Portsmouth, GB (2010).
7. Paik, K.J., Carrica. P.M., Lee, D. and Maki, K., Strongly coupled fluid–structure interaction method for structural loads on surface ships. *Ocean Engng* **36** 1346–1357 (2009).
8. STAR-CCM+, STAR-CCM+ version 7 manual. (2012).

Appendix B

HYDROELASTIC ANALYSIS OF FLEXIBLE BARGE IN REGULAR WAVES USING COUPLED CFD-FEM MODELLING

P.A.LAKSHMYNARAYANANA, P.TEMAREL & Z.CHEN
Fluid Structure Interactions Group, University of Southampton
Southampton, Hampshire, United Kingdom

5th International Conference on Marine Structures, 25th-27th March 2015, Southampton, U.K

Hydroelastic analysis of a flexible barge in regular waves using coupled CFD-FEM modelling

P.Lakshmynarayanana, P.Temarel & Z.Chen
Fluid Structure Interactions Group, University of Southampton, Southampton, U.K

ABSTRACT: The aim of this paper is to investigate the wave-body interaction of flexible floating bodies by coupling RANS/CFD and Finite Element software. A combination of overset and morphing approaches and finite volume solution to allow for the motion of a barge at the free surface is used. Results are presented for the motion response of the three-dimensional (3-D) barge, treated both as rigid and flexible body, in regular head waves using STAR-CCM+, the latter carried out by a two-way coupling between Star-CCM+ and Abaqus. To illustrate this application, the structure of the flexible barge is modelled as a beam, in line with the flexible backbone model used in experiments. The RAOs of vertical displacements, at a number of positions along the barge, calculated using this coupling technique is compared against experimental measurements and two-dimensional (2-D) linear hydroelasticity predictions.

1 INTRODUCTION

Modern seakeeping computations of ships are carried out using a variety of techniques ranging from two-dimensional (2-D) strip theory using potential flow methods to solving fully nonlinear unsteady RANS (Reynolds-averaged Navier-Stokes equations) methods. Application of CFD (Computational Fluid Dynamics) to study wave-body interactions of ships and offshore structures using RANS have increased over the years due to increase in computational power (ISSC. 2012) . Traditionally, seakeeping analysis of ships is carried out treating them as rigid bodies. However, the ever increasing size of ships and offshore platforms have resulted in 'softer' or flexible hulls which require hydroelastic effects to be taken into account when predicting fluid-structure interactions (Bishop & Price 1979). Such investigations are predominantly experimental, using flexible backbone models, or numerically using potential flow solvers (Bishop et al. 1977). Although partial nonlinear potential flow methods are also used, RANS/CFD can fully take into account the free-surface and body nonlinearities as well as viscous effects, making it more efficient and realistic for some problems (Brizzolara et al. 2008).

Presently the majority of investigations using RANS/CFD and FEA are carried out using one-way coupling. When the deformations of the structure are large enough to significantly affect the flow field around it, one-way coupling would omit some important fluid-structure interactions. A two-way coupling method will be more suitable in such cases. Few investigations employing two-way coupling have shown promising results (Paik et al. 2009) (Kim & Kim 2009), but need further investigations.

In this study a two-way coupling between a finite volume CFD method, using Star-CCM+ (version 8.04), and a finite element method (FEM), using Abaqus (version 6.13-1), is applied to assess the hydroelastic effects of a flexible barge in regular head waves. Only symmetric distortions of the barge for a number of wave frequencies are employed and compared against experimental measurements (Remy et al. 2006). 3-D computations are first carried out treating the barge as a rigid body to establish the influence of domain size and mesh refinement along the free surface and the barge. A two-way coupling is then established between Star-CCM+ and Abaqus to investigate the hydroelastic response. The coupling takes place through exchanging pressures and displacements between Star-CCM+ and Abaqus more than once every time-step, namely implicit scheme. The structure is modelled as a non-uniform Timoshenko beam with properties, such as stiffness and mass distribution, as per the model test data. Numerical predictions are also obtained using 2-D hydroelasticty (Bishop et al. 1977). RAO of vertical displacements at various locations along the barge is compared against experimental measurements and numerical predictions to validate the coupling method used.

2 NUMERICAL METHOD

2.1 *Finite Volume Method*

The CFD software used for all computations in this paper is Star-CCM+. Here we present only a brief description of the numerical method implemented and a detailed theoretical background is provided by(Ferziger & Peric 2003).

The numerical method used in Star-CCM+ is a finite volume (FV) method in which the flow is assumed to be governed by RANS equations. The RANS equations reduce to the well known Euler equations for the case of inviscid flow. First, the spatial fluid domain is discretized into a finite number of control volumes (CVs) or cells. The integral form of conservation equation, with the initial and boundary conditions, is then applied to cell centres and simplified into an algebraic system of equations. The governing equations not only contain surface and volume integrals but also time and spatial derivatives. They are solved using a segregated iterative algorithm, called SIMPLE. All integrals are computed using midpoint rule. The Hybrid Gauss-Least Square gradient method is used to solve the transport equations.

Free surface flows are implemented using the Volume of Fluid (VOF) tracking method. In order to account for the position of free surface in multiphase flows and allow for its arbitrary deformation, an additional equation is solved for the volume fraction *c*.

When the motion of a body at a free surface is involved, the position of the body is updated at each iteration. The equations of motion of the body are solved to obtain the velocities and, hence, update the displacements and rotations. The fluid grid is adjusted at every outer iteration to follow the updated position of the moving body.

2.2 *Grid Adaptation in FSI*

In the present study, grid adaptation to follow the motion of body is implemented by two different methods, namely morphing and overset grids, the choice depending on the problem solved. In the case of a two-way coupling, the nodal displacements imported from Abaqus redistribute the mesh vertices by generating an interpolation field throughout the domain. The deformation of the fluid grid must conform to the body and also maintain a good quality of finite volume grid. The arbitrary motion of the mesh vertices is taken into account when solving the fluid transport equations. Star-CCM+ uses a “space conservation law” to balance the volume of a CV as a function of time and the motion of the surface.

Morphing could create problems in the case of large body motions and waves. The deformation of the entire grid could result in the free surface to fall outside the refined region of the grid, resulting in high numerical diffusion before the wave reaches the body. To avoid this problem, an overset or overlapping grid can be used. In this case two regions, background and overset are created, where the background grid is adapted to the free surface. The overset grids are attached to the floating body and move with it freely depending on the motion response.

For rigid body simulations of the barge in head waves, grid adaptation has been carried out using overset grids. In the case of two-way coupling, both morphing and overset is applied to move the grid to follow the barge motions. Morphing condition is set to the boundaries of the barge and it deforms due to the nodal displacements supplied by Abaqus. Floating condition is set as the Morpher boundary condition for the overset, so that it moves freely in accordance with the grid deformation applied by the morpher.

2.3 *Coupling Scheme*

The coupling schemes control the sequence of data exchanges in the simulations. There are two major coupling schemes in Star-CCM+. For a loosely coupled problem an explicit scheme can be chosen. In this scheme, the data or field exchange takes place once every time step. An implicit scheme is chosen when strong coupling is sought as it is more stable than the former, but at a higher computational cost. In the implicit scheme, field exchanges between the software take place at every single iteration within a time step. The explicit scheme was tested with even very small time steps but resulted in pressure divergence.

2.4 *Field data exchange*

The coupling is implemented by exchanging pressure and nodal displacements, the so called field data, between Star-CCM+ and Abaqus. The geometry of the floating body must have the same dimensions and coordinates in both software; otherwise the co-simulation will fail due to inconsistency in topology.

The response of the fluid to the structural deformations is expressed through the grid flux term. It represents the ratio of volume swept due to the movement of cell face from one time step to the next time step. Grid flux intensity can be calculated by the product of normal velocity of the face and its area.

In transient simulations, the initial conditions are far from realistic. For the simulation to settle down during the initial phase, it is recommended to relax the grid flux term by lowering the grid flux URF (under relaxation factor). Large fluctuations in pressure at the fluid-structure interface can be decreased using a lower value of grid flux URF. However, a value of URF less than 0.5 will lead to an unrealistic, time-inaccurate solution, especially for problems requiring dynamic accuracy.

2.5 *2-D Hydroelasticity analysis*

Generalised coordinates for rigid and flexible motions of the barge is calculated using the 2-D hydroelasticity method by (Bishop et al. 1977). In brief, the strip theory is used to calculate the hydrodynamic properties of the barge, using Lewis form representation. The barge structure is modelled as a Timoshenko beam. Modal summation is employed to represent vertical displacement, bending moment and shear force at a specified location. The resultant unified equations of motion in regular waves provide the requisite generalized coordinates for a range of wave frequencies.

3 NUMERICAL SIMULATIONS OF A BARGE IN REGULAR WAVES

3.1 *Barge Characteristics*

The experimental model of a flexible barge consisting of 12 connected caissons is considered for validation of the present numerical method (Remy et al. 2006). Each caisson is clamped to a steel rod which is placed at 57 mm above deck level. The rod has a square cross-section of 1 cm × 1 cm. All the caissons are rectangular sections, except for the bow caisson, which has a bevelled shape. The towing tank dimensions are 30m×16m×1 m.

The main characteristics of the barge and the flexible rod are given in Table 1.

Table 1: Barge characteristics

Length of barge, L_{PP} (caissons + clearance)	2.445 m
Beam	0.6 m
Depth	0.25 m
Draft	0.12 m
KG	0.163 m
Total mass (caissons + equipment)	172.5 kg
Length of each caisson	0.19 m
Mass of each caisson (except bow)	13.7 kg
Mass of bow caisson	10 kg
Moment of inertia of rod	8.33×10^{-10} m^4
Bending stiffness of rod	175 N m^2
Young's modulus of rod	2.1×10^{11} N/ m^2

Vertical, horizontal and torsional bending was allowed for the barge model and tests were conducted in regular and irregular waves of varying headings. In the case of regular wave, the barge motions were measured at 6 different locations, as shown in Table 2 (x, y and z measured from stern, centerline and the keel of the barge) for a number of wave periods.

Table 2: Measuring points from aft of barge

Location	x (m)	y (m)	z (m)
1	2.445	0.0	0.25
3	2.035	0.0	0.25
5	1.625	0.0	0.25
7	1.225	0.0	0.25
9	0.805	0.0	0.25
12	0.19	0.0	0.25

3.2 *Test Conditions*

Two types of simulation were carried out in the present study.

1. Response of the barge, treated as a rigid body, in head regular waves is calculated for the five wave periods, shown in Table 3. The objective is to obtain insight into domain size, damping zones, motion of rigid body and mesh refinement around the body and free surface for each wave period. The rigid body responses calculated using CFD is compared against 2-D predictions.

2. Response of the barge, treated as a flexible body, in head regular waves is calculated for the same periods. A two-way coupling technique is implemented between Star-CCM+ and Abaqus to simulate hydroelastic response of the barge. Comparisons were made against experimental measurements and hydroelastic predictions.

Table 3: Test Conditions

Wave Period (s)	Wave Frequency (rad/s)	Wave Length (m)	Wave Height
1.8	3.490	5.058	100 mm
1.6	3.926	3.996	100 mm
1.2	5.235	2.248	100 mm
1.0	6.283	1.561	100 mm
0.9	6.981	1.264	100 mm

3.3 *Computational Domain*

A 3-D domain is used for all CFD calculations, with x along the barge and y and z in the athwartships and vertical directions, respectively. The lengths of the domain in the inlet-outlet and side wall directions are generally calculated based on L_{PP} or wave length (λ) based on similar ship-wave interaction studies (Peric et al. 2007) (Seng et al. 2012). In the present study, the wavelength to barge length (λ/L) ratio varies from 2 to 0.4. For $\lambda/L \geq 1$, the inlet and wake region is located at about 1.5 λ and 2λ, respectively, from the barge. The length of inlet and wake region for cases $\lambda/L \leq 1$ is 2.0 L_{PP} for both. A numerical beach is provided at the outlet to damp the waves and prevent any reflections. The length of this damping region is set to 1.5 λ. In the CFD simulations, the length of the side wall (y-direction) is fixed as 8 meters (same as the tank) on one side of the barge for all cases. Initially, a reduced length of the side wall (6 meters) was tested for a few frequencies. They showed evidence of wave reflections from the side walls after 4-5 wave periods. The domain sizes selected for each wave frequency, for both rigid body and coupled simulations, are shown in Table 4. Symmetry condition is used for rigid body simulations, whereas full domain is modelled for the co-simulation cases.

Table 4: Summary of domain sizes against wave lengths
* port side only

Wave Length (m)	Location of Inlet (m)	Wake Region (m)	Damping Zone (m)	Side wall * (m)	Water Depth (m)
5.058	7.6	10	7.6	8.0	4.0
3.996	6.0	8.0	6.0	8.0	4.0
2.248	5.0	5.0	3.5	8.0	4.0
1.561	5.0	5.0	2.5	8.0	4.0
1.264	5.0	5.0	2.0	8.0	4.0

3.4 *Meshing Strategy & Boundary Conditions*

Star-CCM+ provides various volume meshing models. In all the present investigations, a combination of trimmer, extruder and overset mesh is used. For the same wave frequency, the mesh refinement used for both rigid body simulations and co-simulations is identical. Trimmer mesher is a robust and efficient method of producing high quality hexahedral meshing with minimum cell skewness. Once the core mesh is created, the extruder mesh produces orthogonal extruded cells for user specified boundaries only. The mesh is extruded from the specific boundary in the normal direction based on the user specified extrusion parameters (i.e. number of layers, stretching ratio and extrusion magnitude). The side wall, in y-direction, and the outlet in all models is extruded using appropriate extrusion parameters. Not only does this aid in saving the global cell count but also dissipates the waves in the far field due gradual coarsening of grid size. Nevertheless, the mesh growth in the extruder region was kept under 1.1 to prevent any numerical reflections arising due to sudden change in grid sizes between adjacent cells (STAR-CCM+ 2012).

The mesh was refined along the free surface region, near the barge and in the wave radiation zone around the barge using volumetric controls. A typical mesh, corresponding to 1.2s wave period, is shown in Figure 1. Mesh refinement was carried out based on the disturbed wave contour around the body. After testing a few cases it was noted that the waves radiated out of the body in a circular pattern. Hence, refinement around the body was also carried out in a manner so as to capture the disturbed wave pattern. In the free surface region, 45-60 cells are placed per wavelength and 12-15 cells per wave amplitude. Around 320 cells per wavelength and 160 cells per wavelength are clustered in the near body region (bow, stern and around body) and wave radiation zone, respectively. The global mesh count for the co-simulation case varied from 2.3 million to 13.6 million.

Boundary conditions were selected so that they mimic the conditions of a towing tank. At the velocity inlet boundary the kinematics of the wave, i.e. the position of the free surface and velocity of the first-order wave as field functions are prescribed. At the outlet boundary, the outlet pressure and the position of free surface is prescribed. The pressure at the outlet is set to the hydrostatic pressure of the wave. All other boundaries are set to no-slip wall condition.

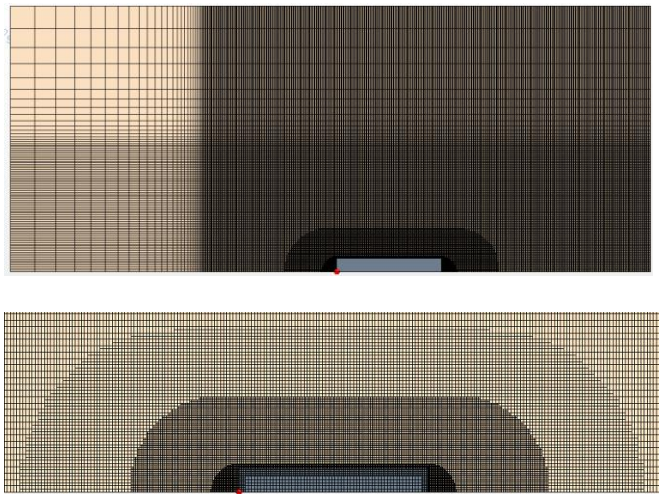

Figure 1. Mesh refinement around the body and the free surface, for wave period of 1.2s

3.5 *Rigid body Simulations*

This section describes the numerical setup and settings specific to the rigid body barge simulations. Due to symmetry of this problem, the computational domain only extends to the port side of the barge.

After an initial orientation of the body is specified by the user, Star-CCM+ automatically creates a new Cartesian coordinate system which is updated showing the position and orientation of the barge throughout the simulation. Body release and ramp time were specified for all simulations which are calculated on the basis of the time step. It is best to allow the fluid flow to initialise and become steady before the calculation of body motions commences. A typical value of 50 time steps is specified as a release time. At the release time, forces and moments are suddenly applied on the body, and can cause shock effect. To minimise this and facilitate a more robust solution by reducing oscillations, a ramp time equal to 10 times the release time is specified.

The VOF under-relaxation factor is decreased from the default value of 0.7 to 0.6. This implies that a fraction of the newly computed solution will be supplied to the old solution, and has been done to increase stability. Consequently, the number of inner iterations was raised to reach a convergent solution. Computations were carried out using inviscid fluid model with an implicit unsteady solver. The 2nd order scheme is chosen for temporal discretisation and convection of segregated flow solver and VOF solver. Time step for each simulation was chosen such that the Courant number on the free surface at all times is less than 0.5.

3.6 *Co-Simulation of the barge*

This section details the fluid solver settings specific to the coupled simulations. The boundary conditions are those used in the rigid body simulations. Co-simulations were also carried out using an inviscid flow model using implicit unsteady solver. The implicit coupling scheme was chosen for all simulations.

The grid flux URF is lowered from a default value of 1.0 to 0.8, implying that the fluid response to structural response is slightly reduced by a fraction commensurate to the URF. This was done to provide stability as many attempts with a higher grid flux URF resulted in quick pressure divergence. For some cases, where pressure peaks were observed even when the morpher was running smoothly, the URF for pressure was lowered to 0.3 from a default value of 0.4. Similar to the rigid body cases, all simulations were run using 2nd order temporal and convective schemes. When carrying out co-simulations using Star-CCM+ and Abaqus, the FSI boundary has to be defined explicitly. The barge boundary is set as the FSI boundary in the fluid mesh.

3.7 *F.E Model*

The structural or finite element mesh is modelled in Abaqus. When beam elements are used to represent structural models, they have to be linked to surface elements that define the actual wetted surface of the body. In this study, the flexible barge is represented using a 2-D beam model, with 48 beam elements. All material and geometric properties are modelled in line with model test data, shown in Table 1.

The elements chosen are the 2-node linear beam element B31 and 4-node quadrilateral surface element SFM3D4, the latter representing the barge surface. B31 is a Timoshenko beam element allowing for transverse shear deformation. Abaqus automatically calculates the transverse shear stiffness values required in the formulation of element. Please note for this investigation zero structural damping was used, since the frequency range in experiments and CFD/FE simulations was below the first resonance. Surface elements have no inherent stiffness but may have mass/ unit area, though none is specified in this case. They can be used to transmit only in-plane forces and have no bending or transverse shear stiffness. The dummy surface elements are linked to the nodes on the beam elements using kinematic coupling constraints. A large number of nodes or surfaces can be constrained to the rigid body motion of control nodes (in this case the beam element nodes) using kinematic coupling. All six degrees of freedom are constrained in the kinematic coupling of beam nodes and the dummy surface, in the sense that the beam deformations are imparted on to the barge hull. The total mass of the barge is distributed on the beam elements.

For the 2-D hydroelasticity analysis the barge is represented as a non-uniform beam element divided into 48 sections, to achieve consistency with the FE model. The mass distribution, moment of inertia for each segment, is similar to the FE model. No rotary inertia is specified for the beam elements.

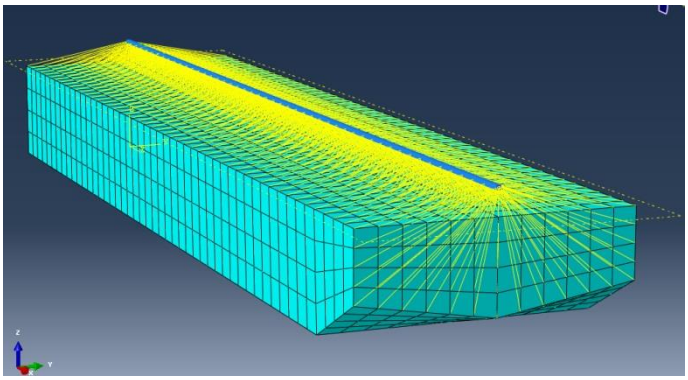

Figure 2. Finite element mesh with the beam and dummy surface linked using kinematic coupling.

4 RESULTS AND DISCUSSION

4.1 *Modal Analysis*

Modal analysis was performed in Abaqus using Block Lancozs eigen value extraction method. The natural frequencies and mode shapes obtained in Abaqus were compared against calculations performed using the finite difference method applied to a non-uniform beam (Bishop et al. 1977), to ascertain the accuracy of the modelling. The dry hull natural frequencies for the first 5 flexible modes are shown in Table 5.

Table 5: Symmetric Dry Hull natural frequencies (rad/s)

Mode	Abaqus	2-D hydroelasticity
2-node	6.01	6.03
3-node	16.43	16.49
4-node	32.00	31.10
5-node	52.66	52.73
6-node	78.426	78.34

4.2 *Simulation results*

The motion responses of the barge treated as rigid and flexible body in regular head waves are presented in this section. Predictions using the inviscid flow option in Star-CCM+ were compared against experimental measurements by Remy et al. (2006) and numerical calculations using 2-D linear hydroelasticity, the latter providing both rigid and distortional displacements along the barge.

Wave elevations were recorded at one L_{pp} in front of the barge. Time history of the wave elevations revealed very little wave dissipation, and maximum decrease in wave height was around 5-6% as the

simulation progressed. Average wave amplitude over 8-10 wave periods was used to calculate the RAOs. The heave and pitch RAOs obtained from the rigid body CFD simulation, denoted by STAR, and the corresponding 2-D hydroelasticity rigid as well as distortional principal coordinate amplitudes, denoted by MARS, are shown in Figure 3.

The rigid body response of the barge, obtain`ned from STAR-CCM+ and denoted by STAR_RIGID, is compared with the 2-D potential flow predictions, denoted by MARS_RIGID, in Figure 4. It can be seen that both numerical results predict the rigid motion response with relatively good accuracy, although discrepancies were noted especially towards the forward end of the barge, e.g. points 1 and 3.

At the forward section of the barge, strong bow waves were seen to develop in the CFD simulations from a wave frequency of 3.926 rad/s and upwards. In addition, with increase in frequency, diffraction becomes more dominant resulting in strong localized bow waves. The instantaneous wave pattern around the rigid barge, for frequencies of 3.926 and 6.0 rad/s, is shown in Figures 5 and 6, respectively. In general, very good agreement is noted at all frequencies at locations from around amidships towards the stern of the barge. At point 12 near the stern of the barge (0.19 m), the RAO of the vertical displacement predicted by CFD at 3.926 rad/s is however larger to that of the linear 2-D linear potential flow analysis. The instantaneous wave contour plot at this frequency shows strong bow and stern waves influenced by pitch motion, as seen in Figure 5. A peak in pitch response can be seen at around 4 rad/s in Figure 3.

The reason for the discrepancy between CFD and 2-D linear analysis predictions at the forward and stern sections of the barge is mainly due to the influence of strong localised wave systems, not very well predicted using a linear potential flow theory. The predictions using CFD is considered more reliable in this case since it accounts for the nonlinear interactions between wave-body. Strong 3-D effects and the bevel shape of the bow could also be one of the influencing factors for the differences observed in the two numerical results for the rigid body analysis.

RAOs of vertical displacements, for the barge treated as a flexible body, are also shown in Figure 4. Those obtained by 2-D hydroelasticity and the two-way CFD/FEM coupling are denoted as MARS_FLEX and STAR_FLEX, respectively. Very good agreement can be seen between the CFD/FEM coupling method and experimental measurements. Comparisons made between the 2-D hydroelasticity numerical prediction and the CFD/FEM coupling also show fair agreement, with some discrepancies observed at higher frequencies. The reason for these differences is attributed to the strong diffraction effects at higher frequencies also prevalent in the flexible body motions. From the amplitude of the 2-node principal coordinate, shown in Figure 3, resonance appears to occur at around 7.5 rad/s, where computations were unfortunately not carried out.

When the rigid and the flexible body responses are compared with each other, vertical displacement of flexible barge is lower, at lower frequencies, towards the bow and stern part of the barge. A clear difference between the two can be observed in the wave contours at 3.926 rad/s by comparing Figure 5 and Figure 7. Strong bow and stern waves are developed at this frequency for the rigid body motions, whereas the flexible body tends to deform following the wave resulting in weak localized waves. This is the reason for larger vertical displacements in the rigid body simulation when compared to the flexible body. At higher frequencies diffraction effect dominates, which results in a similar wave contour around the body for both rigid and flexible body approaches (see Figures 6 and 8), leading to a small difference in predicted vertical displacements.

There are differences between the coupled CFD/FEM simulation results and the experimental measurements in some cases. In general, the predicted response of the flexible barge from amidships to the forward end agrees better with the corresponding measurements. The RAOs are slightly over predicted towards the aft end. It is thought that these differences can be improved by using more refined grids and fine tuning the numerical parameters used in the coupling.

The difference in mesh resolutions between Star-CCM+ and Abaqus could also be a source of instability. The finite element mesh is much coarser when compared to the Star-CCM+ mesh. Investigations using a finer mesh need to be carried out to study grid convergence.

In the coupled simulations constant co-simulation time of 0.005s is set for all cases. The grid size close to the body is quite small and the deformations of the barge are normal to these thin cells. It creates a scenario where the FSI boundary could possibly move more than the thickness of the cell near the boundary. A combination of expected motion and the thickness of cells near the FSI boundary define the time step and co-simulation time. Possibility of using different time steps and their effect on the solution has to be further investigated.

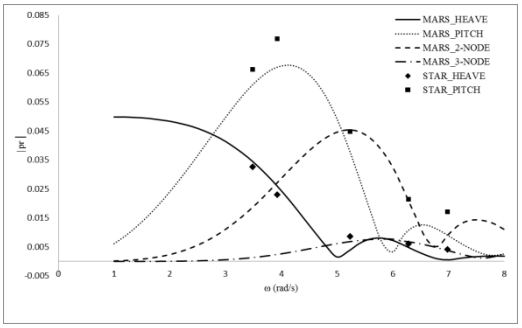

Figure 3: Heave, Pitch RAOs and principal coordinates of barge

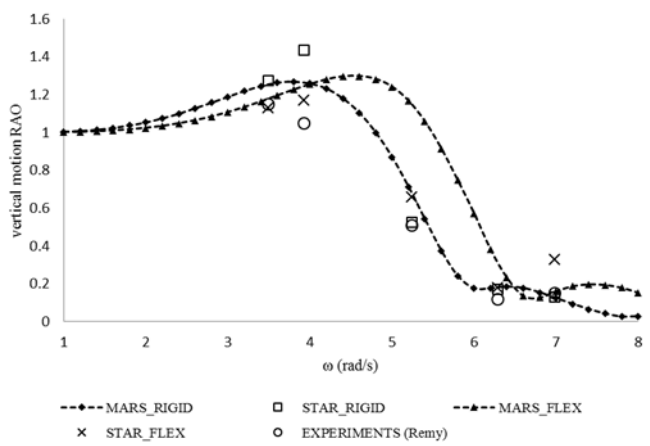

Response at Pt.12

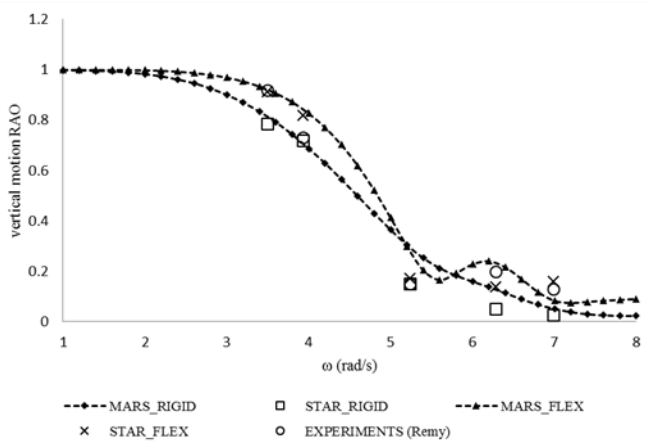

Response at Pt.9

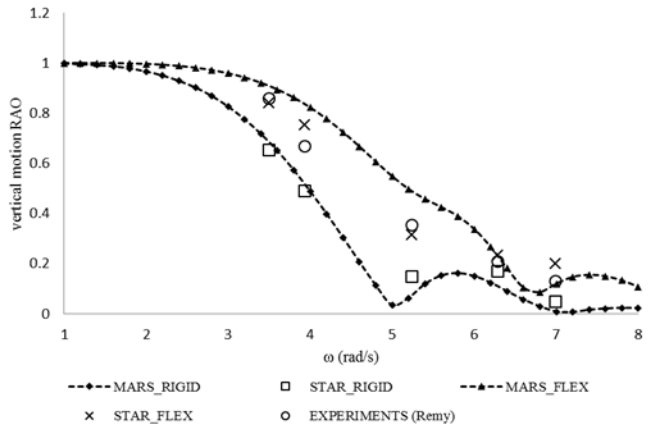

Response at Pt.7

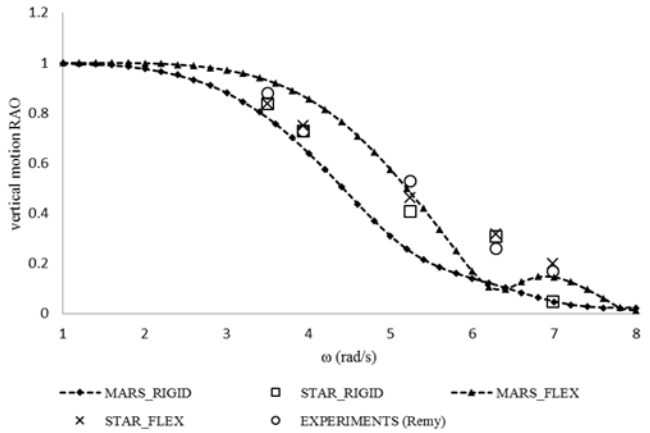

Response at Pt.5

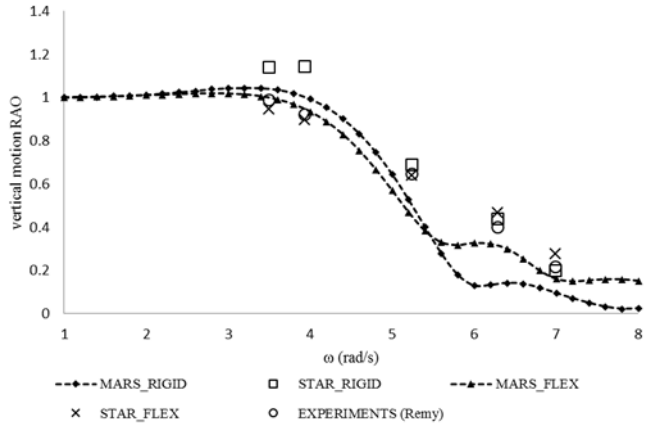

Response at Pt.3

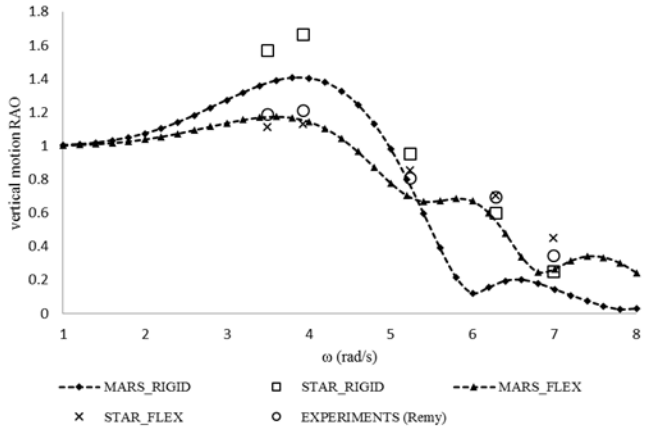

Response at Pt.1

Figure 4.RAOs of vertical displacements along the barge, point 12 near the stern and point 1 near the bow, for both rigid and flexible body analyses

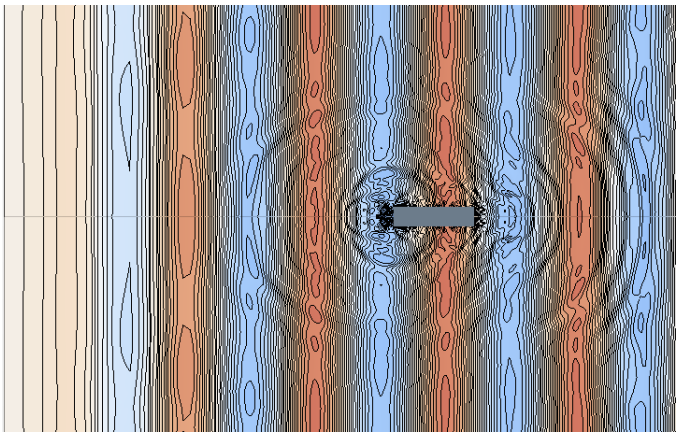

Figure 5. Instantaneous wave contour around the rigid body at a 11.5 s wave frequency of 3.926 rad/s

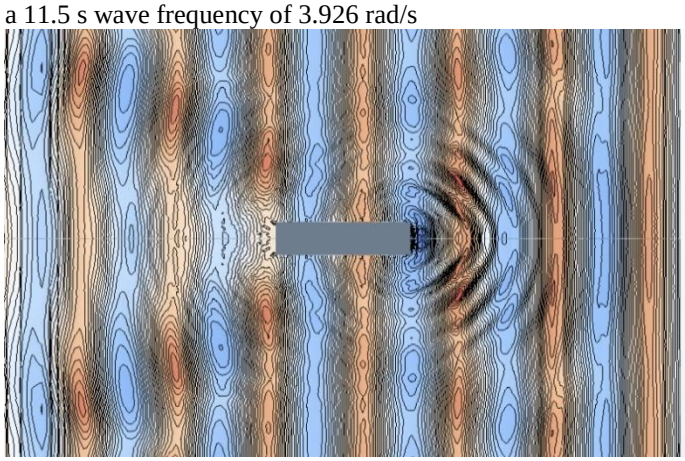

Figure 6. Instantaneous wave contour around the rigid body at 9.5 wave frequency of 6 rad/s

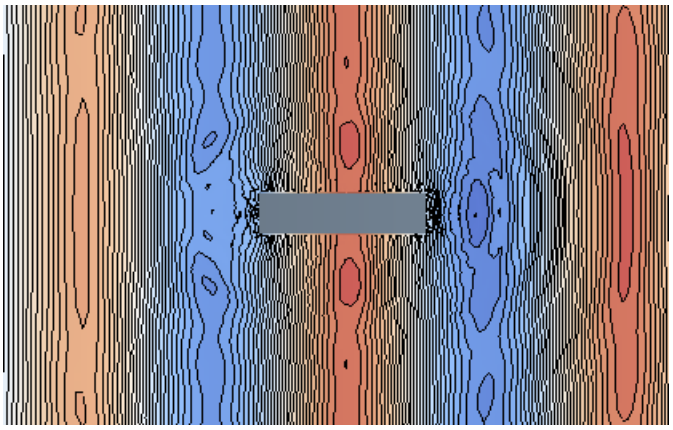

Figure 7. Instantaneous wave contour around the flexible body at 11.5 sec t for wave frequency of 3.926 rad/s

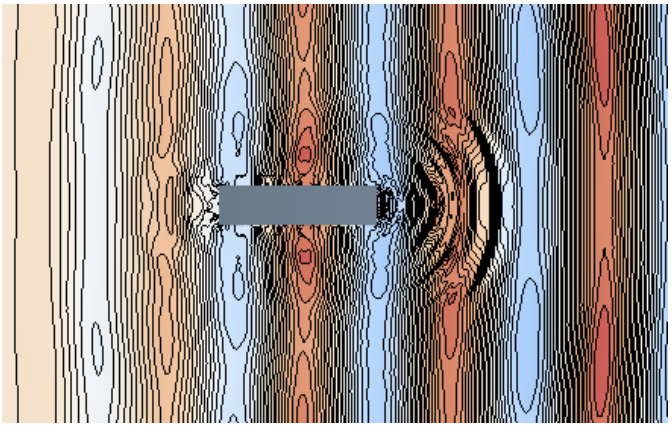

Figure 8. Instantaneous wave contour around the flexible body at 9.5 sec for wave frequency of 6 rad/s

5 CONCLUSIONS

The time domain hydroelastic investigation is carried out using commercially available software Star-CCM+ and Abaqus. The field equations are coupled using an iterative implicit scheme, and a Full Newton solution technique is used for solving the structural dynamics. The numerical solution is compared to experimental measurements and 2-D linear hydroelastic predictions. Calculations are carried out for both rigid body and flexible structural idealisations. Very good agreement is achieved between time domain predictions and experimental measurements in most cases, with some exceptions especially at the forward section of the barge.

Although the comparisons for rigid body motions between the two numerical methods agreed well overall, large differences were observed in the bow and stern regions of the barge at lower frequencies. This is believed to be due to strong bow and stern waves systems mainly influenced by the pitch, which are captured in CFD. CFD solves nonlinear Navier-Stokes equations, even when an inviscid flow model is selected which makes it more realistic than the linear potential flow code. Nevertheless, it should be noted that the rigid body approximation is not suitable for this very flexible barge.

Comparisons made between the present coupling technique and the experimental measurements showed very few discrepancies. Very good agreement was observed at relatively low frequencies, but slight differences were noted at higher frequencies. Strong diffracting wave systems are developed at these higher frequencies and they may be influencing the motion at the bow and stern sections. It is thought that the predictions at these relatively high frequencies can be improved by appropriate mesh refinement of fluid and structural models and coupling parameters (such as time step, URF's etc). This will be studied in detail in future investigations. Of the two hydroelasticity numerical methods, predictions using the coupled CFD method showed a far better agreement with experiments as it allows for nonlinearities. Influence of flexibility is clearly seen in the relatively low frequencies as the body deforms with the wave resulting in weak stern and bow waves, hence; lower vertical displacements when compared to the rigid body approach.

The results show that the coupling technique investigated is reliable and compares well with experimental measurements. The next stage of the investigations will involve applying the coupling technique to predict the forces and bending moments of the barge. Special attention will be focused at higher frequencies where resonance occurs for the 2-node vertical bending mode.

6 REFERENCES

Bishop, R.E.D. & Price, W.G., 1979. *Hydroelasticity of Ships.* Cambridge University Press.

Bishop, R.E.D., Price, W.G. & Tam, P.K.Y., 1977. A unified dynamic analysis of ship response to waves. *Trans. R. Inst Nav. Architects* 119: 363–390.

Brizzolara, S., Couty, N., Hermundstad, O., Ioan, A., Kukkanen, T., Viviani, M. & Temarel, P., 2008. Comparison of experimental and numerical loads on an impact bow section. *Ships and Offshore Structures* 3(4): 305–324.

Ferziger, J. & Peric, M., 2003. *Computational Methods for Fluid Dynamics* 3rd Edition. Berlin: Springer.

ISSC., 2012. Report of the Technical Committee I.2 on Loads. *Proc. 18th Int. Ship and Offshore Structures Congress*: 79–150.

Kim, Y. & Kim, K.H., 2009. Analysis of Hydroelasticity of Floating Shiplike Structure in Time Domain Using a Fully Coupled Hybrid BEM-FEM. *J. Ship Res* 50(1): 31–47.

Paik, K.J., Carrica, P.M., Lee, D. & Maki, 2009. Strongly coupled fluid–structure interaction method for structural loads on surface ships. *Ocean Engng* 36: 1346–1357

Peric, M., Zorn, T., El Moctar, O., Schellin, T. & Kim, Y.S., 2007. Simulation of Sloshing in LNG-Tanks. In *OMAE*.

Remy, F., Molin, B. & Ledoux, A., 2006. Experimental and numerical study of wave response of a flexible barge. In *4th Int. Conf. on Hydroelasticity in Marine Technology:* 255–264.

Seng, S., Andersen, I.M. V & Jensen, J.J., 2012. On the influence of hull girder flexibility on the wave induce bending moments. In *6th Int. Conf. on Hydroelasticity in Marine Technology:* 341-353.

STAR-CCM+, 2012. STAR-CCM+ version 8.04 manual.

Appendix C

COUPLED FLUID-STRUCTURE INTERACTION TO MODEL THREE-DMENSIONAL DYNAMIC BEHVIOUR OF SHIP IN WAVES

P.A.LAKSHMYNARAYANANA, P.TEMAREL & Z.CHEN

Fluid Structure Interactions Group, University of Southampton
Southampton, Hampshire, United Kingdom

7th International Conference on Hydroelasticity in Marine Technology, 16th-19th September 2015, Split, Croatia

7th International Conference on HYDROELASTICITY IN MARINE TECHNOLOGY

Split, Croatia, September 16th – 19th 2015

Coupled Fluid-Structure Interaction to model Three-Dimensional Dynamic Behaviour of Ship in Waves

P.A.Lakshmynarayanana[1], P.Temarel[1] and Z.Chen[1]

[1] Fluid Structure Interactions Group, University of Southampton, U.K

Abstract. Increase in computational power over the recent years has made it possible to investigate fluid-structure interaction problems using RANS/CFD and Finite Element software. However, the majority of these investigations are carried out using one-way coupling, thus omitting important fluid-structure interactions. A strong or two-way coupling between RANS/CFD and FEA is presented in this paper to model symmetric motion and response of flexible floating bodies in regular head waves. To illustrate this application, the RAOs of vertical displacements and wave-induced loads are calculated at various locations along a flexible three-dimensional barge (3-D) barge. The structure of the flexible barge is modelled as beam, in line with the flexible backbone model used in the experiments. The computational results are compared with experimental measurements and two-dimensional (2-D) linear hydroelastic predictions. A preliminary investigation for the static, still water, response of a flexible S-175 container ship model is also presented.

Keywords*: Hydroelasticity; Fluid-Structure interaction; RANS/CFD; wave-induced loads; Coupling; Modal superposition.*

Introduction

In the present study we focus our attention on fluid-structure interactions (FSI) of flexible floating bodies in waves by coupling CFD (Computational Fluid Dynamics) and FEA (Finite Element Analysis) software. Dynamics of structures or hydroelastic theories have to be taken into account when calculating motions and responses of 'softer' or flexible hulls owing to the increasing trend of the size of ships and offshore structures [1, 2]. In such cases, the response of the structure could significantly affect the flow field and fluid loading, resulting in a fully coupled system.

Hydroelastic investigations are predominantly experimental, using flexible backbone models, or numerical ranging from linear to partially nonlinear potential flow solvers [3, 4]. However, solving RANS (Reynolds-averaged Navier-Stokes) equations computationally to predict ship performance can be more efficient and realistic in some cases [5]. RANS/CFD can take into account nonlinearities associated with free surface flow, viscous effects, as well as local flow features [6].

The majority of investigations using RANS/CFD and FEA are carried out using one-way coupling, where the structural response of the structure does not affect the fluid loading. However, a fully coupled CFD/FEA method has to be established to accurately model the responses of flexible floating bodies. Such investigations show promising results [7, 8], but more is needed.

In this study a two-way coupling between a finite volume CFD method, using Star-CCM+ (version 8.04), and a finite element method (FEM), using Abaqus (version 6.13-1), is applied to assess the hydroelastic effects of a flexible barge in regular head waves. Thus, only symmetric distortions of the barge are calculated. 3-D computations are first carried out treating the barge as a rigid body to inform the modeling process. Star-CCM+ and Abaqus have inbuilt modules which makes it possible to couple them without any third party code. The barge is modelled as a non- uniform Timoshenko beam with properties as per the model test [9]. Numerical predictions are also obtained using 2-D hydroelasticity [10]. Predicted RAOs of vertical displacements at various locations along the barge are compared against experimental measurements. RAOs of vertical bending moment (VBM) and vertical shear force (VSF) predicted by the coupled CFD/FEM method are compared with 2-D hydroelastic results due to lack of experimental data. In addition the still water response of the coupled CFD/FEM model of the S-175 container ship is presented.

Numerical Method

Finite volume method

The numerical method used in Star-CCM+ is a finite volume (FV) method in which the flow is governed by RANS equations. In the case of an inviscid flow the RANS equations reduce to the well-known Euler equations, used in this paper. The fluid domain is discretized into a finite number of control volume (CVs). The discretized form of the governing equations is solved using a segregated iterative algorithm, called SIMPLE (Semi-Implicit Method for Pressure-Linked Equations). A detailed theoretical background is provided by Ferziger & Peric [11] .

Multiphase flows are implemented using the Volume of Fluid (VOF) tracking method. A sharp interface for free surface flows is maintained using the HRIC (High Resolution Interface Capturing) discretization scheme which is a blending of first and second order differencing scheme, and switched between them depending on the local Courant number.

The position of the body and the corresponding flow is updated at each iteration when the motion of the body at free surface is involved. The fluid grid is adjusted accordingly.

Grid adaptation and field data exchange in FSI

In the present study, grid adaptation to follow the motion of the body is implemented by two different methods, namely morphing and overset grids. Morpher collects a number of control points and their associated displacements to create an interpolation field and redistributes the mesh vertices.

An overset or overlapping grid consists of two regions; background and overset. The background grid is changed with changing wave length and height to include refinements, in vertical and horizontal directions, required to maintain suitable mesh resolution. The overset grids are attached to the floating body and move with it. This

method is highly efficient when compared to morphing in the case of free surface flows where the body undergoes large motion in waves.

In the case of rigid body simulations of the barge in head waves, grid adaptation has been carried out using overset grids. Both morphing and overset methods are applied to deform the grid in the two-way coupling. Morphing motion is set to the boundaries of the barge which deforms due to nodal displacements received from Abaqus. The overset grid boundaries move in response to the interpolation field created by the morphing motion using the "floating boundary condition" in the morpher.

The coupling is done by exchanging field data, i.e., pressure and nodal displacements between Star-CCM+ and Abaqus. Star-CCM+ uses the natural shape function of the FE topology to map the field data between fluid and structure grids.

Coupling scheme

The coupling scheme controls the sequence of data exchanges in the co-simulations. Star-CCM+ provides two coupling schemes, namely explicit and implicit coupling. In the explicit scheme, or loosely coupled problem, field data exchange takes place once every time step. In the implicit scheme field data is exchanged, by default, at every single iteration within a time step. Strong coupling is associated with dynamic problems where fluid loading and structural velocities change dramatically. The implicit scheme, being more stable, is ideal for such problems, but at a higher computational cost. The explicit scheme was tested with even very small time steps but resulted in pressure divergence; hence, the implicit scheme had to be used.

2-D Hydroelastic analysis

Generalised coordinates for rigid and flexible modes of the barge are calculated using the 2-D hydroelasticity analysis by Bishop et al [10] . In brief, 2-D strip theory is used to calculate the hydrodynamic properties of the barge, using Lewis form representation. The barge structure is modelled as a Timoshenko beam. Modal summation is employed to represent vertical (or symmetric) displacement, bending moment and shear force at a specified location. The solution of the resultant unified equations of motion in regular waves provides the requisite generalized coordinates.

Response of a barge in regular waves

Barge characteristics and Test conditions

The experimental model of a flexible barge comprising 12 connected caissons is considered for validation of the present numerical method [13]. The flexible backbone structure of the barge has a $1cm^2$ square cross-section and is placed at 57 cm above deck level. All caissons are rectangular in shape, except for the bow caisson, which has a beveled shape. Details of the experiments are described by Remy et al [9]. 0 shows the main particulars of the barge and the backbone.

The experimental measurements were carried out in regular (various headings) and irregular waves. Numerical simulations were carried out treating the barge as both rigid and flexible. Only regular head waves were chosen, as shown in 0, for validating the present numerical method, through comparisons with measured vertical displacements at: x/L: 0.08, 0.33, 0.5, 0.66, 0.83, 1.0, where x=0 denotes AP. The wave height (H) is 100mm for all except 50mm for 0.9s wave period. The rigid body modelling provided insight into domain size, damping zones and mesh refinement around the body and the free surface for each wave frequency. Numerical simulations were also carried out using 2-D hydroelasticity, providing the only comparator for VBM and VSF calculated using the co-simulation as these were not measured in the experiments.

Main particulars of barge

Length of barge (caissons + clearance), L	2.445 m
Beam	0.6 m
Depth	0.25 m
Draft	0.12 m
KG	0.163m
Total mass (caissons + equipment)	172.53 kg
Bending stiffness of backbone (EI)	175 N m^2

Domain sizes for regular wave periods and lengths used (* port side only)

Wave period (s)	Wave length (m)	Location of inlet (m)	Wake region (m)	Damping zone (m)	Side wall * (m)	Water depth (m)
1.8	5.058	7.6	10	7.6	8.0	4.0
1.6	3.996	6.0	8.0	6.0	8.0	4.0
1.2	2.248	5.0	5.0	3.5	8.0	4.0
1.05	1.711	5.0	5.0	3.5	8.0	4.0
1.0	1.561	5.0	5.0	2.0	8.0	4.0
0.9	1.264	5.0	5.0	2.0	8.0	4.0

Computational fluid domain and boundary conditions

The barge is aligned with the x-axis, with the stern at x=0, and y and z-axis in the athwarthships and vertical directions, respectively. The domain sizes for individual wave frequencies, for both rigid and coupled simulations, are shown in 0. A numerical beach of 1.5 λ (wavelength) is set at the outlet to reduce wave oscillations and prevent any reflections. Symmetry condition is used for the rigid body simulations, whereas full domain was modelled for the co-simulation cases. The length of the side wall (y-direction) is fixed as 8m on one side of the barge for all cases, as per experiments.

Boundary conditions were specified to mimic conditions in a towing tank. At the velocity inlet boundary the kinematics of the wave, i.e. the position of the free surface and velocity of the first order wave as field functions are specified. At the outlet boundary, the hydrostatic pressure of the wave and position of the undisturbed free surface are specified. All other boundaries are set to no-slip wall condition. A detailed description of the computational domain, grid design and numerical settings are given by Lakshmynarayanana et al [13] .

Computational grid design

A combination of trimmer, extruder and overset mesh is used for all CFD simulations. The body and free surface grid refinement is identical for both rigid body and co-simulations for the same wave frequency. Cartesian grids aligned with the free surface are desirable for free surface applications using VOF multiphase flows. Trimmer mesher produces a base mesh of hexahedral cells aligned with the free surface and trims this base mesh at the input hull surface creating polyhedrons. Once the base mesh is created, the side wall, in y-direction, and the outlet is extruded using user specified extrusion parameters (i.e. number of layers, stretching ratio and extrusion length) to produce orthogonal cells. Nevertheless, the mesh growth was kept under 1.1 to prevent any numerical reflections arising due to sudden change in grid sizes between adjacent cells [14].
The grid was refined along the free surface region, close to the barge and in the wave radiation zone around the barge using volumetric controls, as shown in 0 for 1.2s wave period.

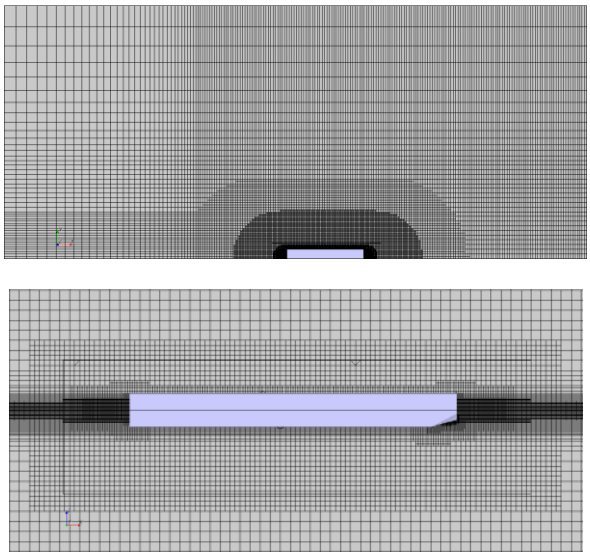

Grid refinement around the body and free surface for wave period of 1.2 s.

The waves radiated from the body form a circular wave contour in the bow and stern regions of the barge [15]. Hence, refinement around the body was also carried out to capture the disturbed wave pattern. In the free surface region, 45-60 cells are placed per wavelength and 12-15 cells per wave amplitude. Around 320 cells per wavelength and 160 cells per wavelength are clustered close to the barge and the wave radiation zone, respectively. The global mesh count for the co-simulation case varied from 2.3 million to 13.6 million. With grids of this size one can hardly find mesh sensitivity analyses in the literature on wave-body interactions. Nevertheless, Kim et al [16] performed convergence analysis for the radiation problem of a uniform flexible barge and concluded that the refinement effects were not significant except for very low frequencies of oscillation.

Solution strategy and numerical settings

Computations for both models were carried out using inviscid fluid model with an implicit unsteady solver. Temporal discretization and convection of segregated flow solver and VOF solver are 2^{nd} order accurate. Time step for the simulations were chosen such that the Courant number on the free surface at all times is less than 0.5. Iterative Implicit coupling scheme was chosen for the coupled simulations.

In the case of rigid body, body release and ramp times were specified based on the time step. It is best to allow the fluid flow to initialize and become steady before the calculation of body motions commences. A value of 50 time steps is specified as a release time. To minimize the effect of suddenly applied forces at release time, and facilitate a more robust solution by reducing oscillations, a ramp time equal to 10 times release time is specified.

The time-step size for both fluid and structural models in the co-simulation was the same. 12 inner iterations per time-step were used in the fluid solver and 2 iterations per data exchange were performed, different from the default in section 2.3, resulting in a total of 6 exchanges. The co-simulation displacement residuals reduced by an order of 4 at every time-step.

All simulations were run in parallel mode with single precision on the University of Southampton High Power Computing facility Iridis 4. It consists of a total of 12320 cores with each node containing 16 cores of 2.6GHz processing speed and 4GB RAM. For the co-simulations, the CPU hour for 1 sec of real time simulations varied from 35 hours to 126 hours, depending on the total mesh size.

F.E model

The flexible backbone is modelled using 48 2-node linear B31 beam elements in Abaqus 6.13-1. The beam elements are linked to dummy surface elements, 4-node quadrilateral SFM3D4, that represent the actual wetted surface of the barge. B31 is a Timoshenko beam element allowing for shear deformation. The shear stiffness evaluated by Abaqus based on the cross-section. Surface elements have no inherent stiffness but may have mass/unit area, though none is specified in this case. The dummy surface elements are linked to the nodes on the beam elements using kinematic coupling constraints, as shown in 0. All six degrees of freedom are constrained in the

kinematic coupling of beam nodes and the dummy surface, in the sense that the beam deformations are imparted on to the barge hull. The total mass of the barge is distributed on the beam elements as non-structural mass. The responses in waves are evaluated using two-way coupling between CFD and FEA. The solution for displacements, deformations, stresses and forces in ABAQUS is carried out using the virtual work principle. In the case of beam elements bending moments and shear forces are obtained from the stresses.

In 2-D hydroelastic analysis, the non-uniform beam is divided into 48 sections, to achieve consistency with the FE model. The mass distribution, moment of inertia for each segment, is similar to the FE model. Rotary inertia is assumed to be zero. The responses in waves are evaluated using modal analysis [1].

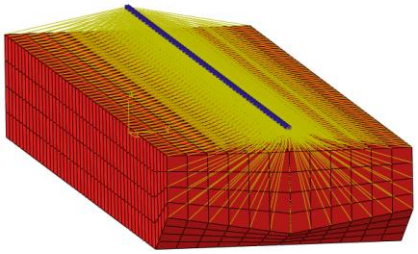

FE mesh: beam and dummy surface elements linked using kinematic coupling.

Results

Modal Analysis and free motion

Modal analysis was performed in Abaqus using the Block Lancozs eigen value extraction method. The natural frequencies and mode shapes obtained in Abaqus were compared to 2-D hydroelasticity calculations which use the finite difference (FD) method. The dry hull natural frequencies for the 2-node mode shape are 6.01 rad/s and 6.03 rad/s, for Abaqus and FD, respectively. The corresponding values for the 3-node mode shape are 16.43 rad/s and 16.49 rad/s.

A free decay test was simulated for the flexible barge to compare the wet natural requency of the barge with the experiments. For this test, the barge was initially inclined at 5 degrees to the still water line in both CFD and FE models. The Power Spectral Densities of the time histories of vertical displacement at the bow, amidships and the stern were obtained. The corresponding wet natural frequency for the 2-node mode is 6.2 rad/s and compares well with 5.9 rad/s obtained in the experiments.

Dynamic response of the barge

The responses of the barge treated as rigid and flexible body in regular head waves are presented in this section. Wave elevations were recorded at distance L in front of the barge. Average wave amplitude over 8-10 wave periods was used to calculate the RAOs. The maximum decrease in wave height for this window was only around 5-

6%. The rigid and hydroelastic predictions are distinguished by RIGID and FLEX, respectively, in 0. Predictions from CFD simulations (rigid and flexible) and 2-D hydroelasticity are denoted by STAR and MARS, respectively. Coupled simulations using wave heights in Section 3.1 is denoted by STAR_FLEX_0.1. It should be noted that the experimental values contain both rigid displacement and deformation.

Vertical displacements in waves

In general, the rigid body response predicted by 2-D hydroelasticity compares well with the CFD results. However discrepancies were noted, especially towards the forward part of the barge – see Figure 3(d). The predicted rigid body displacements at amidships show very good agreement. At the forward section, strong bow waves were seen to develop in the CFD simulations, influenced by pitch motion, from a wave frequency of 3.93 rad/s and upwards, shown in 0. With increase in frequency, diffraction becomes more dominant resulting in strong localized bow waves which is not well predicted by the 2-D linear analysis. The predictions using CFD is considered more reliable at forward and stern locations as it accounts for the nonlinear interaction and 3-D effects between wave and body - a drawback of 2-D strip theory.

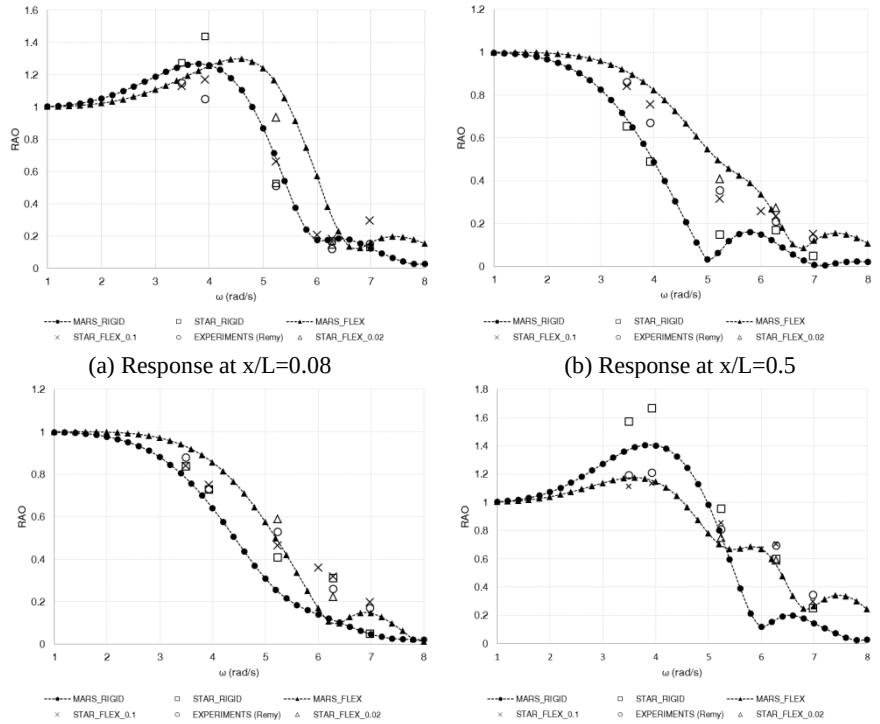

(a) Response at x/L=0.08

(b) Response at x/L=0.5

(c) Response at x/L=0.66

(d) Response at x/L=1.0

RAOs of vertical displacement along the barge at x/L=0.08, 0.5, 0.66, 1.0 from AP

RAOs from the CFD/FEM co-simulation, shown also in Fig.3, compare very well with the experimental measurements, especially from amidships to the forward end of the barge. The present method overpredicts the distortion at the aft end and amidships when compared with the experiments; maximum difference 15%. A grid convergence study is not conducted in the present simulations. Investigations using a finer mesh need to be carried out, in the future, to observe their effect on the solution.

2-D hydroelastic and CFD/FEM coupled predictions show fair agreement, although differences, of the order of 50%, can be observed at higher frequencies. The difference is attributed to strong diffraction effects at higher frequencies also prevalent in flexible body motions, albeit at higher frequencies as shown in 0. Of the two numerical methods, predictions using CFD coupling show much better agreement with experimental data. The ratio H/L≈1/25 possibly resulting in significant nonlinear effects. To linearize the problem and make the comparison with 2-D linear predictions more realistic, a smaller wave height of 20 mm (H/L=1/122) was tested for 5.24 rad/s and 6.28 rad/s in the coupled CFD/FEM simulations, denoted as STAR_FLEX_0.02. The displacements at most locations for the coupled cases now shift towards the 2-D linear hydroelastic predictions, resulting in better agreement. Although a small difference still exists between the two numerical methods, it is evident that magnitude of nonlinearities is one of the main reasons for the discrepancy in the previous cases.

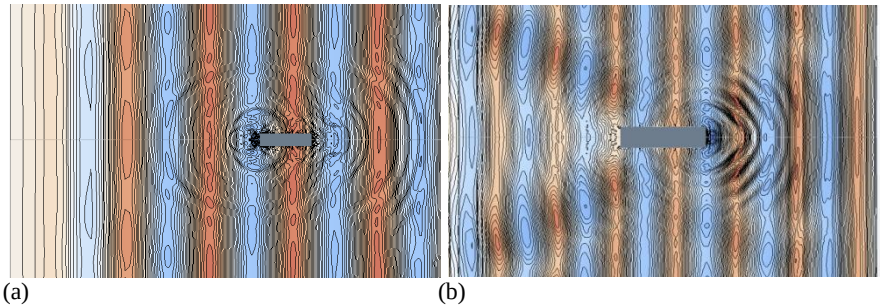

(a) (b)

Wave contours around the rigid body for (a) 3.93 rad/s at 11.5s (b) 6.28 rad/s at 9.5 s

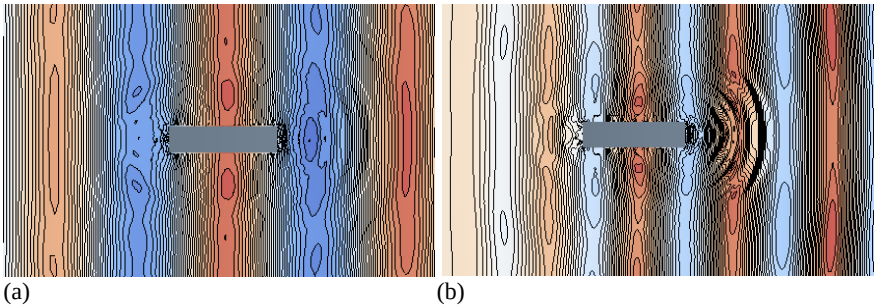

(a) (b)

Wave contour around flexible body for (a) 3.93 rad/s at 11.5s (b) 6.28 rad/s at 9.5 s

Vertical bending moment and shear force in waves

RAOs of VBM and VSF are shown in Figures 6 and 7, together with comparisons from 2-D hydroelasticity analysis. As can be seen from Figure 6, the first resonant peak is observed around 5.5 rad/s, which corresponds to λ/L=1 or ship-wave matching. In general, there is a fair agreement in RAO VBM, except at 5.24 and 6.28 rad/s, where the coupled CFD/FEM predictions are much smaller than 2-D linear predictions. To minimize the effects of nonlinearity, calculations were carried out for a wave height of 20mm at 5.24 rad/s and 6.28 rad/s and 10mm at 5.24 rad/s. For these cases, an increase in VBM at amidships and at 0.66L is observed, also observed in the corresponding displacements in Figure 3 when wave height was reduced. This still leaves a difference of about 30% between the 2-D linear and CFD/FEM predictions at amidships. No significant improvement is observed at the other two locations. Whilst examining the attitude of the barge in waves relatively large displacements in the longitudinal direction were observed. More investigations on the effect of this unphysical "head reach" on the VBMs (and VSFs) is required.

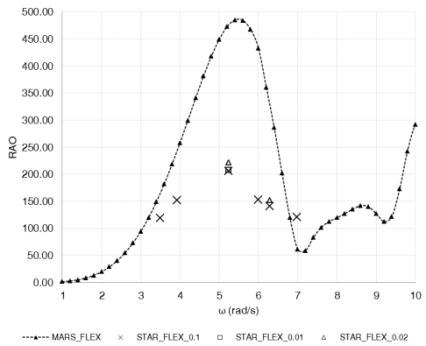

(a) Response at x/L= 0.33

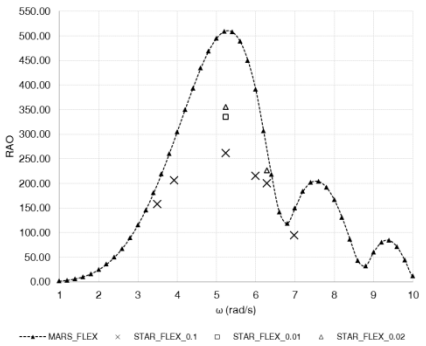

(b) Response at x/L= 0.5

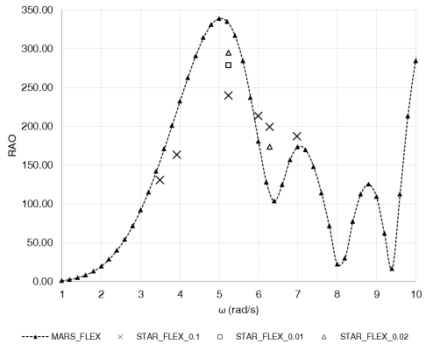

(a) Response at x/L= 0.66

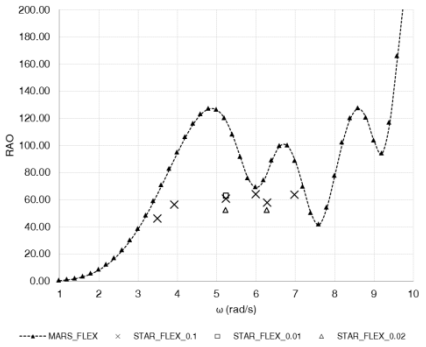

(b) Response at x/L= 0.83

RAOs of VBM along the barge for the flexible body analysis.

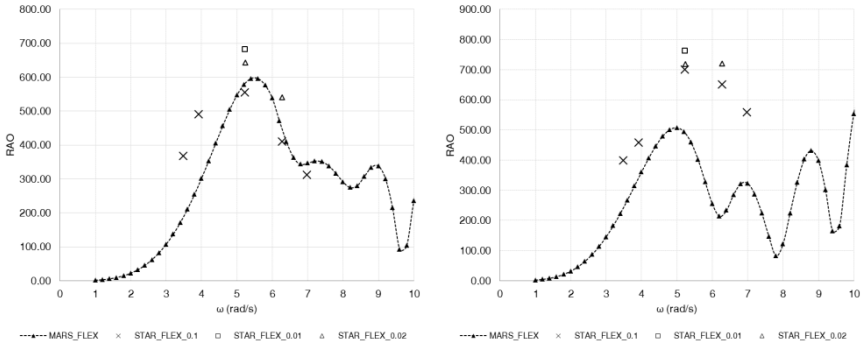

(a) Response at x/L= 0.33 (b) Response at x/L= 0.83

RAOs of VSF along the barge at x/L= 0.33 and 0.83 for the flexible body analysis.

The RAO VSF, shown in Figure 7, also show differences between the 2-D linear and coupled CFD/FEM predictions, of the order of 30%, the only exception being the stern location at x/L=0.08. No improved agreement could be obtained from the coupled CFD/FEM simulations with smaller wave heights. Lack of experimental data makes it difficult to reliably conclude as to which method is more accurate.

Response of the flexible barge in still water

The still water response of the barge was co-simulated and compared again with 2-D predictions, to shed light in the differences observed in waves. The static responses for the coupled CFD/FEM case were calculated after the forces and displacements had attained a steady value in the time domain. The still water VBM and deflection are shown in 0. The 2-D VBM is obtained using net load integration and modal summation, denoted as STATIC and MODAL, respectively. As can be seen the static VBM predicted by coupled CFD/FEM is 12 times larger than the 2-D static analysis. At the forward end of the barge, a high non-zero moment is also noted in the coupled simulation, which for a free-free beam must be close to zero. Even the deflections along the length are over predicted.

In the original FE model, shown in Figure 3, the number of beam nodes and longitudinal sections on the dummy surface were the same. To investigate the effect of a finer FSI surface, the longitudinal sections were doubled and each beam node was now linked to two longitudinal sections of the hull surface. The results are denoted as STAR_FLEX_REFINED in 0 and show no improvement.

The overall predicted static deflection is approximately 1 and 2cm, for the 2-D and coupled CFD/FEM methods. This is equal to or twice the backbone height , which is 1cm. Coupled CFD/FEM simulation was run using 10 times larger bending stiffness than that shown in Table 1, to assess sensitivity of VBM to deflection, denoted by STIFF. Furthermore, a uniform stiff rectangular barge was also co-simulated, denoted by RECT_STIFF. The stiffer barge has deflections and VBM much closer to the 2-D predictions and the uniform stiffer barge also has nearly zero VBM at FP. This analysis illustrates that there may be particular issues when evaluating loads using coupled CFD/FEM for this very flexible and nearly uniform barge.

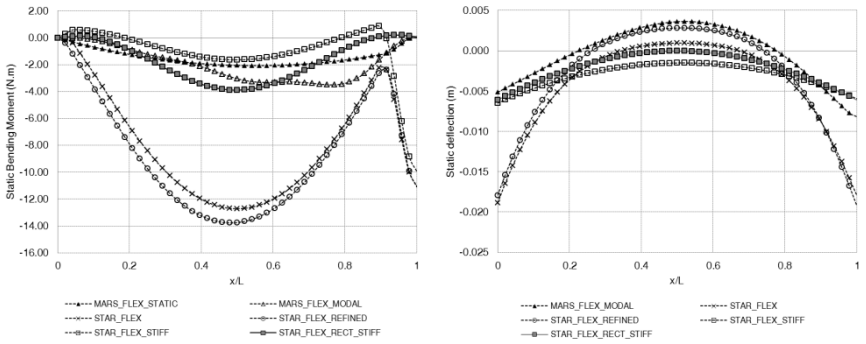

(a) Bending moment (b) Static deflection

Still water bending moment and deflection of the flexible barge

Still water response of S-175 container ship

The coupled CFD/FEM method is next applied to the S-175 containership model [17]. Due to the problems experienced with the barge in still water, the static response of S-175 was compared with 2-D method. The CFD and FE modeling follows the same process described in Sections 3.3 to 3.6 and the backbone properties are obtained from Wu & Hermundstad [18] using 20 beam elements and 9908 dummy surface elements. The CFD and FE models are shown in Figure 9, the former comprising of 700,000 cells. The predicted static VBM and VSF, shown in Figure 10, agree well with each other.

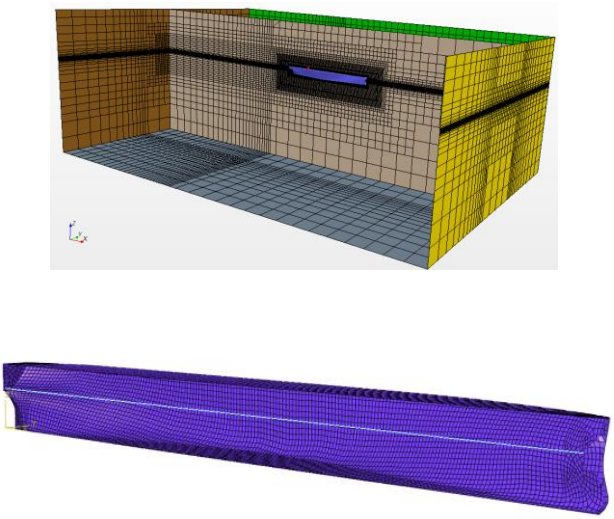

CFD and FE mesh for the S-175 containership

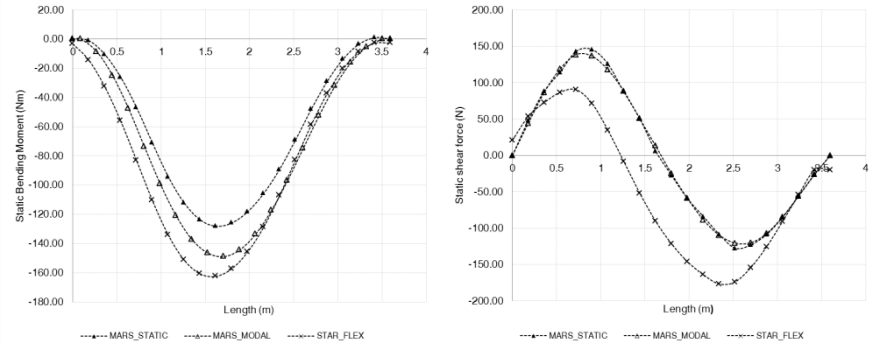

(a) Bending moment (b) Shear force

Still water bending moment and shear force for S-175 containership

Conclusions

The principal aim of this paper is to apply a coupled time domain CFD/ FEM analysis to investigate hydroelastic response of bodies in waves. This is achieved using commercially available software Star-CCM+ and Abaqus. The target application is the simulation of flexible barge in regular head waves. Calculations were carried out for both rigid body and flexible structural idealisations.

Very good agreement is achieved for the RAOs of vertical displacement between the CFD/FEM coupling and experimental measurements in most cases, with some exceptions especially at the forward sections of the barge. Differences observed between the coupled CFD/FEM simulations and 2-D linear predictions are mainly attributed to the influence of strong bow and stern waves systems, nonlinearities and 3-D effects. RAOs of VBM and VSF in waves using the two numerical predictions showed significant differences, especially in way of ship-wave matching region. Co-simulations carried out using small wave heights, to linearize the response, showed slight variation in VBM amidships indicating the influence of nonlinearities. Nevertheless, the difference in bending moment amidships was about 30%; the coupled CFD/FEM method predicting smaller response.

Still water VBMs calculated using CFD/FEM coupling showed significant dependence of the VBM on the magnitude of barge stiffness, hence deformation. It is believed that this may be due to this barge being very flexible, rather than a generic issue in the coupled CFD/FEM method. A preliminary investigation of still water VBMs for the S-175 containership showed promising results.

The results presented show that the coupling technique investigated is reliable and compares well with experimental displacements for a flexible barge. Discrepancies are observed between CFD/FEM coupling and 2-D hydroelastic predictions for bending moments and shear forces. An attempt has been made to explain the reason for these differences; however, lack of experimental data for the barge makes verification difficult. Further investigations are required, e.g. along the lines suggested in section 4.2.2. It is worth noting that investigations on FSI using CFD and FEA, e.g. [5, 7 and 8] perform the coupling between CFD and a solver based on modal analysis rather

than FEA. Co-simulation of the S-175 containership and comparison with available experimental measurements will follow.

Acknowledgements

The authors acknowledge the support of The Lloyd's Register Foundation through its University of Southampton Technology Centre and Lloyd's Register . The authors also thank Professor Molin and Mr. Remy for providing experimental data.

References

Bishop, R.E.D. & Price, W.G., 1979. *Hydroelasticiy of Ships*, Cambridge University Press.

Bishop, R.E.D., Price, W.G. & Wu.Y, 1986. A general linear hydroelasticity theory of floating structures moving in a seaway. *Phil. Trans. R. Soc. London*, A316, pp.375–426.

ISSC., 2012. Report of Committee I.2: Loads. *In Proceedings of the 18th International Ship and Offshore Structures Congress, Rostock*, Germany. 1, pp.79–150.

ITTC, 2014. The Seakeeping Committe final report and recommendations. *In the Proceedings of 26th ITTC*, Copenhagen.

Piro, D.J. & Maki, K.J., 2013. Hydroelastic analysis of bodies that enter and exit water. *Journal of Fluids and Structures*, 37, pp.134–150.

Querard, A.B.G., Temarel, P. & Turnock, S.R., 2009. The hydrodynamics of ship-like sections in heave, sway, and roll motions predicted using an unsteady Reynolds averaged Navier–Stokes method. In*: J. Engng Maritime Environment*, pp.227–238.

Seng, S., Andersen, I.M. V & Jensen, J.J., 2012. On the influence of hull girder flexibility on the wave induce bending moments. *Hydroelasticity in Marine Technology*. pp. 341-353.

Oberhagemann, J., Kromer, M., Cabos, C. & El Moctar, O., 2012. A fluid-structure coupling method based on field methods and a structural mode decomposition. *Hydroelasticity in Marine Technology*. pp. 267–276.

Remy, F., Moilin, B. & Ledoux, A., 2006. Experimental and numerical study of wave response of a flexible barge. *Hydroelasticity in Marine Technology*. pp. 255–264.

Bishop, R.E.D., Price, W.G. & Tam, P.K.Y., 1977. A unified dynamic analysis of ship response to waves. *Trans. R. Inst Nav. Architects*, 119, pp.363–390.

Ferziger, J. & Peric, M., 2003. *Computational Methods for Fluid Dynamics 3rd Edition*., Springer, Berlin.

Malenica, S., Moan, B., Remy, F. & Senjanovic, I., 2003. Hydroelastic reponse of a barge to impulsive and non-impulsive wave loads. *Hydroelasticity in Marine Technology*. pp. 107–115.

Lakshmynarayanana, P., Temarel, P. & Chen, Z., 2015. Hydroelastic analysis of flexible barge in regular waves using coupled CFD-FEM modelling. *In MARSTRUCT*. pp. 95–103.

STAR-CCM+, 2012. STAR-CCM+ version 8.04 manual.

Kim, Y. & Kim, K.H., 2009. Analysis of Hydroelasticity of Floating Shiplike Structure in Time Domain Using a Fully Coupled Hybrid BEM-FEM. *J. Ship Res.*, 50(1), pp.31–47.

Kim, J. H., Lakshmynarayanana, P., & Temarel, P. (2014). Added mass and damping coefficients for a uniform flexible barge using VOF. In ICHD.

Wu, Y., Chen, R. & Lin, J., 2003. Experimental Technique of Hydroelastic Ship Model. *Hydroelasticity in Marine Technology*. pp. 131–142.

Wu, M. & Hermundstad, O.A., 2002. Time-domain simulation of wave-induced nonlinear motions and loads and its applications in ship design. *Marine Structures*, 15(6), pp.561–597.